Dottorato in Scienze Molecolari e Biomolecolari
Dipartimento Scienze e Tecnologie Biologiche Chimiche e Farmaceutiche (STEBICEF)
Settore Scientifico Disciplinare SSD CHIM/09

Rational design of Carbon Nanodots as potential theranostic agents in breast cancer

IL DOTTORE
MARA ANDREA UTZERI

IL COORDINATORE
GIOVANNA PITARRESI

IL TUTOR
GENNARA CAVALLARO

CO TUTOR
NICOLÒ MAURO

CICLO - XXXV
ANNO CONSEGUIMENTO TITOLO - 2023

Index

1. Abstract

Carbon nanodots (CDs) have aroused increased attention as promising nanotools for drug delivery, fluorescence imaging, and NIR-induced photothermal therapy, due to their versatile and responsive surface, distinctive tunable fluorescence from the blue to the red region, and excellent photothermal conversion capability. This combination of physico-chemical and optical features in a unique nanometer platform offers the advantage of concurrent tumor treatment and monitoring of nanosystems biodistribution and cancer tissues. Therefore, the theranostic approach in cancer treatment improves early diagnosis and therapeutic outcomes, avoiding the limitations of unspecific conventional chemotherapy [1]. However, the structural, surface, and optical profile of CDs is strongly influenced by the synthetic scheme and the post-synthetic surface engineering adopted, allowing to design and modulate the physico-chemical and optical features of CDs in function of the applicative requirements [2–4].

The thesis focuses on the rational development of novel CDs synthesis, purification, and surface functionalization schemes for the development of theranostic nanosystems for breast cancer diagnosis and therapy. In a first step, in order to obtain highly homogeneous CDs with performant fluorescence properties in the red/NIR region and photothermal conversion capacity, different combinations of reagents (e.g. urea, citric acid, indocyanine green) were tested under solvothermal conditions, demonstrating for the first time how high operating pressure ($P > 18.5$ bar) can be effectively exploited to obtain performant CDs in cancer theranostic. However, a major limitation in the extensive application of CDs is the low yield that characterizes the synthetic processes. Therefore, in a second step, a new purification scheme was developed to maximize the yield, overcoming one of the major obstacles in the development and application of CDs-based nanosystems. At a later stage, the opportunity to synthesize CDs on a large scale enabled the development of a new strategy of surface functionalization of CDs with poly (D, L-lactide) by melt extrusion-induced transesterification process. This surface modification method was proven to be effective, scalable, and industrializable, paving the way for wider use of CDs in the development of nanosystems and nanocomposites for biomedical applications. In order to expand the application potential of CDs in the theranostic treatment of breast cancer, three different CDs-based hybrid nanosystems have been developed that combine fluorescence imaging with different therapeutic approaches. The versatility and surface reactivity of CDs have enabled the development of theranostic nanosystems for the delivery of different classes of drugs (e.g., irinotecan, doxorubicin, sildenafil), such as polymeric micelles and nanoparticles encapsulating CDs, and hybrid nanosystems consisting of diametrically surface functionalized CDs with modified cyclodextrins. The rational design of CDs-based nanosystems with performant theranostic properties enables the effective combination of fluorescence imaging with various therapeutic strategies, such as targeted drug delivery, ROS production induced by nitrogen and sulfur codoped CDs (intrinsic cytotoxicity), and/or activation of various programmed cell death pathways (e.g., apoptosis, necroptosis, autophagy) through NIR-induced photothermal therapy. Extensive characterization of the diverse theranostic nanosystems developed has demonstrated the versatility and multifunctionality of CDs in the formulation, which can be modulated through careful synthesis and surface design, and the potential of the combined therapeutic approach in the treatment of cancer therapy.

2. Introduction

2.1. Breast Cancer

Carcinogenesis is a multifactorial process that is primarily caused by both genetic predispositions and environmental causes [5]. The process of carcinogenesis takes place in three defined phases: i) initiation; ii) promotion; iii) progression. In the first phase (initiation), a stem cell acquires one or more mutations escaping from the homeostatic control of growth. The second phase (promotion) consists of the clonal expansion of the initiated cell that gives rise to a population of mutated cells. Subsequently (progression), the initiated cells convert to a malignant phenotype by acquiring additional genetic mutations. The latter stage includes the clonal evolution of tumor tissue [6]. The main mechanisms supporting the progression phase include evasion to programmed cell death mechanisms of apoptosis, high mitotic index, enhanced angiogenesis, resistance to anti-growth signals, and the ability to metastasize [7].

Nowadays, the incidence of cancer-caused deaths is steadily increasing becoming one of the leading causes of death worldwide. According to the GLOBOCAN 2020 data, breast cancer is currently one of the most frequently diagnosed cancers and the 5th cause of cancer death, with an estimated number of 2.7 million new cases worldwide by 2030 [8,9]. Invasive breast cancers encompass broad-spectrum tumor subtypes that vary in terms of clinical profile, behavior, and morphology. The World Health Organization (WHO) distinguishes at least 18 different histological types of breast cancer [10]. In detail, breast cancer (BC) is divided into several subtypes based on the expression of specific heterogeneous biomarkers, such as estrogen hormone receptor (ER), progesterone receptor (PR), and human epidermal growth factor receptor 2 (HER2) [11–13].

Based on receptor expression, breast cancer could be categorized into four groups:

i) BC expressing estrogen receptor (ER+);
ii) BC expressing progesterone receptor (PR+);
iii) BC expressing human epidermal receptor 2 (HER2+);
iv) Triple-negative breast cancer (TNBC) (ER−, PR−, HER2−) [14,15].

Molecular classification independently from histological subtypes classified invasive breast cancer into five molecular subtypes based on biomarker expression:

i) Luminal A (ER+ and/or PR+);
ii) Luminal B (ER+, HER2+ and/or PR+);
iii) HER2-enriched (HER2+);
iv) Basal-like (ER−, PR−, HER2−);
v) Normal-like (ER+) [5]

Gene expression analysis has thus identified several distinct breast cancer types that differ significantly in morphology, prognosis, and possible therapeutic strategies [16,17]. In general, ER receptor-positive tumors are well-differentiated, less aggressive, and tend to have a better prognosis than PR+ tumors [18,19]. HER2+ tumors are among the most aggressive, grow more rapidly, and have a generally worse prognosis. However, these tumors respond successfully to anti-HER2 targeted therapy [19,20]. TNBC that does not express hormone receptors is particularly difficult to treat, associated with poor prognosis and weak response to treatment, often requiring combination therapies [21,22].

Despite increased knowledge about the molecular profile of different cancer cells associated with early detection, breast cancer remains a largely incurable disease due to the heterogeneity of breast tumors [23]. Typically, heterogeneity is related to similar tumor types that are subtyped (inter-tumor heterogeneity), but also within tumors of the same type (intra-tumor heterogeneity). Therefore, tumor tissue may consist of different phenotypic subpopulations of cancer cells with different functions, marker expression, drug resistance, and clinical outcomes [13,24]. Intra-tumor heterogeneity results from the ability of tumor cells to adapt to changes in the microenvironment, often caused by conventional chemotherapy or radiotherapy and a significant lack of oxygen and specific nutrients [24]. This behavior reflects differences in tumorigenicity, senescence induction, signaling pathways, migration, angiogenesis, and the different response of tumor cells to anticancer drugs [25].

2.1.1. Tumor microenvironment: components and functions

The heterogeneity of breast cancer is also related to another peculiar aspect of tumor tissue, such as the multiple components of the tumor microenvironment (TME) [26,27]. It is increasingly recognized that human tumors do not consist of a homogeneous collection of neoplastic cells, but of a complex network in which malignant cells interact with a significantly altered and complex surrounding stroma, which creates a unique cancer environment that emerges in the course of tumor progression [28,29] This TME is created and continuously shaped by the interactions of the tumor with the host, orchestrating molecular and cellular events in the surrounding tissues. TME is now recognized as a critical element in tumor development and progression, as well as a measurable parameter of treatment response.

The TME can be considered at three levels, local (intratumor), regional (in the breast tissue), and distant (metastatic tissue) [30].

Each microenvironment is composed of multiple components:

i) Cancer-associated fibroblasts (CAF);
ii) Cells of the immune system (T cells, B cells, NK cells, dendritic cells, macrophages);
iii) Adipocytes;
iv) Endothelial cells;
v) Extracellular matrix-ECM (e.g. collagen IV, laminin, fibronectin, and glycosaminoglycans);
vi) Vascular system (blood and lymphatic);
vii) Soluble factors (e.g. cytokines, hormones, growth factors, and enzymes) [31,32] (Figure 1).

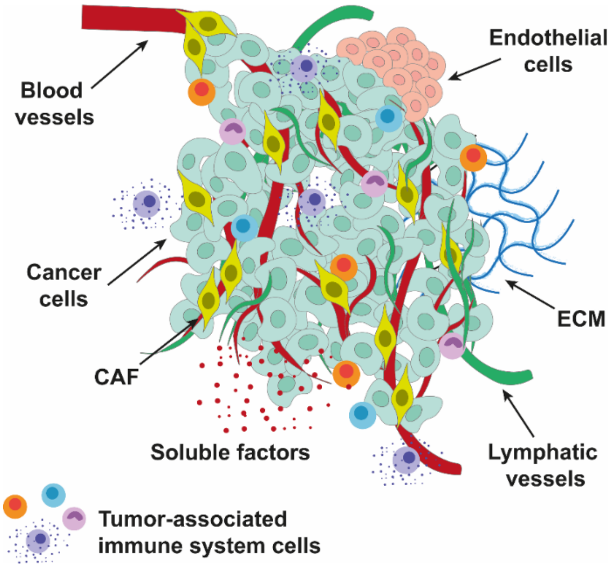

Figure 1. *Representation of tumor microenvironments and constituting elements.*

Although immune cells, stromal cells, vascular vessels, and ECM constitute the hallmark of cancers, the composition of the tumor microenvironment varies between tumor types.

TME through a dynamic and reciprocal relationship that develops between cancer cells and non-cancer components supports cancer cell survival, invasiveness, and metastatic dissemination, promoting the progression of cancer [33,34]. Tumor-associated stromal cells are a heterogeneous population that includes carcinoma-associated fibroblasts (CAFs), mesenchymal stem cells (MSCs), tumor-associated macrophages (TAMs), endothelial cells, pericytes, adipocytes, and lymphocytes. Unlike normal stroma which suppresses carcinogenesis, tumor stroma co-evolves with the tumor and dynamically adapts to the needs of tumor cells, promoting cancer progression [35,36]. Specifically, in solid cancer tissues, CAFs have demonstrated pathological relevance due to their wide range of functions. CAFs secrete growth factors that have a key component in ECM remodeling and deposition, stimulation of angiogenesis and vascular permeability, and immunosuppression [37,38]. This complex interaction between cells and the ECM eventually leads to more invasive tumor cells that can rupture connective tissue and metastasize [31].

The ECM is a three-dimensional network of proteins such as collagen IV, laminin, fibronectin, and glycosaminoglycans such as hyaluronic acid (HA), chondroitin sulfate, and heparan sulfate, which provide physical support [39]. However, the microarchitecture of ECM is surprisingly dynamic and versatile [40,41]. In addition to its structural roles, the ECM also guides the passage of cytokines and growth factors between cells, acting as a reservoir and thus enabling intercellular communication [40]. These growth factors are released as a result of remodeling of the ECM operated by metalloproteinases (MMPs) [39], such as MMP1, MMP7, MMP10, MMP11, and MMP14, secrete by adipocytes [34]. Therefore, an aberrant ECM also promotes tumor growth by preventing normal T-cells differentiation and maturation and the control of the immune system over tumor cells [41].

2.2. Conventional clinical approach and limitations

Nowadays, the heterogeneity of breast cancers represents a critical obstacle to the identification of the specific tumor type and the main challenge of appropriate and successful cancer management [24].

The principal clinical approach in cancer treatment consists of surgery, chemotherapy, hormone therapy, and radiotherapy. The main goal of non-metastatic breast cancer therapy is surgery to eradicate tumor mass and regional lymph nodes, preventing recurrence. Systemic therapy, on the other hand, can be either preoperative (neoadjuvant) or postoperative (adjuvant). The therapeutic approach has been chosen according to breast cancer subtypes [42]. For example, hormone therapy (e.g. tamoxifen, anastrozole, exemestane) is the most common therapeutic approach for ER+ BC to inhibit hormone production from the ovary [43]; while in the case of HER2+ BC, different anti-HER2 monoclonal antibodies (e.g. trastuzumab, pertuzumab, ado-trastuzumab emtansine) have been employed in combination with conventional cytotoxic drugs (e.g. docetaxel, doxorubicin, irinotecan). The treatment of TNBC is the most challenging tumor type and, in general, is treated with a combination of chemotherapy drugs or a combination of chemotherapy and monoclonal antibody against vascular endothelial growth factor [43–45]. However, conventional chemotherapy suffers from some important limitations:

i) Most known chemotherapeutic drugs are poorly soluble in water, leading to the need for appropriate formulation for their administration;
ii) Traditional chemotherapy shows marginal selectivity for cancer cells, resulting in major side effects and a strong impact on the patient's quality of life;
iii) The efficacy of chemotherapy is strongly influenced by multidrug resistance (MDR) phenomena [46,47].

In general, anticancer drugs target highly proliferative cells. However, a high mitotic index is common to both cancer and normal cells such as bone marrow, gastrointestinal mucosa, hair follicles, and gonads. This nonspecific mechanism of action quickly leads to severe side effects (e.g. myelosuppression, nausea, vomiting, hair loss, and reduced fertility), which have dose-limiting consequences [48]. In addition, the active principle of any anticancer drug is to induce DNA damage either directly (e.g. platinum-based drugs) or indirectly (e.g. topoisomerase inhibitors). The cellular response to DNA damage is repair or cell death. However, the DNA damage repair checkpoints of cancer cells are often dysfunctional influencing the effectiveness of DNA-damaging drugs [49].

2.2.1. Mechanisms of multidrug resistance

The efficacy of chemotherapy is also severely limited by MDR phenomena, which remain a major obstacle in cancer treatment. Drug resistance may be intrinsic to the characteristics of cancer tissues and cells (intrinsic drug resistance) or may be acquired during the treatment resulting in relapse after a variable time interval (acquired resistance). MDR in general is well defined at a genetic/epigenetic level, resulting in dysfunction of apoptosis, adaptive response, increased metabolic activities, loss of specific oncogenes, or more efficient repair of DNA damage (Figure 2.) [50,51].

Environmental-mediated drug resistance is one of the first obstacles in the diffusion and accumulation of drugs in cancer tissues and to treatment efficacy. The tumor stroma and ECM can form a protective microenvironment that allows cancer cells to resist the effects of drugs, also increasing the risk of relapse. The dense ECM represents a physical barrier that restricts the diffusion of drugs, limiting their accumulation and efficacy locally. In addition, the ECM can be reactive to drug treatment, becoming stiffer (increased deposition of collagen) and thus further reducing drug penetration [50]. The dense nature of the tumor stroma also leads to the compression of tumor vessels and increased interstitial pressure, which may hinder drug transport into and through tumor vessels [49]. Interactions between ECM and cells also contribute to drug resistance (adhesion-mediated drug resistance), making it rigid locally. Adhesion-mediated drug resistance was mainly caused by fibronectin and collagens, which are ligands for integrins. Several studies demonstrated that triple-negative MDA-MB-231 breast cancer cells were more resistant to chemotherapy (e.g. vincristine, paclitaxel) due to the ECM-cell interactions via integrin. In parallel, resistant Her2-positive breast cancer cells showed higher expression of integrin than drug-sensitive parental cells [50,52]. Integrin-mediated drug resistance is not limited to chemotherapies but is extended to radiotherapy [52].

Furthermore, as extensively discussed above, tumors are characterized by an important degree of molecular heterogeneity [53], whereby drug resistance can also be ascribed to the therapy-induced selection of a resistant minor subpopulation of cells that were present in the original tumor. Extensive studies have shown that MDR phenomena were initially linked to several cell membrane transporter proteins that promote drug efflux. These efflux proteins, named ATP-binding cassettes (ABC), are a family of transmembrane proteins that regulate flux across the plasma membrane [47].

There are three types of protein correlated to MDR:

i) Multi-drug resistance protein 1 (MDR1), also known as P-glycoprotein;
ii) MDR-associated protein 1 (MRP1);
iii) Breast cancer resistance protein (BCRP) [54].

MDR1 is associated with chemotherapy failure and is overexpressed in many tumors including leukemia, prostate, lung, and breast cancer [55–58]. Although drug solubility, distribution, metabolism, and elimination (pharmacokinetic) are all important factors that can limit the amount of drug that effectively reaches cancer cells, MDR-associated ABC proteins strongly affect the efficacy of chemotherapy determining the need to use large doses of chemotherapic [47] (Figure 2).

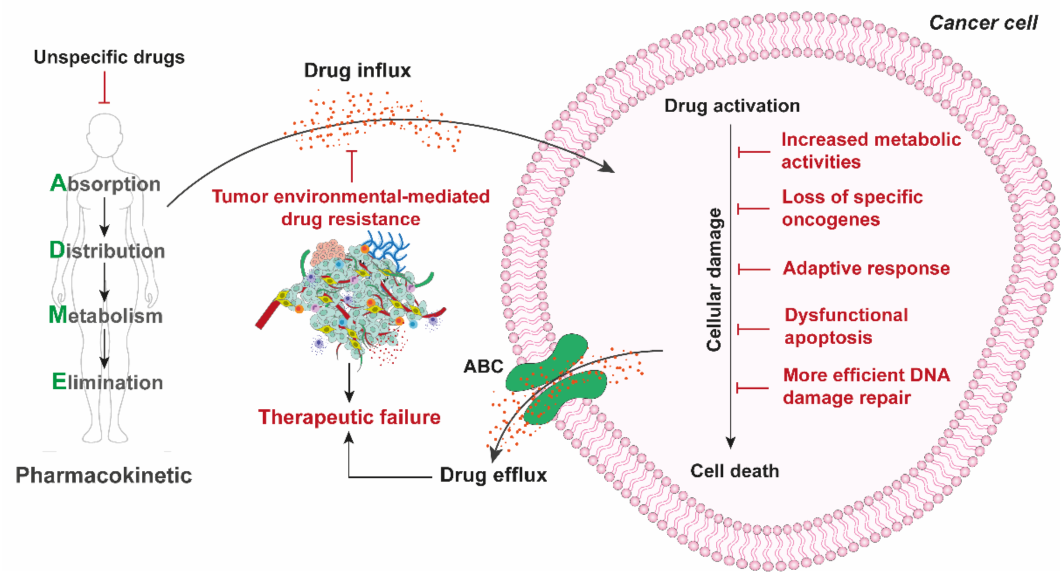

Figure 2. *Schematic representation of principles of drug resistance. Pharmacokinetic (PK) of unspecific drugs limit the amount of systemically administered drugs that reached the tumor. The accumulation of drugs in tumor tissue was also limited by the complex and dynamic TME that limits drug diffusion (environmental-mediates drug resistance). Cancer resistance highly involves intrinsic or acquired factors such as dysfunctional apoptosis, adaptive response, increased metabolic activities, loss of specific oncogenes, or more efficient DNA damage repair.*

Several strategies have long been used to overcome the obstacles of MDR (e.g. combinational therapy, chemosensitizers). However, these approaches do not efficiently prevent treatment failure and cancer recurrence [59].

Notably, new and innovative approaches to reverse drug resistance using drug delivery nanosystems have been developed. These consist of nanosized particles designed to deliver therapeutic payloads to tailor therapeutic regimes and treat the disease more effectively with less toxicity, and hold great promise in the fight against cancer [59,60].

2.3. Nanomedicine in cancer therapy: opportunities and challenges

Nanomedicine based on the development of nanosized drug delivery systems (DDS) has attracted increased attention as a viable strategy to overcome the severe limitations of conventional therapeutic approaches to cancer diseases [61]. DDSs have peculiar properties such as nanoscale dimensions (1-200 nm), high specific surface area, and variable physico-chemical characteristics [61,62].

Loading drugs into nanocarriers can offer many advantages over the use of free drugs:

i) Modulate the pharmacodynamic and pharmacokinetic profile of the drug;
ii) Prevent premature interaction with the biological environment;
iii) Avoid rapid degradation and elimination of the drug;
iv) Enhancing selective accumulation in the tumor tissue avoiding undesired side effects and MDR phenomena;
v) Release the drug in a stable and controlled manner [63–65].

Nanocarriers include a plethora of possible designs and architectures of organic or inorganic materials. Nanomaterials can be classified into polymer-based, lipid-based, and inorganic nanocarriers. Polymer-based nanocarriers include dendrimers, polymeric nanoparticles, micelles, and nanogels. Lipid-based nanocarriers include liposomes, exosomes, and solid lipid nanoparticles. Inorganic nanocarriers, on the other hand, can be divided into carbon-based nanocarriers (e.g. carbon nanotubes, carbon nanodots, graphene), metallic nanoparticles (e.g. gold nanoparticles, silver nanoparticles, iron oxide nanoparticles), and quantum dots [66] (Figure 3).

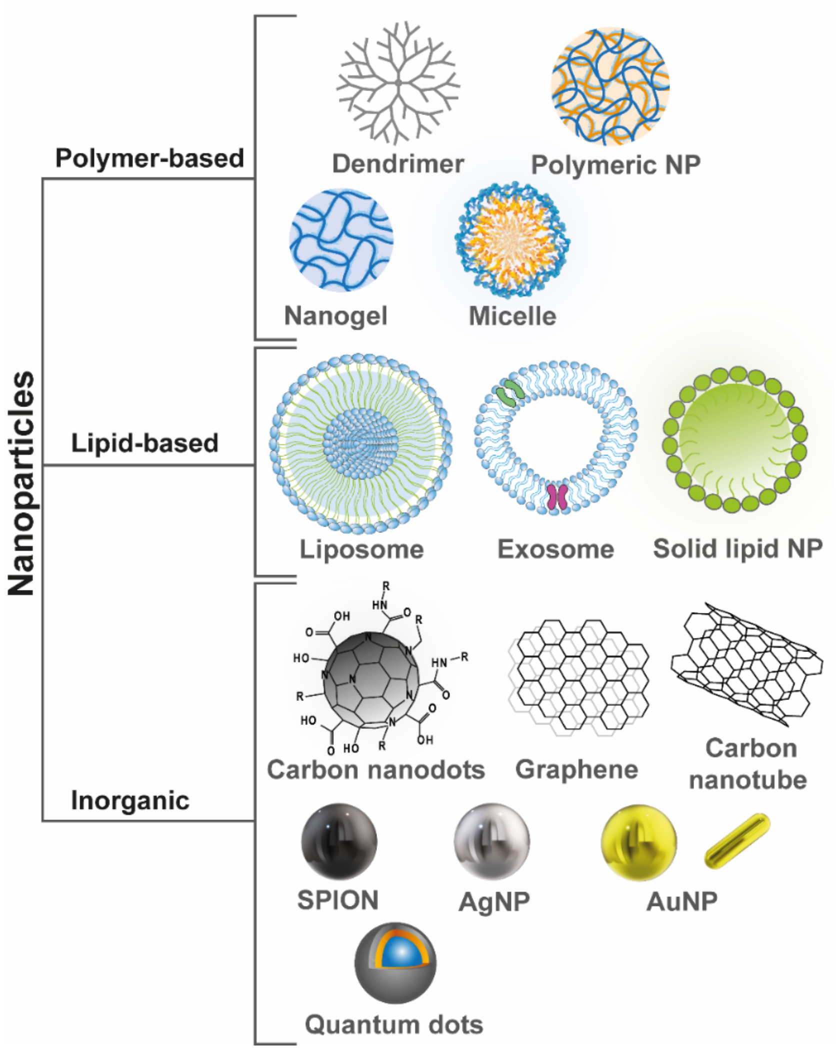

Figure 3. *Examples of nanosystems for drug delivery in cancer nanomedicine.*

2.3.1. Rational design of nanosystems to overcome biological barriers

A rational design of nanocarrier in terms of size, shape, charge, and surface is necessary to target tumors by circumventing numerous biological barriers. To this end, a thorough understanding of the physiology of healthy tissues and the pathophysiology of cancer tissues is crucial (Figure 4) [67].

- *Reticuloendothelial System*

The reticuloendothelial system (RES), also known as the mononuclear phagocyte system (MPS), negatively affects the ability of NP to be internalized by the tissue and constitutes the first obstacle that nanoparticles must avoid. Mononuclear phagocytic cells include monocytes, which circulate in the blood, and dendritic cells and macrophages, which are present in tissues such as liver, spleen, lungs, and bone marrow [68]. Phagocytic cells can recognize nanoparticles by inducing the release of cytokines (e.g. tumor necrosis factor, interleukins, interferons) that promote phagocytic cell-mediated clearance of nanoparticles from the bloodstream and local tissue inflammation [63,69]. Recognition by RES could be promoted by the interaction of proteins, lipids, or other macromolecules on the nanoparticle surface through a process also known as opsonization [67,70]. Therefore, rational modifications of nanoparticle surface could be a valid and necessary strategy to escape from the RES and prolong their circulation time. For this reason, several surface passivation strategies have been proposed, such as the involvement of zwitterionic ligands such as cysteine, glutathione, or PEGylation which has proven to be a valid passivating agent. PEGylation allows for the formation of a hydration shell on the nanoparticle surface, which makes the interaction with opsonins thermodynamically and sterically unfavorable, thus preventing their recognition by RES.[67,71].

- *Renal filtration and elimination*

In the designing of nanoparticles, the glomerular basement membrane of the kidney, which is involved in filtration and elimination, must also be considered. In particular, after the fenestrated endothelium with 70-100 nm pores, the nanoparticles must pass through the glomerular membrane (meshwork structure with 2–8 nm pores) and the epithelium with filtration slits (4–11 nm) [72]. Particle size and charge are both important parameters to consider in the renal clearance of nanocarriers. Spherically positive nanoparticles with a diameter of 6-8 nm have been shown to have a higher clearance than those negatively or neutrally charged of the same size [63]. At the same time, elongated forms such as carbon nanotubes have been shown to pass efficiently due to their long axis, despite their large molecular mass. In light of these considerations, diverse strategies could be employed, such as reducing the size of nanoparticles, modeling their shape, or developing biodegradable nanoparticles able to dissolve into smaller particles that can be easily removed [73]. Therefore, for the design of clinical nanomedicines, it is crucial to assess the trade-off between minimizing premature renal clearance of nanomedicines (diameter < 5 nm) to maintain their therapeutic effect and promoting their safe excretion from the body to prevent long-term toxicity [63].

- Pathophysiological barriers in cancer

Unlike normal vascularization, the general characteristics of tumors include a network of fenestrated blood vessels (gaps of 1-500 nm) and poor lymphatic drainage, which induce non-specific diffusion of free drugs. The inadequate function of poorly organized cancer vessels creates an oxygen and nutrient gradient, which is another crucial factor affecting drug delivery to all tumor cells. The defective vascular network can generate distinct microenvironments within tumor tissues that contribute to inter- and intra-tumor heterogeneity and influence clinical outcomes[74]. In addition, tumor tissues are characterized by distinctive features compared to normal cells, such as an acidic pH gradient, high glutathione concentration, or over-expression of peculiar enzymes (e.g. proteases, peptidases, hydrolases, and lipases) [75].

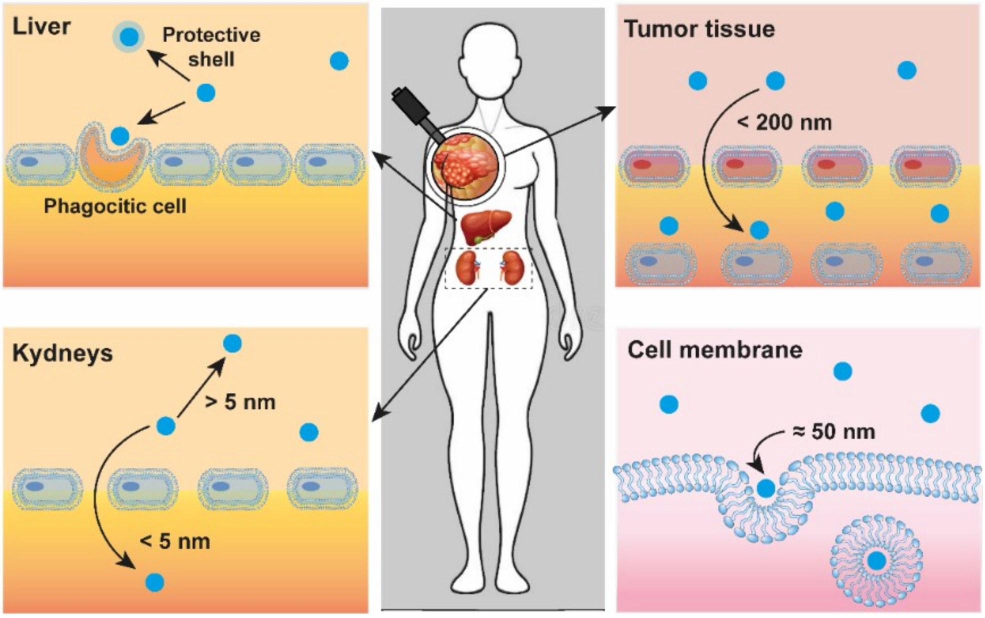

Figure 4. *Abilities of nanomedicines to overcome biological barriers of normal and cancer tissues.*

Therefore, the rational design of nanosystems with peculiar properties enables the advantageous exploitation of the physiopathological and physiological characteristics of tumor and normal tissues, respectively, and efficient cancer treatment [76].

2.4. Therapeutic strategies in nanomedicine

In order to overcome the biological barriers and the current severe limitations of conventional chemotherapy, nanoparticles can be designed to exploit different therapeutic strategies. The targeting approaches commonly used in nanomedicine can be divided into: i) passive targeting; ii) active targeting; iii) stimuli-responsive.

2.4.1. Passive targeting

Heterogeneous vascularization and poor lymphatic drainage strongly contribute to the complex topography and variable interstitial pressure within tumor tissues, which collectively result from dysregulation of vascular endothelial growth factor (VEGF), nitric oxide, bradykinin and tumor necrosis factor (TNF) production [74,77]. Thus, increased permeability and heterogeneity of the vascular network of cancer tissues result from the rapid and defective formation of new vessels (angiogenesis), modification of existing vessels, and the recruitment and differentiation of bone marrow-derived endothelial precursors (vasculogenesis) [78]. In contrast to the unspecific diffusion of free drugs, the nanometer size of DDSs allows extravasation through leaky vessels and accumulation in tumor tissues due to inefficient lymphatic drainage (Figure 5). This phenomenon, known as the enhanced permeability and retention (EPR) effect, could be a valid strategy to improve the therapeutic index of the drug and its pharmacological efficacy [74].

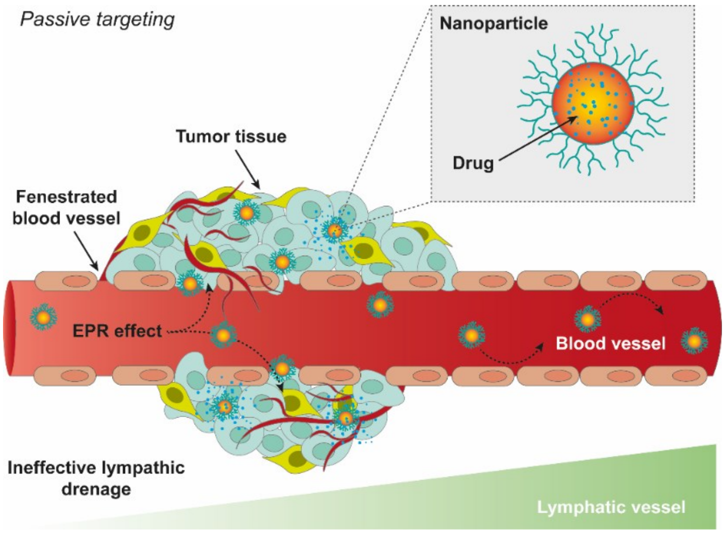

Figure 5. *Representation of passive targeting of nanoparticles based on enhanced permeability and retention (EPR) effect of cancer tissues.*

Currently, several passively targeted DDSs are in clinical use (e.g., Doxil™, Abraxane™, Marqibo™, DaunoXome™, and Onivyde™ in the US; Myocet™ and Mepact™ in Europe; Genexol-PM™ in Korea; and SMANCS™ in Japan) [64]. In addition to these, several other DDSs, including EndoTAG-1, AZD2811, and CPX-1 have also demonstrated safety and/or therapeutic effects in clinical studies [79].

The EPR effect is influenced by several factors, such as size and shape of the nanosystems. It was demonstrated that the use of smaller nanoparticles can allow enhanced extravasation and deeper penetration into the tumor [80]. Diverse studies on nanoparticles of different average sizes suggest that the threshold size for extravasation into tumors is < 200 nm [81]. For example, Tang et al. showed by comparing the distribution of silica nanoconjugates with diverse average sizes (20, 50, and 200 nm) that a diameter of 50 nm allows for the greatest tumor penetration and retention over time and the consequent highest pharmacological efficacy [82] (Figure 4.). Another possible strategy reported in the literature is the development of multistage nanosystems capable of disassembling into their smaller components [73,83]. In addition, diffusion and convection of nanocarriers through the tumor interstitium are further hindered by an intratumoral pressure gradient, which is influenced by the dynamic remodeling of ECM (as reported in Section .2.2.) [84,85]. These peculiar features of cancers contribute to the generation of a distinct tumor microenvironment, which allows for inter- and intra-tumor spatial and temporal heterogeneity and a variable EPR effect, adding an additional level of complexity to the control of DDS extravasation [35,61,62].

Therefore, taking into account these peculiar features of tumor tissues, optimization of the physiochemical properties of DDSs is crucial to exploit the tumor pathophysiology and must therefore be personalized to each tumor type, location, and stage to maximize therapeutic efficacy [86]. Although passive targeting approaches constitute the basis of clinical therapy, the random nature of this approach makes it difficult to control the process, which in some cases suffers from several limitations [60].

2.4.2. Active targeting

Another targeting strategy is represented by active targeting. This approach involves decorating nanocarriers on the surface with targeting agents that can be selectively recognized by cancer cells through antigens or receptors [79,87] (Figure 6). To maximize specificity, the targeting agent must be uniquely expressed on the surface of cancer cells or overexpressed on target cells compared to normal cells [62,87]. A wide range of targeting agents have been studied, such as proteins (e.g. transferrin, antibody, and their antigen-binding fragments), nucleic acids (aptamers), vitamins (e.g. folic acid, biotin), carbohydrates (e.g. hyaluronic acid), peptides (arginine– glycine–aspartic acid, RGD) [60]. The binding of some targeting ligands to their cellular receptors can cause receptor-mediated internalization, facilitating nanoparticles transport and subsequent drug release within cells via a specific pathway once the particles reach the extracellular space of tumor. In the function of the receptor-dependent or independent endocytic pathway, intracellular trafficking can also be controlled [88]. For example, macromolecules taken up by clathrin-dependent receptor-mediated internalization (e.g. transferrin, riboflavin) are typically destined for lysosomal degradation. On the other hand, clathrin-independent internalization (e.g. folic acid, biotin) leads to endosomal accumulation and sorting in a non-degradative way [89]. To further promote DDS accumulation in the target tissue, surface ligands can also be employed to target intravascular tumor cells or tumor blood vessel endothelial cells (e.g. vascular cell adhesion molecule-1, $\alpha_v\beta_3$ integrin, vascular endothelial growth factors) [90,91].

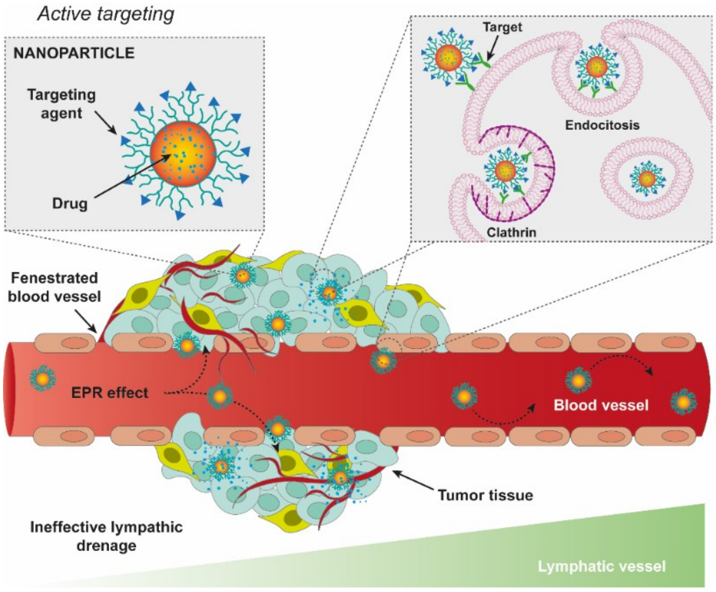

Figure 6. *Representation of active targeting of targeted nanoparticles and possible pathways of cell internalization.*

Therefore, the choice of targeting ligand is fundamentally governed by: i) the specific characteristics of the target receptor, including the receptor expression, whether internalization is required; ii) the design and biodistribution of the nanoparticle itself; iii) the peculiar properties of the target tumors [92].

2.4.3. Stimuli-responsive nanosystems

The rational design of multifunctional nanocarriers capable of sensing and responding rapidly to signals from the tumor microenvironmental or external factors has attracted increasing attention to develop more performant and flexible nanosystems [93]. Such stimuli can result in a change in nanoparticles size, zeta potential, or carrier disassembly, promoting nanoparticle penetration deep into the tumor and endocytosis by tumor cells, thereby achieving much more efficient tumor cell targeting and local drug release [71]. The next generation of smart nanocarriers, also known as stimuli-responsive nanocarriers, can respond to two classes of stimuli:

i) External stimuli (e.g. light, magnetic field, ultrasound);

ii) Internal stimuli (e.g. acidic pH, enzymes, hypoxia, elevated reductive conditions) [94–100] (Figure 7).

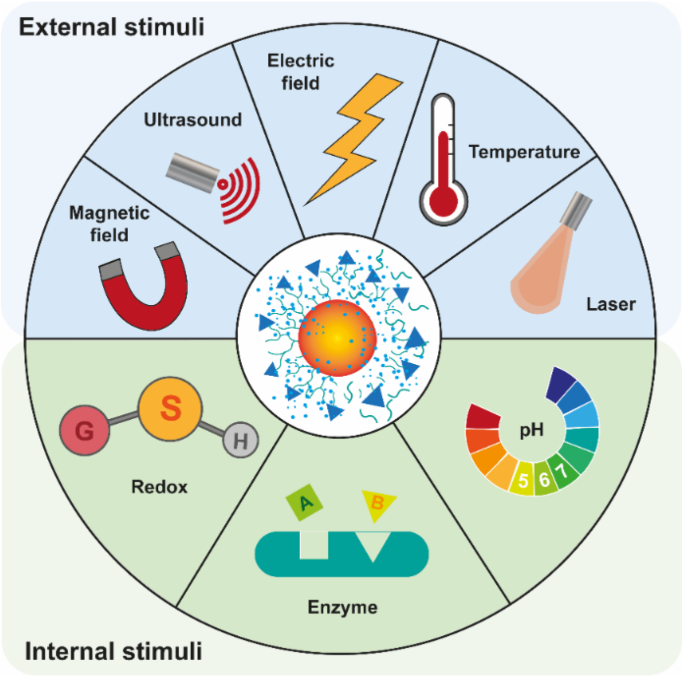

Figure 7. *External and internal stimuli exploitable in the design of stimuli-responsive nanosystems.*

- *pH-responsive nanosystems*

The most widely used triggers for stimuli-responsive nanosystems, due to their universality in most solid tumors, are represented by the acidic pH, including the pH of the extracellular tumor microenvironment ranging to 6-7 and intracellular endosomes and lysosomes characterized by a pH of 4-6 [101]. The decreased pH is caused by the increased glucose uptake and aerobic glycolysis in cancer cells, which leads to an increase in lactate production [102,103]. The mechanisms of various pH-sensitive nanocarriers with different design basis include ionizable chemical groups, acid-labile chemical bonds, pH-sensitive peptides, and pH-responsive. However, numerous researches demonstrated that there are some limitations in exploiting the acidic pH of the tumor microenvironment. First of all, the acidic pH is typical of the region near blood vessels, limiting the effectiveness of pH-responsive nanosystems in the function of their localization in tumor tissue. Moreover, sometimes pH differences between the normal tissue and tumor tissue are not significant enough to trigger responsiveness [71].

- *Enzyme-responsive nanosystems*

The upregulated enzymes by tumor cells and tumor stroma is another important trigger for the design of enzyme-responsive nanosystems [104,105]. The development of nanomaterials incorporating specific moieties (enzymatic substrates) that can be recognized and degraded by overexpressed enzymes allows for tumor-confined and spatiotemporal drug release, thereby achieving superior efficacy in tumor-targeting, enhanced deep tumor penetration, and cellular internalization with reduced side effects [106]. There are several types of enzymes overexpressed in solid tumors, including proteases (e.g., matrix metalloproteinase and cathepsin B), peptidases (e.g., aminopeptidase, legumain), hydrolases (e.g. hyaluronidase) and lipases (e.g., phospholipase A2) [71,106]. The expression level of enzymes is correlated to the type of tumor. For example, legumain and cathepsin are particularly overexpressed in several cancer cells such as breast cancer, gastric cancer, and colorectal cancer [106]. Extracellular enzymes such as matrix metalloproteinases and hyaluronidases are ubiquitously upregulated in tumor tissues.

- *Redox-sensitive nanosystems*

This class of stimuli-sensitive nanosystems takes advantage of intracellular concentrations of glutathione (GSH) (approximately 2-10 mM) one thousand times higher than those in the extracellular space (approximately 2-10 μM) [107,108]. More importantly, compared with healthy cells, the level of GSH is about four times higher in cancer cells. The huge concentration gradient in GSH can efficiently ensure the responsiveness of the redox-sensitive nanosystems [108]. These type of nanosystems typically contains disulfide bonds that are susceptible to the rapid cleavage by GSH. The presence of disulfide bonds can achieve several functions including nanosystem disassembly, degradation, and fast drug release. Several disulfide bond-based redox-responsive nanosystems have been developed, these redox-sensitive DDS should be designed carefully to make them not only stable in the blood circulation but also in the tumor tissue before entering into tumor cells [109–111].

Although internally triggered delivery systems are generally effective in achieving site-specific drug delivery, their efficacy is limited by the variability of the inter- and intra-individual tumor microenvironment. Therefore, the development of systems responsive to external stimuli is of particular interest to achieve better spatio-temporal control and reduce the variability in response dictated by the heterogeneity of tumor tissues [112].

- *Ultrasound-responsive nanosystems*

Drug delivery and release from nanocarriers can also be triggered by external ultrasound due to thermally- or mechanically-induced effects. Ultrasound not only can trigger the release of drugs from carriers, but it can also increase the permeability of biological barriers (e.g. cell membranes, blood-brain barrier) through the formation of cavitation bubbles and increased temperature, resulting in enhanced drug diffusion [113]. In addition, another useful mechanism of ultrasound results from the energy lost from ultrasound waves that propagate through tissue and are partially absorbed and scattered. These events push away nanoparticles by enhancing their extravasation and diffusion through the tumor matrix [114].

- *Magnetic-responsive nanosystems*

Magnetic-responsive nanoparticles, such as superparamagnetic iron oxide nanoparticles (SPIONs), are also being studied for drug targeting applications. The main advantages of magnetic-responsive DDSs are that by employing a non-invasive magnetic field they can be guided or held in place and heated to trigger drug release or to produce hyperthermia/ablation of tissue [115,116].

- *Light-responsive nanosystems*

Among the several stimuli exploited to develop stimuli-sensitive DDSs, light irradiation has attracted increased attention due to the ease of fine-tuning its intensity, spatio-temporal exposure, and non-invasiveness of the approach. The absorbance of photon energy by materials depends on the corresponding band gap energy in the highest occupied molecular orbital [113]. Considering that UV/UVvis light is absorbed by several endogenous chromophores (such as oxy- and deoxyhemoglobin, lipids, and water), light-responsive nanosystems operating in this wavelength range have some limitations [117]. For these reasons, NIR-responsive nanosystems are particularly interesting and efficient due to high tissue penetration and low invasiveness of NIR light [113]. Severe light-based strategies have been used to design novel smart DDSs that can be classified into three broadly defined categories: i) photochemically triggered, in which the absorbed light energy is sufficient to break covalent bonds directly or through a photochemical reaction; ii) photoisomerization, in which the excess energy causes structural changes; iii) photothermal, in which the energy of the absorbed photons is dissipated via vibrational motion into heat [118] (view Section 2.7.1.).

2.5. Theranostics: from drug delivery to imaging

Awareness of the extreme complexity of tumor tissues and the important intra-individual and inter-individual variability has led to the need to combine therapeutic strategies and diagnostic approaches in a single nanoplatform to enable early diagnosis and real-time monitored treatment (Figure 8) [119]. The combinatorial approach emerges as an alternative to the separate administration of diagnostic probes and pharmacologically active molecules. The efficient combination of therapy and diagnosis in a single nanosystem (theranostics) conducted to an extreme versatility of theranostic nanoplatform, would contribute to the development of optimized and individualized treatment protocols, offering the opportunity to perform a "personalized nanomedicine" [120]. The main goal of the personalized theranostic approach is to combine the plethora of advantages offered by the use of nanosized DDSs (e.g. improved pharmacokinetics, reduced side effects, controlled drug release) with concurrent diagnosis, monitoring of the disease progress, therapeutic response, and real-time drug distribution [121]. The ability to monitor drug distribution and accumulation in target or off-target tissues offers numerous advantages. Firstly, screening for drug accumulation at the target site makes it possible to identify patients who respond positively to treatment from others who require a different therapeutic approach. In addition, undesired accumulation in healthy tissues can be assessed, favoring the determination of the possible risk of patients developing serious side effects [119,122]. Therefore, the possibility to have early feedback in real-time offers the important advantage to optimizing the therapeutic approach with the best safety profile, permitting better disease management without waiting for traditional endpoints and possibly understanding the causes for failure of some drug targeting approaches [120]. To achieve this goal, nanosystems are the most promising platforms for the development of multifunctional theranostic nanosystems due to their versatile design that allows contrast agents to be integrated into the core and/or the surface [123].

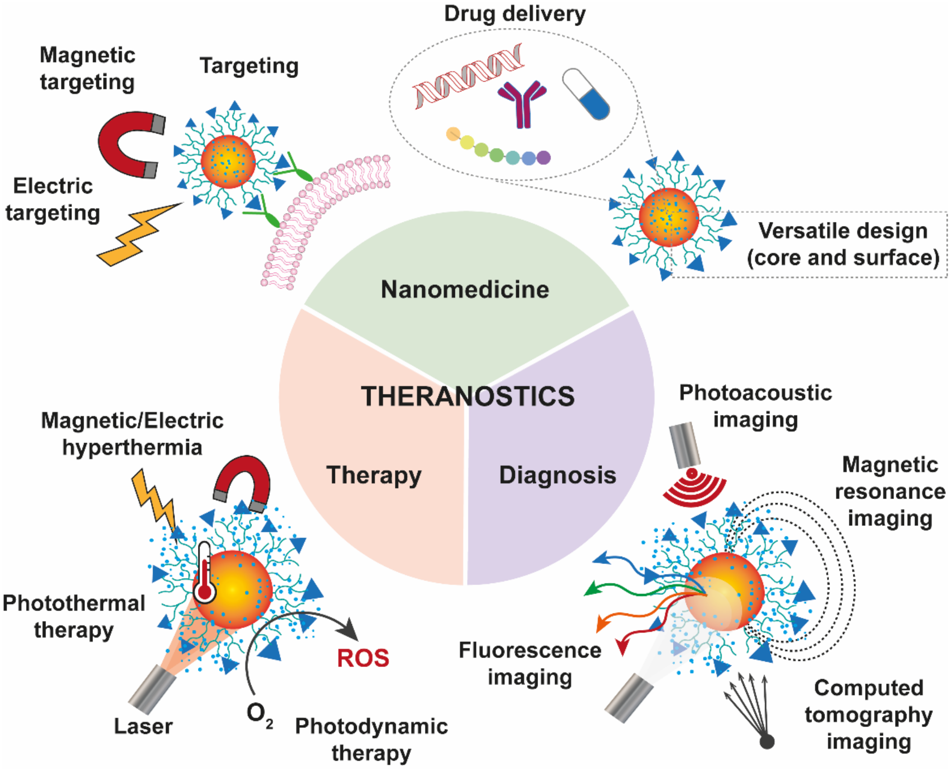

Figure 8. *Theranostics results from the advantages of the use of nanomedicine with the combination of different therapeutic strategies and imaging modalities.*

2.5.1. Imaging modalities

Numerous imaging modalities have been developed and the advantages and limitations of each approach have been deeply investigated.

- *Magnetic resonance imaging*

Magnetic resonance imaging (MRI) is a non-invasive imaging technique that exploits strong magnet and radiofrequency waves to produce images of internal organs. MRI has become the most widely used diagnostic tool due to its high spatial resolution and unlimited tissue penetration [124–126]. The most explored magnetic nanoparticles are the superparamagnetic iron oxide nanoparticles, also known as SPIONs, due to their biocompatibility and ease of synthesis [127]. Although numerous MR contrast agents have been developed and used for clinical diagnosis, the disadvantages of this modality are low sensitivity, time-consuming use, and high cost [124].

- *Computed tomography imaging*

Computed tomography (CT) is an imaging modality used to obtain three-dimensional images of the tissue of interest, combining X-ray images taken from diverse angles [124,126,128]. The use of targeted CT contrast agents allows for increased differentiation between normal and cancer tissues. Several alternative contrast nanoagents have been proposed in this field such as nanosystems containing iodinated compounds, bismuth-based nanoparticles, and gold nanoparticles (AuNPs) [129,130]. Although CT allows rapid diagnosis, high spatial resolution, and deep tissue penetration, related radiations, and contrast agents are often associated with important collateral effects [131].

- *Photoacoustic imaging*

Photoacoustic imaging (PAI) is a diagnostic approach that exploits a pulsed laser as an energy source and ultrasonic waves as signals [132,133]. The principle of operation is the ability of in vivo components (e.g. hemoglobin, melanin, myoglobin) to convert incident light energy to heat (photothermal effect). This temperature increase induces a thermoelastic expansion that produces ultrasonic waves. To maximize photoacoustic signals in vivo, diverse PAI contrast agents with high photothermal coefficients have been developed. These agents include, for example, organic contrast agents (e.g. indocyanine green, evans blue, fluorescent proteins), AuNPs, silver nanoparticles (AgNPs), SPIONs, quantum-dots (Q-dots), and carbon nanodots (CDs). The PAI technique offers high contrast and resolution, but low sensitivity and limited tissue penetration compromise its use [124].

- *Fluorescence imaging*

Fluorescence imaging (FLI) involves the detection of light emission of fluorophores by the absorption of light at a specific wavelength [124,126,134]. In particular, for in vivo applications, near-infrared (NIR) fluorescent agents have aroused increased attention due to their enhanced deep tissue penetration and low scattering and autofluorescence of tissue components (biological transparent window) [135]. Representative fluorophores with peculiar NIR absorption profiles include organic dyes (e.g. indocyanine green, fluorescein isothiocyanate, alexa fluor 750), Q-dots, AuNPs, and CDs [134,135]. Compared to other imaging modalities, FLI is non-invasive and gives high-contrast and resolution images, in fact, depending on the wavelength exploited, some problems of tissue penetration may be reported [136].

Compared to conventional organic dyes, Q-dots initially emerge as a valid alternative due to their superior fluorescence, resistance to photobleaching, and long blood circulation time [137–139]. Q-dots are semiconductor nanocrystals of 2-10 nm in size such as cadmium selenide, cadmium telluride, indium phosphide, and indium arsenide [138], characterized by tunable multicolor fluorescence as a function of average size [137]. However, their application is strongly affected by cadmium nephrotoxicity [140]. Unfortunately, even for gold nanoparticles that have shown excellent optical properties, photostability, biocompatibility, and biodegradability remain critical obstacles to their clinical translation [141]. Carbon nanodots, due to their low toxicity and brilliant fluorescent profile, emerge as a promising theranostic agent for the development of drug delivery nanoplatform useful in cancer therapy and diagnosis by high-resolution fluorescence imaging.

2.6. Carbon Nanodots (CDs)

CDs were discovered serendipitously in 2004 during the process of purification of single-walled carbon nanotubes through preparative electrophoresis. Since then, CDs have gradually become a rising star in the family of carbonaceous nanomaterials [142].

CDs are a new class of carbon nanomaterials with sizes in the range of 1-10 nm, which have aroused increased attention in recent decades due to their superior optical properties, low toxicity, chemical- and photo-stability, water solubility, ease of synthesis and versatile chemical surface (Figure 9). This combination of properties allows CDs to be used in a very wide range of applications such as bioimaging, sensing, photovoltaics, theranostics, and optoelectronics [142–144]. In particular, multicolor fluorescence from blue to near-infrared (NIR) has gained particular interest in the development of long-wavelength emissive CDs-based nanoplatforms as a new powerful strategy of fluorescence imaging (FLI) useful in cancer diagnosis. Moreover, carbon nanodots also proved to be excellent nanoheaters due to their ability to photothermally convert NIR light into heat, making them a promising candidate in the field of photothermal therapy (PTT) and fluorescence imaging [1] in cancer treatment (Figure 9).

From a structural standpoint of view, CDs are quasi-spherical 0-D carbon-based nanoparticles typically composed of carbon, oxygen, nitrogen, and hydrogen [145], characterized by a range of possible core structures (e.g. graphitic, amorphous, C_3N_4 crystalline core) and surface functional groups (e.g. carboxyl, hydroxyl, amine, amide) (Figure 9.). The core structure, surface state, and size distribution, which consequently determine the chemical, physico-chemical, and optical properties of CDs, depend closely on the synthetic approach adopted [2,146].

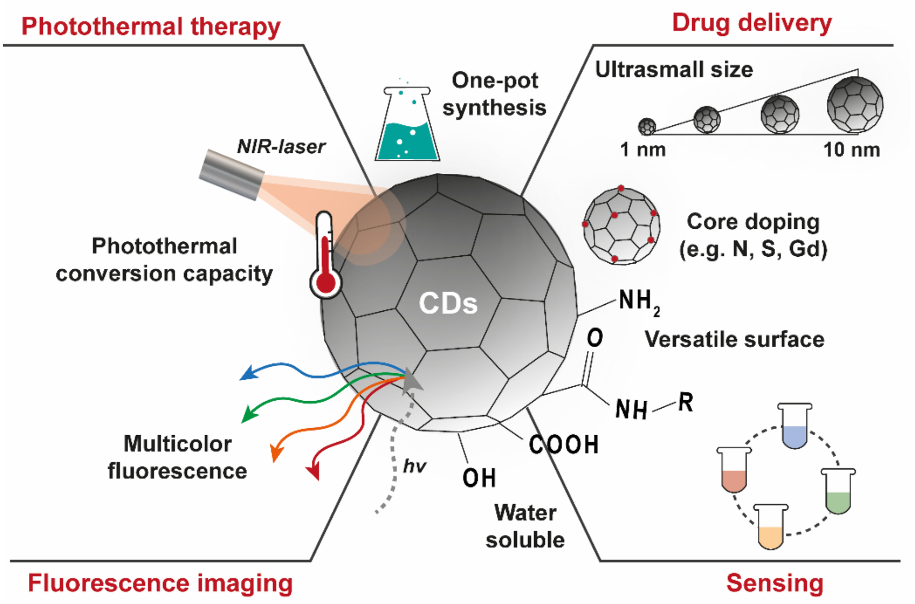

Figure 9. *Schematic representation of CDs' structural, chemical, and optical properties, and relative possible biomedical applications.*

2.6.1. Methods of synthesis

Approaches for CDs synthesis can generally be classified into two main groups: top-down and bottom-up methods [144] (Figure 10).

In the top-down approach, CDs are generated by chemical or physical processes of cutting relatively macroscopic carbon structures, such as carbon nanotubes, graphite columns, graphene, or suspended carbon powders (Figure 10). An important advantage of top-down synthesis routes is that the resulting CDs typically have homogeneous and well-defined structures similar to the structure of the precursors [147]. However, these types of CDs do have not native fluorescence, but require surface passivation with polar moieties to impart high fluorescence [148].

In contrast, bottom-up methods take advantage of the carbonization of different molecular precursors (e.g. citric acid, urea, aminoacid, polymers), typically chosen for their low melting points (Figure 10). In addition, the selection of molecular precursors rich in heteroatoms (e.g. urea, thiourea, lysine) allows the production of doped CDs for example with nitrogen, sulfur, or phosphorus [149]. A major advantage of bottom-up routes is that the resulting CDs are particularly fluorescent without the need for post-synthetic chemical modifications. Bottom-up syntheses are more versatile than top-down approaches because they allow CDs structures to be easily modulated and the core and surface to be doped with heteroatoms [2].

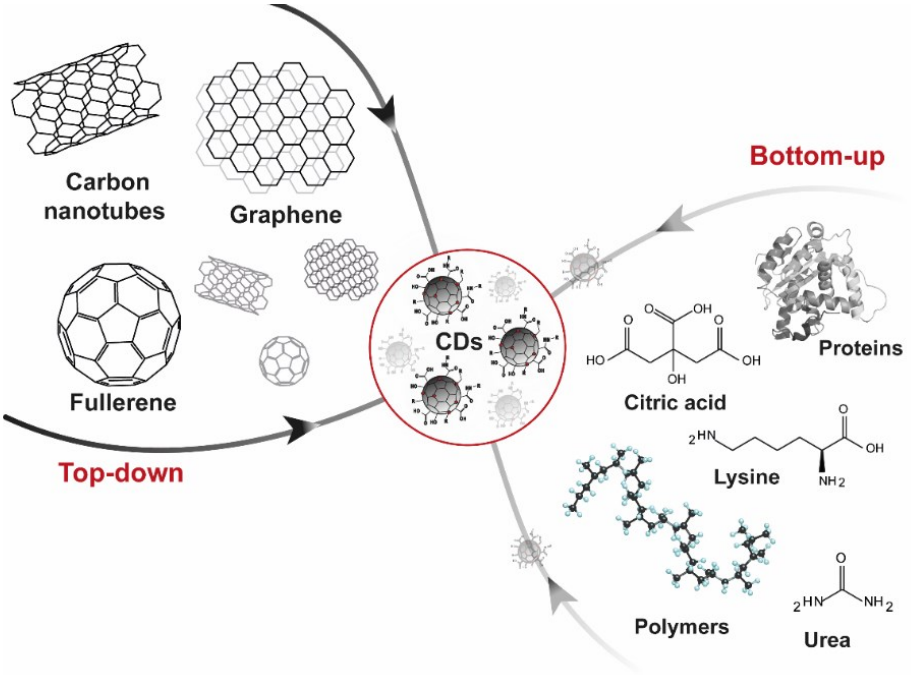

Figure 10. *Top-down and bottom-up synthesis methods of CDs and relative examples of starting reagents.*

The most common top-down approaches include:

i) laser ablation;

ii) electrochemical oxidation [150].

- *Laser ablation*

Laser ablation was the first method exploited for the synthesis of CDs. This top-down method is used for the production of different types of nanoparticles by exploiting the interaction between the pulsed laser beam and the surface of the solid precursors [148]. Traditional synthesis by laser ablation involves several steps and rigid reaction conditions. Hu et al., therefore, designed a one-step protocol for CDs synthesis by laser ablation, irradiating a suspension of graphite powder in polymer solution with a 1064 nm laser. This approach conducts the simultaneous surface passivation of CDs, determining the formation of natively fluorescent CDs. Therefore, by selecting the starting precursors and solvent, it was possible to prepare CDs with distinctive optical and physico-chemical profiles. Moreover, it was observed that changing the pulse duration from 0.3 ms to 1.5

ms allows for modulating the size of CDs from 3 nm to 13 nm. Therefore, the nucleation and growth process could be modulated by varying the pulse duration [151]. On the other hand, Reyes et al. demonstrated the correlation between the wavelength of the laser employed and the size distribution of the obtained CDs. In detail, they demonstrated that the ablation of graphite in acetone at 355 nm allows the formation of highly homogeneous crystalline CDs with an average size of 5 nm, while the use of a 532/1064 nm laser induces the production of carbon aggregates. Moreover, the homogenous crystalline CDs were highly fluorescent probably due to the active participation of acetone as a reagent that induce the surface functionalization of CDs with ketone groups [152].

- *Electrochemical oxidation*

Electrochemical synthesis exploits a redox reaction that takes place in an electrochemical cell under the influence of an electric current applied between two electrodes separated by the electrolyte. The electrochemical synthesis of CDs was first demonstrated by Zhou et al. when they produced graphitic CDs using multi-walled carbon nanotubes as the electrode in an electrochemical cell by applying a potential cycle between -2.0 to +2.0 V. The CDs obtained were spherical with an average size of 2.8 nm and an emissive profile in the blue region [150]. Another important aspect of electrochemical synthesis is the influence of the alkaline environment as demonstrated by Li et al. They demonstrated that graphitic CDs synthesized from graphite in an alkaline environment allow for a bright emission, which does not occur under acidic conditions. Thus, it seems to be that the fluorescence of CDs may be related to the surface oxidation state induced by the presence of OH^- groups favored by the alkaline environment [153].

Bottom-up methods include:

i) microwave-assisted synthesis;
ii) solvothermal decomposition;
iii) hydrothermal decomposition [150].

- *Microwave-assisted synthesis*

Similar to the laser ablation route, microwave-assisted synthesis can also provide intense energy to break off the chemical bonds of starting reagents. The microwave technique has become an increasingly popular method as a potential strategy to overcome some problems related to conventional heating processes such as inhomogeneous heating that results in the broad size distribution of the nanoparticles obtained [154]. This approach of synthesis is a cost-effective, convenient method of heating and eco-friendly, that offers largely reduced reaction time [155]. The synthesis of CDs by microwave pyrolysis was first proposed in 2009 by Zhu et al. CDs were produced from different amounts of poly-(ethylene glycol) (PEG_{200}) and diverse saccharides (e.g. fructose and glucose) in an aqueous solution. The CDs obtained were characterized by an amorphous structure and tunable fluorescence, but only in the presence of PEG_{200} demonstrating its possible implication as surface passivating [156].

- *Thermal decomposition*

The synthesis of CDs by thermal decomposition exploits the dehydration and carbonization of molecular precursors driven by thermal reactions, usually carried out in the aqueous or organic phase (hydrothermal or solvothermal synthesis) upon heating in an autoclave at the precise temperature and pressure conditions [155]. The use of thermal conditions results in an increase or alteration of the solubility of the reagents in the solvent, allowing their physical and chemical interactions and the nucleation of carbonaceous structures [157]. However, the synthesis parameters are much more difficult to control (view Section 2.6.3.) and the raw product is particularly heterogeneous and requires intense purification [2].

2.6.2. Methods of purification and isolation

Several synthetic routes, particularly bottom-up approaches, tend to produce small fluorescent molecules and CDs that are highly heterogeneous in terms of structure, size distribution, and surface state, which, as previously debated, are reflected in their optical properties. Therefore, taking into account that homogenous size distribution is the first requirement for the biomedical application of CDs, a strong purification step is necessary after synthesis. The purification step is crucial to remove the by-products of the reaction and thus to isolate the sub-population of CDs with a different size distribution, absorption capacity, emission profile, and quantum yield [146,158]. The most common purification methods are dialysis, centrifugation, precipitation, and chromatography. Usually, CDs are isolated by precipitation in no-solvents, typically ethanol. However, this procedure gives rise to a very low reaction yield due to the very good dispersibility of CDs in a wide range of polar and non-polar solvents. Heterogenous CDs with low yield are also obtained by purification using the dialysis method [2,159]. In ref. [154,160], gel permeation chromatography was employed to purify raw products obtaining homogenous CDs. Very recently, a novel work-up procedure has been introduced to obtain the highest reaction yield reported in the literature. This approach consists of removing the reaction solvent using a rotary evaporator and directly purifying the redispersed product in water using a particular chromatography [159]. In detail, size exclusion chromatography (SEC), exploiting a combination of resin with a different cut-off, is shown to be effective in isolating homogeneous sub-population of CDs with different size distributions and optical profiles [3,146,158,159].

2.6.3. Tuning CDs profile through pre-synthetic design

In light of the range of possible CDs profiles and the wide range of applications, researchers focused their attention on identifying an effective synthetic strategy to achieve precise control of the performance of CDs, in terms of size distribution, chemical structure, and optical properties [1] (Figure 11).

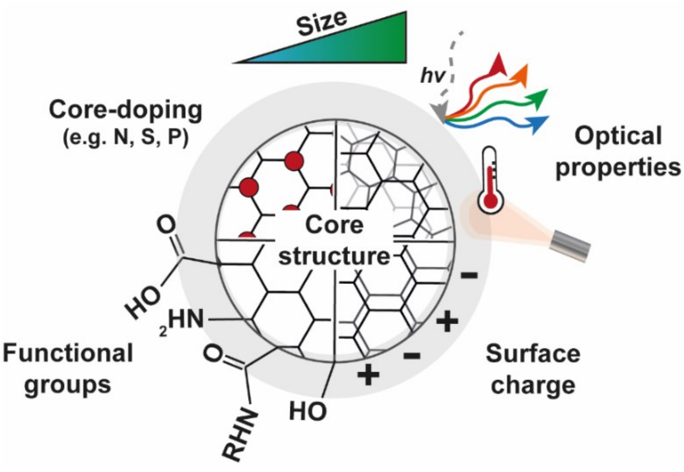

Figure 11. *Structural, chemical, and optical properties of CDs modulable through the synthesis scheme.*

The high flexibility of bottom-up strategies has led to an explosion in the number of studies focusing on CDs, resulting in countless CDs with different properties and applications [161]. A major advantage of the bottom-up approach to CDs is the possibility of producing nanoparticles with specific properties. An important property to customize would be the emission of CDs with a focus on red/NIR-emitting CDs. CDs are attractive light-emitting materials for a variety of applications, where modulation of their emissive properties would therefore be a winning strategy [154]. As reported in the literature, there are some aspects of the scheme of synthesis to be taken into consideration, such as the starting reagents and their molecular ratio, solvent, temperature, pressure, and time of reaction. All of these parameters, if chosen and modulated rationally, make it possible to obtain CDs with a distinctive profile. For example, the thermal process at high temperatures, up to 300 °C, has been demonstrated to lead to the production of carbon nanotubes or graphitic carbon materials. Instead, when carbonization is performed at a temperature below 300 °C, the dehydration and polymerization processes result in ordered CDs with various surface functional groups [157]. Another important thermodynamic parameter for designing CDs with defined size and optical distribution is represented by the operating pressure in solvothermal synthesis. In detail, it was demonstrated that the average size and the surface content of carboxyl groups of CDs decreased by increasing the operative pressure from 8 bar to 18.5 bar. Moreover, CDs synthesized at higher pressure conditions displayed a remarkable emission profile in the red region, while at lower reaction pressure the obtained CDs showed more fluorescence in the green region [3]. Therefore, the adopted operating pressure proved to be another key parameter to be taken into account for a rational design of CDs with established properties. Furthermore, Huo et al. demonstrated the influence of the reaction solvent on the fluorescence of CDs. In detail, the authors synthesized CDs from urea and citric acid by thermal approach in four different solvents like water, DMF, DMF/ethanol, and DMF/acetic acid, demonstrating how the fluorescence shift from the blue to the red region, respectively [162]. Moreover, as reported in other work in the literature, DMF proved to be the key solvent obtaining red-emissive CDs, probably due to the higher content of surface carboxyl functional groups [3,158,159,162]. The choice of precursors also highly affects the surface functional groups of the resulting nanoparticles. For example, polyamines, citric acid, and urea are particularly effective in introducing amines and carboxylate groups onto the surface of CDs, allowing post-synthetic functionalization reactions. Furthermore, bottom-up methods allow multiple precursors to be used to obtain CDs with different structures and properties [154]. Bottom-up approaches make it easy to introduce heteroatoms that dope the core and surface of CDs, modulating their structural and optical properties, and obtaining CDs with the highest emission efficiencies reported in the literature. Doping is an effective method to modulate the intrinsic properties of CDs. The introduction of heteroatoms tunes the HOMO-LUMO energy gaps, modulating the electronic and optical properties [149]. Nitrogen, sulfur, boron, and phosphorous represent the most common dopants. In particular, doping CDs with nitrogen atoms appears to dramatically enhance the red fluorescence and emission quantum yield by introducing new electron trapping on the surface state, which is correlated with high radiative recombination yield. The high level of N-doping obtained by conducting the synthesis with a high amount of doping agent leads to the formation of particular networks such as carbon nitride nanocrystals [149,163], which are impossible to obtain by top-down methods. On the other hand, doping CDs with sulfur atoms seems to introduce new transitions that extend the absorption spectrum toward the red and NIR regions, consequently improving the capacity to convert NIR light into heat (photothermal conversion) [159]. In light of this panorama, although the rational design of an efficient synthesis scheme of highly homogeneous CDs with performing optical properties is still a major challenge, there is also growing awareness of the innumerable parameters that can be modulated to obtain performing CDs for the application of interest.

2.6.4. Core structure

The core of CDs is quite synthesis-dependent, offering the possibility to design diverse sub-types of CDs. Based on the core structure, CDs can be classified in:

i) graphene quantum dots;
ii) graphitic carbon dots;
iii) amorphous carbon dots;
iv) β-C_3N_4 carbon dots [2] (Figure 12).

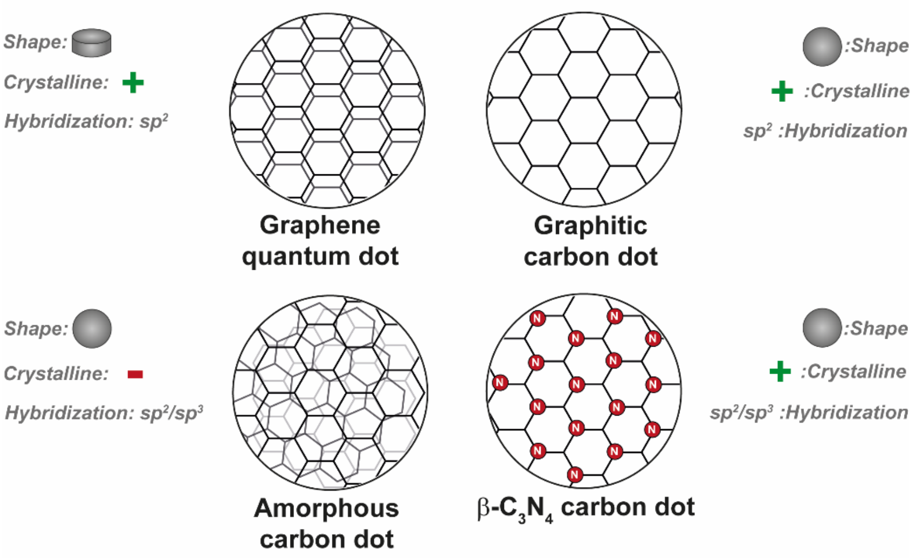

Figure 12. *Possible structure of CDs core as graphene, graphitic, amorphous, and β-*C_3N_4*, and relative shape, crystalline, and hybridization.*

Graphitic CDs, like graphite, are characterized by a spherical core composed of layers of sp^2-hybridized carbon stacked on top of each other. Unlike graphene quantum dots, the latter are not spherical particles but small disks of 1-3 layers of graphene stacked on top of each other. However, graphene quantum dots and graphitic dots have a similar optical profile. Typically, spherical-shaped graphitic CDs are the most common in the literature and are synthesized by a top-down approach [164–166]. Other possible CDs core structures can be obtained with high levels of N doping that allow the formation of graphitic (g-C_3N_4) or β-crystalline (β-C_3N_4) carbon nitride structures [146,167]. The two variants of carbon nitride CDs are very different. g-C_3N_4 is similar to graphite consisting of the repetition of a layer formed by three hexagonal rings of carbon and nitrogen hybridized sp^2. In contrast, β-C_3N_4 is a hexagonal network of tetrahedral structures of carbon hydridized sp^3 connected to trigonal sp^2 nitrogen atoms. The latter is obtained when the level of nitrogen doping is particularly high and forces the core structure to deviate from its graphitic nature [168]. CDs with C_3N_4 core structure have aroused particular attention due to their improved emissive and photothermal conversion capacity. Many examples of amorphous CDs reported in the literature consist of a mixture of carbon structure hybridized sp^2 and sp^3 in variable proportions and without a repetitive structural element. Amorphous CDs show a high fluorescence similar to that of crystalline CDs [169–172].

2.6.5. Tuning CDs profile through post-synthetic surface modifications

Careful integration of pre- and post-synthetic schemes is a powerful strategy to improve the functionality of nanomaterials in light of their perspective applications [149,154]. A key to producing advanced CDs that can meet precise requirements and perform specific functions is to further engineer the surface of CDs through ad hoc designed post-synthetic strategies by modifying the surface coating or integrating diverse functionalities (Figure 13). Therefore, another important intrinsic factor of CDs is the versatility of the surface functional groups (e.g. carboxyl, hydroxyl, amine, amide groups) that make CDs easily functionalized by different strategies (e.g. amidation, esterification, alkylation, imidation) [1]. As mentioned above, the surface state of CDs is determined by the synthetic scheme adopted and is reflected in their optical and biological properties. The concept of surface passivation of CDs as a strategy to improve their quantum efficiency was introduced by Sun et al. in 2006. In this work, CDs were surface-passivated with an amino PEG_{1500}, demonstrating that PEGylation is a valid strategy to induce a redshift of the emission peak and an increase in quantum yield [173]. The effectiveness of PEGylation as a strategy to tune optical properties of CDs was since been investigated by diverse authors. For example, in Ref. [158] surface passivation of CDs with a heterobifunctional PEG_{2000} induces an enhancement of absorption in the red region and a subsequent redshift of the emission band. In light of the possible application of CDs as theranostic nanosystems, another important aspect to consider is their interaction with biological component and their bioelimination. The ultra-small size of CDs ensures their bioelimination and prevents their accumulation and retention in organs, making them suitable for biomedical applications. Therefore, their average diameter is often smaller than the glomerular basement membrane cut-off (< 5 nm), which induces premature renal excretion [174]. As a consequence, surface passivation of CDs could also be exploited to increase their average size avoiding premature renal bioelimination. Moreover, surface functionalization of CDs demonstrated also a valid strategy to improve their biocompatibility by reducing the recognition and clearance by the RES [175]. The biocompatibility of CDs could also be affected by their interaction with serum proteins and the consequent formation of dot-protein aggregates that negatively affect their capacity to interact with cells. As reported in the literature, the surface state and charge of CDs could promote their interaction with serum protein [176]. In particular, CDs rich in surface of carboxyl groups seems to interact more with proteins [3]. Therefore, rational surface passivation of CDs could be an attractive strategy to avoid the CD-protein aggregate formation by modulating the surface state and charge of CDs. Finally, CDs surface-engineering could be exploited to introduce new functions, such as conjugating targeting agents, improving their appealing for in vivo applications [158].

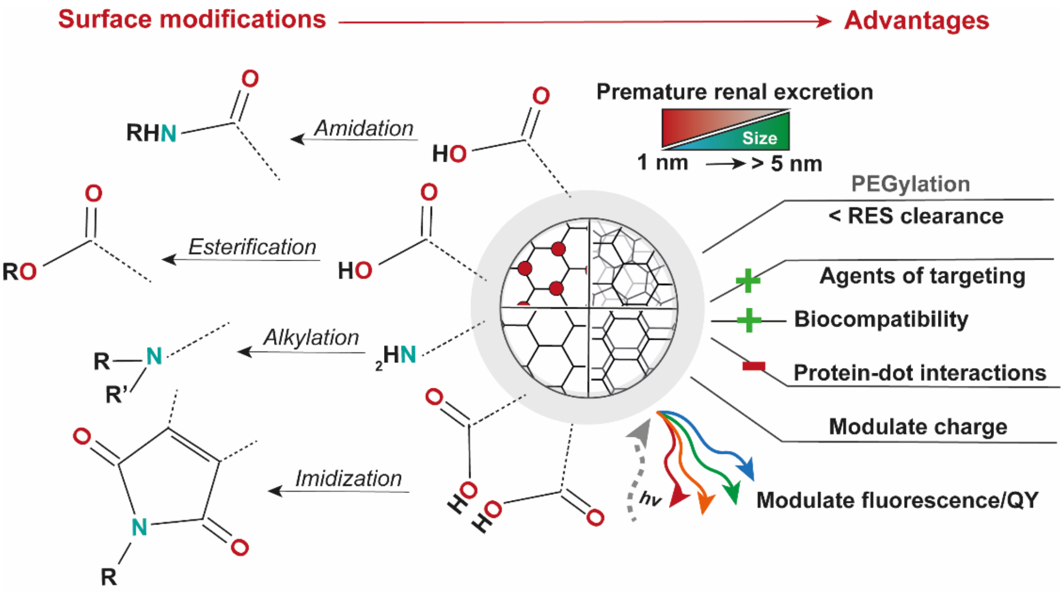

Figure 13. *Strategies of CDs surface modifications and relative possible advantages and functions.*

2.6.6. Fluorescence properties and tunability

Fluorescent carbon nanodots emerge as promising contrast agents in fluorescence imaging due to their tunable multicolor fluorescence from the blue to the red/NIR region, high quantum yield, and exceptional good photostability. The possibility to tune their emissive profile within the biologically transparent window (600-1100 nm) represents the major challenge for many researchers. However, although the well-known correlation between the surface, size, core, and emission spectra of CDs has been reported, modulation of CDs emission by a rational combination of reagents and conditions is not easy [1,177].

Two main radiative mechanisms, quantum confinement, and surface state, have been reported to explain the phenomena of emission. The theory of quantum confinement was carried out from the observation of graphene quantum dots emission, which seems to depend on the number of graphene-like rings or more in detail on the size of sp^2 domains

[2,178–180]. Taking into account the quasi-spherical shape, the ultra-small size, and the graphitic core structure of CDs, it is possible to hypothesize that their emission originates from a similar quantum confinement effect, in which the emissive chromophore would be the nanometric size [2,178,179,181]. In fact, following this proposed theory, some works reported a regular dependence of emission on diameter size. In detail, a study of CDs with different sizes highlighted a blueshift of the emission band with decreasing size [181]. However, other works evidenced the exact opposite of the theory of quantum confinement, evidencing a redshift of the emission band of CDs as size decreases [167]. This conflicting evidence has led to the belief that the CDs emission cannot be exclusively related to the intrinsic state, but is influenced by extrinsic surface-related contributions, such as surface defect, surface charge traps, or surface state [173,178]. Numerous experimental evidences support this hypothesis. For instance, as previously reported, surface passivation, solvents, and degree of oxidation (amount of carboxyl groups) [182] were demonstrated to strongly affect the emission quantum yield, probably by changing the number of surface emissive traps. Another recent theory has proposed that an electron transfer from core states to surface traps occurs during the photo-excitation and the fluorescence is due to the inverse recombination transition [183]. Despite several studies and proposed theories, the origin of fluorescence is still an open and much-debated topic. The most intriguing characteristic of CDs fluorescence is its tunability, which consists of the dependence of the emission peak on the excitation wavelength. Like the origin of fluorescence, also the origin of tunability is not unclear and highly debated. Many authors attribute the fluorescence tunability to the degree of inhomogeneity observed in most CDs synthesized with different synthetic routes [146,184]. The large heterogeneity of most CDs samples, in terms of size, structure, and surface state, is pointed out by the complex absorption and emission spectra. Several experiments based on the single-dot investigation have been conducted to refute this hypothesis [185–188]. Despite the extremely contrasting results reported, most authors still agree in associating the origin of tunability with the inhomogeneity of nanoparticles size and surface state due to the absence of tunability in the single dot or highly homogeneous sub-population isolated by SEC [2].

2.6.7. Photothermal conversion capacity

Another interesting property of CDs is represented by their photothermal conversion capacity, which increased their application in the field of photothermal therapy (PTT). Some authors reported diverse CDs able to act as potential nanoheaters. Ref. [189] reported CDs with a photothermal conversion efficiency of 58.2 % under a 635 nm laser with a power set at 2 W cm^{-2}. Ref. [190] reported CDs with a photothermal conversion efficiency of about 50 % under a 732 nm laser irradiation with a power density of 1 W cm^{-2}. As previously discussed in Section 2.5.3., co-doping of CDs with nitrogen and sulfur atoms was demonstrated to be a valid strategy to improve the absorption properties in the NIR region and then the no-radiative recombination phenomena. For example, Qu et al. obtained co-doped CDs with a photothermal conversion capacity of 59.19 % under irradiation with a 655 nm diode laser [177].

Therefore, CDs emerge as promising nanoheaters, comparable to the most noted photothermal agents proposed, such as gold nanorods and graphene oxide, but with the most interesting biological properties for prospective biomedical applications [191].

2.6.8. Sensing the external environment

The fluorescence of CDs is very sensitive to the external environment, more in detail to external agents such as ions or molecules [192–194], solvents [185,195], or pH [196–198]. These peculiar features could be exploited in the field of sensing and bioimaging. The capacity of CDs to interact with positively charged metal cations (e.g. Ag^{+}, Pb^{2+}, Hg^{2+}, Cu^{2+}, Fe^{3+}) is correlated to negatively charged surfaces due to the rich content of carboxyl in groups. The formation of this complex induces a quenching of CDs fluorescence, which could be attributed to the electron transfer from CDs surface to metal ions [192–194,199], similar to quenching phenomena observed in complex cations-organic dyes. For example, in ref. [192] were synthesized and selected seven kinds of CDs for the detection of six types of metal ions (Ag^{+}, Pb^{2+}, Hg^{2+}, Cr^{2+}, Cd^{2+}, Fe^{3+}). For each metal ion, there exists a unique fluorescence fingerprint that allows the qualitative identification of unknown metal ions in a specific environment. The capacity of CDs to act as photo-activated electron donors are not limited to metal ions. For example, Wang et al. synthetized green-emissive CDs for the detection of reduced glutathione exploiting the fluorescence quenching induced by the formation of the CDs-GSH complex [200].

The surface functional groups are also correlated to the diverse optical response of CDs at diverse pH [196–199], probably due to variable surface charge at different acid/basic conditions [201]. Otherwise, ref [199]. reported N-doped CDs that undergo fluorescence quenching at acidic pH, probably due to the protonation of pyridinic N atoms on the CDs surface. While, Zhang et al. synthesized N, S-codoped CDs whose fluorescence intensity is very intense at acidic pH (pH=1-2), while the intensity decreased at pH 3 until it turn off in the pH range 8-13 [196].

The fluorescence of CDs is also highly sensitive to external solvents. Diverse solvation studies demonstrated how the polarity of the solvent influences fluorescence, quantum yield, and non-radiative decay rates in the function of hydrophilic and/or hydrophobic surface functional groups [185,195].

2.7. Carbon nanodots in cancer theranostics

The application of CDs in controlled drug delivery has been widely explored in cancer therapy due to their ultra-small size, versatility and rich surface chemistry that combined with the pharmacokinetic advantages of nanomaterials make CDs a promising drug delivery system [202,203]. The extraordinary capacity of CDs to act as drug delivery systems, and fluorescent, photodynamic, and photothermal agents simultaneously, aroused increased attention in the rational design of multifunctional engineered CDs, more or less complex, as theranostic nanoplatforms in cancer therapy, diagnosis, and monitoring [4,158,204,205]. This powerful combination of features has increased exponentially over time the use of CDs in the field of photothermal therapy, photodynamic therapy, and/or chemotherapy in diverse combinations with fluorescence imaging.

2.7.1. Image-guided photothermal therapy (IG-PTT)

Photothermal therapy (PTT) is an emergent therapeutic strategy, which employs near-infrared (NIR)-responsive nanoabsorbers, such as CDs, able to convert light energy into localized heat upon NIR laser irradiation to induce selective cell death. The therapeutic modality and efficacy of PTT significantly depend on the degree of temperature increase induced by the nanoheaters [206]. More in detail, the photothermal approach includes two possible strategies, hyperthermia, and thermal-ablation. Hyperthermia consists of an increase in temperature just above the physiological temperature (about 42 °C) to induce cytotoxic effects only on cancer cells due to their higher thermal sensitivity than normal cells [207]. This localized increased temperature changes the vascular permeability increased blood flow and reduced the level of hypoxia. Instead, thermal ablation consists to reach a higher temperature (> 47 °C) inducing the complete eradication of the cell exposed [208]. In the photothermal approach, at a temperature of about 40-45 °C, irreversible cell damage occurs only after prolonged exposure (from 30 to 60 minutes) impacts cell membrane integrity, and inhibits DNA replication. On the contrary, at a temperature above 60 °C (thermal-ablation approach), the time that is required to achieve irreversible cell damage decreases exponentially due to the rapid protein denaturation, inactivation of vital enzymes, and immediate cytotoxic effect that leads to coagulative necrosis [209]. However, in contrast to hyperthermia, the operative temperature range of thermal ablation is not selective for cancer tissue, but damage also the nearby healthy tissues. The combination of precise NIR laser and nanoheaters selectively accumulated in tumor tissue confers to either the photothermal approach unique advantages in cancer therapy including high specificity, minimal invasiveness, and precise spatial-temporal selectivity [206]. The combination of photothermal therapy with fluorescence imaging, also known as image-guided photothermal therapy (IG-PTT), allows for ensuring the localization of the nanoparticles and the safety and efficacy of the photothermal approach in real time. In recent years, the combination of more than one therapeutic approach in a single nanoplatform, such as the combination of PTT with chemotherapy, has attracted the most attention as a promising strategy to overcome MDR phenomena and the heterogeneous response of cancer cells to chemotherapy [122,210,211]. Moreover, PTT demonstrated to amplify the antitumor effect of chemotherapy by rendering tumor cells more susceptible to anticancer drugs [212,213]. The activation of the apoptosis pathway represents the fundamental mechanism of action of the most common anticancer drug [47]. The apoptosis pathway could be activated through the death receptor-mediated apoptosis pathway (extrinsic pathway) [214,215] and/or the mitochondrion-induced apoptosis pathway (intrinsic pathway). The extrinsic pathway could be induced by tumor necrosis factor α (TNFα) or Fas ligand (FasL) that leads to the cascade activation of caspase 8 and caspase 3 in sequence. Whereas, the balance between proapoptotic and antiapoptotic factors regulates the activation of caspase 9 as well as of the intrinsic pathway [216,217]. However, diverse types of cancer are characterized by a marked resistance to apoptosis, resulting from disrupted apoptosis machinery, overactivated prosurvival signaling pathways, increased expression of the therapeutic target, activation of alternative compensatory pathways, high degree of molecular heterogeneity in tumor cells, upregulation of drug transporters and multidrug resistance [218]. Recently, the growing number of works focusing on the use of nanoheaters-induced photothermal therapy has highlighted its ability to activate diverse programmed regulated cell death (RCD) pathways like necroptosis, autophagy, and apoptosis [219]. Necroptosis is a caspase-independent regulated necrotic cell death modality, that could be activated also in absence of pro-apoptotic factors, representing an interesting alternative way for RCD to bypass apoptosis resistance. Rather necroptosis is induced by TNFα and the activation of receptor-interacting protein kinase (e.g. RIPK1, RIPK3) and mixed lineage kinase domain-like protein (MLKL), that regulate the inhibition of caspase 8 and promote the formation of the necrosome [220,221]. It is important to underline that diverse types of cancers have shown downregulation of the key mediators of the necroptosis pathway, suggesting that cancer cells try to evade necroptosis to survive [219,220,222]. Moreover, several studies reported in the literature emphasized that necroptosis involved also the activation of antitumor immunity, including antigen presentation, cross-priming of CD8+ T cells, and the production of IFN-γ [221,223,224]. In Ref. [224] CDs functionalized on the surface with PEG-biotin and loaded with irinotecan were developed as a strategy to elicit diverse RCD pathways to overcome MDR and apoptosis resistance in breast cancer. In contrast to treatment with irinotecan-loaded nanoparticles that promote the apoptosis pathway, the combinatorial approach demonstrated effectiveness in simultaneously activating apoptosis and necroptosis with excellent anticancer efficacy.

In light of these considerations, the possibility to trigger necroptosis by a simple, non-invasive, and accurate method like NIR laser-mediated PTT, represents an increasing and interesting strategy to maximize the efficacy of the treatment overcoming the apoptosis resistance phenomena [219,221].

2.7.2. Image-guided photothermal/photodynamic therapy

Photodynamic therapy (PDT) emerging as an interesting therapeutic approach due to its non-invasive nature, and reduced side effects, and represent a valid alternative to the conventional approach and relative MDR phenomena. The PDT was focused on inducing cancer cell death by the production of reactive oxygen species (ROS), such as singlet oxygen or free radicals, by a photosensitizer and a photoactivable agent under NIR-laser irradiation. PDT can be easily performed using a NIR-photoactivable agent with an emission band overlapped with the absorption of one of the photosensitizers, in order to reach the highest efficiency of energy transfer. Indeed, the production of ROS was based on the ability of the photosensitizer to transfer the absorbed photon energy to the surrounding oxygen molecules generating ROS [225,226]. The regulation of ROS levels is crucial for cellular life revisiting a dual role in the function of its concentration. In fact, moderate levels of ROS contribute to the control of cell proliferation and differentiation; on the contrary, high levels of ROS (oxidative stress) increase receptor and oncogene activity, with the possibility to damage lipids, proteins, and DNA [227]. Conventional

NIR-sensitive photosensitizers like porphyrin, phthalocyanines, and bacteriochlorin derivates demonstrated able agent for concurrent cancer imaging and therapy, and some of these have been approved in the clinic (e.g. Photolon®, Fotolon®, and Tookad®) [228]. However, the current applications are often limited by their poor water solubility, photostability, and low absorbance capacity in the biological transparent window [229]. As for fluorescence imaging, quantum dots (Q-dots) have been proposed to improve the PDT potentiality of photosensitizers due to their excellent optical properties and water solubility. However, the use of Q-dots brings with it an important toxicity problem related to the presence of heavy metals, as previously anticipated.

Carbon nanodots due to their functional combination of optical properties, size, and biocompatibility emerge as potential PDT and FLI agents exploitable in image-guided photodynamic therapy (IG-PDT) [225,228]. Some examples of engineered CDs in cancer IG-PDT were reported in the literature [230–232]. For example, Huang et al. developed a conjugate of CDs and chlorine-6 that showed efficient photodynamic capability and excellent contrast in fluorescence imaging as compared to the use of chlorine-6 [232].

Therefore, the use of CDs as carrier of photosensitizers in PDT offers several advantages: i) improving the stability and solubility of photosensitizers in aqueous/biological media; ii) reducing the cytotoxicity of photosensitizers; iii) improving the circulation half-time and increasing the diffusion in tumor tissues [228].

2.7.3. New outlook in cancer theranostics

More recent studies have reported various nanoparticles, such as carbon nanomaterials, metal nanoparticles, and 2D materials can trigger autophagy pathways [233]. Autophagy is a highly regulated process that degrades proteins and recycles cellular products or damaged organelles, playing a key role in maintaining cellular homeostasis. In order to preserve cellular homeostasis, autophagy provides an adaptive and inducible response to cellular stress induced by external chemical or physical agents [234,235]. Therefore, nanomaterials able to overstimulate ROS production can lead to autophagy cell death or adaptive response to maintain homeostasis [236]. An interesting housekeeping response consists of the activation of diverse forms of stress and in particular in the overproduction of ROS [237]. In ref. [238] was studied the cytotoxic profile of negative-charged CDs, passivated with neutral PEG and passivated with positive polyethylene imine (PEI). In this study, for the first time, was highlighted differences in cell cycle, ROS generation, and cytotoxicity correlated to different surface passivation and more in detail to the diverse surface state in terms of charge. Therefore, the present study offers a new view on the toxicity of CDs, which cannot be traduced as a simple reduction in cell viability but as the capacity of CDs to induce ROS generation acting as anticancer agent. In another recent work, carbon nanodots were demonstrated to induce the activation of the autophagy system in cancer cells through the stimulated production of ROS, which serves as a buffer to control the level of stress and reduce the cytotoxic effects or to lead to cell death by apoptosis [233]. Another work reported in the literature proposed N, S-codoped CDs that demonstrate to improve the intracellular ROS generation inducing an effective anticancer effect. ROS production was ascribed to the capacity of CDs to interact with the electron transport chain in the mitochondrial membrane [239].

These works lead the way to study the implication of the surface functional groups and surface charge in their ability to stimulate an overproduction of ROS and explore the intrinsic cytotoxic effect of CDs as a novel therapeutic strategy for cancer without the use of conventional chemotherapeutic drugs.

3. Aim of the work

Nanomedicine aims to overcome limitations of unspecific conventional chemotherapy (e.g. severe side effects, multidrug resistance, poor bioavailability, dose-limiting toxicity) and the complexity of tumor tissues, exploiting the unique properties of nanocarriers to modulate the pharmacokinetic and pharmacodynamic profiles of drugs, enhancing their therapeutic index and improving the patient's quality of life [76,240]. The necessity of more personalized, non-invasive, and efficient treatments in the fight against breast cancer has aroused considerable attention in the development of innovative multifunctional nanosized tools able to simultaneously act as multimodal therapeutic nanoplatform (e.g. chemotherapy, photothermal therapy, photodynamic therapy) and contrast agent in non-invasive fluorescence imaging [241]. This combinatorial approach (theranostics) allows for combining early diagnosis, real-time monitoring, and targeted therapy of tumors, contributing significantly to the ever-growing field of personalized medicine [119]. In particular, the combination of diverse therapeutic approaches allows for circumventing the well-known intra-tumor heterogeneity of cancer tissues, multidrug resistance (MDR), and apoptosis resistance, demonstrating a valid strategy to induce selective cell death by the activation of diverse regulated cell death (RCD) pathways (e.g. apoptosis, necroptosis, autophagy) [224,242].

A wide range of light-responsive nanomaterials has been proposed for fluorescence imaging and/or photothermal therapy within the biological transparency window, such as organic dyes, carbon nanomaterials, and metal nanoparticles. However, despite the high photostability of metal nanoparticles against conventional organic dyes, they suffer from low renal excretion and organ accumulation, which imply potential long-term toxicity phenomena limiting their clinical applications [175]. Among the plethora of photo-responsive nanomaterials proposed, carbon nanodots (CDs) emerge as potential 0D carbon-based nanomaterials due to their potential combination of water-solubility, versatile surface, lower toxicity, fluorescence properties, photothermal conversion capacity, and photostability. In particular, red/NIR-emitting CDs have shown the most promising properties in cancer theranostics, since they emit light that can pass through biological tissues without being absorbed to give information on their localization by high-resolution fluorescence imaging [243]. However, the biomedical applications of CDs as theranostic agent as such or in more complex hybrid nanoplatforms is highly affected by severe limitations in the design of performant CDs [1]. In detail, the huge access to starting monomers and protocols, as well as the lack of full control in all synthesis parameters involved in low yield and deficiency control of CDs profile, often obtaining heterogeneous CDs with preferential fluorescence in the blue/green region with poor interest for biomedical applications [2]. Moreover, the ultra-small size of CDs, although on the one hand, it constitutes a great advantage by avoiding their undesired organ accumulation, on the other hand, average size under the glomerular cut-off of 5 nm results in undesired premature renal excretion [1]. Therefore, a careful and rational design of the synthesis scheme as well as of the surface of the CDs constitutes necessary and fundamental steps to increase the biomedical interest in the use of carbon nanodots.

In the present thesis work, the different aspects and steps involved in the development of multifunctional carbon nanodot-based nanoplatforms have been deeply explored, from the rational synthesis to surface engineering of CDs as far as to the design of more complex nanosystems exploitable in breast cancer theranostics. The first focus goal was to design and test diverse solvothermal synthesis schemes and work-up strategies, in order to obtain peculiar performant CDs for biomedical applications. In detail, diverse combinations of reagents (e.g. urea, citric acid, indocyanine green, DMF) and thermodynamic parameters of synthesis (e.g. time, pressure, temperature) have been studied, understanding their potential to modulate the structure of the core, the surface functional groups, the optical properties (e.g. absorbance, fluorescence, photothermal conversion) and the biological profile of CDs. Doping of CDs with nitrogen and/or sulfur has been explored to obtain crystalline CDs with brilliant red/NIR fluorescence and photothermal conversion efficiency, also revealing the key correlation of the surface state of CDs with their functional capacity to interact with biological components (e.g. plasmatic proteins, mitochondrial). In a second step, in order to employ the appeal of CDs in the development of theranostic nanoplatform, diverse surface engineering strategies have been studied from the pegylation/alkylation by amidation to the transesterification with PLA chains, as well as the incorporation inside the polymeric matrix or self-assembling core-shell nanostructures. The covalent functionalization of CDs or their use as a functional material in polymeric nanostructures was exploited as strategies for overcoming some limitations in the use of CDs in cancer theranostics (e.g. premature renal excretion, dot-dot/dot-serum protein interactions). The range of carbon dot-based nanoplatforms proposed was rationally designed, carefully choosing each element in order to efficiently combine the fluorescence properties and/or photothermal conversion capacity of CDs with the advantages impinged by the polymeric shell or structure (e.g. water stability, increased drug loading, biodegradability, targeting properties, average size). The diverse design of carbon dots allows for exploring different combinations of fluorescence imaging and therapeutic strategies such as chemotherapy (e.g. doxorubicin, irinotecan, sildenafil), CDs-triggered ROS production, and/or photothermal therapy. Each step has been thoroughly studied and characterized in order to reconstruct all the key aspects in the synthesis and engineering of carbon nanodots, and to investigate the potential of the different therapeutic approaches in the therapy and diagnosis of breast cancer.

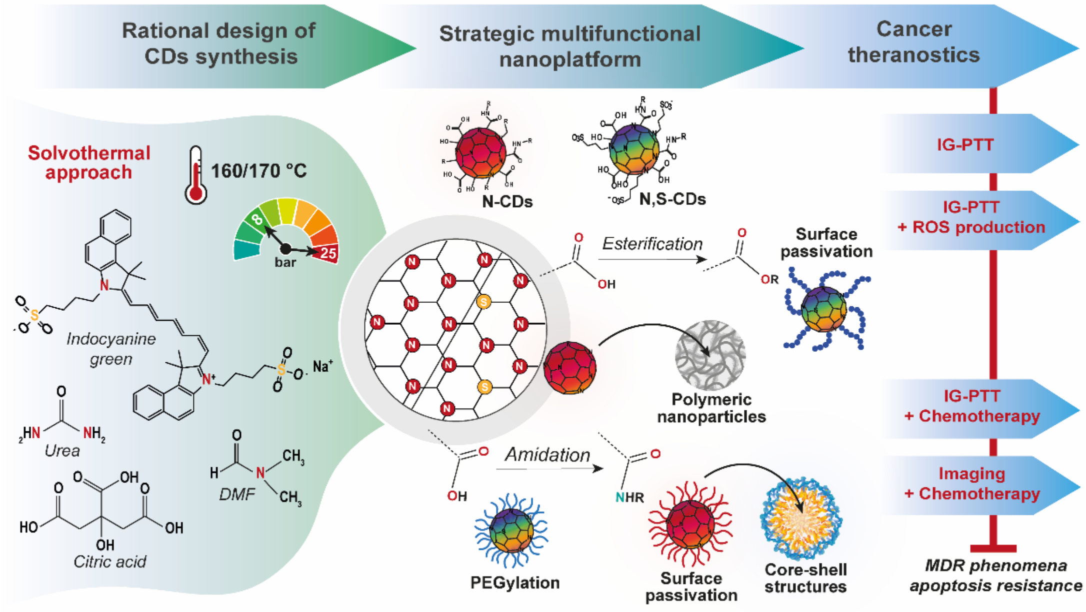

Figure 14. *Summary scheme of the aim of the work: from the design of carbon nanodots to the development of multifunctional nanosystems for the diagnosis and therapy of breast cancer.*

4. Results Discussion and Conclusions

4.1. Pressure-dependent synthesis of N-doped carbon nanodots as a tool to modulate their physico-chemical and optical profile

A consistent synthesis of Carbon Nanodots (CDs) with an established and controlled physico-chemical profile is precluded owing to the impossibility of fully controlling the thermodynamic parameters during the synthesis, thus limiting their possible use in medical applications. The possibility of tuning the photoluminescence of CDs as a function of monomer ratios, reaction temperature, solvent composition, and doping agents, to obtain CDs with optical properties suitable for a plethora of applications, still constitutes the challenge of many research groups [112,150,244]. Although pressure is a thermodynamic parameter that plays a crucial role in solvothermal reactions in terms of viscosity, density, and crystal lattice energy, to the best of our knowledge there are no studies that report the effect of the operative pressure on the structure, dimensions, and optical features of CDs [245,246] Herein, a solid solvothermal protocol exploiting for the first time the fine controlling of temperature and pressure to obtain CDs with tunable optical and structural properties was developed. Here, it was demonstrated that by manipulating the operating pressure it is possible to obtain highly homogeneous nitrogen-doped CDs with tunable multicolor fluorescence and NIR photothermal conversion capability. Moreover, the proposed strategy of synthesis allows for obtaining peculiar biological properties, like cytocompatibility and NIR-triggered photothermal cytotoxic properties, highly desirable in precision medicine (Figure 15).

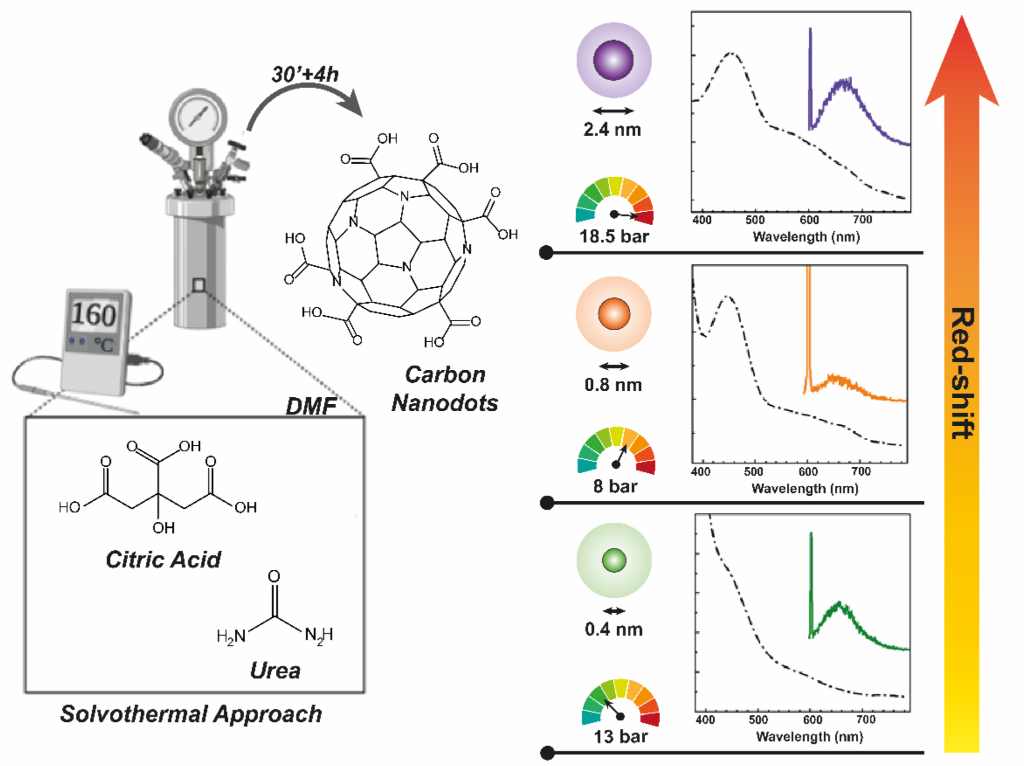

Figure 15. *Graphical abstract.*

4.1.1. Synthesis of N-doped Carbon Nanodots at different operating pressure

Modulating the operating pressure of the reactor from 8 to 18.5 bar during the solvothermal decomposition of urea and citric acid in N, N-dimethylformamide (DMF) different emissive-CDs were obtained. CDs were synthesized in the condition of nitrogen doping to obtain optimal optical properties since it seems to be a crucial factor. Three pressures were chosen to study the pressure-dependent behavior of the emission spectrum and size distribution of CDs, namely 8, 13, and 18.5 bar. The selected operating pressure was reached within 45 min and kept for about 2h, through a micrometric tuning of the reactor valve. As shown in Figure 16 the trend of the pressure recorded during the reactions, suggests that the selected pressure was reached and maintained a plateau over time after 50 minutes of warm-up solvothermal reactions. Only for the synthesis at a higher pressure of 18.5 bar, the plateau was registered after 150 min. As supported by the literature, these conditions are suitable to provide the necessary time for forming ordered crystals typical of nitrogen-doped CDs [158].

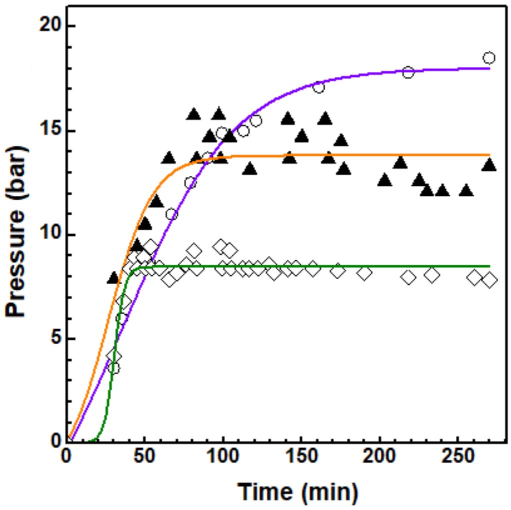

Figure 16. *Pressure trend in the function of the reaction time monitored during the synthesis of CDs.*

All the CDs obtained consisted of a mixture of amorphous carbonaceous sub-materials and heterogeneous green-, orange- and red-emissive CDs but in different percentages. The different sub-populations with peculiar sizes, surfaces, and optical properties were isolated by exclusion chromatography (SEC). In detail, to eliminate by-products and the smallest materials, crude CDs were purified by a strategic combination of two Sephadex stationary phases packed with an increasing cut-off from G15 to G25. After purification by SEC three main fractions per each reaction were isolated. Usually, one emits in the green region of the visible spectrum, another in the orange, and the last prevailingly in the red region. A first analysis of the optical properties successfully allows the selection of fractions of each sample of CDs with the top red fluorescence. Red fluorescence represents the focused goal in fluorescence imaging applications to obtain high-resolution images within the biologically transparent window. The reaction yield of the three selected fractions, named CDs_{8bar}, $CDs_{13bar,}$ and $CDs_{18.5bar,}$ is strictly affected by the operating pressure (Table 1). In particular, the yield of CDs emitting in the red region increased by increasing the pressure (4 %, 8 bar; 5.7 %, 13 bar, and 11.6 %, 18.5 bar), suggesting that red-emitting CDs can be efficiently obtained at the higher pressure studied. On the contrary, the yield of the green fractions decreased with the operating pressure (from about 14 % to 1 %, at 8 and 18.5 bar, respectively). In contrast, the yield of the orange fractions had a maximum of 13 bar and decreased at higher and lower pressures (Table 1).

Table 1. *Yield (%) of green-, orange- and red-emitting CDs collected of CDs$_{8bar}$, CDs$_{13bar}$, and CDs$_{18.5bar}$.*

	Yield CDs$_{Green}$ (%) ^{a}	***Yield CDs$_{Orange}$ (%)*** ^{a}	***Yield CDs$_{Red}$ (%)*** ^{a}
CDs$_{8bar}$	14.3	6.4	4.0
CDs$_{13bar}$	5.4	8.1	5.7
CDs$_{18.5bar}$	0.9	4.1	11.6

^{a} Calculated on a weight basis considering the weight of starting monomers completely dehydrated

4.1.2. Physico-chemical characterization

To compare only the red-emitting CDs$_{8bar}$, CDs$_{13bar}$, and CDs$_{18.5bar}$ the chemical surface state was established by FTIR analysis (Figure 16). The FTIR spectra show diagnostics bands typical of hydroxyl, carbonyl, and amide groups relative to O-H stretching (3436 cm^{-1}), C = O (1384–3178 cm^{-1}), and C-H vibration (2915 cm^{-1}), but with different ratio [158][146][247]. In detail, the carboxyl/amide band heights highlighted that CDs$_{18.5bar}$ are characterized by a higher amount of carboxylic acid groups on the CDs surface compared to the samples obtained at lower pressure. On the contrary, the CDs$_{13bar}$ and CDs$_{8bar}$ would seem richer in amide groups. Therefore, the amount of carboxyl groups is directly proportional to operating pressure, whereas the amide groups follow an opposite trend (Figure 17 and Table 2).

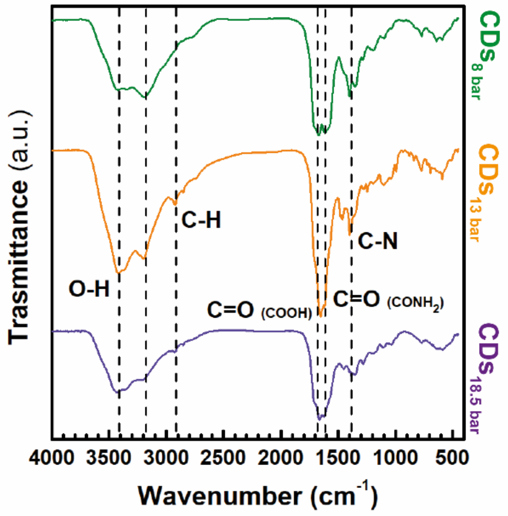

Figure 17. *FT-IR spectra of CDs$_{8bar}$, CDs$_{13bar}$, and CDs$_{18.5 bar}$.*

These data were also confirmed by ζ-Potential measurements reported in Table 2, where it is manifest that CDs$_{18.5bar}$ have a higher amount of surface negative charge relative to carboxylic acids (−33 mV and about −19 mV for CDs$_{18.5\ bar}$ and CDs$_{13bar}$/CDs$_{8bar}$, respectively). Following the literature, the surface composition has a critical role for nanomaterials, since it could affect many parameters in the biomaterial/tissue interface such as cell uptake, nano-toxicity, protein absorption, biodistribution, and immune system [248,249] Thus, the operating pressure could be a key parameter to modulate the yield of red-emitting CDs, their surface functional groups, and their biological behaviors.

Table 2. *Z-average, PDI, and ζ -potential of CDs$_{8bar}$, CDs$_{13bar}$, and CDs$_{18.5\ bar}$ by DLS analysis.*

Sample	***Z-Average [a] (nm)***	***PDI [a]***	***Z-Average [b] (nm)***	***PDI [b]***	***ζ-Potential [a] (mV)***	***ζ-Potential [b] (mV)***
CDs$_{8bar}$	1.9	0.06	128.3	0.253	-18.4 ± 6.5	-5.5 ± 1.2
CDs$_{13bar}$	2.4	0.1	267.5	0.498	-19.6 ± 8.6	-6.0 ± 1.1
CDs$_{18.5bar}$	5.3	0.02	210.8	0.373	-33.6 ± 5.9	-6.2 ± 1.7-
DMEM	-	-	91.8	0.219	-	-10.1 ± 8.4

[a] Data obtained by DLS analysis in ultrapure water at 37 °C.

[b] Data obtained by DLS analysis in supplemented DMEM at 37 °C.

4.1.3. Size distribution determination by Atomic Force Microscopy (AFM)

Another parameter that affects the biomaterials/tissues interactions is the size distribution of nanoparticles [248,249]. Even if CDs are small enough (< 5 nm) to be eliminated by normal renal clearance, interactions with biological components also depend on the size distribution of nanoparticles. Therefore, modulating the size distribution of CDs allow tuning the parameter over-mentioned helpful in the design of safe effective nanomedicines with negligible side toxic effects [128]. Here, the operating pressure provides a simple way to obtain highly homogeneous CDs with size distribution proportional to the pressure adopted.

The influence of the operating pressure on the size distribution of the CDs and the involvement of the particle size distribution in emission phenomena by interfacial electron mechanisms was evaluated by AFM analysis. CDs$_{18.5bar}$, CDs$_{13bar,}$ and CDs$_{8bar}$ micrographs and size distribution obtained from the particle heights were reported in Figure 18. As shown in Figure 18b, the process of purification adopted allows obtaining

CDs with narrow size distribution. The mean diameter varied from 0.45 to 2.4 nm as the operative pressure increased, suggesting that tuning the pressure during the reaction allows for modulating the size distribution of the CDs. It might be noticed that non-spherical CDs were obtained at 8 bar, consisting of 0.45 nm in height extended unidirectionally up to about 1 nm in width (Figure 18a). While at lower pressure (8 bar) crystal growing is incomplete, it is noteworthy that high pressure is required to provide spherical CDs and complete multidirectional crystal growth. The mechanism of this phenomenon is associated with directional stress on the solubility of compounds produced during the dehydration and carbonization of the starting monomers. In fact, under compressive forces, the solubility of the stressed faces is higher and the degree of supersaturation of the liquid affects the crystal growth of the stressed faces [250].

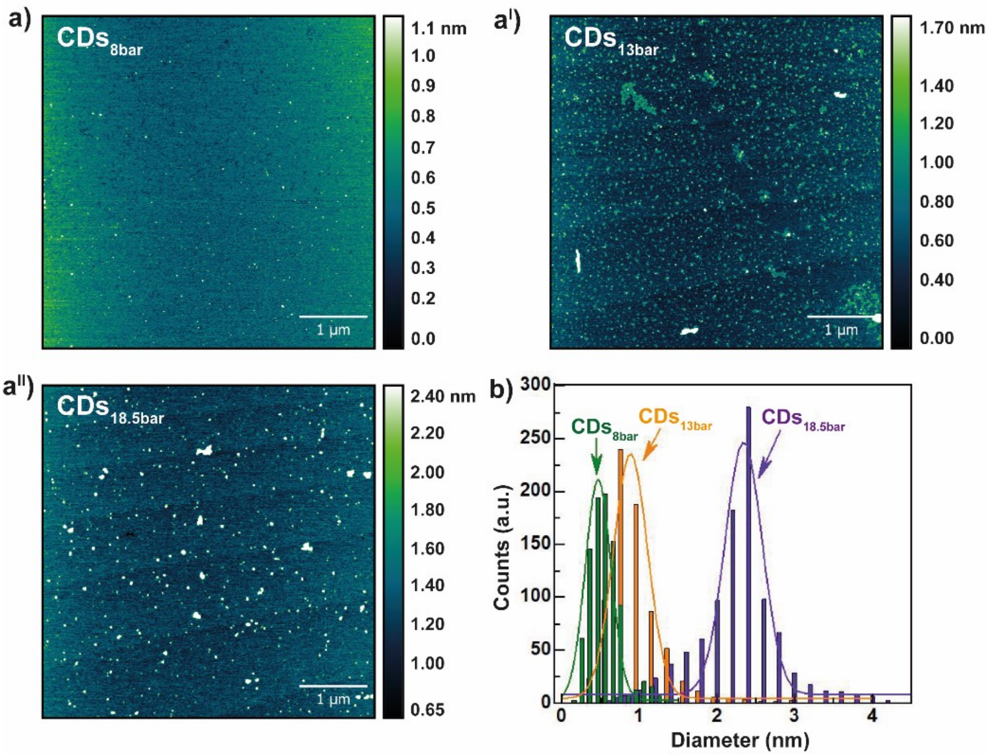

Figure 18. *AFM micrographs of CDs$_{8bar}$ (a), CDs$_{13bar}$ (b), and CDs$_{18.5bar}$ (c) and relative size distribution (d).*

4.1.4. Optical characterization

Previews publications report that doping nanoparticles with sulfur or compounds able to be incorporated into the crystals during the growing processes represents a prominent strategy to synthesize CDs with red/NIR fluorescence. However, this strategy does not guarantee that the control of the chemical composition and physicochemical properties of CDs results in the arduous production of standard nanoparticles suitable for biomedical use. Considering that the photoluminescence of CDs is highly affected by the size and functional groups, here, it was exploiting the pressure of the synthesis process to obtain nitrogen-rich CDs with a significant red shift [251]. To evaluate the red emission properties of CDs$_{18.5bar}$, CDs$_{13bar}$, and CDs$_{8bar}$, absorption spectrum, and emission spectra were recorded and reported in Figure 19. All CDs are characterized by a complex absorption spectrum consisting of three main bands at about 350, 450, and 600 nm (Figure 18a). These bands are associated with the three main emission bands in the green, orange, and red emission regions, respectively. In particular, the band at 350 nm is particularly remarked for the CDs$_{8bar}$ sample, decreased up to hinted for the CDs$_{13bar}$ and the CDs$_{18.5bar}$ respectively. In contrast, the bands at 450 and 600 nm sharply increased in the CDs$_{18.5bar}$ and CDs$_{13bar}$ spectra, with a prevalent band at 600 nm for the CDs$_{18.5bar}$. In order to investigate the emission properties of the CDs in the red region, emission spectra were recorded under an excitation wavelength of 600 nm (Figure 19b), confirming that the operating pressure is an underestimated parameter in the solvothermal synthesis of CDs which provides a versatile and fine control of the physicochemical properties of CDs. In fact, it was observed a significant red shift of 10 nm for the CDs$_{18.5bar}$ if compared with parent samples (CDs$_{8bar}$ and CDs$_{13bar}$) and a higher quantum yield (QY%) for the CDs$_{18.5bar}$ (4.3 % vs. 2.4 %), implying that the higher operating pressure adopted in the synthesis of CDs (18.5 bar) provided significant improvements in the emission properties of CDs in the red region, desirable for medical applications [247,252].

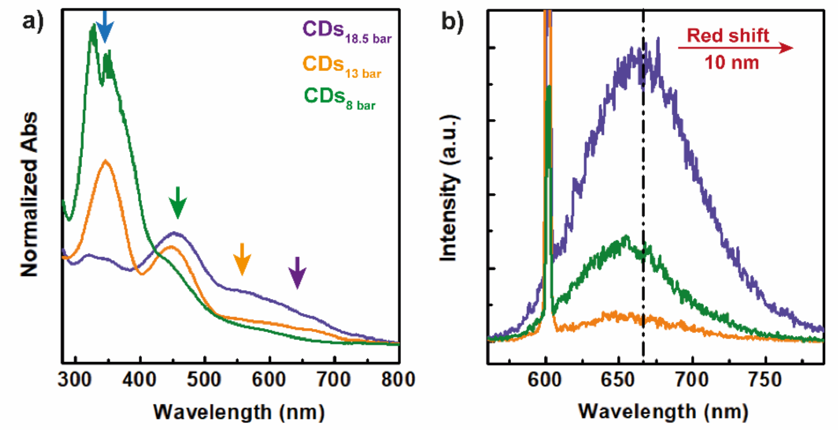

Figure 159. *UV spectra (a) and emission spectra recorded under excitation at 600 nm of CDs$_{8bar}$ (green lines), CDs$_{13bar}$ (orange lines), and CDs$_{18.5\ bar}$ (violet lines).*

4.1.5. Determination of photothermal conversion capacity

The photothermal abilities of the selected red-emitting $CDs_{18.5bar}$, CDs_{13bar}, and CDs_{8bar}, each sample (0.2 mL) at a concentration of 0.1 mg mL^{-1} was evaluated exciting using a diode laser of 810 nm with a power of 5 W cm^{-2} for 300 s. Temperature was measured and reported as a function of the exposure time (Figure 20). Ultrapure water was used as a negative control for comparative purposes. $CDs_{18.5bar}$ sample provided a much more distinct photothermal ability since it allows reaching 69 °C after 300 s exposure. According to the higher absorption property observed in the red range of the UV-vis spectrum (Figure 19a). Although all CDs samples proved capable of increasing the temperature of the medium under NIR exposure up to at least 55 °C, far beyond the photothermal threshold useful in cancer hyperthermia (43 °C). However, all CDs allow tuning NIR photothermal effect to generate hyperthermia by controlling the exposure time and laser power, which could supply the minimum temperature needed to eradicate tumors and avoid damage in healthy tissues [212,213,253]. In particular, under the selected experimental conditions the medium reached 43 °C after barely 25 s of laser exposure for the $CDs_{18.5bar}$ sample. At the same time, the same temperature was obtained after 40 s and 75 s for the CDs_{8bar} and CDs_{13bar}, respectively. Therefore, the photothermal kinetics under NIR laser excitation confirms that the increasing pressures and the optimal absorbance in the transparent window ensure greater photothermal performance in the NIR region, which is necessary for image-guided phototherapy in deep tissues.

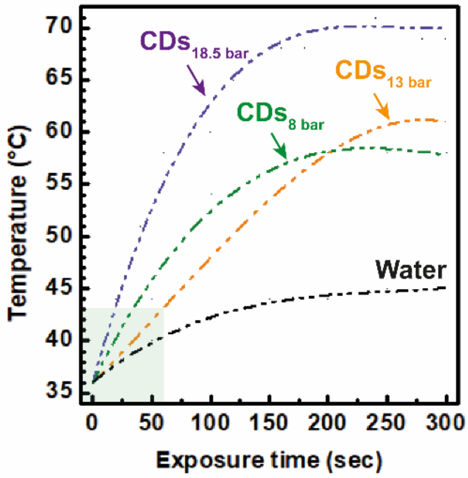

Figure 20. *Kinetics of hyperthermia in the function of exposure time under irradiation with an 810 nm diode laser with power fitted at 5 W cm*$^{-2}$ *for 300 s.*

4.1.6. Cytocompatibility assay of N-doped CDs and NIR-triggered cancer cell death study

In vitro cytocompatibility of the selected red-emitting fraction of $CDs_{18.5bar}$, CDs_{13bar}, and CDs_{8bar} was evaluated on the breast cancer cell model (MDA-MB-231) after 48 h incubation within a concentration range of 0.05–1 mg mL^{-1}. Cell viability is expressed as the percentage of cells alive in comparison to the untreated control (100% viability). As reported in Figure 21. cell viability followed a dose-dependent trend in the entire range of concentration. In particular, cell viability decreased as the concentration increased. However, the CDs obtained at different pressure were different cytocompatibility profiles. In particular, CDs_{8bar} displayed excellent cytocompatibility (> 90 %) over the entire range studied, whilst a lower cytocompatibility was recorded for the CDs_{13bar} sample at the higher concentration tested. Surprisingly, the $CDs_{18.5bar}$ sample provoked a significant cell death at concentrations higher than 0.25 mg mL^{-1}. These data suggest that the different nature of the CDs surface observed might play a crucial role in the biological profile of these nanomaterials.

In light of the controllable high photothermal performance of the red-emitting CDs, it was evaluated their ability to induce human breast cancer cell death by NIR-triggered photothermal ablation. Therefore, the second experimental set was conducted on MDA-MB-231 after an incubation time of 48 h by irradiating each well with an 810 nm diode laser for 300 s with power fitted at 5 W cm^{-2}. The photothermal ablation was measured as a reduction in cell viability after the laser treatment and results were compared with cells treated only with CDs (Figure 21). According to literature data, the 810 nm diode laser treatment alone at suitable power density (0.1–10 W cm^{-2}) has a bio-stimulating effect, which reflects on cell proliferation and thus is considered biocompatible [212,254–256]. In contrast, cells exposed to either $CDs_{18.5bar}$, CDs_{13bar}, or CDs_{8bar} show a remarkable dose-response reduction in cell viability after laser irradiation. Like other tested nano-heaters, the treatment of MDA-MB-231 with a harmless dosage of NIR diode laser (300 s, 5 W cm^{-2}) provoked the activation of CDs within the therapeutic window and the local release of heat to provoke a selective cell death [257–260]. In detail, CDs_{8bar} need a higher concentration to induce cancer cells death by photothermal ablation (IC_{50} = 0.45 mg mL^{-1}) if compared with the parent CDs (CDs_{13bar}, IC_{50} = 0.125 mg mL^{-1}; $CDs_{18.5bar}$, IC_{50} < 0.05 mg mL^{-1}). Besides, $CDs_{18.5\ bar}$ was able to provoke 100% of cell death under NIR laser treatment at a very low dosage (<50 µg mL^{-1}), involving complete eradication of cancer cells [261]. Thus, the operating pressure allows tuning both the physico-chemical and biological properties of CDs, providing a key synthetic parameter to design new nanomaterials adaptable to medical requirements.

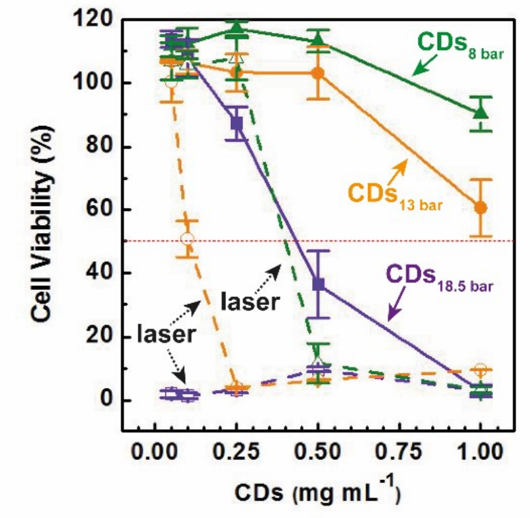

Figure 21. *Study of cytotoxicity (compact lines) and photothermal activities (dotted lines) in vitro on 2-D model of MDA-MB-231.*

4.1.7. Study of CDs-serum protein interactions by DLS analysis

When nanoparticles with a high specific surface state and charge are in biological fluids, they can interact with proteins to form a protein shell with various conformations named protein corona, which can negatively affect their physicochemical properties and the ability of cell internalization [262–267]. Thus, the interaction of the selected red fractions of $CDs_{18.5bar}$, CDs_{13bar}, and CDs_{8bar} with DMEM serum protein was established by exploring the formation of aggregate after incubation at 37 °C by DLS measurements. As shown in Table 2, all CDs samples interact with DMEM proteins giving rise to bigger proteins-dots aggregates within the range of 120–270 nm. In particular, CDs with the higher amount of surface carboxylic functions, namely $CDs_{18.5bar}$ and CDs_{13bar}, showed a stronger interaction with DMEM serum protein affording to proteins-dots nano-aggregates of about 210 and 270 nm in diameter, respectively.

In accordance, CDs_{8bar} with the lower amount of carboxylic acid and lower ζ-Potential (≈−19 mV) are much more cytocompatible. On the opposite, cell viability tends to decrease at the higher dosage tested (0.5–1 mg mL^{-1}) for the CDs obtained at higher pressure (Figure 21, Table 2). This behavior can be explained considering that CDs are prone to provoke electrostatic adsorption of serum proteins of the medium on their surface to give rise to nano-aggregates of about 270 nm in diameter and quasi null ζ-Potential (≈−6 mV) (Table 2). The reduction of the ζ-Potential elicited a time-dependent flocculation of the CDs into nano-aggregates. As consequence, the amount of corona protein on the surface is proportional to the size of the nanoparticles (CDs$_{18.5bar}$ are five times bigger than CDs$_{8bar}$, Table 2). This could significantly change nanoparticles' biological behavior, suggesting that the formation of corona protein might be involved in the cytotoxicity mechanisms of such CDs [268].

4.1.8. In vitro cell internalization study

Taking into account the possible use of the selected red-emitting fractions of CDs$_{18.5bar}$, CDs$_{13bar}$, and CDs$_{8bar}$ in imaging applications, their cell internalization was evaluated by fluorescence microscopy. In detail, MDA-MB-231 cells were incubated with an equivalent amount of either CDs$_{18.5bar}$, CDs$_{13bar}$ or CDs$_{8bar}$ for 6 h, and cell uptake was evaluated by tracking the red self-fluorescence of CDs and blue fluorescence of nuclei marked with a DAPI solution (Figure 22). Figure 22 shows a certain ability of all CDs samples to enter cancer cells under physiological conditions in DMEM, since red-emissive CDs show a specific nuclear localization (Figure 22a–c). However, as expected, cell cultures were highly contaminated by aggregates visible before washing up wells with DPBS using the Texas red channel (data not shown), corroborating the tendency of CDs to provide significant nano-aggregates in DMEM, and limiting their possible use in vivo. Therefore, a strategic surface engineering of these CDs must be considered as a functional strategy to limit the adsorption of corona proteins and increase the average surface diameter, avoiding rapid renal clearance and improving their therapeutic efficacy in vivo.

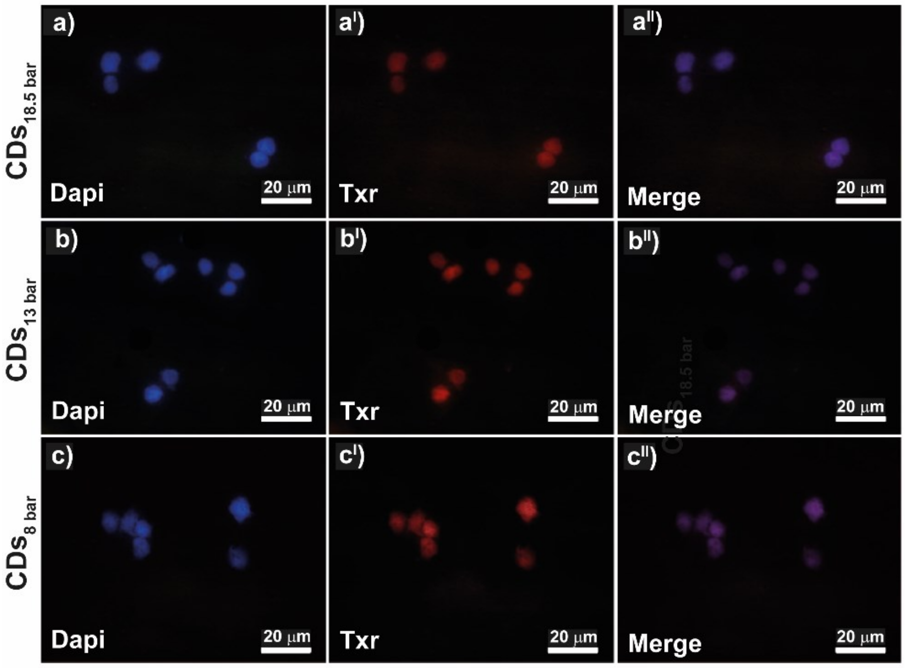

Figure 22. *Uptake study by fluorescence microscopy in a multichannel fashion of CDs after 24 h of incubation. DAPI (a,b,c), texas red (a',b',c'), and merge (a'',b'',c'') images are reported.*

4.1.9. Conclusion

In this work, it was explored a bottom-up synthesis strategy of fluorescent CDs to modulate their size distribution, surface state, optical properties (fluorescence and photothermal conversion capacity), and biological profile. The parallel solvothermal bar to the synthesis of CDs from urea and citric acid at different operating pressure (from 8 to 18.5 bar) highlighted the key role of pressure in the design of CDs with peculiar physicochemical, optical, and biological profiles. The crucial role of pressure as a thermodynamic parameter could allow for synthesized performant CDs for image-guided photothermal applications. In detail, it was observed a red shift of fluorescence proportional to the increased pressure and improved yield of red-emitting CDs at higher pressure. Moreover, the reddest fluorescent CDs obtained at the higher pressure also show a considerable absorption in the NIR region, determining the correlated good NIR photothermal conversion capacity. Indeed, the operating pressure highly impacts the size distribution of CDs. As demonstrated by AFM characterization. In particular, the average size of CDs was proportional to the operating pressure, passing from 0.45 to 2.4 nm, demonstrating that 8 bar is not a sufficient pressure to induce the complete formation of the crystal. Proportionally to the increased average size, it was observed an increment of the surface carboxyl groups can be correlated to the improved red fluorescence. Biological characterization of breast cancer cells allows for demonstration of the capacity of CDs to act as fluorescence and photothermal NIR-sensitive agents, exploitable in fluorescence imaging-guided photothermal therapy. However, although the present work demonstrates the key role of pressure in profiling CDs, the extremely low yield of the synthesis processes is still a major limitation in their use in the biomedical field.

4.2. Innovative decagram-scale synthesis of multicolor N,S-doped carbon nanodots as photothermal nanotools with selective anticancer properties

One of the most limiting drawbacks in the use and application of CDs is the extremely low reaction yield obtained up to now lower than the 3% w/w.

Here, an innovative protocol of synthesis and work-up of highly homogeneous N, S-codoped carbon nanodots in decagram-scale quantities was proposed for the first time, bypassing one of the major obstacles in the use of CDs for real-world biomedical applications. In detail, indocyanine green (ICG) is used as a bidentate SO_3^- donor able to tune surface groups and emission bands of carbon nanodots obtained by carbonization of citric acid and urea in DMF in solvothermal conditions. The co-doping involves various surface states providing transitions in the visible, thus allowing tunable multicolor emission from blue to the red region and excellent NIR-photothermal conversion efficiency useful in bioimaging applications and image-guided phototherapy in cancer theranostics. Moreover, sulfur-doping confers pro-oxidant activities by increasing NIR-triggered ROS generation in cancer cells compared to healthy cell lines. The oxidant stress can be locally increased by irradiating cells treated with N, S-doped CDs with an 810 nm diode laser at a lower power density of 2.5 W cm^{-2}. Therefore, this work provided a solid high-yield scheme of preparation of multicolor N,S-CDs with intrinsic cytotoxic activity toward cancer cells able to act as therapeutic and diagnostic agents, useful in breast cancer theranostics (Figure 23).

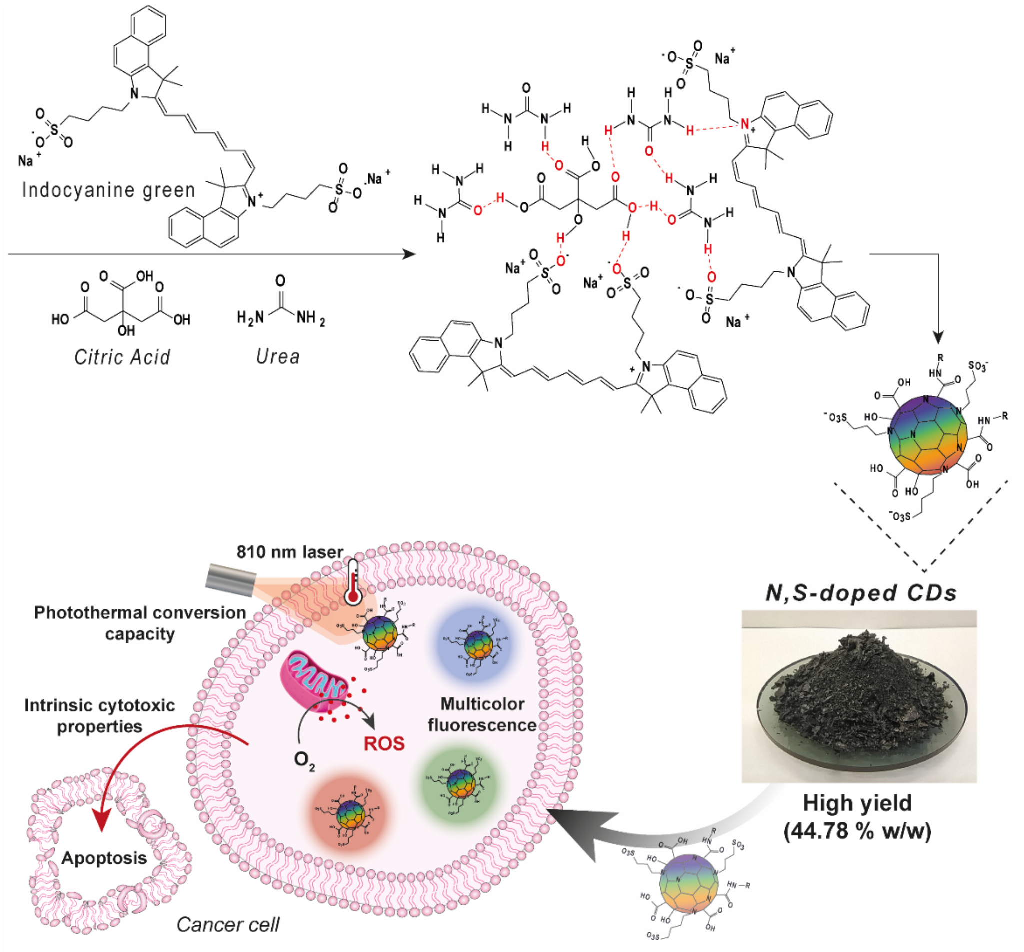

Figure 23. *Graphical abstract.*

4.2.1. Synthesis of N, S-doped Carbon nanodots (N,S-CDs)

In previous work, it was demonstrated that the decomposition of urea and citric acid in the strategic stoichiometric ratio, the use of DMF as the solvent, and appropriate conditions of temperature and pressure allowed obtaining red emitting CDs with suitable fluorescence quantum yield (QY of 4 %) and photothermal conversion efficiency (≈ 32 %), desired in cancer theranostics [3,158,224]. Taking into account these considerations, the main starting goal of the present work was to explore how the S-surface groups affect the photothermal performance of the dots, exploring that as a strategy to improve and extend their optical properties into the red and near-infrared (NIR) region. The second focus goal of the present work is to advance a synthetic and work-up protocol to improve the reaction yield, as necessary steps towards industrialization and real-world biomedical applications.

The designed CDs also attempt to strategically combine advanced optical properties with peculiar intrinsic anticancer features since CDs can penetrate and diffuse into the cell, interact with mitochondria and the genetic material, and provoke ROS production and G0/G1 phase arrest in cancer cells. Therefore, the design of promising functional nanomaterials with an intrinsic capacity to induce ROS-triggered DNA damage could be a valid rationale strategy in cancer therapy [269,270]. Therefore, nitrogen and sulfur co-doped carbon nanodots, namely N,S-CDs, were prepared by a bottom-up approach which consists of the solvothermal decomposition in N, N-dimethylformamide (DMF) of citric acid, urea, and indocyanine green (ICG) used as sulfonate donor chromophore (Figure 25) [271,272]. ICG having two alkyl sulphonate groups linked to nitrogen atoms can theoretically be involved in N-doping during the solvothermal decomposition (18–25 bar, 170 °C) and crystallization of urea and citric acid (Figure 24).

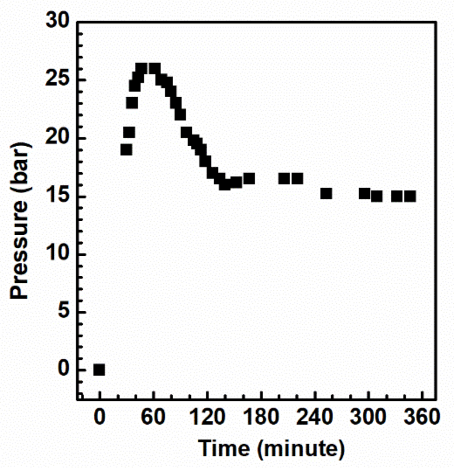

Figure 24. *Pressure trend in the function of time reaction monitored during CDs synthesis.*

Therefore, ICG was chosen as a doping agent to provide C-N, C-S, C-S=O, and SO_3 groups at the CDs surface (Figure 25). For this consideration, we employed an equimolar amount of citric acid and urea (roughly 58 mmol per each) and a non-stoichiometric amount of ICG (about 0.5 % on a molar basis). The idea was to introduce defect-controlled crystallization of the core derived from the decomposition of the starting monomers and to insert SO_3^- groups on the CDs surface. As the diverse work reported in the literature, carbon nanodots are usually isolated by precipitation using ethanol or other solvents. Successively, the heterogeneous crude product was purified using many chromatographic procedures. However, CDs have good dispersibility in many polar and non-polar solvents, as a result the step of isolation by purification negatively affects the yield of reaction giving rise to a very low reaction yield from 0.01 to 5 % on a weight basis. Similar results are observed using dialysis, which conducts on heterogeneous samples with very low reaction yields. Here, the work-up of the sample was radically changed to allow the production of homogeneous CDs with the highest reaction yield reported in the literature panorama (i.e., 21.769 g), corresponding to 44.78 % w/w. In detail, the DMF of the solvothermal decomposition product was removed by a rotatory evaporator, obtaining a dark powder that was dispersed in ultrapure water by sonication. Successively, the aqueous dispersion of raw CDs was purified by size exclusion chromatography using a gradient of Sephadex with increasing cut-off as stationary phase and simple water as eluent (Figure 25).

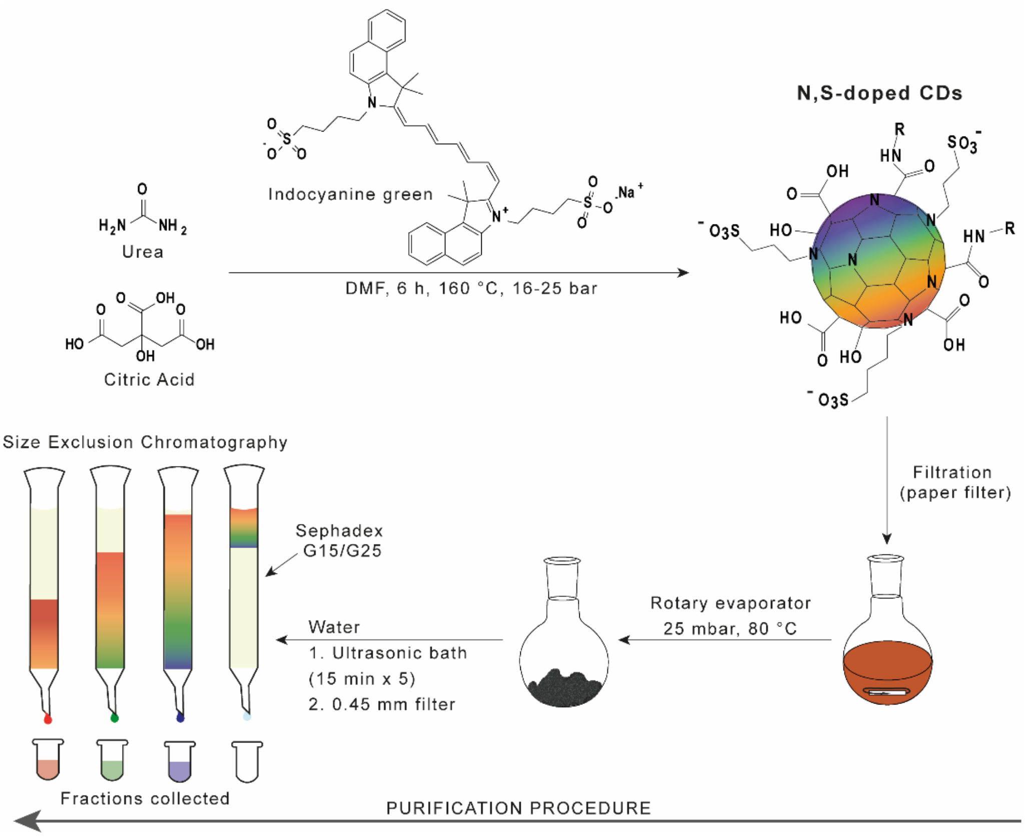

Figure 25. *Scheme of solvothermal synthesis and purification by SEC of N,S-CDs.*

Two main fluorescent fractions were collected from chromatography after the first elution of amorphous by-products, named F1 and F2. F1 was characterized by a predominant emission band in the violet-blue region, which is of poor biological interest for in vivo biomedical applications (Figure 26). The F2 fraction possessed a multicolor emission behavior with bright emission bands also in the orange-NIR region (Figure 33b).

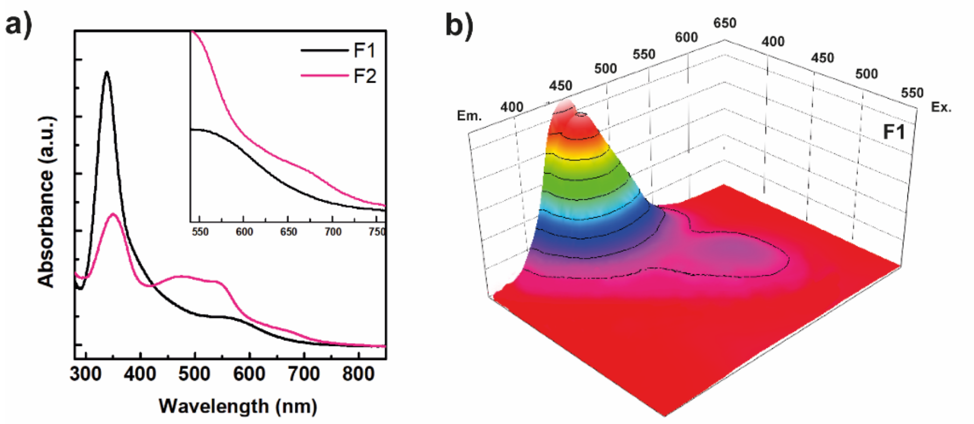

Figure 26. *UV spectra of F1-2 of N,S-CDs (a) and 3D fluorescence spectrum of N,S-CDs F1.*

4.2.2. Structural characterization of N,S-CDs

The morphologies and size distribution of the fractions selected, F1 and F2, were investigated by atomic force microscopy analysis (AFM). The size distribution of each fraction was extrapolated from several AFM micrographs considering the heights of each dot. In detail, AFM micrograph of F1 fraction (Figure 27a) highlighted single CDs of about 5 nm in height and many aggregates, reflecting in heterogeneous size distribution. Indeed, as reported in Figure 27b, F2 sample was characterized by highly homogeneous CDs with an average diameter of 5.3±0.4 nm and a very narrow size distribution. F2 fraction represents about 46 % of the pure product (≈ 10 g) and is the best in terms of size distribution and was selected for further characterization.

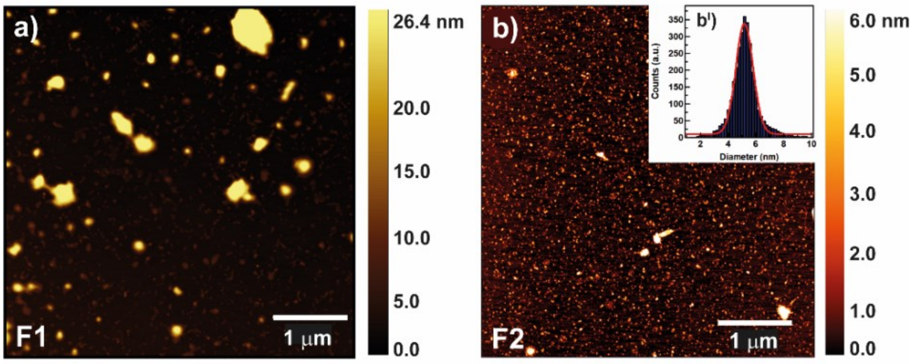

Figure 27. *AFM micrographs of N,S-CDs F1 (a) and F2 (b). Size distribution of N,S-CDs F2 (b').*

In order to evaluate the structure of the N,S-CDs core, HR-TEM analysis was performed investigating several dots. CDs show a regular crystalline lattice of type β-C_3N_4 with an average size of 5 nm (Figure 28), highlighting an elevated structural homogeneity. HR-TEM image (Figure 28a’) shows spherical carbon dots with hexagonal β-C_3N_4

monocrystal, as indicated by the good agreement between its 2-dimensional Fourier transform (FT) and the calculated diffraction pattern of bulk hexagonal β-C_3N_4 (space group P63/m, space group number 176) with a = b = 6.38 Å, c=2.395 Å in the [214]-zone axis.

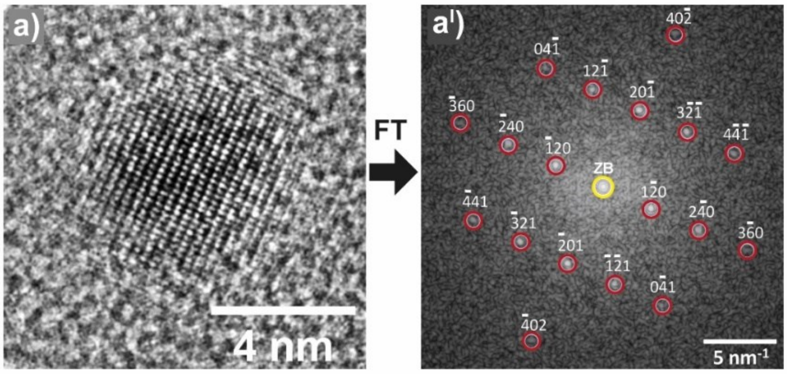

Figure 28. *HR-TEM micrograph of isolated N,S-CDs (a) and the calculated diffraction pattern of bulk hexagonal β-C_3N_4 by Fourier Transform (FT) (a').*

4.2.3. Physico-chemical characterization by spectroscopy techniques

FT-IR and XPS analysis were employed to evaluate the N,S-CDs surface state. As reported in Figure 29, the FT-IR spectrum of CDs revealed many vibration bands attributable to hydroxyl (3420 cm^{-1}), amine (3200 cm^{-1}), amide (amide I band, 1640 cm^{-1}), carboxyl (asymmetric stretching at 1715 cm^{-1}), and sulfonate/sulfoxide groups (1391 and 1283 cm^{-1}). Moreover, there are bands attributable to C-N (1463 cm^{-1}), C-O-C-N (1212 cm^{-1}), and C-S (992 cm^{-1}) vibrations. These vibrational bands suggested that different surface polar groups characterized CDs, which implies high dispersibility in different polar solvents.

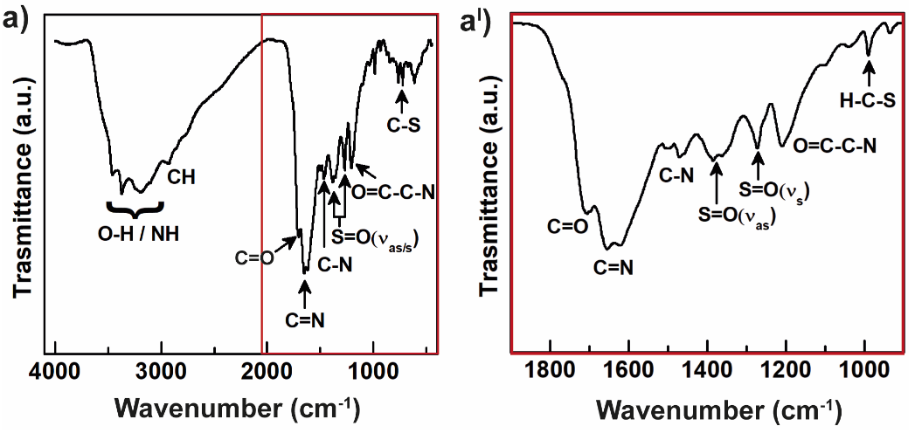

Figure 29. *FT-IR spectrum of N,S-CDs (a) and zoom of spectrum in the range 1900-900 cm^{-1} (a') with relative attributions.*

This chemical profile is highly desirable for further functionalization and manipulation steps to improve their physicochemical and dimensional properties for a specific application. Furthermore, CDs present -SO_3^- surface groups provide stable anionic charges under physiological conditions ($5.5 < pH < 7.4$) (Figure 30.), due to their pKa being less than 3. This aspect of CDs surface state allows for avoiding dot-dot interactions due to ζ-potential changes induced by protonation phenomena during their biodistribution in vivo [273].

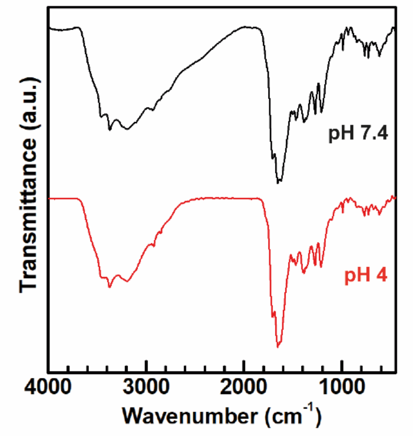

Figure 30. *FT-IR spectrum of N,S-CDs at physiological pH and acid pH.*

The surface chemical profile of CDs revealed by FT-IR study was confirmed by XPS analysis (Figure 31), confirming the main bonds previously observed in the FT-IR spectrum (Figure 29). More in detail, SO_3^- groups of indocyanine green were successfully inserted on the CDs surface (about 1.1 %) as shown by diagnostic peaks of C-S and C-SOx (S=O, SO_3^- or SO_4^{-2}) groups in the Sp_2 core levels (168 eV) (Figure 31a). Moreover, XPS study revealed that only a few sulfur atoms occasionally doped the CDs crystalline core (< 0.1 %) in the form of C-S defects, following HR-TEM measurements. In the C1s signal (Figure 31a'), distinctive contributions related to C-C, C-OH, C-S, and C-N (286.0 eV) and around 288.0 eV attributable to amide and carboxyl functions, confirming the high amount of carbonyl groups at the CDs surface. In detail, about 10 % and 5 % of surface functional groups are amide (287.6 eV) and carboxyl (288.9 eV) functions, respectively. The high-resolution scan of the N1s peak around 400.0 eV (Figure 31a'') confirms the presence of amide functions and some prim- or sec-amine groups (1.4 %). Lastly, the deconvolution of the O1s XPS signal confirmed the spectral signatures of OH, C=O, and S=O groups, following FTIR analysis, suggesting about 11 % of amides, 6 %

of carboxyl acids, 9 % of hydroxyls, and 1 % of sulfonates, as above calculated (Figure 31a’’’).

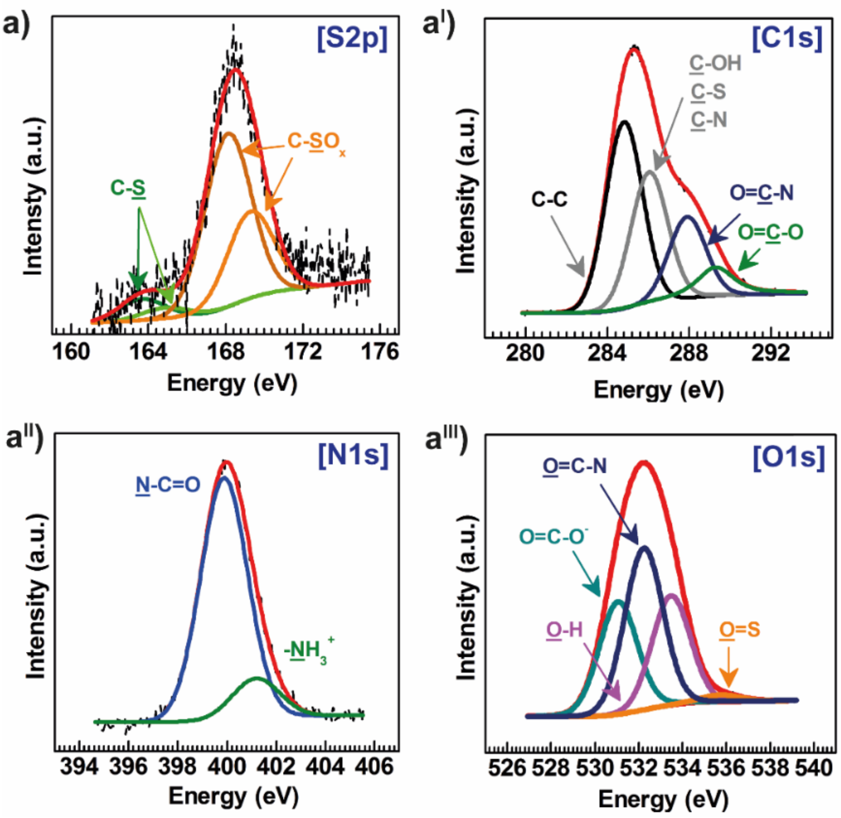

Figure 31. *XPS analysis and deconvolution of the rough spectra (a-a’’’) of N,S-CDs.*

4.2.4. Thermal characterization by coupled DSC-TGA analysis

DSC and TGA analysis were performed to evaluate the thermal stability of carbon nanodots and the amount of surface functional groups on a weight basis. The analyses were conducted within a temperature range of 20-600 °C, applying a heating rate of 10 °C min^{-1} (Figure 32a). As shown in Figure 32a, no significant weight loss and thermal transitions were revealed in the sample thermograms in the range of 20-160 °C, indicating that the sample was stable within this temperature range. By contrast, increasing the temperature at 160 - 400 °C a broad endothermal transition was observed, followed by a further decomposition peak within 200-600 °C of 920 J g^{-1} (Figure 22a’), attributable to the decomposition of surface functional groups of CDs. In parallel, the thermogravimetric curve (Figure 22a) highlighted a weight loss of 41 % w/w up to 600 °C (Figure 22a’). These evidences suggest that CD’s core represents about 60 % of the nanodot, while the total amount of surface groups (amides, carboxyl, hydroxyls, sulfonates, and amines) represent about 40 % of the sample considered, according to the XPS analysis (Figure 31.).

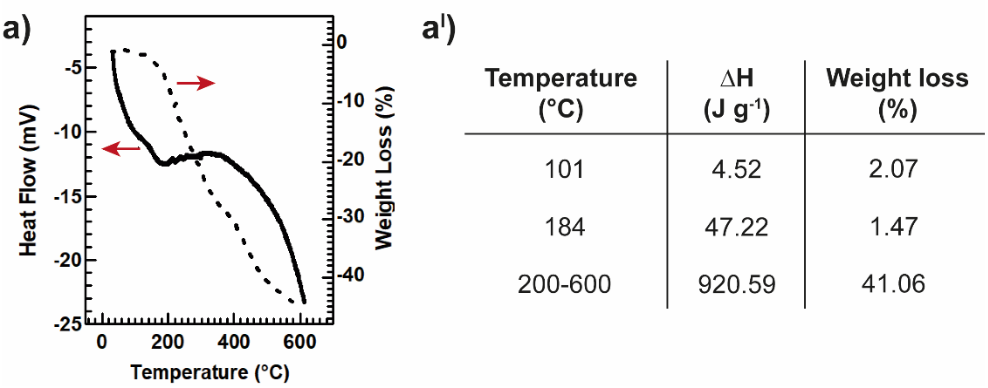

Temperature (°C)	ΔH ($J\ g^{-1}$)	Weight loss (%)
101	4.52	2.07
184	47.22	1.47
200-600	920.59	41.06

Figure 32. *DSC coupled TGA analysis (a) and extrapolated values of differential enthalpy and weight loss in function of the temperature (a').*

4.2.5. Optical Characterization

The optical absorption spectrum of N,S-CDs (Figure 33a) shows a sharp UV absorption band below 300 nm attributable to the core states and a complex series of electronic transitions in the visible range, with peculiar peaks at 350, 440, 540, and 670 nm, certainly associated with surface states, as well-established from previous studies [2]. In contrast, the optical absorption profile of CDs does not show the typical peak of ICG at 780 nm, confirming its successful decomposition during the solvothermal process, acting as a donor of -SO_3^- groups to the CD surface. The absorption spectrum of simpler β-C_3N_4 CDs generally displays a single dominant band at 400 nm related to transitions coupling core states to surface carboxylic groups [167,274]. Here, the spectrum in Figure 33a. is very different and complex to precisely correlate the many bands to specific chemical surface moieties of N,S-CDs. However, the strongly complex optical absorption spectrum toward the red and NIR regions could be ascribed to a highly multifunctional surface where -SO_3^- introduces new transitions. Indeed, previous studies on S-doped dots had already observed similar absorption profiles but less pronounced than those observed here [275]. The subsequent emission properties were deeply investigated in light of the complex absorption properties of N,S-CDs. In terms of emission properties, the very broad absorption leads to a wide tunability of the CDs fluorescence. As shown in Figure 32b-c, N,S-CDs exhibit a strong fluorescence tunability, displaying an emission peak that continuously shifts from 420 to 700 nm (Figure 33b), varying the excitation wavelength from 355 to 660 nm. Together with the correlated changes of the decay lifetime (Figure 33c), a variation in the QY efficiency was observed, changing from 6 % in the green to less than 1% in the NIR region. The nanosecond decays lifetime and QY efficiency proportionally decrease as a function of the excitation wavelength, suggesting a reduction of the non-radiative rate recombination. Then, the emission profile and QY in different solvents were evaluated.

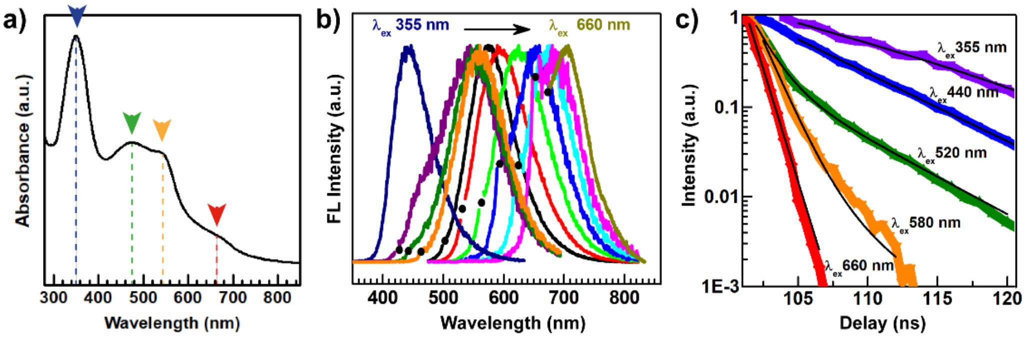

Figure 33. *UV spectrum (a), emission spectra at different excitation wavelengths (355, 420, 440, 460, 500, 530, 560, 590, 620, 650, 660 nm) (b) and decay of fluorescence at diverse excitation wavelength with fitting curves (c).*

As shown in Figure 34 fluorescence shifts in different solvents were observed, revealing a very sensitivity to the character of the external environment. Also, QY depends on the solvent which is almost 3-fold lower in water as compared to the other tested solvents. These observations suggest a proper surface functionalization of N,S-CDs with different polymers could be an effective strategy to increase their emission efficiency and profile.

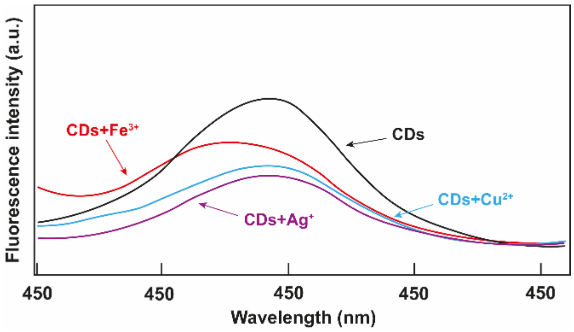

Figure 34. *Emission spectra of N,S-CDs in presence of cations (Fe^{3+}, Ag$^{+,}$ and Cu^{2+}).*

4.2.6. NIR-induced photothermal conversion capacity evaluation

Considering the extended absorption spectrum of N,S-CDs with significant extensions into the deep-red, a considerable photothermal effect under near-infrared (NIR) irradiation is strongly expected. Therefore, the temperature increase induced by intensity laser radiation at 810 nm was monitored by a thermal imaging camera. As can be noted in Figures 34a-b, after three minutes of NIR-laser irradiation at 5 W cm^{-2} of power density, an aqueous solution of N,S-CDs at a concentration of 0.5 mg mL^{-1} heats up to about 80 °C. It should be noted that after 5 minutes of laser exposure, the sample reached a steady state (Figure 35a), implying that the thermal relaxation of the sample is balanced by the dissipation of energy towards the environment. At 800 nm and 2.5 W cm^{-2} power density, the temperature increase is about 33 °C, significantly higher than that of other carbon-based nanoparticles with similar structures at comparable concentration [276,277], attributable to the long absorption band observed in the NIR region (Figure 33a).

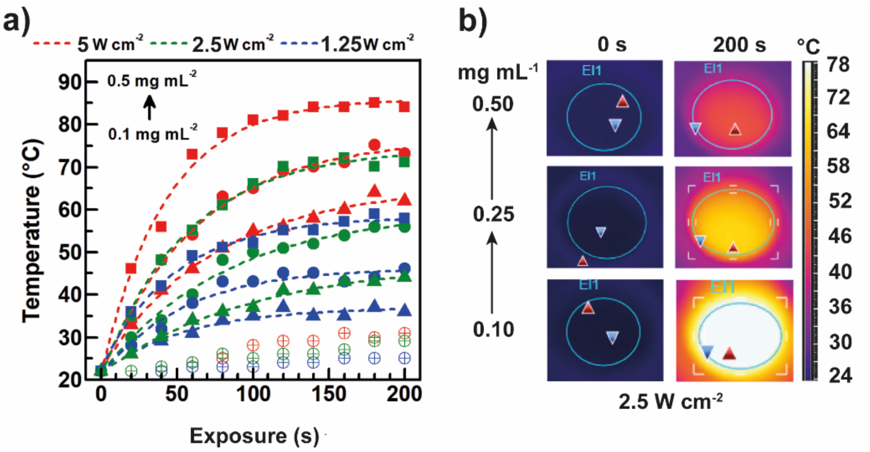

Figure 35. *Kinetic of hyperthermia at different concentrations of N,S-CDs (0.1, 0.25, and 0.5 mg mL^{-1}) under 810 nm laser irradiation with power fitted at 5, 2.5, and 1.25 W cm^{-2} (a). Thermographs of aqueous N,S-CDs dispersion (0.2 mL per well) with increasing concentration under 810 nm laser irradiation (200 s, 2.5 W cm^{-2}) (b).*

In reference to a previously reported method [278], the photothermal efficiency of the N,S-CDs carbon nanodots was calculated by considering the photothermal kinetic of a dispersion of carbon nanodots in ultrapure water placed into a 1 cm quartz cuvette evaluating the heat generation of the N,S-CDs dispersion under NIR-light irradiation (laser on) and heat dissipation (laser off) (Figure 36).

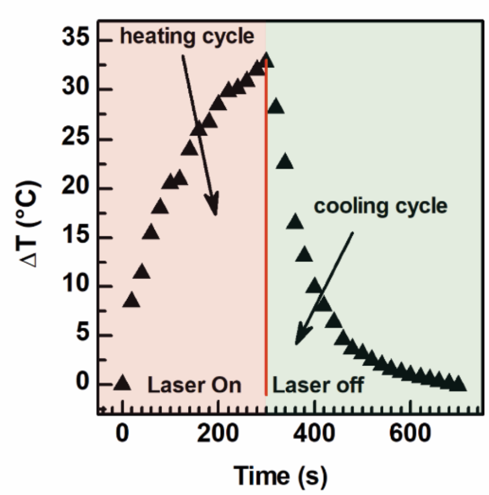

Figure 36. *Photothermal conversion efficiency evaluation: heating profile (red section) under an 810 nm laser irradiation (300 s, 2.5 W cm^{-2}) and cooling profile turning off the laser (green section).*

Here, it was assumed that all the light absorbed by CDs is transformed into heat. Under NIR irradiation, the change in temperature T is described by the energy balance equation (1):

$$\sum_i m_i C_i \frac{dT}{dt} = E_{abs} - E_{loss} \tag{1}$$

where E_{abs} is the heat induced by the absorbed energy, E_{loss} is the heat dissipated in the surrounding medium and t is the irradiation time. While m_i and C_i are the mass and specific heat capacities of each element (i) comprising the entire physical system (i.e., CDs, deionized water, and cuvette). The mass of tested N,S-CDs was insignificant compared to the mass of the solvent and the cuvette. Moreover, the heat capacity of N,S-CDs is also much smaller than that of water. Thus, the mass and heat capacity can be assumed to be the one of water. Energy transfers can be described by the following equations:

$$E_{abs} = P(1 - 10^{-A\lambda})\eta \tag{2}$$

$$E_{loss} = hS(T_t - T_0) \tag{3}$$

where P represents the incident NIR-laser power, Aλ is the absorbance value of the N,S-CDs dispersion at the excitation wavelength of the laser, η is the photothermal conversion efficiency, h is the heat transfer coefficient, S is the surface enclosed by the N,S-CDs dispersion, and T_0 is the room temperature. Then, Eq. (1) can be rewritten substituting Eq. (2) and (3) as follows:

$$\frac{dT}{dt} = \frac{P(1-10^{-A\lambda})\eta}{\sum_i m_i C_i} - \frac{hS(T_t - T_0)}{\sum_i m_i C_i} \tag{4}$$

Equation (4) can be simplified by introducing two constants A and B:

$$A = \frac{P(1-10^{-A\lambda})\eta}{\sum_i m_i C_i} \tag{5}$$

$$B = \frac{hS}{\sum_i m_i C_i} \tag{6}$$

Thus obtaining the simplified Eq. (7):

$$\frac{dT}{dt} = A - B(T_t - T_0) \tag{7}$$

By integrating Eq. (7) from 0 to t, the temperature transient (T_t) for an arbitrary initial temperature value (T_i) results as:

$$T_t = T_0 + \frac{A}{B}(1 - e^{-Bt}) + (T_i - T_0)e^{-Bt} \tag{8}$$

In order to retrieve η, it is needed to measure the temperature variation of the N,S-CDs dispersions as a function of time during both the photothermal heating (laser on, $A \neq 0$ and $T_i = T_0$) and the subsequent cooling (laser off, $A = 0$ and $T_i > T_0$). Thus, obtaining equations (9) and (10), respectively:

$$T_t = T_0 + \frac{A}{B}(1 - e^{-Bt}) \tag{9}$$

$$T_t = T_0 + (T_i - T_0)e^{-Bt} \tag{10}$$

By fitting the experimental curve with equation (4), the values of A and B can be extrapolated and employed to calculate the experimental photothermal conversion efficiency η:

$$\eta = \frac{A \sum_i m_i C_i}{P(1-10^{-A\lambda})} \tag{11}$$

The photothermal efficiency of N,S-CDs at 800 nm is estimated to be 46 ± 4 %, comparable to the most promising nanoheaters as gold nanorods [279] (≈ 55 %) and graphene oxide [280] (≈ 58 %), promising for applications of these nanomaterials in photothermal therapy.

4.2.7. Cytocompatibility study

Cytotoxic profile of N,S-CDs with and without NIR-laser stimulation was studied on different cancer, pre-cancer, and healthy cell lines evaluating the cell viability of each cell line after a defined time of incubation with an increasing concentration of nanosystem. In detail, human bronchial epithelial cells (16-HBE) and human fibroblasts (NHDF) were used as healthy cell lines, breast epithelial cells (MCF-10A) were employed as a pre-cancerous cell line model, and breast cancer cells (MCF-7, MDA-MB-231, and SK-BR-3) were used as cancer cell lines with different phenotypes, receptors expression, and inclination to form metastases. Selective anticancer effects of N,S-CDs expressed in terms of cell viability toward cancer and pre-cancerous cells after an incubation time of 48 h with an increasing amount of N,S-CDs dispersed in DMEM were compared (Figure 37). N,S-CDs showed an optimal cytocompatibility up to 0.5 mg mL^{-1} (100%) for the healthy cell lines tested (e.g. 16-HBE and NHDF). Only at the higher concentrations tested was observed a minor cytotoxic effect corresponding to a cell viability of 75 % for the bronchial epithelial cells, highly beyond the typical IC_{50} values reported for CDs (<0.25 mg mL^{-1}), and much more marked reduced cell viability to about 20 % for fibroblasts [205,281]. Therefore, N,S-CDs are broadly cytocompatibility 0.5 mg mL^{-1} for both healthy cell lines (Figure 37). Surprisingly, a dose-dependent cytotoxic effect on both pre-cancerous (MCF-10A) and cancerous (MCF-7, MDA-MB-231, and SK-BR-3) cell lines were observed at a concentration higher than 0.25 mg mL^{-1} (Figure 37). However, it is important to highlight that pre-cancerous MCF-10A cells show a cell viability of about 100 % after 48 h of incubation with N,S-CDs at 0.25 mg mL^{-1}; while, MDA-MB-231 cells treated under the same conditions exhibit the major toxic effects corresponding to a cell viability of about 70 %. The dose-dependent cytotoxic effect was observed on cancerous and pre-cancerous cells also after 24 h of incubation. In light of these considerations, the cytotoxic effect of these CDs decreased passing from healthy to cancerous cells (IC_{50} healthy > IC_{50} pre-cancerous > IC_{50} > cancerous) (Figure 37), suggesting that these N,S-CDs seem to be able to stimulate a sustained and selective cytotoxic effect, suitable to provide innate anticancer properties useful for medical applications.

4.2.8. NIR-induced photothermal effect in vitro

Moreover, as previously demonstrated N,S-CDs exhibit a marked NIR-photothermal conversion capacity, potentially exploitable to locally induce an increment of the intracellular temperature as well as to simultaneously trigger regulated cell death pathways (RCD), such as necroptosis and phagocytosis, by hyperthermia [1,4,224,282]. Thus, the NIR-triggered nanotoxicity was compared to effects obtained from cells treated only with N,S-CDs for 48 h, to prove that further effective anticancer phototherapeutic insults can be induced on demand under a no-invasive and high penetrating 810 nm laser. For these reasons, the second set of experiments was carried out using the same conditions adopted and tested above, but also treating cells with NIR-laser for 200 s at power fitted at 2.5 W cm^{-2}. The power density was selected based on the photothermal profile, in order to reach a useful temperature within the range of 42–65 °C to induce photothermal hyperthermia or ablation. As expected, all cell lines tested showed an exposure-dependent anticancer effect as reported in Figure 37 the complete ablation of all the cultured cells was observed after 48 h of incubation with N,S-CDs at 0.5 mg mL^{-1} combined with a NIR-induced temperature increase beyond 70 °C. On the contrary, no considerable synergistic photothermal anticancer effects were observed at concentrations lower than 0.25 mg mL^{-1}, except for MCF-10A. It should be noticed that only NIR-triggered hyperthermia ($T < 44$ °C) allows the selective killing of cancer cells preserving the healthy ones, although a fine control of the cell temperature is precluded during laser exposure in vitro [283]. On the contrary, photothermal ablation ($T > 45$ °C) provokes unspecific cell death in vitro of normal and cancer cells. However, NIR-induced cell ablation can be exploited for the selective removal of the entire tumor mass in vivo under remote spatio-temporal control of an 810 nm laser. Overall, the observed data suggest that the combination of the innate anticancer effect observed for cancerous and pre-cancerous cells and the local NIR-photothermal ablation of primary tumors can be exploited to maximize anticancer treatment with poor side effects.

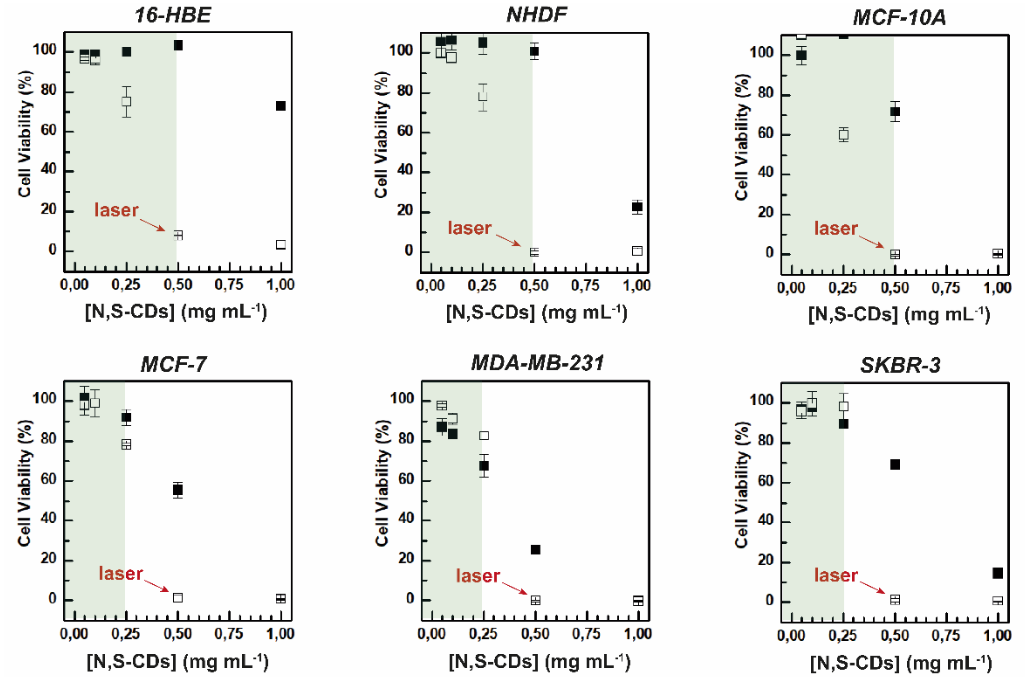

Figure 37. *Cytotoxicity of N,S-CDs with and without 810 nm laser exposure (200 s, 2.5 W cm^{-2}) after 48 h of incubation on six different cell lines (16-HBE, NHDF, MCF-10A, MCF-7, MDA-MB-231, and SKBR-3).*

4.2.9. Cell Reactive Oxygen Species (ROS) evaluation in vitro

In order to better understand the selective growth inhibition effects on pre-cancerous and cancerous cells observed without NIR-laser treatment, it was evaluated the capacity of the proposed nanoparticles to interact with the mitochondria membrane inducing intracellular ROS generation, especially in cancer cells. This mechanism was explored taking into account scientific works reported in the literature describing that CDs obtained from the solvothermal decomposition of citric acid and urea might exhibit selective antiproliferative activities against different cancer cells such as choriocarcinoma cells (JAr/Jeg-3 cell lines), due to local laser-triggered ROS production, although highly biocompatible towards different healthy and cancer cell lines [284,285]. Interesting data suggest that ROS are not simply mitochondria by-products that damage cells, but are implicated in diverse intracellular signaling pathways which regulate tumor microenvironment as well as cancer cell homeostasis [281,286]. In particular, the strong production of ROS, especially in cancer cells, also provokes overexpression of antioxidant proteins, thus preserving intracellular redox homeostasis [205,212]. Therefore, the inherent anticancer effect observed for the proposed N,S-CDs could be ascribed to a metabolic dysregulation induced by an uncontrolled intracellular overproduction of ROS triggered by nanomaterials. In light of these considerations, intracellular ROS production was evaluated to establish cancer cell death mechanisms induced by nanomaterials in comparison to healthy cell ones. The intracellular amount of ROS in all healthy, pre-cancerous, and cancerous cell lines chosen was evaluated using a redox-sensitive fluorescent probe, namely DCFH-DA, by a microplate reader. DCFH-DA consists in a cell-permeable probe that can be hydrolyzed to the free carboxylate (DCFH) by intracellular esterase and then oxidated to fluorescent dichlorofluorescein (DCF). Green fluorescence of DCF can be detected by confocal microscopy or microplate reader, thus allowing quantitation of ROS and in particular hydrogen peroxide. Results were compared with tert-butyl hydroperoxide a standard inductor of oxidative stress used as a positive control, and dextran used as a negative control. As reported in Figure 38, a dose-responsive increase of intracellular ROS level was observed in all cell lines tested, but with significant changes in the production of ROS passing from healthy to cancerous cells. In particular, the relative amount of ROS produced in 16-HBE and NHDF at the higher concentration tested of N,S-CDs (1 mg mL^{-1}) is about ten- and five-fold lower than the positive control, respectively. On the contrary, the amount of ROS produced in MCF-10A, MCF-7, MDA-MB-231, and SK-BR-3 at the higher concentration tested, comparable to the positive control, is about six-fold higher than that produced by healthy cells. Moreover, in pre-cancerous and cancerous cells treated with N,S-CDs within 0.25 – 0.5 mg mL^{-1} the level of ROS is from two- to three-fold higher (Figure 38). It is noteworthy that compared to the other breast pre-cancerous and cancerous cell lines, MDA-MB-231 breast cancer cells generate the highest amount of ROS, demonstrating much more sensitivity to oxidative stress induced by N,S-CDs at doses higher than 0.1 mg mL^{-1}. However, no significant changes can be observed at lower dosages. This trend suggests the innate capacity of N,S-CDs to induce cancer-specific modifications to ROS homeostasis, implying that this mechanism would be targeted for selective and precise therapeutic approaches. In accordance with cell viability data reported in Figure 36, N,S-CDs proved capable of selectively killing only pre-cancerous and cancerous cells, due to the increased ROS production level and the consequential oxidative stress. Literature data suggest that sulphur doping of CDs confers the capacity to stimulate ROS production by interacting with the electron transport chain in the mitochondrial membranes [270]. However, this is the first time that ROS production is recorded preferentially in cancer cells instead of normal cells into this range of concentration (0.25 – 1 mg mL^{-1}), suggesting an excellent anticancer potential of this innovative nanomaterial.

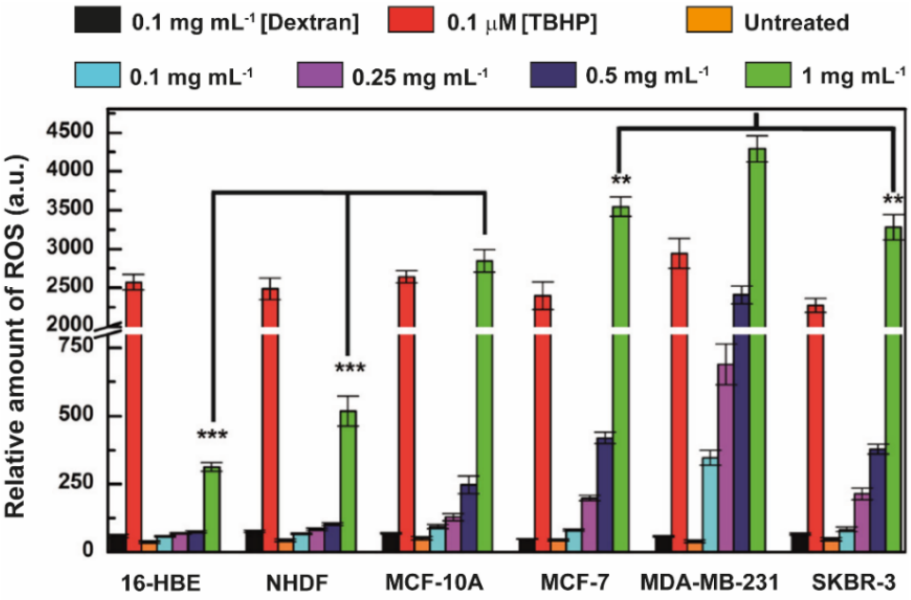

Figure 38. *ROS assay in vitro on cell lines incubated for 24 h with N,S-CDs (0.1, 0.25, 0.5, and 1 mg mL^{-1}). Dextran solution (1 mg mL^{-1}) and TBHP (50 μM) were used as the negative and positive control, respectively.*

The production of ROS in cells was evaluated also by combining the inherent and selective cytotoxic effect of N,S-CDs, and the hyperthermia owing to NIR light exposure at low power density (Figure 39). The levels of ROS in healthy, pre-cancerous, and cancerous cells treated with N,S-CDs at concentration beyond 0.25 mg mL^{-1} were measured after NIR-laser irradiation for 200 s at 2.5 W cm^{-2}. According to cell viability data, no significant difference between healthy and cancer cell lines was observed for all the cells considered. Compared with unexposed cells, these findings are of great significance, revealing the possibility to restrict the cytotoxic effects to a tumor mass by confined NIR light treatments.

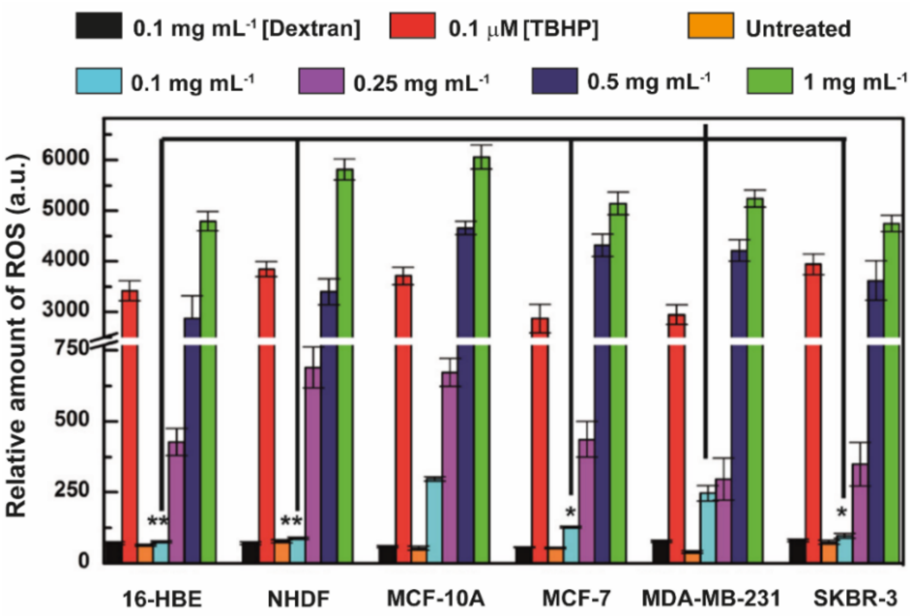

Figure 39. *ROS assay in vitro on cell lines incubated for 24 h with N,S-CDs (0.1, 0.25, 0.5, and 1 mg mL^{-1}) and irradiated with 810 nm laser (200 s, 2.5 W cm^{-2}). Dextran solution (1 mg mL^{-1}) and TBHP (50 μM) were used as the negative and positive control, respectively.*

4.2.10. Study of uptake on cell culture in vitro

Cell internalization of N,S-CDs on all the considered cell lines was evaluated by exploiting the self-tracking abilities from the blue to the red region by fluorescence microscopy. As reported in Figure 40-41, there are no observed significant differences between breast cancer cells and normal cells in terms of cell uptake and intracellular internalization pathways adopted. The uptake and cell localization of N,S-CDs were established on all cell lines after 6 h (Figure 40) and 24 h (Figure 41) of incubation to correlate how a different mechanism of internalization can affect the cytotoxicity profile of these CDs. Besides, we performed the uptake measurements by fluorescence microscopy in a multichannel way (from green to red region) to assess their potential in bioimaging, diagnosis, and image-guided therapy. No significant changes in the intracellular localization of N,S-CDs were observed comparing data over time (Figure 40-41). However, cell uptake shows cell line-dependent internalization and localization in different compartments of N,S-CDs. N,S-CDs demonstrated a good contrast in the green channel (Fitc) and red channel (TxR), involving excellent potential in multicolor bioimaging applications. N,S-CDs appear preferentially localized inside cytosolic vesicles in breast cancer cell lines like MCF-7 and SKBr-3, while MDA-MB-231 are characterized by a much more restricted nuclear and perinuclear localization of nanoparticles. Although more discrete, pre-cancerous cells (MCF-10A) display a similar cell localization (Figure 41d-d’’’), which explains well why the compatible cytotoxic profile (Figure 37). Considering healthy cell lines, N,S-CDs appear localized into cytosolic endosomes and slightly in nucleus and endosomes for fibroblasts (NHDF) (Figure 41e-e’’’) and bronchial epithelium (16-HBE) (Figure 41f-f’’’), respectively. The human bronchial epithelial cell line, namely 16-HBE, forms a pseudo-stratified monolayer characterized by tight junction proteins which limits cell transport mechanisms [287]. Therefore, the different intracellular localization observed could be ascribed to a prevailingly passive mechanism of transport for 16-HBE. Overall, the higher sensitivity observed in pre-cancerous and cancerous cells, suggested faster internalization by endocytosis for breast cancer cells since nanoparticles appear widely localized into the cells, including endosomes, cytosol, and nuclei. In fact, cancer cells are characterized by well-known multiple dysregulated proteins, that promote cell migration and invasion [283]. These characteristics corroborate the hypothesis that redox stress at the mitochondria level and thus irreversible cell damages are correlated to the sustained transport of nanoparticles observed in cancer cells, instead of healthy ones, explaining the higher and selective toxicity observed for several kinds of breast cancer cells (Figure 37-38).

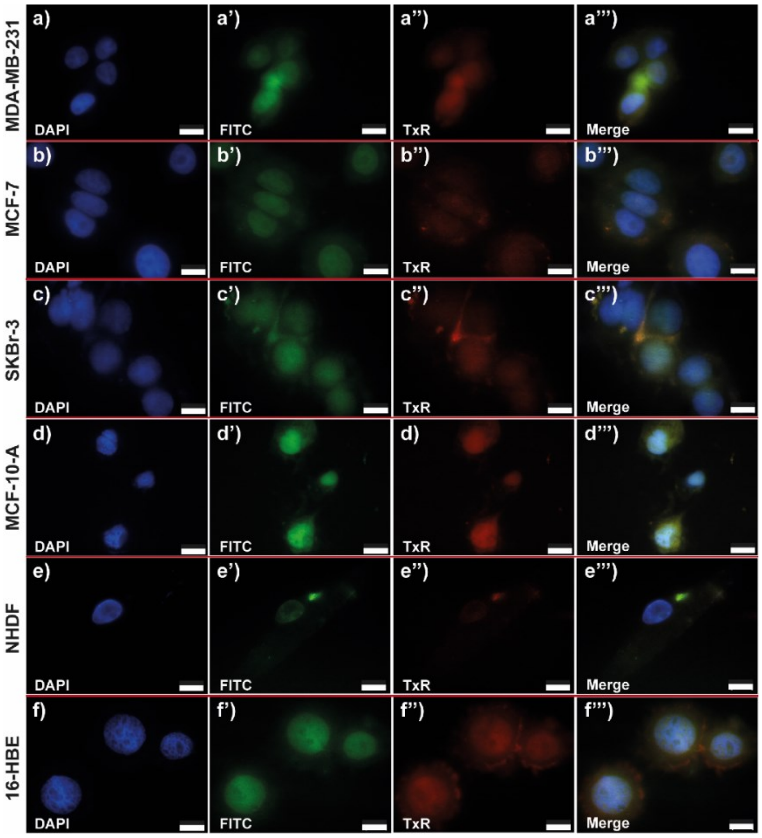

Figure 40. *Uptake study by fluorescence microscopy after 6 h of incubation.*

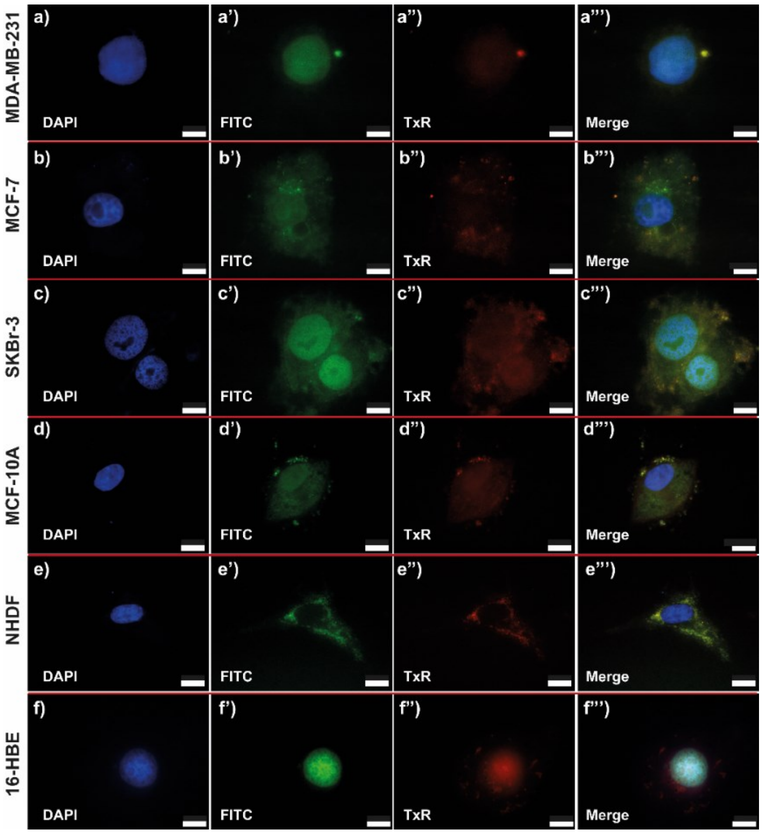

Figure 41. *Uptake study by fluorescence microscopy after 24 h of incubation.*

4.2.11. Conclusions

Here, it was proposed for the first time an efficient protocol of synthesis and purification of highly homogeneous N,S-codoped CDs in decagram-scale, useful in a wide range of biomedical applications. The proposed CDs were synthesized from urea, citric acid, and indocyanine green (ICG) in solvothermal conditions. ICG was exploited as a bidentate SO_3^- donor to achieve core and surface doping, and peculiar optical properties. The co-doping allows for the extension of the absorption properties of CDs in the entire visible range, favoring a multicolor fluorescence from the blue to the red region and excellent photothermal conversion capacity in the NIR region. N,S-doped CDs demonstrated extended biocompatibility on six different cell lines, demonstrating powerful nanoheaters to induce selective cancer cell death under 810 nm diode laser stimulation. Moreover, sulfur doping was demonstrated to impinge pro-oxidant activities by triggering an increased ROS generation in breast cancer cells (MCF-7, MDA-MB-231, and SKBr-3) and breast pre-cancerous cells (MCF-10A) compared to normal cells (NHDF and 16-HBE), that can be improved under NIR irradiation (2.5 W cm^{-2}). Cell uptake studies by fluorescence microscopy demonstrated the capacity of N,S-CDs to act as a contrast agent in a multicolor fashion. The uptake micrographs show a different cell localization in healthy cell limes compared to cancer cells probably correlated to a diverse pathway of internalization. Therefore, this work, first of all, proposed a decagram-scale of CDs synthesis, which allow for overcoming applicative limitations correlated to low yield, and opens a debate on the rational design of next-generation nanomaterials with intrinsic anticancer properties.

4.3. Advanced surface functionalization strategy of N,S-doped carbon nanodots via heterophase melt-extrusion transesterification with Poly (D, L-lactide)

As deeply explored in the literature, carbon nanodots (CDs) can be synthesized in a one-step bottom-up or top-down synthesis procedure from a plethora of starting natural products or synthetic organic compounds at different temperatures and pressure conditions [3,142]. The resulting CDs core and surface functional group features define their shape, size distribution, optical properties (e.g. absorption, fluorescence, photothermal conversion), and biological profile (e.g. cytocompatibility, dot-protein interactions) [155,288,289]. Therefore, it has been recognized that the modulation of the CDs features can be rationally tuned by a strategic design of the scheme of synthesis and/or by post-surface passivation and functionalization. A key way to obtain advanced hybrid nanomaterials able to supply precise requirements and acquire specific functions could be an ad hoc designed post-synthetic surface engineering strategy by modifying the surface state or by integrating diverse functions. Covalent modifications have aroused increased attention to achieve better control of the size, shape, and physical properties. Additionally, surface passivation can be also exploited to increase the electron cloud density and introduce surface energy traps that could positively affect the optical profile of CDs [149,154]. Different surface modification methods are introduced based on the characteristics of CDs and their possible applications (e.g. amide coupling, sialylation, esterification, sulfonylation). Among them, amide coupling is the most common strategy of surface passivation due to the good stability of the amide bond and the rich content of carboxyl and amine groups on CDs surface. On the other hand, there are few works of literature regarding esterification, probably because these reactions are particularly difficult to carry out [290]. In light of these considerations, the development of alternative strategies for post-synthesis surface modifications of CDs is highly desired to increase their functionalities and promote their use in a broad range of biomedical applications.

Herein, due to the possibility to synthesize CDs in large scale, for the first time an innovative strategy of surface functionalization by melt-extrusion transesterification of CDs, useful in the preparation of hybrid amphiphilic nanoparticles composed of a carbon core and a polymeric shell of poly (D, L-lactide) (PLA), was proposed. Extrusion demonstrated to be a valid, simple, scalable, and industrialized strategy for the one-pot functionalization of CDs on the surface by extrusion-induced transesterification with PLA chains (CDs-PLA), constituting an important step in the large-scale production of carbon nanodot-based nanosystems (Figure 42).

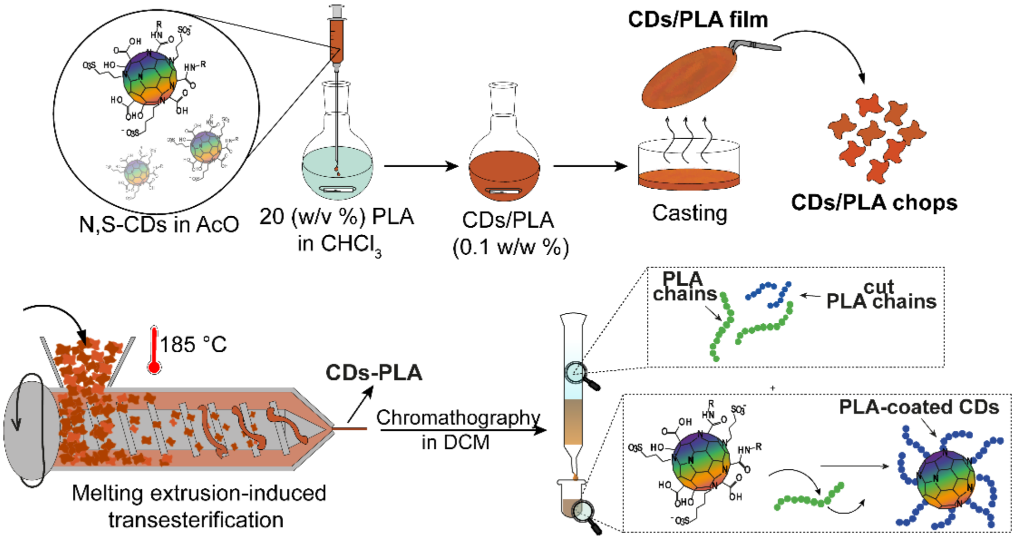

Figure 42. *Graphical abstract.*

4.3.1. Surface functionalization of CDs with Poly (D, L-lactide) by heterophase melt-extrusion transesterification

The N,S-doped carbon nanodots (N,S-CDs) exploited in this work were synthesized by a solvothermal approach as previously described in Section 4.2. [159]. The efficient protocol of synthesis and purification adopted allowed to obtain decagram-scale quantities of highly homogeneous N,S-CDs (d = 5.3 ± 0.4 nm) with a multicolor fluorescence profile (from green-QY 6 % to NIR-QY 1 %) and high NIR-photothermal conversion efficiency. The high yield scheme of preparation allows for overcoming one of the main drawbacks of CDs synthesis route as the extremely low yields, usually lower than 5 % w/w, which categorically precludes bulk application of CDs.

The main advantage of CDs over other carbon-based nanostructures is the versatile surface chemistry that can be exploited for further modifications to modulate or add features, inspiring the preparation of novel hybrid nanostructures. These CDs bear different surface polar groups amenable to further surface functionalization, such as carboxyl, hydroxyl, amide, and sulfonate/sulfoxide. In particular, hydroxyl groups at the N,S-CDs surface could be in principle exploited to provoke one-pot solid/liquid heterophase transesterification of polyesters (e.g., PLA, PCL, and PLGA) by melt-extrusion processes [291].

Poly(lactide acid) (PLA), approved by the US Food and Drug Administration (FDA), has outstanding advantages over other polymers like renewability, biocompatibility, and processability. Moreover, PLA in contact with biological fluids undergoing degradation into non-toxic and carcinogenic products to the human body like H_2O and CO_2. These attractive properties make PLA an excellent material for biomedical applications from tissue engineering to nanomedicine. Furthermore, PLA due to its greater thermal processability in comparison to other biomaterials, like PEG and PCL, can be processed by a wide range of techniques (e.g. film casting, extrusion, blow molding, fiber spinning), making it appealing for industrial application in different fields [292,293].

Melt-extrusion transesterification is already described for polyester mixtures in order to produce cost-effective copolymers with tunable mechanical and chemical properties [294–296]. Indeed, extrusion processes represent an interesting cost-effective tool to manufacture biodegradable polymers like PLA, and to induce diverse solvent-free chemical reactions in the presence or not of catalysts (e.g. ester copolymerization, grafting, and functionalization) [292,293]. In contrast to the very recently reported extruded hybrid CDs/PLA mixtures, in which the extrusion process was exclusively used to allow the mixing of solid components in a physical blend [297].

Herein, the principle of the heterophase melt-extrusion process was exploited to induce the direct transesterification between the hydroxyl groups at the CDs surface and the ester bonds of PLA chains chosen as a biocompatible polymer. This route yielded PLA-coated CDs, named CDs-PLA, embedded into the hydrophobic matrix of unbounded PLA chains. The obtained amphiphilic hybrid nanostructures could be exploited in a variety of ways, for example as a functional excipient of more complex DDS, like core-shell nanosystems, such as a strategy to increase hydrophobic surface favoring hydrophobic drug loading and controlled drug release and impinge theranostic properties (e.g. fluorescence and photothermal conversion capacities) [4].

In detail, as represented in Figure 43, to obtain PLA-coated CDs (CDs-PLA) a dispersion of crystalline N,S-CDs in acetone was slowly added dropwise into a 20 % PLA solution, thus achieving a homogeneous dispersion of PLA with the 0.1 % w/w of CDs (CDs/PLA). The percentage of CDs used to prepare the mixing was rationally chosen to allow obtaining a uniform colloidal distribution of CDs into the PLA matrix, free of aggregates and precipitate induced by dot-dot interactions. Besides, preliminary experiments showed us that increasing the percentage of CDs beyond 0.1 % w/w provides dot-dot interactions that negatively affect the formation of homogenous and ordered PLA-coated CDs and also induce the fluorescence quenching of CDs. Instead, this scheme of preparation provides homogeneous chops of CDs/PLA from the solvent casting procedure. CDs/PLA chops obtained by solvent-casting were extruded as filaments at 185 °C.

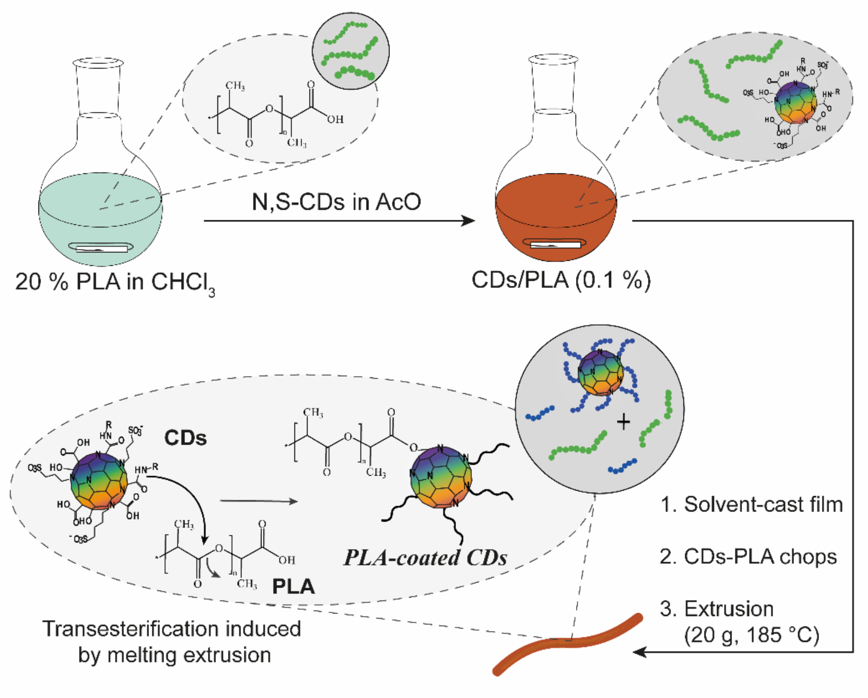

Figure 43. *Preparation scheme of PLA-coated CDs (CDs-PLA) by melting extrusion-transesterification.*

4.3.2. Chemical characterization of CDs-PLA

FT-IR analysis was employed to preliminarily evaluate the effective surface functionalization of CDs on CDs-PLA film-casting compared to starting CDs and PLA (Figure 44). As reported in Figure 43a, N,S-CDs are characterized by several vibration bands attributable to hydroxyl (3420 cm^{-1}), amine (3200 cm^{-1}), amide (amide I band, 1640 cm^{-1}), carboxyl (asymmetric stretching at 1715 cm^{-1}), and sulfonate/sulfoxide groups (1391 and 1283 cm^{-1}). PLA-CDs spectrum resembles the characteristic FT-IR profile of PLA reported in Figure 44b. As shown in Figure 44a’, compared to PLA spectrum in the CDs-PLA spectrum the intensity ratios I_{1129}/I_{1083} and I_{1041}/I_{1083} are higher.

Moreover, also the peaks within the fingerprint region (1129 and 1083 cm^{-1}) do not show the same symmetry exhibited in the PLA spectrum, suggesting an increased OH bending. It is also important to notice that in the CDs-PLA spectrum, the peak at 753 cm^{-1} shows in the PLA spectrum splits into two peaks centered at 753–734 cm^{-1}, hinting at different O-C=O/OH ratios which implies higher OH bending vibrations in the PLA-CDs spectrum attributable to transesterification processes efficiently occurred during extrusion. Substantial differences were observed between CDs-PLA and non-extruded CDs/PLA spectra (Figure 44a''). In detail, symmetric peaks at 1129–1083 cm^{-1} and a single peak more intense at 753 cm^{-1} can be noted for CDs/PLA. This evidence supported melt-extrusion transesterification between ester bonds of PLA and hydroxyl groups of CDs, with the consequent formation of PLA-coated CDs, and the molecular weight reduction of some PLA chains. As reported for the mixture of polyesters and polyols, it is possible to hypothesize that the extrusion process of the CDs/PLA blend provides the required energy to establish covalent interactions between PLA chains and CDs, thus leading to the formation of PLA-coated CDs.

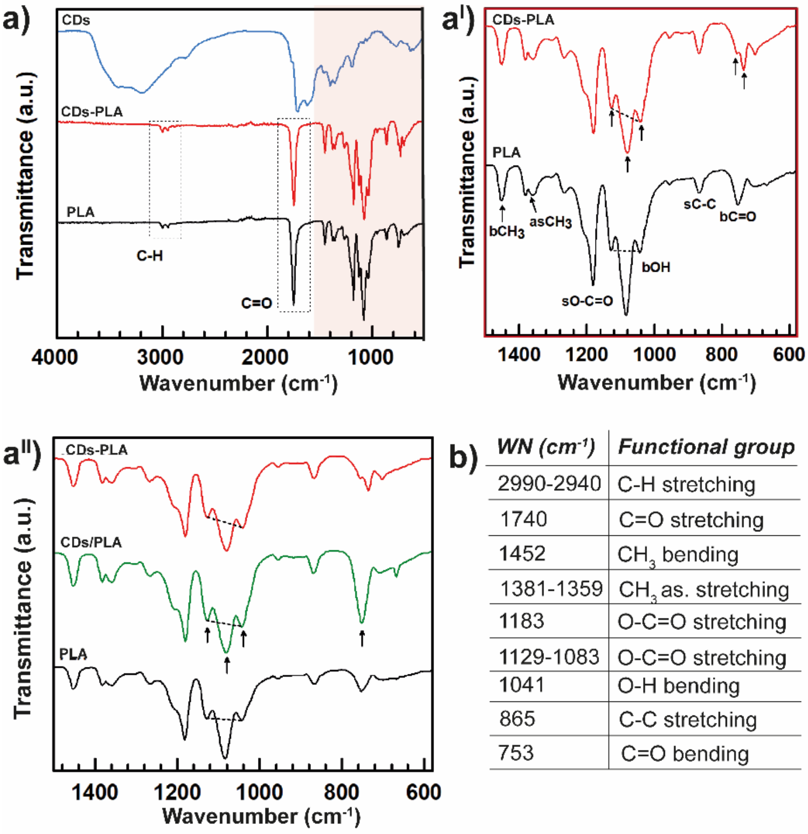

WN (cm^{-1})	*Functional group*
2990-2940	C-H stretching
1740	C=O stretching
1452	CH_3 bending
1381-1359	CH_3 as. stretching
1183	O-C=O stretching
1129-1083	O-C=O stretching
1041	O-H bending
865	C-C stretching
753	C=O bending

Figure 44. *FT-IR characterization: spectra of CDs, PLA, and CDs-PLA (a); focus of FT-IR spectra of CDs-PLA and PLA in the range 580-1550 cm^{-2} (a'); FT-IR spectra of CDs/PLA blend,*

CDs-PLA, and PLA in the range 580-1550 cm^{-2} (a''). Table of characteristics bands of PLA spectrum and relative attributions.

SEC traces are reported in Figure 45. supported this evidence. In particular, the plain PLA consists of a bimodal molecular weight distribution (= 154000 Da, PD = 1.84), while in the extruded material SEC profile appear three distinct and narrower peaks ascribable to the PLA-coated CDs, the main PLA matrix, and the cleaved PLA chains (: greater than 500000 Da, 168,000 Da, and 87000 Da, respectively). According to the reaction scheme proposed in Figure 43, it is noteworthy that changes observed in the PLA molecular weight distribution provide clear evidence of the extrusion-induced transesterification process.

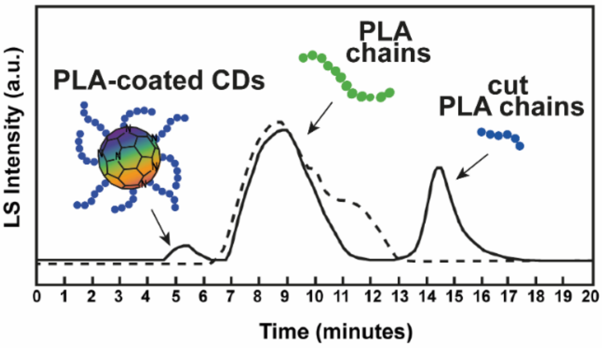

Figure 45. *SEC traces of extruded sample composed of PLA-coated CDs, PLA chains, and cut PLA chains from transesterification reaction.*

In order to confirm the structure of the PLA-coated CDs, CDs-PLA was purified by GPC, using chloroform as eluant, collecting two fractions, a colorless fraction of pure PLA and a brownish fraction containing fluorescent PLA-coated CDs. Then, the latter was analyzed by ^{1}H-NMR spectroscopy. The ^{1}H-NMR spectrum is reported in Figure 46. shows typical peaks of PLA with a doublet at 1.56–1.59 ppm relative to CH_3 protons, and a quadruplet at 5.12–5.19 ppm attributable to the CH proton. The ^{1}H-NMR profile of PLA-coated CDs conclusively confirmed the effective surface functionalization of CDs with PLA chains, supporting the FTIR and SEC data.

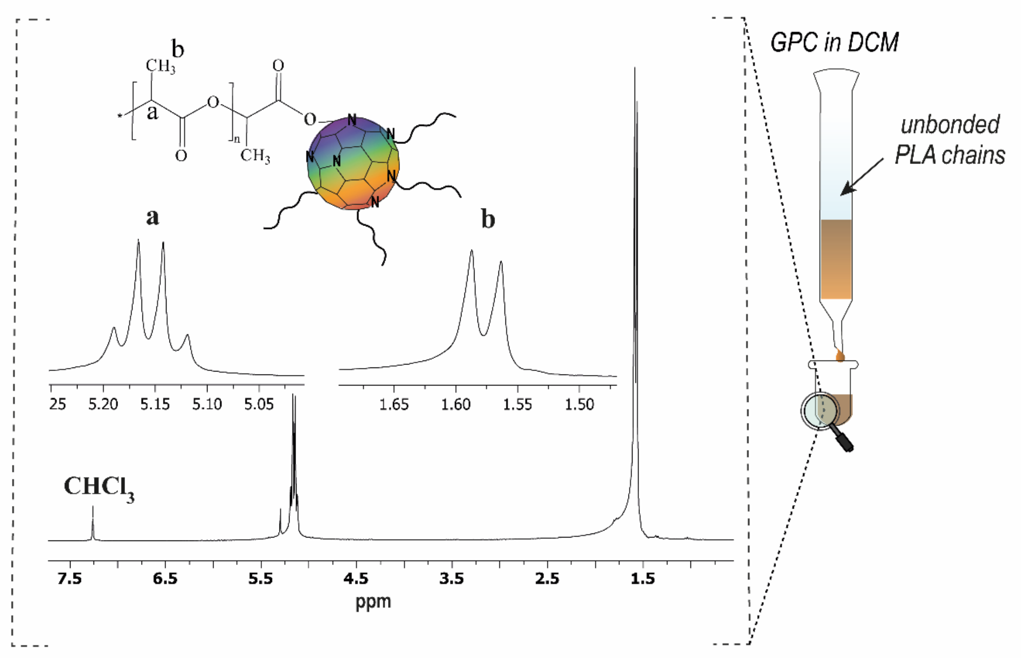

Figure 46. *^{1}H-NMR spectra of PLA-coated CDs sample purified by gel permeation chromatography (300 MHz, $CHCl_3$ d_1).*

4.3.3. Thermal characterization by coupled DSC/TGA technique

CDs-PLA thermoplastic behavior was evaluated by DSC/TGA analysis performed within a temperature range of 20–600 °C and a heating rate of 10 °C min^{-1}. The thermal profile was compared to those obtained for plain PLA and CDs. As shown in Figure 47, in CDs thermogram no significant weight loss and thermal transitions were revealed before 160 °C, demonstrating their remarkable thermal stability. Broad endothermal transitions were detected in the range of 160–400 °C, followed by a marked decomposition up to 600 °C. In fact, the thermogram of CDs reported in Figure 47a' displays a weight loss of 41 % w/w corresponding to the thermal decomposition up to 600 °C, attributable to the decomposition of CDs surface functional groups. Indeed, in contrast to organic fluorescent probes, the excellent thermal stability of CDs makes them easily processable by extrusion process at high temperatures, without incurring thermo-induced degradation phenomena and consequent photobleaching [298]. The thermogram profile of CDs-PLA was similar to that of PLA but with considerable differences in terms of melting temperature (Tm) and decomposition temperature (Td) (Figure 47). While PLA possesses a sharp Tm at 170 °C and an endothermal Td at about 356 °C, CDs-PLA displayed two endothermal transitions at 167 °C and 176 °C (Figure 47a), attributable to the two different PLA distributions detected by SEC analysis, and a higher Td at about 363 °C (Figure 47a’). The thermogravimetric curves (Figure 47a’) of the CDs-PLA and the plain PLA displayed a comparable weight loss (97.54 and 94.56 % w/w up to 378 °C, respectively), due to the degradation of main PLA chains and rapid decrease in molecular weight at this temperature condition [299]. The different thermal stability profile of the CDs-PLA also demonstrates the effective covalent functionalization of CDs surface with PLA chains (PLA-coated CDs).

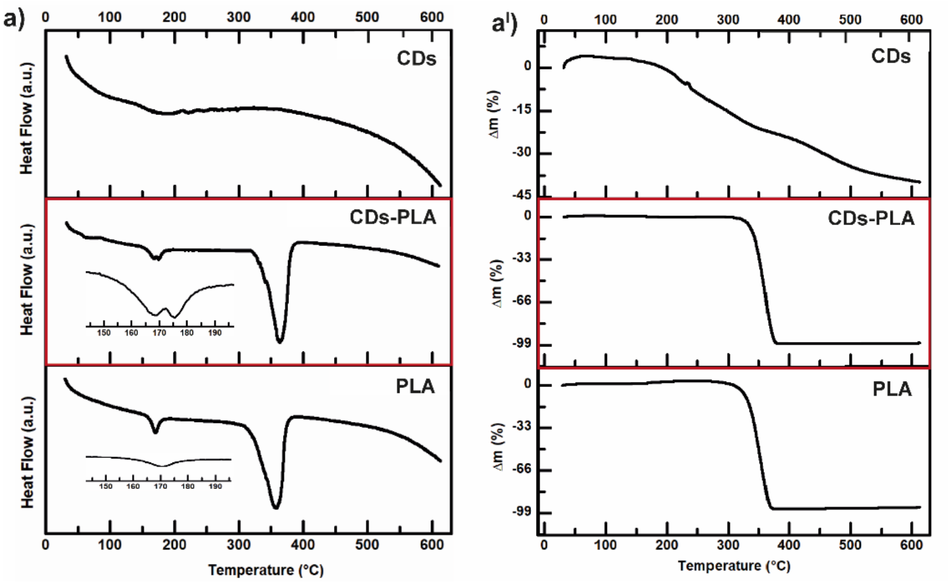

Figure 47. *DSC coupled TGA analysis of CDs, CDs-PLA and PLA.*

4.3.4. Optical characterization

In Figure 47a is reported the absorption spectrum of bare CDs with normalized emission spectra obtained under excitation at different wavelengths. The absorption spectrum displays a series of different electronic transitions in all the visible ranges probably associated with heterogeneous CDs in terms of surface states featuring high radiative rates. Exciting at different wavelengths in the visible range CDs show a typical tunable emission from the blue to the red region of the spectra. However, as well-known in the literature, changing the surface state of CDs by PLA-coating impinged the optical profile of CDs-PLA if compared with starting CDs. As shown in Figure 48b., CDs-PLA display similar emission tunability but with some differences. In detail, compared to bare CDs, under the same wavelength of excitation, CDs-PLA displayed a huge blueshift of the emission band accompanied by variations of the band shape (Figure 48c).

As reported for other CDs in the literature, the CDs fluorescence is very sensitive to different solvents (Figure 48d) [150,243,300]. As shown in Figure 48d, their emission blueshifts were more evidenced by decreasing the polarity of the solvent (from water to acetone). Therefore, taking into account that PLA is non-polar, the presence of PLA-coating on CDs surface is expected to induce an emission blueshift. These changes in the observed emission profile supported the strong covalent interactions between CDs surface and PLA. Despite this modification, the emission quantum yield was not strongly affected and substantially remained unaltered (≅1 % in the red) in all the phases of preparation (bare CDs, CDs/PLA, and CDs-PLA). Then, the PLA-coated CDs preserved the optical profile of starting CDs, making this surface passivation strategy useful for a variety of preparation and applications.

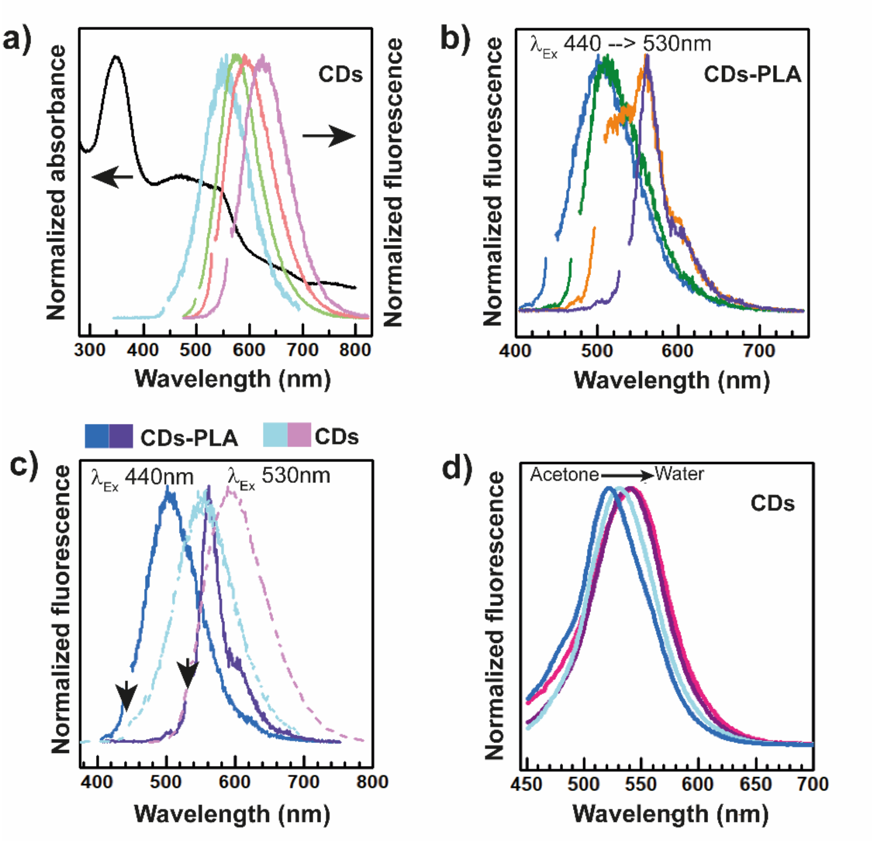

Figure 48. *Optical characterization: UV spectrum and emission spectra under different excitation wavelengths (440, 500, 530, and 560 nm) of CDs (a); emission spectra under different excitation wavelengths (440, 480, 500, and 530 nm) of CDs-PLA (b); emission spectra under excitation at 440 and 530 nm of CDs-PLA and CDs (c); emission spectra of CDs under excitation at 440 nm in water (blue line), ethanol (light blue line), dimethyl sulfoxide (purple line) and acetone (pink line) (d).*

In order to evaluate differences in the emission lifetime time-resolved nanosecond spectroscopic measurements were also performed. As can be observed in Figure 49, the surface coating of CDs with PLA chains induces an increase in the nanosecond lifetime from 5.5 ns to 6.2 ns, supporting the effective formation of strong covalent bonds between CDs and PLA chains as well as the effective formation of PLA-coated CDs.

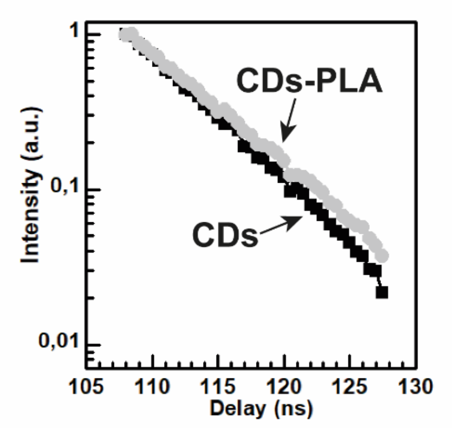

Figure 49. *Fluorescence decay profiles of CDs and CDs-PLA.*

4.3.5. Conclusions

Herein, we designed for the first time a cost-effective and industrially scalable one-pot surface functionalization of CDs with PLA chains by heterophase melt-extrusion transesterification process. Transesterification between hydroxyl groups at the CDs surface and PLA ester bonds by heterophase melt-extrusion demonstrated a valid strategy to obtain PLA-coated CDs (CDs-PLA) at mild conditions compatible with the thermal stability of CDs. The obtained PLA-coated CDs preserve the fluorescence properties of native CDs but with a moderate blue shift of the emission band due to the hydrophobic nature of the PLA shell. The hydrophobic CDs could be employed in the development of hybrid nanostructures for cancer theranostics. Overall, the proposed strategy represents a successful and innovative strategy for CDs surface functionalization without the use of activating or catalysts under extreme conditions, exploitable for the surface modification of CDs with a wide range of materials.

4.4. Production of PLGA nanoparticles incorporating N-doped carbon nanodots and irinotecan for image-guided chemo-photothermal therapy of breast cancer

The present work aims to maximize the applicative potential of CDs by developing stable theranostic hybrid nanosystems obtained by encapsulating highly hydrophilic N-doped CDs in PLGA nanoparticles. The hybrid CDs-PLGA nanoparticles are designed for the delivery of irinotecan to breast cancer cells. Herein, the attention was focused on the formulation aspect of the nanosystem and in particular, on evaluating how the amount of encapsulated CDs (1–20 %) affects the features of polymeric nanoparticles, not only conferring their peculiar optical properties, such as photothermal and fluorescent properties, needed in theranostics, but also having a strategic role in the formation and stabilization of the nanosystem in aqueous media. The present work demonstrates how the increased content of CDs from 1 to 20 % (on a weight basis) positively impinge on the loading and release of the drug, improving drug loading (~4.5 %) and favoring a sustained drug release over time, obtaining more stable irinotecan-loaded nanosystems performing in chemo-photothermal therapy and fluorescence imaging, as demonstrated by in vitro studies (Figure 50).

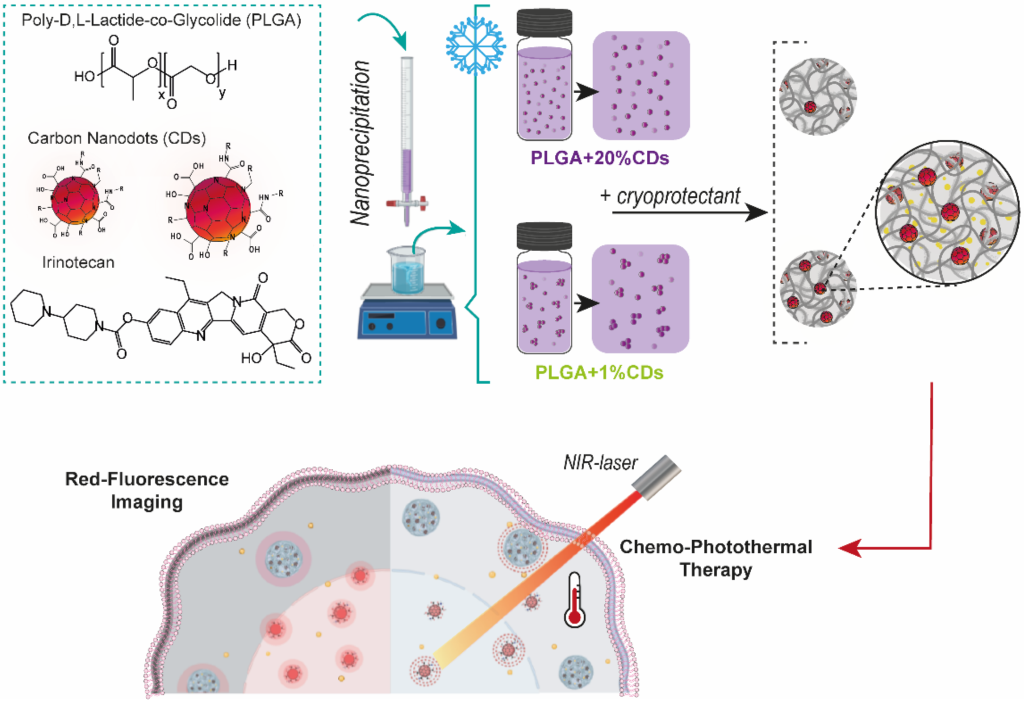

Figure 50. *Graphical abstract.*

4.4.1. Synthesis and characterization of N-doped CDs

The N-doped CDs selected for preparing the PLGA-CDs hybrid nanoparticles were synthesized by solvothermal approach and widely characterized, as reported in previous work [158]. Carbon nanodots (CDs) were prepared from the decomposition of urea and citric acid in anhydrous DMF. This bottom-up synthetic approach usually conducts a mixture of amorphous carbonaceous materials and crystalline nanoparticles with an average size of 1–10 nm. As deeply investigated, this heterogeneous mixture impinges on the optical properties and the development of effective nanosystems for biomedical applications. Thus, the raw product was purified by size exclusion chromatography (SEC) to isolate CDs with a homogeneous size distribution, and specific surface functional groups and to select the most red-emitting fractions of CDs with marked NIR-triggered photothermal capacity.

Size distribution obtained from the heights of the nanoparticles was studied by atomic force microscopy (AFM) and reported in Figure 51a-a'. AFM micrograph showed nanodots with an average diameter of 1.5 nm and a narrow size distribution useful for their potential biomedical applications.

FTIR spectroscopy (Figure 51b) was employed to investigate surface functional groups of N-doped CDs. The selected CDs were characterized by hydroxyl, amine, and amide surface groups and a high content of carboxyl group. The IR spectra show many diagnostic bands such as O-H stretching (3420 cm^{-1}), N-H stretching (3200 cm^{-1}), asymmetric (1711 cm^{-1}), and symmetric COOH stretching (1381 cm^{-1}), and the amide I band (1620 cm^{-1}).

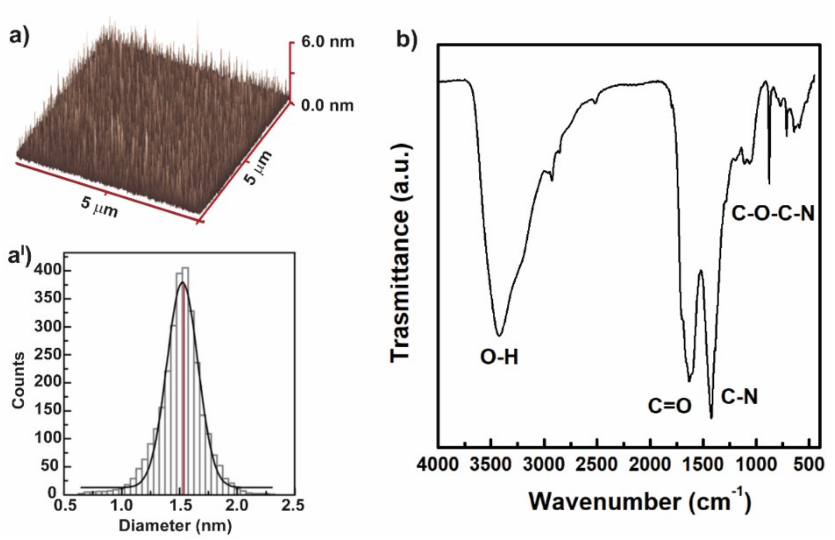

Figure 51. *AFM image (a) and size distribution (a') of CDs. FT-IR spectrum and relative attributions of CDs (b).*

The optical properties of CDs in terms of absorption and emission properties were deeply investigated. The selected CDs showed different peculiar absorption bands in the entire UV/vis spectrum. In light of the absorption bands, the emission spectrum was recorded under excitation at 540 nm, displaying a significant red emission band from 580 to 750 nm with a peak at 610 nm (Figure 52). The photoluminescence profile of these CDs is of particular interest in theranostic applications since an emission within the biological transparent window (red-NIR bands) is the minimum optical requirement to obtain high-resolution images in fluorescence imaging. Hence, the selected CDs are suitable excipients to produce performant PLGA nanoparticles with theranostic properties given imaging-guided anticancer therapies.

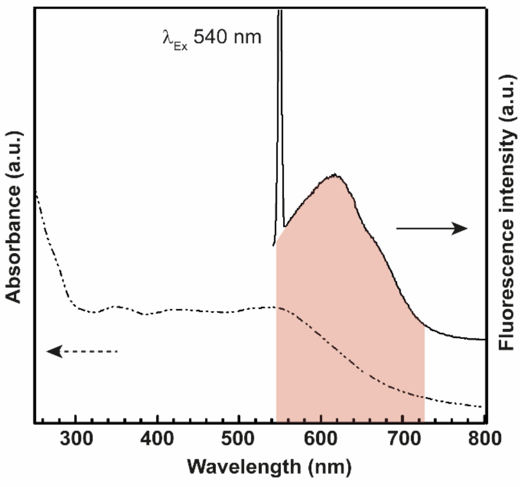

Figure 52. *Absorption (dotted line) and emission spectra (compact line) of CDs.*

4.4.2. Preparation of PLGA-CDs hybrid nanoparticles by nanoprecipitation technique

The selected red-emitting CDs were employed as a functional excipient to obtain smart PLGA-CDs nanoparticles with fluorescence and photothermal features and high stability in aqueous media. Taking into account the principle of the EPR effect, a size between 10-200 nm increases the circulation lifetime of nanosystems in the bloodstream and their selective accumulation in tumor tissue and microenvironment. Therefore, the encapsulation of the CDs inside bioresorbable nanoparticles represents not only a strategy to impinge theranostic properties, but also a valid approach to avoid rapid renal clearance [83]. The most popular materials for the preparation of bioresorbable nanoparticles are represented by the use of polymers [301]. In this panorama, polyesters like polylactic acid (PLA), poly-ε-caprolactone (PCL), and poly-D, L-lactide-co-glycolide (PLGA) emerge as an effective and versatile class of biodegradable polymers to produce pharmaceutical formulations for drug delivery and tissue engineering applications [302–306]. In particular PLGA, an FDA-approved copolymer has received great attention for the production of drug delivery systems as in the organism, it can be hydrolyzed in metabolites such as lactic acid and glycolic acid, which can be successively metabolized in H_2O and CO_2 taking part to the Krebs cycle. In light of these considerations, the systemic toxicity associated with its use is minimal [307]. PLGA-based nanocarriers offer innumerable advantages allowing an optimal bioavailability of the encapsulated drugs, reducing the phenomena of premature degradation in the biological compartments [308], providing a controlled drug release by degradation kinetics and targeted delivery [309], and facilitating the cell internalization of the bioactive molecules thus reducing side effects [310]. However, literature reported opposite opinions suggesting that sometimes PLGA-based nanosystems show an undesired premature or initial burst drug release or both. Moreover, PLGA-based nanosystems also show other limitations like instability in the aqueous environment and in some cases a relatively low drug loading capacity.

The rational idea was to entrap CDs inside PLGA-based nanoparticles during the process of production by solvent displacement method, known as nanoprecipitation. The goal is to modify their bulk physicochemical properties in terms of photoluminescence, photothermal sensitivity, and water stability. In fact, a proper amount of CDs might be sufficient to impinge the surface properties of the hybrid nanoparticles, thus conferring suitable hydrophilicity due to the distinct polar surface groups of CDs.

We prepared PLGA-CDs nanoparticles by nanoprecipitation by dripping an organic PLGA/CDs homogeneous colloidal dispersion in a large excess of “non-solvent”. The formation of well-dispersed nanoparticles is induced by the rapid diffusion of the organic solvent in water. We obtained nanoparticles with low (1 %) and high (20 %) CDs content to evaluate the effects of the CDs on the stability and optical properties. The size distribution and surface charge of all the obtained formulations were investigated by dynamic light scattering techniques. Unfortunately, it was observed that the PLGA-CDs nanoparticles containing a low content of CDs (PLGA-CDs1%) underwent aggregation after the lyophilization process and redispersion was not allowed. Therefore, according to available literature data, cryoprotectant agents were required to avoid this stability problem. Usually, PLGA-based nanoparticles can be stabilized using a variety of cryoprotectants, such as PVA, PVP, and sucrose, in a range of concentration from 2 to 5 % w/v [311–313].

4.4.3. Study of cryo-stability by Dynamic Light Scattering (DLS)

DLS measurements were performed on redispersed freeze-dried samples additive with common cryo-protectors at different concentrations (Figure 53), in order to understand which type and concentration of cryoprotectant agent ensure the best redispersion of PLGA-CDs1% nanoparticles. The best result, in terms of Z-average and PDI, was obtained with 5 % sucrose (d = 70 nm; PDI = 0.224), while, 10 % w/v polyvinylpyrrolidone (PVP) allows a discrete redispersion in terms of size, but with a polydispersity value too high (d = 116.6 nm; PDI = 0.910).

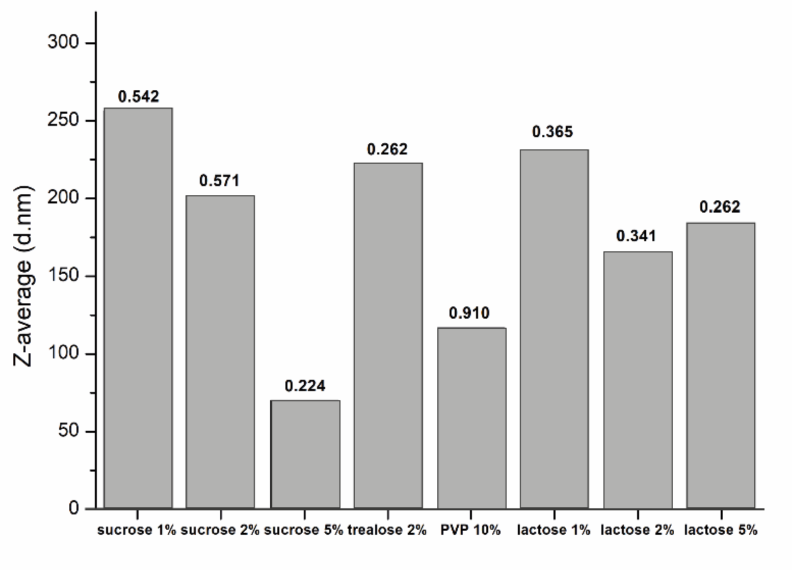

Figure 53. *Z-average values by DLS analysis of PLGA-CDs1% nanoparticles with diverse tested cryoprotectant agents.*

Differently, for the PLGA-CDs nanoparticles containing a major amount of CDs (PLGA-CDs20%) was observed a slightly higher diameter (from 54 to 74 nm) and a better redispersion after lyophilization, obtaining a stable colloidal dispersion using a significantly lower amount of cryoprotectant equal to 1% w/w PVP (Table 3). In fact, while the PLGA-CDs20% sample without cryoprotectant gives rise to a slight aggregation after the lyophilization process (d = 291 nm, data not shown), while comparable dimensions and polydispersity index to the starting sample (d = 93.2 nm; PDI = 0.181) (Table 3) were obtained adding only 1 % of PVP in the PLGA-CDs20% sample. The different redispersion observed between PLGA-CDs20% and PLGA-CDs1% nanoparticles can be ascribed to the different surface charges of the nanoparticles ascribable to the presence of CDs on the surface of the hybrid nanoparticles. Therefore, zeta-potential measurements were performed on freshly prepared samples to verify this hypothesis. PLGA-CDs1% nanoparticles showed a quasi-neutral charge ($\zeta = -5.7 \pm 4.4$), while the zeta-potential was quite negative ($\zeta = -30.3 \pm 17.6$) for PLGA-CDs20%. These data involve that the higher stability of the hybrid nanoparticles in aqueous media was suggested by carboxyl groups of CDs on the surface of PLGA-CDs20% nanoparticles. This difference is due to the higher surface arrangement of CDs (negatively charged) in the PLGA-CDs20% nanoparticles compared to that of PLGA-CDs1%, where the amount of CDs is too low to provide a significant surface modification.

Table 3. DLS analysis of Z-average and PDI of empty and drug-loaded nanoparticles pre-lyophilization and post-lyophilization with cryoprotectant.

Samples	***Pre-lyophilization***		***Post-lyophilization (+ cryoprotectant)***	
	Z-Average (nm)	***PDI***	***Z-Average (nm)***	***PDI***
PLGA-CDs1%	54.78	0.117	70 [a]	0.224 [a]
PLGA-CDs20%	74.36	0.167	93.2 [b]	0.181 [b]
PLGA-CDs1%@IT	157.9	0.024	181.2 [a]	0.067 [a]
PLGA-CDs20%@IT	102.5	0.111	133.9 [b]	0.120 [b]

[a] Cryoprotectant: 5 % sucrose

[b] Cryoprotectant: 1 % PVP 40 kDa

4.4.4. Dimensional evaluation of PLGA-CDs nanoparticles by Atomic Force Microscopy (AFM)

AFM studies also confirmed the lower tendency of the PLGA-CDs20% nanoparticles to form bigger aggregates. As shown in Figure 54a, PLGA-CDs1% nanoparticles strongly tend to form aggregates of about 50 nm in diameter after drying the aqueous dispersion on mica discs. Whilst AFM micrographs of the PLGA-CDs20% sample do not highlight aggregates after evaporation of water, but only well-defined nanoparticles with roughly 45–50 nm in diameter. This evidence confirms the key role of CDs in the stabilization of nanoparticles in aqueous media (Figure 54b). Furthermore, it is also important to notice that there are no observed free CDs in the AFM micrograph of the PLGA-CDs20% sample suggesting that hybrid nanoparticles consist of CDs embedded in a PLGA matrix responsible for the optical properties observed below.

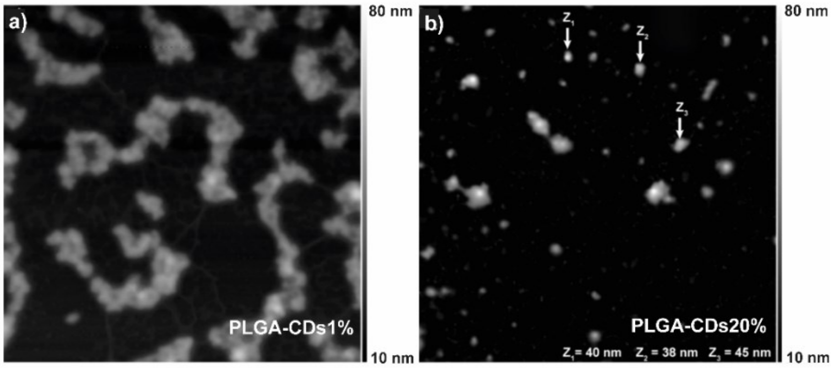

Figure 54. *AFM micrographs of PLGA-CDs1% (a) a PLGA-CDs20% (b).*

4.4.5. Optical and Photothermal Characterization of the PLGA-CDs NPs

In light of their possible application in IG-PPT, the photothermal and red fluorescence properties of PLGA-CDs nanoparticles were established. Therefore, the emission spectra recorded under excitation at 540 nm of both nanoparticles were compared with that of nude CDs. As evidenced in Figure 55a both PLGA-CDs nanoparticles spectra preserve the same characteristic emission band of the CDs UV profile in the red region. In detail, an increase in CDs content in nanoparticles from 1 to 20 % is associated with changes in the emission band trend. In detail, the shoulder at 650 nm is more pronounced in nanoparticles with 20 % of CDs, similar to nude CDs, in contrast to a flattening of the emission bands associated with a lower content of CDs (1%). This phenomenon can be due to dot-dot interactions in the PLGA-CDs20% sample, which reflect surface electronic transitions responsible for more intense red emission, useful in fluorescence imaging applications. The ability of both nanoparticles to convert NIR light into heat to act as nanoheaters in IG-PPT was evaluated by irradiating a dispersion of either a PLGA-CDs20% or PLGA-CDs1% dispersion in water and monitoring the temperature increase in function of the time of laser exposure by using an optical fiber. The conditions used for the two samples were different due to the different content of nanoheaters in the two PLGA-CDs nanoparticles. In particular, photothermal kinetics time was attained using an 810 nm laser diode source for 150 s with a power of 2.5 W cm^{-2} and 300 s at 7 W cm^{-2} for the PLGA-CDs20% and PLGA-CDs1%NPs, respectively. As expected, a higher amount of CDs (20% on a weight basis) confers to the nanoparticles a sharper photothermal conversion capacity compared with the PLGA-CDs1% containing a lower amount of CDs (Figure 55b.). It might be noticed that this trend is corroborated by the lower potency used for the PLGA-CDs20% sample, which was three times lower than that employed to obtain comparable photothermal results with PLGA-CDs1%. In detail, the PLGA-CDs20% sample reaches the minimum temperature of hyperthermia (42 °C) [314] after about 30 s of laser treatment at 2.5 W cm^{-2}, while the second one needs twice the irradiation time at 7 W cm^{-2}. Therefore, a higher amount of CDs has a multifunctional role to obtain good physicochemical stability in aqueous media and in preparing the PLGA-based nanoparticles with promising optical properties in terms of fluorescence and photothermal properties, needed for their application in IG-PTT.

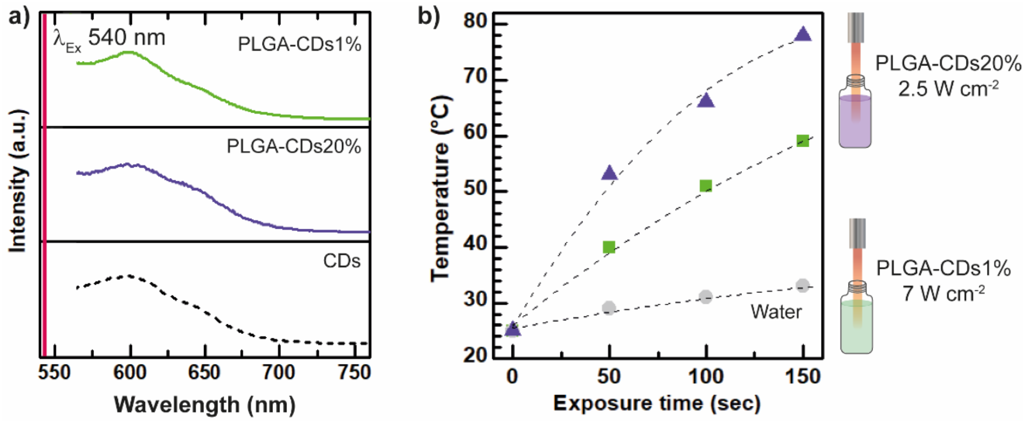

Figure 55. *Emission spectra of PLGA-CDs nanoparticles and CDs (a). Kinetic of hyperthermia in the function of the exposure time of PLGA-CDs nanoparticles (b).*

4.4.6. Preparation and characterization of irinotecan-loaded PLGA-CDs nanoparticles (PLGA-CDs@IT)

The irinotecan-loaded nanoparticles, PLGA-CDs1%@IT and PLGA-CDs20%@IT, were prepared using the same protocol for the empty PLGA-CDs samples. Briefly, an established amount of irinotecan hydrochloride was added to the PLGA/CDs colloidal dispersion. The drug loading of PLGA-CDs nanoparticles was evaluated by HPLC analysis. Results show that the percentage of CDs entrapped into nanoparticles is relevant in ensuring higher drug loading (DL). In fact, PLGA-CDs20% nanoparticles have an improved DL of 4.73 ± 0.15 % w/w compared with that of PLGA-CDs1% nanoparticles (DL of 3.5 ± 0.11 %). Drug-loaded nanoparticles were characterized in terms of size distribution, as reported in Table 3. As shown the entrapment of CDs into PLGA nanoparticles highly affect the drug loading and the size distribution of both samples. In particular, the presence of % CDs during the loading affords nanoparticles with dimensions about three times higher than that obtained for the PLGA-CDs1% sample (54 vs. 158 nm). Therefore, the loading of irinotecan hydrochloride can affect the arrangement of drug-loaded PLGA-CDs nanoparticles. Indeed, nanoparticles with hydrodynamic diameter three times bigger are formed in the presence of irinotecan for the PLGA-CDs1% and almost two times bigger for the PLGA-CDs20% (Table 3). This evidence can be ascribed to the strong interaction between cationic irinotecan and anionic CDs due to the opposite charge possessed under the adopted conditions. No changes were observed after the lyophilization process for both PLGA-CDs1%@IT and PLGA-CDs20%@IT nanoparticles (Table 3).

4.4.7. Irinotecan release evaluation from PLGA-CDs@IT nanoparticles

The kinetic drug release of irinotecan from the PLGA-CDs@IT nanoparticles under physiological conditions (PBS pH 7.4) was evaluated using the dialysis method. As can be seen in Figure 56 the amount of CDs in the PLGA-CDs nanoparticles positively influences the release kinetics. In detail, it can be observed that PLGA-CDs1%@IT nanoparticles released approximately all the irinotecan payload in 10 h, comparable to the kinetic release of PLGA nanoparticles reported in the literature [315]. On the contrary, PLGA-CDs20%@IT displayed prolonged and sustained release over time, avoiding the burst effect and releasing only 50 % of its payload in 48 h. As widely reported in the literature, the NIR-triggered photothermal effect as well as the localized temperature increase induced by activated nanoheaters as CDs, allows a faster and more focused drug release [177,254]. However, the drug release kinetics of both PLGA-CDs nanoparticles seems not to be affected by the laser irradiation, conducing to kinetics comparable to those obtained from untreated nanoparticles. It is possible to hypothesize that the failed burst drug release induced by laser treatment is due to the inability of the nanosystem to disassemble in the function of a temperature increase. Therefore, considering the superior photothermal and photoluminescence capacity and the higher stability and sustained drug release profile, the PLGA-CDs20%@IT nanoparticles were selected as the most promising candidate for the successive study of anticancer efficacy and bioimaging.

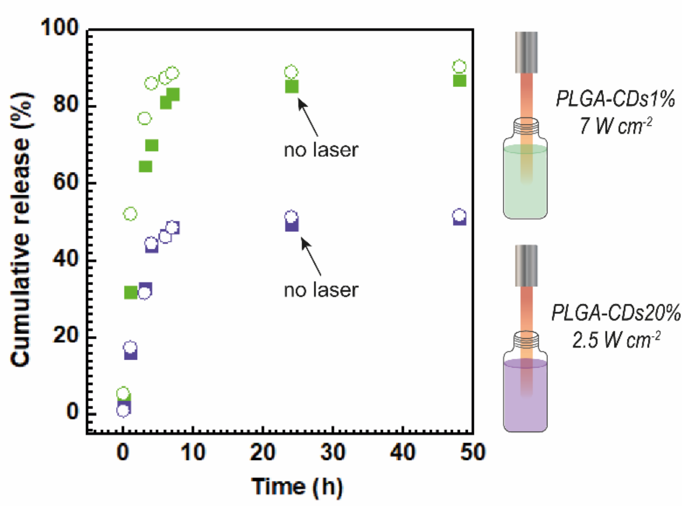

Figure 56. *Profile of cumulative drug release (%) in function of time of PLGA-CDs1% and PLGA-CDs20% with and without laser irradiation.*

4.4.8. Biological characterization of PLGA-CDs20%@IT nanoparticles

The anticancer activity of the PLGA-CDs20%@IT nanoparticles was evaluated in vitro on the MDA-MB-231 cell line after 24 h and 48 h of incubation. As illustrated in Figure 57a-a', the cell viability decreased with the incubation time and increasing the amount of irinotecan, suggesting a time- and dose-dependent efficacy. In light of the demonstrated brilliant NIR-photothermal conversion efficiency of CDs, it was evaluated their capacity to induce cancer cell death by photothermal ablation [316]. Hence, the second set of experiments evaluated the combination of the NIR-triggered photothermal ablation of cancer cells and the cytotoxic effect induced by the irinotecan released in situ (Figure 57a-a'). In detail, the treated cells with PLGA-CDs20%@IT nanoparticles for 24 h and 48 h were successively irradiated with an 810 nm laser diode for 100 s with power fitted at 2.5 W cm^{-2}. Similarly, to the previous experimental set, the efficacy of the chemo-photothermal treatment was evaluated as a reduction of cell viability compared to the untreated control. As shown in Figure 57a, the photothermal treatment seems much more effective if compared with the free drug for all the concentration ranges considered and markedly different from untreated cells after 24 h of incubation. A similar trend was observed for the cells treated after 48 h of incubation (Figure 57a'). The effective ablation of cancer cells observed for the cells treated with PLGA-CDs20%@IT at concentrations higher than 75 μg mL^{-1} can be ascribed to the important high temperatures reached during the laser treatment. Indeed, in a parallel experiment, the temperature increase of dispersions of PLGA-CDs20% nanoparticles in DMEM at the same conditions used for the in vitro cytotoxic studies (5–150 µg mL^{-1}) was measured at scheduled time intervals to evaluate the corresponding hyperthermic effect. As shown in Figure 57b, the kinetics of heating appears to depend on the concentration of PLGA-CDs20% nanoparticles. In particular, up to a concentration of 75 µg mL^{-1} and after 200 s of laser exposure, the temperature reaches 60 °C (Figure 57b), explaining well why cells are efficiently ablated under these conditions (Figure 57a-a').

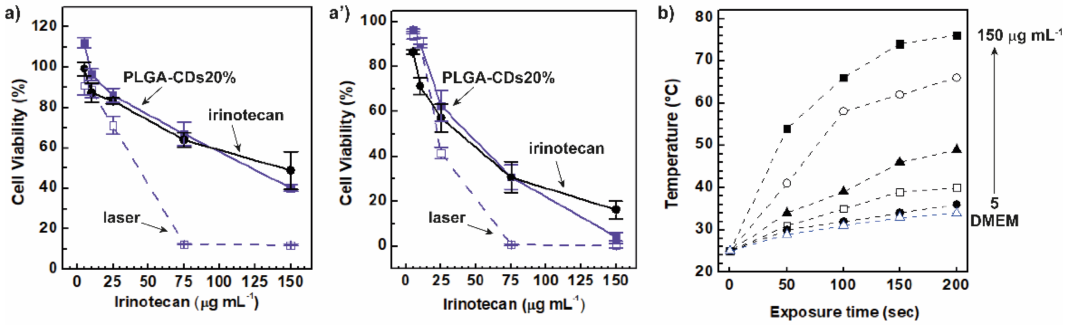

Figure 57. *Study of cytotoxicity of PLGA-CDs20%@IT with and without laser irradiation (100 s, 2.5 W cm^{-2}) compared to free irinotecan on 2D model of MDA-MB-231 after 24 h (a) and 48 h (a') of incubation. Kinetic of hyperthermia at biological concentrations tested in vitro (b).*

The IC$_{50}$ and maximum inhibition (I$_{max}$) values reported in Table 4 highlight the higher potency of the PLGA-CDs20%@IT nanoparticles compared with the free drug. The IC$_{50}$ values of the NIR-treated PLGA-CDs20%@IT nanoparticles after 24 h and 48 h of incubation were about half of the values obtained from the untreated PLGA-CDs20%@IT nanoparticles and lower than that obtained from free irinotecan. The Imax values were about two times higher than that detected for both cells treated with the free drug and the PLGA-CDs20%@IT nanoparticles after 24 h of incubation, suggesting a superior efficacy of the photothermal treatments.

Table 4. IC$_{50}$ and I$_{max}$ values extrapolated from the cytotoxic study in vitro.

Samples	***IC$_{50}^{24h}$ (µg mL^{-1})***	***IC$_{50}^{48h}$ (µg mL^{-1})***	***I$_{max}^{24h}$ (%)***	***I$_{max}^{48h}$ (%)***
Irinotecan	143.76	38	51.18	83.75
PLGA-CDs20%@IT	121.12	45.10	59.80	95.79
PLGA-CDs20%@IT + laser	43.14	22.30	88.15	99.69

On the whole, these data confirm the potent anticancer effect of the theranostic approach adopted, combining chemotherapy and photothermal therapy in a unique biodegradable and bio-eliminable hybrid nanoplatform like PLGA-CDs20% nanoparticles.

4.4.9. Uptake study on cell culture in vitro

In light of the applicative purpose of this work, the ability of PLGA-CDs20% nanoparticles to act as a contrast agent in FLI was evaluated by fluorescence microscopy ($\lambda_{Ex} = 559$), tracking the nanosystem in living breast cancer cells (MDA-MB-231) after 6 h and 24 h of incubation. As displayed in Figure 57, the PLGA-CDs20% nanoparticles yield an excellent contrast in red fluorescence once internalized inside cancer cells. The red fluorescence nanoparticles appear prevailingly localized inside MDA-MB-231 nuclei and/or perinuclear (Figure 58a–a") just after 6 h from the incubation and more marked after 24 h (Figure 58b–b"), suggesting that cell internalization in MDA-MB-231 is time-dependent. However, considering that the nuclear pores are about 10 nm in diameter and the nanoparticles have a diameter of about 100 nm, they may not be localized into cell nuclei. Therefore, it is possible to hypothesize that the intracellular microenvironment allows the disassembly of the nanoparticles and the consequent release and nuclear diffusion of CDs.

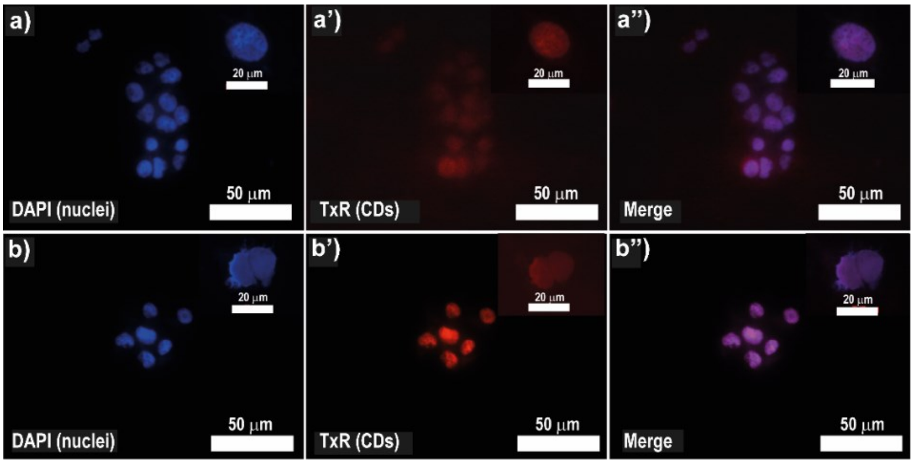

Figure 58. *Cell uptake study of PLGA-CDs20% after 6 h and 24 h of incubation.*

4.4.10. Conclusions

Here, hybrid nanoparticles (PLGA-CDs) were developed as potential theranostic nanoplatforms useful in image-guided photothermal cancer therapy. The proposed nanoparticles were composed of red emissive CDs embedded in a PLGA matrix in order to obtain a biodegradable and bio-eliminable nanoplatform able to combine drug delivery, photothermal, and fluorescence imaging properties. Carbon nanodots demonstrate to be a multifunctional excipient able to impinge theranostic properties, but also to stabilize the hybrid nanoparticles in physiological fluids, improve the drug loading and favor a sustained drug release in the function of their concentration in the PLGA matrix. In parallel, the encapsulation of CDs into a biodegradable polymeric matrix allows for increasing the average size avoiding premature renal excretion. The key role of CDs was demonstrated by evaluating the size distribution by DLS and AFM analysis of two hybrid nanoparticles with increasing content of CDs (PLGA-CDs1% and PLGA-CDs20%), which highlights how the highest content of CDs allows for reducing the particle size and avoid aggregation due to the different surface charges of the nanoparticles ascribable to the presence of CDs on the surface of the PLGA-CDs nanoparticles The PLGA-CDs20% nanoparticles demonstrated a good red fluorescence and photothermal conversion capacity in vitro on breast cancer cells. Moreover, the PLGA-CDs20% combinatorial approach of drug release and photothermal therapy demonstrated to be a valid therapeutic approach to induce effective cell death. The role of CDs ad multifunctional excipients represents a promising strategy in the formulation of nanoparticles useful in image-guided photothermal therapy (IG-PTT) of breast cancer.

4.5. Hydrophobic N-doped carbon nanodots coated with hyaluronic acid derivative as NIR-responsive hybrid nanosystems to deliver doxorubicin in cancer theranostics.

This work proposed the strategic design of hyaluronic acid-coated red-emissive carbon dots (N-doped CDs), with a well-structured hydrophobic core capable of loading and delivering a high amount of doxorubicin (Doxo) (> 9 % w/w) and acting as fluorescent and NIR-responsive agent in image-guided photothermal therapy. The rational idea is to exploit in a unique micelle-like superstructure the brilliant NIR photothermal conversion and red fluorescence of CDs and the ability of hyaluronic acid (HA) shell of stabilizing nanomedicines in the aqueous environment and targeting cancer cells overexpressing CD44 membrane receptors. This strategic combination allows for a smart theranostic agent useful in cancer imaging and NIR-triggered chemo-phototherapy of solid tumors. To fulfill this goal, hydrophobic CDs, named HCDs, were used as a multifunctional excipient to induce the self-assembling of the amphiphilic polylactide acid-grafted hyaluronic acid derivatives (HA-g-PLA), yielding to theranostics and biodegradable core-shell superstructures. Here, it was explored the potentiality of the synergistic effects of chemo-phototherapy combined with red fluorescence imaging in unique hybrid core-shell nanostructures like HA-g-PLA/HCDs (Figure 59).

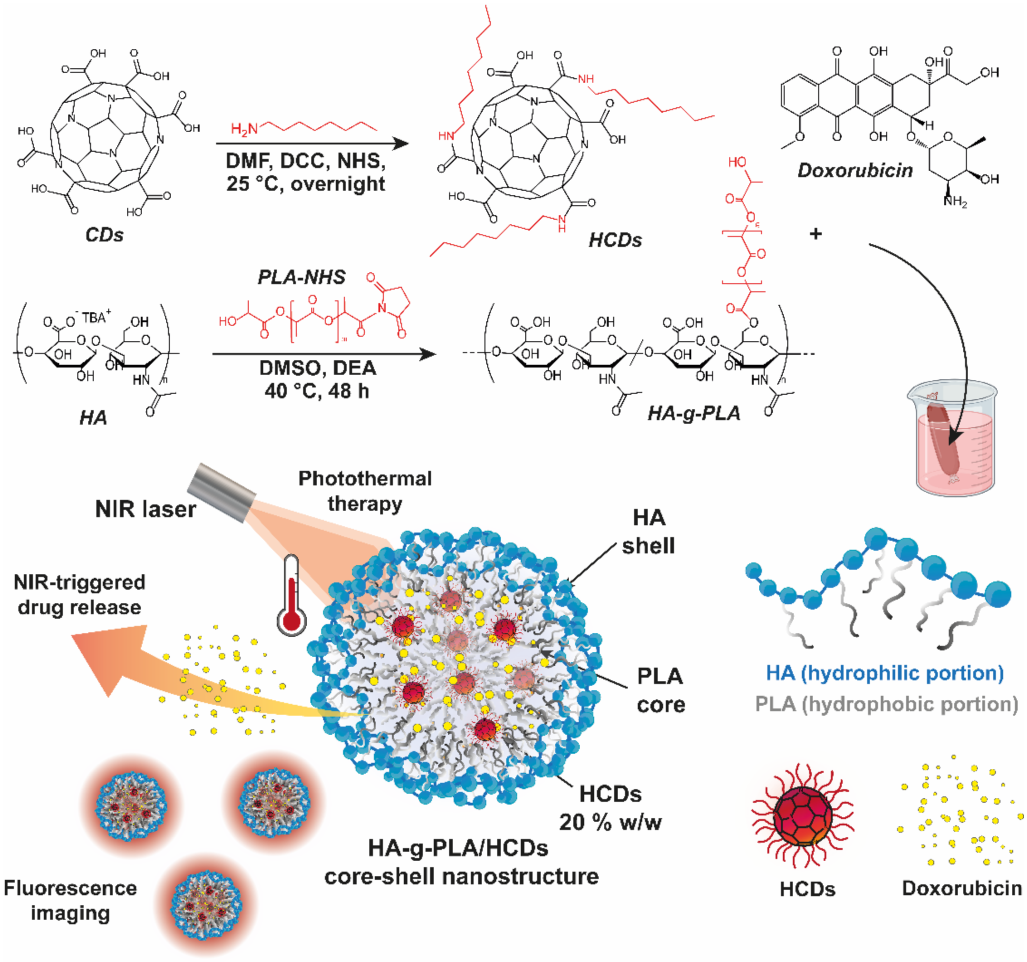

Figure 59. *Graphical abstract.*

4.5.1. Synthesis of the amphiphilic hyaluronic acid copolymer grafted with PLA chains (HA-g-PLA)

Among the plethora of materials useful in the production of drug delivery systems (DDS), hyaluronic acid (HA), the major constituent of the extracellular matrix (ECM), emerged as a performant biomaterial to obtain DDS with superior water stability and targeting capabilities [301,317]. HA is particularly attractive in precise anticancer therapy due to its high specificity and affinity for CD44 receptor overexpressed in different cancer cells, which conduce to receptor-mediated endocytosis [318]. Furthermore, HA is susceptible to hydrolysis as well [319]. Consequently, HA-based nanosystems may undergo intracellular hydrolysis by hyaluronidase (HYAL-1 and HYAL-2), overexpressed in different types of cancer, giving rise to ultrasmall by-products bio-eliminable by macrophages or renal clearance [320,321]. However, HA consists of a linear hydrophilic polysaccharide formed from disaccharide units of N-acetyl-d-glucosamine and glucuronic acid that alone can not spontaneously self-assemble into core-shell nanostructure exploitable for the delivery of hydrophobic drugs, but it requires a partial hydrophobization. Many side hydrophobic moieties have been investigated to obtain amphiphilic HA copolymers with self-assembly behavior in aqueous environments, such as polyesters or discrete aliphatic chains [318]. Among these polylactide acid (PLA), poly-ε-caprolactone (PCL), and poly-D, L-lactide-co-glycolide (PLGA) have aroused great scientific interest due to their physico-chemical characteristics, biodegradability, and biocompatibility [302]. Besides, collapsed composed matrix consisting of hydrophobic drugs and biodegradable polymer chains able to self-assemble would favor drug-controlled release [322][205].

Therefore, an amphiphilic copolymer of HA, consisting of HA ($\overline{M}n$ = 112 kDa) grafted with low molecular weight PLA chains ($\overline{M}n$ = 13 kDa), named HA-g-PLA, was synthesized by esterification between hydroxyl groups of HA and an end-chain activated N-hydroxysuccinimidyl ester of PLA and under mild basic conditions (Figure 60).

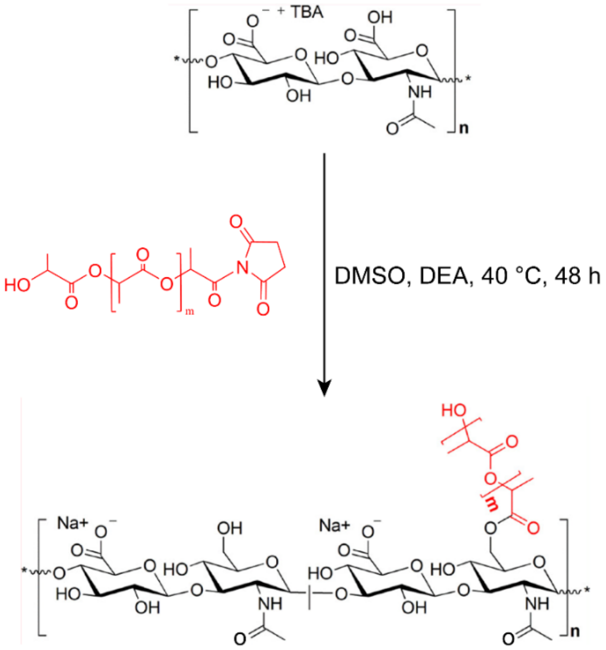

Figure 60. *The synthesis scheme of PLA-grafted hyaluronic acid (HA-g-PLA).*

The molecular weight of the main HA backbone was chosen to avoid reaching the specific gelling point of high molecular weight HA, which would negatively affect the assembling mechanisms, and maintain HA biological properties up to 10 mg mL^{-1} [323]. In parallel, PLA chains were selected as hydrophobic moieties to obtain self-assembling amphiphilic copolymers in an aqueous environment. The reaction was carried out using a PLA/HA molar ratio of 0.1 to partially functionalize the starting HA chains with hydrophobic side chains to provide a discrete hydrophobization of the HA backbone.

The derivatization degree (DD) of the HA was investigated by ^{1}H-NMR and evaluated by comparing the integrals of HA unit protons with those of the PLA side chains. The DD was about 2 % on a molar basis, corresponding to about four PLA moieties per HA chain (Figure 61).

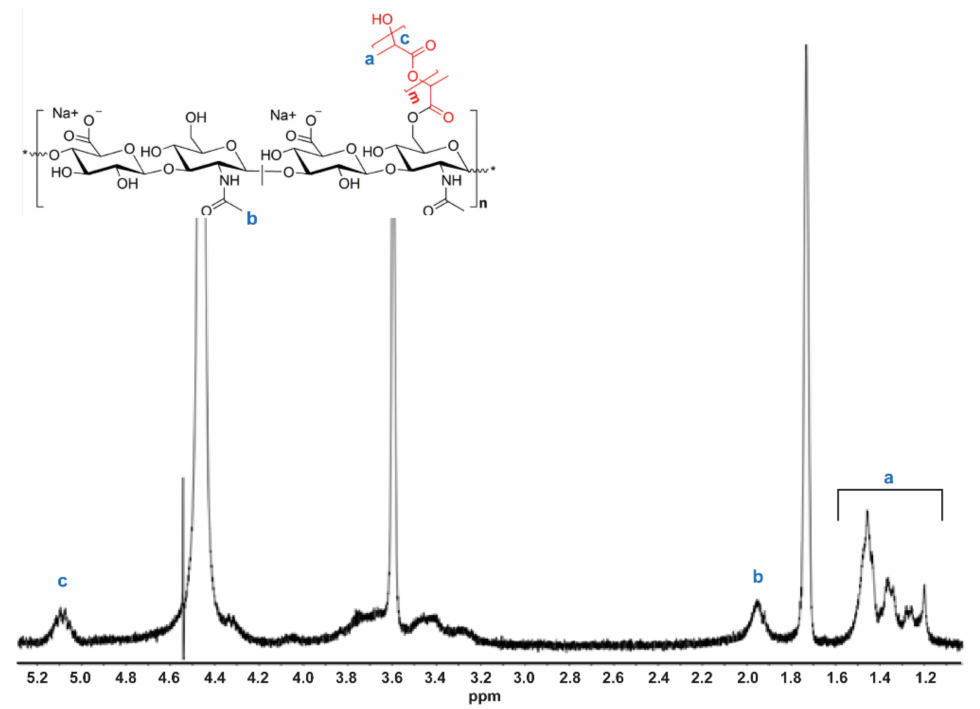

Figure 61. *^{1}H-NMR spectrum of HA-g-PLA (300 MHz, DMSO d$_6$).*

According to ^{1}H-NMR data, the SEC analysis reveals a copolymer with an average number molecular weight of 168 kDa.

4.5.2. Self-assembling capacity of HA-g-PLA copolymer

The pyrene fluorescence assay was carried out to evaluate the ability of HA-g-PLA to self-assemble into stable core-shell nanostructures (Figure 62). HA-g-PLA demonstrated able to assemble into core-shell nanostructures at a concentration higher than 43 µg mL^{-1}. This amphiphilic copolymer of HA was designed to spontaneously self-assemble, entrapping hydrophobic carbon nanodots and a high amount of anticancer drugs such as Doxo into the hydrophobic core. Besides, the hydrophilic HA shell was chosen to impinge active targeting features toward CD44 receptor cancer cells [288,324].

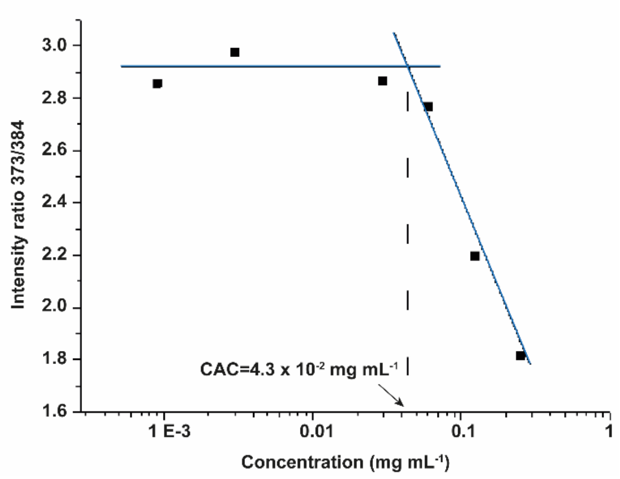

Figure 62. *Pyrene assay for the evaluation of CAC of HA-g-PLA.*

4.5.3. Synthesis of the hydrophobic carbon dots (HCDs)

Starting crystalline red-fluorescent N-doped carbon nanodots were synthesized by a bottom-up method and widely characterized as reported in Section 4.4.1. [158]. The selected red-emissive CDs are characterized by a rich content of surface carboxyl groups, useful as reactive groups for further surface functionalization, but make the CDs surface highly hydrophilic and unable to bind anionic or hydrophobic drugs such as most elective anticancer drugs [325]. Besides, electrostatic repulsions between the CDs surface and the carboxyl groups of HA-g-PLA negatively affect the formation of theranostic supramolecular assembled nanosystems able to deliver hydrophobic drugs. To overcome these limitations the hydrophobization of CDs with discrete aliphatic chains such as octylamine (C8) by surface passivation of the carboxyl groups represents an incisive strategy to provoke spontaneous self-assembling of the amphiphilic copolymer HA-g-PLA in the presence of hydrophobic CDs, henceforth named HCDs, into core-shell micellar-like nanostructure (HA-g-PLA/HCDs). These HA-g-PLA/HCDs combine the typical optical features of CDs with the ability of amphiphilic HA derivatives to deliver hydrophobic anticancer drugs, useful in theranostics chemo-photothermal cancer therapy. Thus red-emitting CDs were conjugated with octylamine by an amide coupling reaction exploiting the carboxyl surface functional groups of the bare CDs and the amine terminal function of octylamine (Figure 63). The activation of carboxyl groups by N,N′-dicyclohexylcarbodiimide (DCC) and N-hydroxysuccinimide (NHS) coupling gives rise to, after purification, carbon dots passivated on the surface with hydrophobic aliphatic chains (HCDs). The adopted synthetic scheme is scalable and reproducible in terms of functionalization degree and high yield (60%), and allows obtaining an efficient surface functionalization under mild conditions.

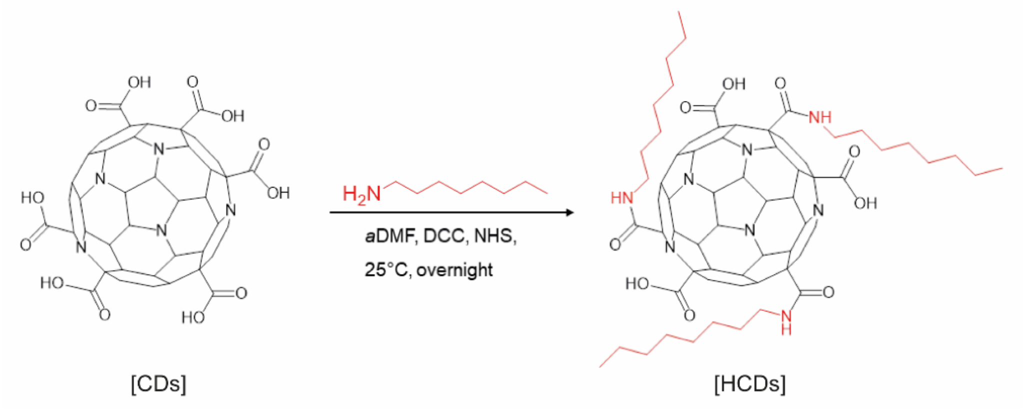

Figure 63. *The synthesis scheme of hydrophobic CDs (HCDs).*

4.5.4. Chemical characterization of HCDs

The surface wettability of HCDs was investigated by equilibrium contact angle measurements (Figure 64 a-a') to evaluate how C8 moieties on CDs surface affected the affinity of CDs for hydrophobic compounds. As expected HCDs display a marked hydrophobicity in comparison with the nude CDs ($\theta > 90°$ and $\theta < 90°$ for the HCDs and CDs, respectively.

The surface passivation with hydrophobic agents was also confirmed by observing the different partitions of nude CDs and HCDs in an o/w biphasic system ($CHCl_3/H_2O$). As illustrated in Figure 64b, HCDs result much more affine to the $CHCl_3$ phase, in contrast to nude CDs, demonstrating that the hydrophobization of CDs with C8 chains significantly impinges the partition behavior for HCDs. The hydrophobic character of HCDs suggests their potential incorporation into the hydrophobic core of micelle-like nanostructures obtained by self-assembling amphiphilic copolymers such as HA-g-PLA. The effective surface functionalization of CDs was also evaluated by FTIR analysis, confirming the presence of amide bonds and aliphatic chains, accompanied by the reduction of surface carboxyl groups [326]. As shown in Figure 64c, the bare CDs show hydroxyl (3420 cm^{-1}) and carbonyl stretching vibrations (1708 cm^{-1}) relative to the presence of several carboxyl reactive groups suitable for amide coupling. The FTIR spectra of HCDs confirmed the successful formation of the amide bonds, as demonstrated by the reduction of the carboxyl band at 3327 cm^{-1} and the appearance of the I amide band at 1630 cm^{-1}. Furthermore, the presence of CH vibrations (2927-2852 cm $^{-1}$) confirmed the presence of alkyl chains on the HCDs surface.

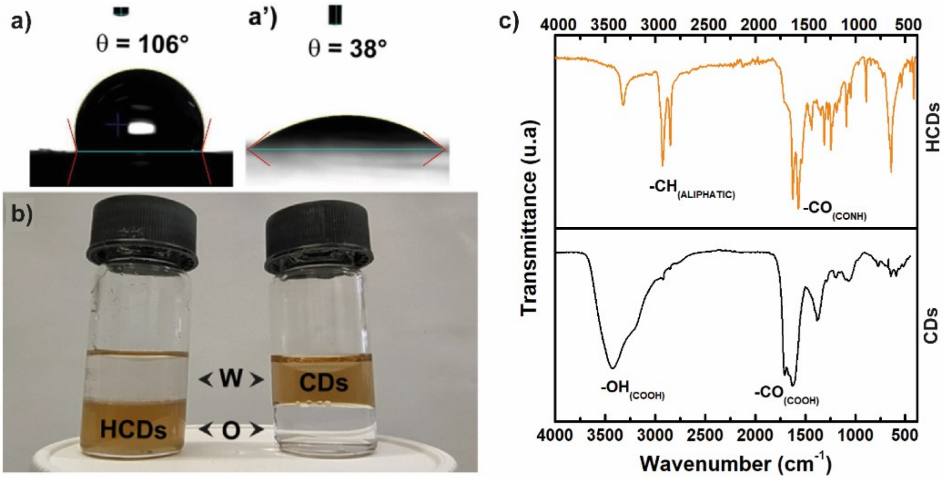

Figure 64. *The contact angle of HCDs (a) and CDs (a'). Repartition of HCDs and CDs in a biphasic system water/chloroform (b). FT-IR spectrum of HCDs and CDs (c).*

Then, the amount of C8 chains on the HCDs surface was evaluated by ^{1}H-NMR using acetone as an internal standard. As shown in Figure 65, the HCDs spectrum presents the characteristic peaks of octylamine at 0.89 ppm and 1.28 ppm, relative to the CH_3 and CH_2, respectively. The depletion of the characteristic peak at 2.58 ppm, related to the CH_2 bound to the amine, and the shift of this peak to higher fields suggest a successful conjugation via amide coupling with aliphatic chains.

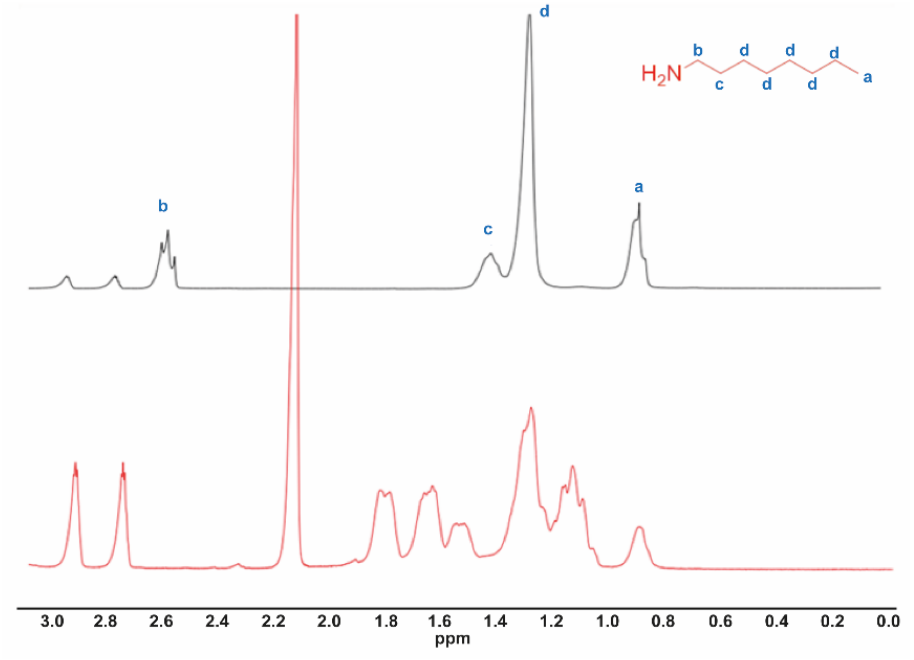

Figure 65. *The ^{1}H-NMR spectrum of HCDs with internal standard (acetone) compared to that of octylamine.*

The functionalization degree of HCDs was calculated by comparing the peak relative to acetone (6H; δ 2.13 ppm) with that relative to octylamine (3H; δ 0.89 ppm), following the equation reported below:

$$n_a : \frac{\int H_{2.13ppm}}{6} = n_c : \frac{\int H_{0.89ppm}}{3}$$

where nA and nC are the moles of acetone and octylamine in the analyzed sample respectively.

The functionalization degree in octylamine was found to be 30 ± 2 % w/w, corresponding to a functionalization of 3.8 meq g^{-1} of CDs. Considering that from previous titration data, the amount of carboxyl groups of bare CDs is equal to 5.5 meq. g^{-1}, under the used experimental conditions, the functionalization degree in octylamine corresponds to 69 % of the available carboxyl groups [158].

4.5.5. Optical characterization of the hydrophobic carbon dots (HCDs)

To understand the potentiality of HCDs to be used as fluorescence contrast agents, their red fluorescence properties were evaluated and compared with that of nude CDs. As shown in Figure 66a, the HCDs spectrum, similar to the nude CDs spectrum, displayed a complex absorption spectrum characterized by different bands in the entire UV/UV-vis range. The emission spectrum of HCDs and nude CDs were collected in DMF under excitation at 540 nm. As reported in Figure 66b, HCDs, and nude CDs have shown comparable emission spectra. It is important to notice that although HCDs have shown a slightly reduced photoluminescence compared to nude CDs, no quenching phenomena were observed and HCDs preserve the emission profile of the starting CDs. An important advantage of HCDs is that unlike native hydrophobic CDs, obtained from solvothermal decomposition processes from hydrophobic compounds (e.g. melamine and benzoic acid), hydrophobic CDs obtained by post-surface functionalization with C8 moieties do not suffer from π-π stacking interactions or dot-dot aggregation phenomena which usually induce the turning off of the characteristic emission bands of CDs [327]. The emission spectrum of HCDs was characterized by a principal peak at about 570 nm with two shoulders at about 608 and 645 nm of particular interest and necessary for high-resolution fluorescence imaging, useful in cancer diagnosis of primary and secondary tissues [3][328].

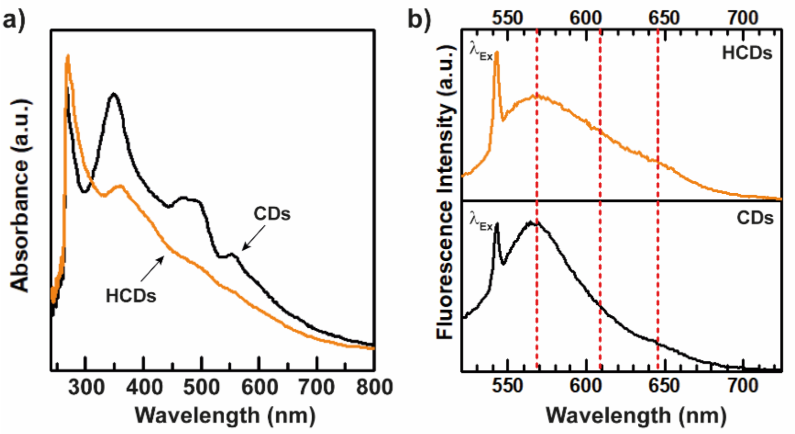

Figure 66. *UV spectra (a) and emission spectra under excitation at 540 nm (b) of HCDs (orange lines) and CDs (black lines).*

4.5.6. NIR-induced photothermal conversion study of HCDs

The ability of HCDs to act as photothermal agents in IG-PTT was evaluated by irradiating a water dispersion of either bare CDs or HCDs (0.1 mg mL^{-1}) with an 810 nm NIR-laser and measuring the temperature increase (ΔT) as a function of the laser exposure. Temperature increases were normalized by the number of dots at equal concentrations and reported as the function of the exposure time, to compare the photothermic effect of each other. As evidenced in Figure 67, HCDs possess a remarkable photothermal conversion capacity, greater than that shown by bare CDs. In detail, HCDs after about 42 s of laser exposure reach the minimum temperature of hyperthermia (43 °C) needed to eradicate tumors. In contrast, for the bare CDs a laser exposure four times higher is required to reach the same temperature. The higher photothermal conversion observed for the HCDs in an aqueous environment can be ascribed to hydrophobic surface interactions, which restrict the surfaces' intramolecular rotation around C8 bonds, giving rise to heating by vibrations which contribute to dissipation phenomena. Overall, the red fluorescence properties displayed by the HCDs and the efficient photothermal conversion capability make them a potential candidate for cancer IG-PTT applications.

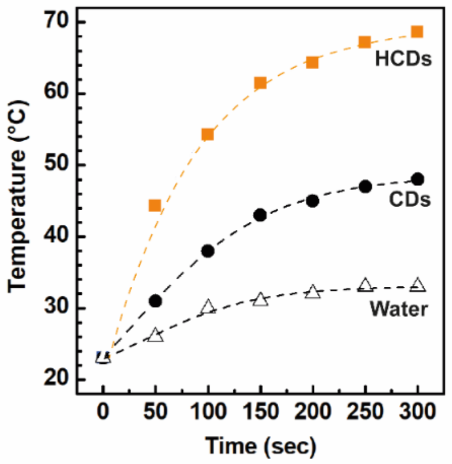

Figure 67. *Kinetics of hyperthermia in the function of irradiation time with an 810 nm laser of an aqueous dispersion of HCDs and CDs. Water was used as control.*

4.5.7. Self-assembling of the hyaluronic acid-dressed HCDs (HA-g-PLA/HCDs)

The obtained HCDs were employed as a functional excipient to impinge theranostic features to the core-shell nanostructures able to be internalized through active targeting through the affinity of the hyaluronic acid shell for the CD44 receptor overexpressed in most cancer cells [329]. The HA-g-PLA/HCDs were prepared by spontaneous self-assembling of the HA-g-PLA copolymer in a mixture of water and DMSO, considering an HCDs theoretical loading of 20 % on a weight basis (Figure 68), by dialysis method. Dialysis of the water/DMSO dispersion against water allowed the diffusion of DMSO and the complete self-assembling of hybrid core-shell HA-g-PLA/HCDs nanostructures in water. Moreover, no precipitation of HCDs was observed and the diffusion of free HCDs outside the membrane was completely excluded by the absence of the typical absorption bands in the waste, suggesting their complete encapsulation within the hydrophobic PLA core of HA-g-PLA micelle-like superstructures.

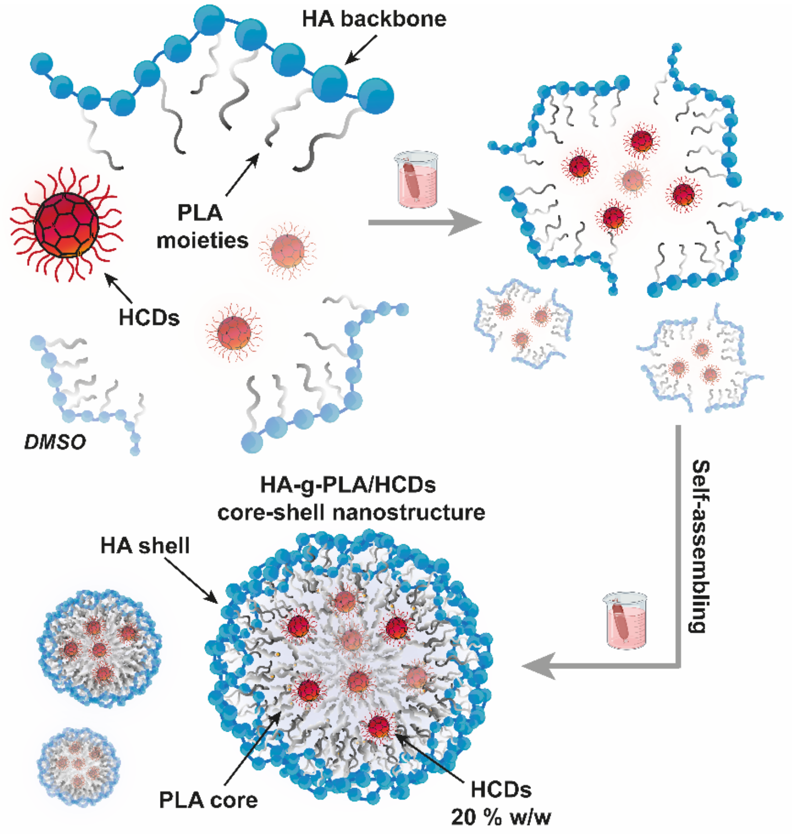

Figure 68. *Schematic representation of self-assembling HA-g-PLA/HCDs core-shell nanostructures by dialysis method.*

The zeta-potential analysis confirmed the encapsulation of HCDs into the PLA core. In fact, no significant changes in the surface charge distribution occurred after the incorporation of HCDs in the micelle-like nanostructure (≈ -33 mV and ≈ -26 mV, respectively), suggesting that HCDs are distributed only into the hydrophobic core (Table 5). The reason can be attributed to the higher partition coefficient and lower carboxyl function density at the surface observed for the HCDs compared to the nude CDs.

The strong chain entanglements between the C8 moieties of HCDs and the PLA side chains of the HA-g-PLA significantly impinge positively on the self-assembling of the superstructures, inducing a sharp reduction of the nanosystem diameter (from 739 nm to 330 nm). Therefore, the encapsulation of HCDs into the hydrophobic core of HA-g-PLA core-shell nanostructures implies the formation of a collapsed and well-structured hydrophobic core (Table 5).

Table 5. *Z-average, PDI, and zeta-potential of HA-g-PLA, HA-g-PLA/HCDs, and HA-g-PLA/HCDs@Doxo by DLS analysis.*

Samples	***Z-Average (nm)***	***PDI***	***ζ-Potential (mV)***
HA-g-PLA	739 ± 11	0.187 ± 0.010	-33.3 ± 11.6
HA-g-PLA/HCDs	329 ± 5	0.274 ± 0.008	-28.9 ± 10.8
HA-g-PLA/HCDs@Doxo	390 ± 8	0.104 ± 0.001	-31 ± 6.7

4.5.8. Stability study of HA-g-PLA/HCDs

The physicochemical stability of the HA-g-PLA/HCDs was evaluated both in the physiological medium (PBS pH 7.4) and in the tumor microenvironment (acetate buffer pH 5.5) by DLS analysis (Figure 69). DLS measurements allow studying the size distribution as a function of the incubation time at 37 °C up to 72 h. HA-g-PLA/HCDs display excellent stability under physiological conditions as demonstrated by the constant size distribution over time of about 330 nm. In contrast, the acidic conditions highly affected the size distribution of HA-g-PLA/HCDs, which underwent a sharp increase at t_0 up to about 700 nm and gradually decreased over time to 550 nm after 72 h at 37 °C. This behavior at acid conditions could be ascribed to a rapid cleavage of the ester bonds between the PLA and the HA moieties at the surface and simultaneous acid-induced degradation of the PLA chains. These phenomena thus provoke rapid swelling of the HA shell and the consequent surface destruction of the PLA core, explaining well the biphasic trend observed in Figure 69 at pH 5.5.

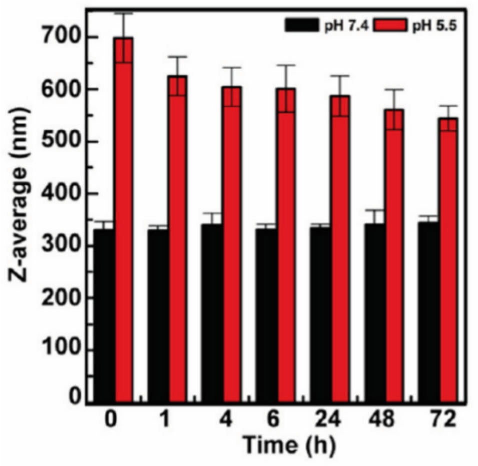

Figure 69. *Study of stability at physiological (pH_7.4) and cancer conditions (pH=5.5) of HA-g-PLA/HCDs by DLS analysis of Z-average.*

4.5.9. Preparation and characterization of the drug-loaded hyaluronic acid-coated HCDs (HA-g-PLA/HCDs@Doxo)

The Doxo-loaded hyaluronic acid-coated HCDs, namely HA-g-PLA/HCDs@Doxo, were prepared by self-assembling the HA copolymer in the presence of both HCDs and Doxo (20 % w/w). The idea was to exploit the hydrophobic character of HCDs into the core to maximize the amount of Doxo loaded during the formation of the collapsed hydrophobic core of the HA-g-PLA/HCDs in aqueous dispersion. The drug loading of HA-g-PLA/HCDs@Doxo was measured spectrophotometrically and was found to be 9.63 ± 0.049 % (w/w), corresponding to an encapsulation efficiency of about 48 %. Compared to other examples reported in the literature for similar self-assembled amphiphilic copolymers [330], this encapsulation efficiency results very high, probably ascribed to the greater hydrophobic surface of HCDs in the core of the superstructures available for interaction with doxorubicin the presence.

The morphological characterization of these core-shell nanostructures was investigated by atomic force microscopy (AFM). As reported in Figure 70 a-a'', AFM images show nanoaggregates of HA-g-PLA/HCDs of about 60 nm in height in the dry state. The size distribution of the dried sample is much lower if compared to the same sample in water (about 300 nm, Table 5), due to the lack of the hydration sphere in the dried micelles-like structures if compared with the sample in water dispersion. This suggests that the average size of these nanostructures could be controlled by tuning the molecular weight of the HA in the function of the specific application. It is important to notice that neither free HCDs nor free Doxo was observed in the AFM image, suggesting the successful encapsulation of both elements during the self-assembling procedure.

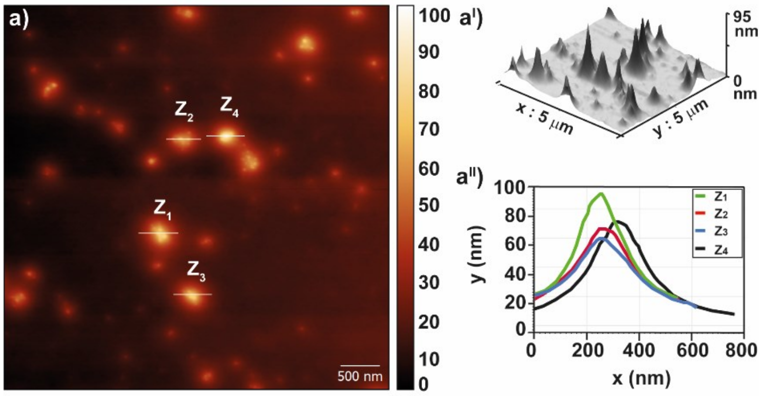

Figure 70. *AFM images (a-a') and size distribution (a'') of HA-g-PLA/HCDs@Doxo.*

As shown in Table 5, DLS data do not reveal significant differences in terms of Zeta-potential and size distribution between the drug-loaded and empty HA-g-PLA/HCDs nanostructures, suggesting that Doxo do not perturb chain entanglements mechanisms during self-assembling.

4.5.10. Drug release kinetics evaluation of HA-g-PLA/HCDs@Doxo with and without NIR-exposure

The ability of the HA-g-PLA/HCDs@Doxo to release the doxorubicin payload was established in physiological conditions (PBS pH 7.4) and tumor microenvironment-TME conditions (acetate buffer pH 5.5) at 37 °C, with and without a NIR laser exposure at suitable power density. Figure 71a shows that HA-g-PLA/HCDs@Doxo displayed a slow and sustained drug release over time under physiological conditions, avoiding the undesirable burst effect. Indeed, the free Doxo rapidly diffused in 2 h, displaying a sharp burst effect in the first minutes after the incubation at 37 °C. In contrast, HA-g-PLA-HCDs@Doxo retained its payload, releasing only 10 % of doxorubicin after 48 h. Conversely, at acid conditions of pH 5.5, HA-g-PLA-HCDs@Doxo releases the drug payload faster reaching about 58 % within 48 h. This behavior suggests that HA-g-PLA-HCDs@Doxo can favorably release Doxo in the TME in a pH-dependent modality (Figure 71a). This trend release is following the different behavior of the nanostructures observed in the two media, as well as the hydrolytic phenomena of the polylactic acid moieties at acidic pH, which lead to swelling and consequent erosion of the nanostructure

(Figure 71a) thus increasing a larger surface which favors the diffusion of doxorubicin. The NIR-triggered photothermal effect mediated by entrapped HCDs could allow a faster drug release due to a thermal-induced destabilization of the hydrophobic core [254,331] Indeed, the HA-g-PLA-HCDs@Doxo can release an amount of Doxo two times bigger at pH 7.4 if compared to the not irradiated nanosystems as demonstrated by the NIR-induced drug release kinetic reported in Figure 71a. The NIR-triggered drug release trend at pH 5.5 was similar, even if much more restrained, and was observed at pH 5.5 (66 % release vs 58 %). The possibility to locally release the drug payload in the site of action on demand represents a promising therapeutic strategy to minimize the side effects and avoid multidrug resistance due to the restricted biodistribution of the drugs. The NIR-induced temperature increase at the same concentration tested in the NIR-triggered drug release study and under an 810 nm diode laser exposure for 300 s at 5 W cm^{-2} was also evaluated (Figure 71b). HA-g-PLA-HCDs show good photothermal conversion properties, reaching the minimum temperature for hyperthermia (42-43 °C) after less than 200 s of irradiation.

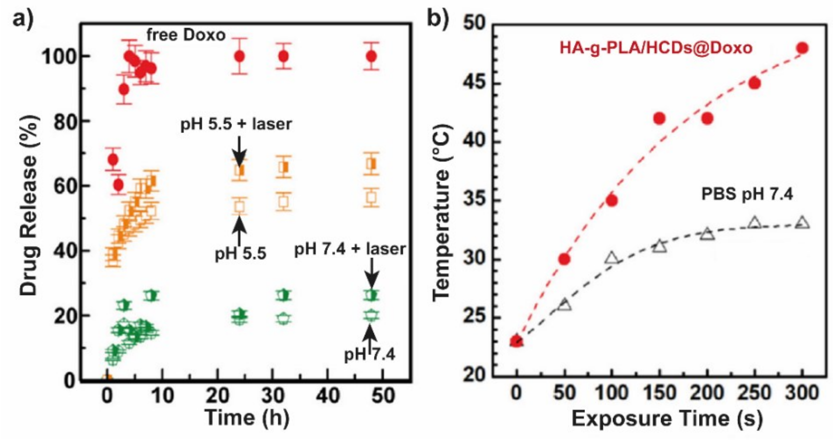

Figure 71. *Profile of cumulative drug release at physiological (pH=7.4) and cancer conditions (pH=5.5.) of HA-g-PLA/HCDs@Doxo with and without laser exposure, compared to the profile of diffusion of free Doxo (a). Kinetic of hyperthermia at conditions of drug release study (b).*

4.5.11. Cytocompatibility of HA-g-PLA/HCDs and anticancer efficacy assay of HA-g-PLA/HCDs@Doxo

The in vitro cytotoxic effects of the HA-g-PLA/HCDs were carried out on cultures of two different breast cancer cell lines, namely MDA-MB-231 and MCF-7, after 24 h of incubation (Figure 72). Cell viability values treated with HA-g-PLA/HCDs demonstrated a high cytocompatibility (100 %) within the range of concentration tested (up to 300 g mL^{-1}) on either MCF-7 (Figure 72a) and MDA-MB-231 (Figure 72a’). Cell viability assay was repeated on both cell lines, applying an 810 nm NIR laser at power fitted at 7 W cm^{-2} to evaluate the NIR-triggered hyperthermia effects due to the empty nanostructures. Hyperthermia levels were previously established on the dispersion of HA-g-PLA-HCDs in DMEM (30 µg mL^{-1}), irradiating the sample with 810 nm diode laser under the same conditions and then tested in vitro, in order to establish the optimal experimental setting to give rise suitable hyperthermia (44 - 47 °C) during in vitro cell culture conditions. This power density and exposure were proven biocompatible by other studies published elsewhere using both cell lines [212,254,255]. Figure 72 shows a remarked cytotoxic effect at the highest dose (> 150 g mL^{-1}) due to dose-dependent photothermal-induced damage that occurred for both cell lines.

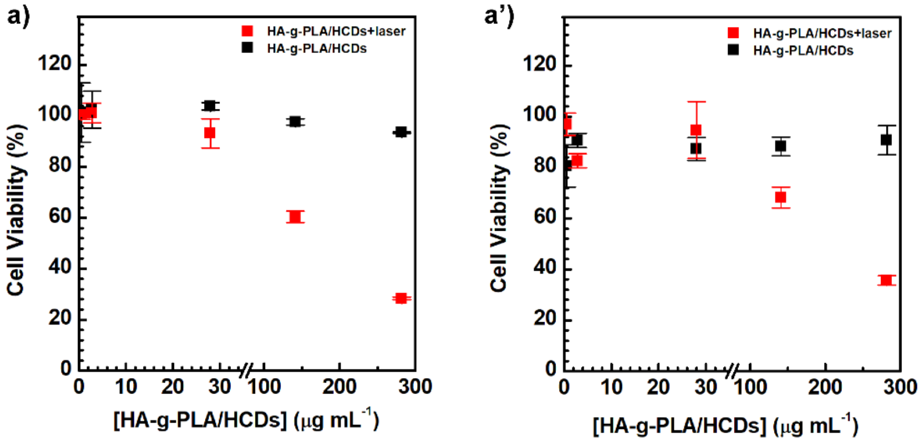

Figure 72. *Cytocompatibility of HA-g-PLA/HCDs with and without laser irradiation (300 s, 7 W cm*$^{-2}$*) on MCF-7 (a) and MDA-MB-231 (a’).*

To evaluate the cytotoxic effect of the drug-loaded HA-g-PLA/HCDs@Doxo nanosystem, the equivalent amount of HA-g-PLA/HCDs (i.e., from 0.271 to 0.00054 mg mL^{-1}). As shown in Figure 73, cell viability decreased with the increase in the amount of HA-g-PLA/HCDs@Doxo suggesting a dose-dependent cytotoxic effect for both cell lines. In order to evaluate the therapeutic effect of the NIR-triggered hyperthermia combined with the on-demand local drug release, the second set of experiments was performed. In detail, after 24 h of incubation cells treated with HA-g-PLA-HCDs@Doxo were irradiated with an 810 nm diode laser using the selected hyperthermia condition (300 s, 7 W cm^{-2}). In both cell lines, cell viability exponentially decreased following a dose-dependent response that resembles those observed for the unexposed samples

(Figure 73), even with some qualification. In particular, the chemo-photothermal therapy approach by HA-g-PLA-HCDs@Doxo allows a much more marked cytotoxic effect than the empty nanosystem, reaching almost 0 % in cell viability at a concentration of 150 g mL^{-1} (eq. Doxo dosage of 20 M).

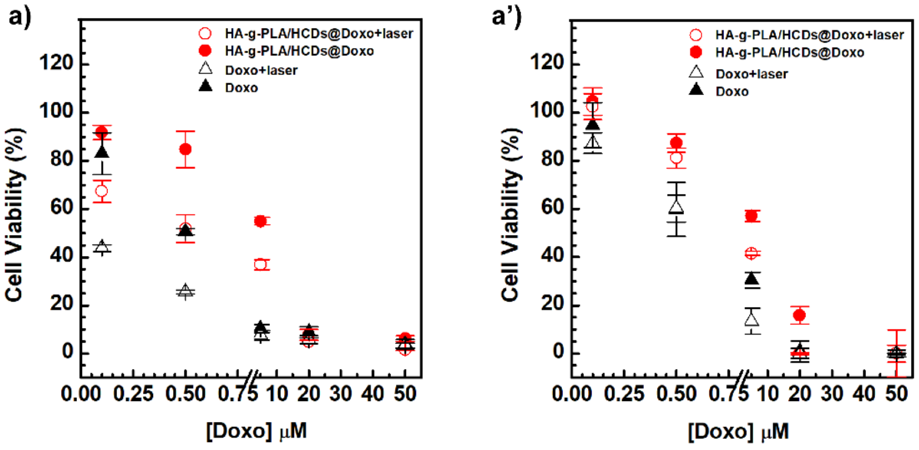

Figure 73. *The cytocompatibility of HA-g-PLA/HCDs@Doxo and free Doxo with and without laser irradiation (300 s, 7 W cm^{-2}).*

Besides, it is necessary to underline that the potency of the chemo-photothermal treatment with HA-g-PLA-HCDs@Doxo, expressed as IC_{50} value (Table 6), was comparable to that of free Doxo, even if at a lower available dose. Indeed, cytotoxic effects associated with the use of the free drug are usually higher because it is promptly available and freely diffuses throughout the cell membranes, provoking damage. The different cytotoxic effects of NIR-treated HA-g-PLA-HCDs@Doxo on MCF-7 and MDA-MB-231 cells (IC50 0.56 µM vs 0.94 µM) are ascribed to the noteworthy susceptibility of MCF-7 than MDA-MB-231 cells.

Table 6. *IC_{50} values of free Doxo, HA-g-PLA/HCDs@Doxo, and HA-g-PLA/HCDs@Doxo laser treated after 24 h and 48 h of incubation.*

Samples	***MCF-7***	***MDA-MB-231***
	IC_{50}^{24h} (µM)	***IC_{50}^{24h} (µM)***
Doxorubicin	0.50 ± 0.2	0.69 ± 0.3
HA-g-PLA/HCDs@Doxo	6.50 ± 0.1	7.67 ± 0.8
HA-g-PLA/HCDs@Doxo + laser	0.56 ± 0.1	0.94 ± 0.2

Therefore, taking into account the HA-g-PLA/HCDs potential as a fluorescence imaging agent, on-demand NIR-triggered drug release, and chemo-photothermal efficacy, these nanocomposite superstructures represent promising anticancer theranostic platforms useful for IG-PTT applications in cancer theranostics.

4.5.12. Gene expression analysis on treated MDA-MB-231 and MCF-7 cell lines in vitro

The cytocompatibility of HA-g-PLA-HCDs was also studied at the molecular level, evaluating presumptive cell death mechanisms triggered by HA-g-PLA/HCDs@Doxo micelles upon NIR irradiation. In detail, the differential mRNA expression levels of 10 genes (BECN1, CASP7, ATG3, CASP9, BAX, PARP1, BCL-2, RIPK1, BCL-XL, and TNFα), recognized to exert a functional role in cell death pathways like apoptotic, autophagic, and necrotic/necroptotic pathways, were assessed in MDA-MB-231 and MCF7 breast cancer cell lines. The mRNA expression levels were evaluated by PCR real-time technique using a specific oligonucleotide primer for each gene considered (Table 7).

Table 7. *Primer sequences employed in the gene analysis of cell death pathways by RT_PCR.*

Gene name	***Accession number***	***Primer sequence (5'-3')***
ATG3 autophagy related 3 homologs (ATG3)	NM_022488	ACTGATGCTGGCGGTGAAGATGGT GCTCAACTGTTAAAGGCTGCC
BCL2-associated X protein (BAX)	NM_004324	TCAGGATGCGTCCACCAAGAAGTG TGTCCACGGCGGCAATCATC
B-cell CLL/lymphoma 2 (BCL2)	NM_000633	ATCGCCCTGTGGATGACTGAGTGC CAGGAGAAATCAAACAGAGGC
BCL2-like 1 BCL2L1 (BCLXL)	NM_138578	GCCACTTACCTGAATGACCACCAA CAACCAGCGGTTGAAGCGTTCCT
Beclin 1, autophagy related (BECN1)	NM_003766	CTGGACACTCAGCTCAACGTCACT CTAGTGCCAGCTCCTTTCGA
Caspase 7, apoptosis related cysteine peptidase (CASP7)	NM_001227	CGGAACAGACAAAGATGCCGAGA GGCGGCATTTGTATGGT

Caspase 9, apoptosis-related cysteine peptidase (CASP9)	NM_001229	GTTGAGGACCTTCGACCAGCTCAA CGTACCAGGAGCCACTCTT
Poly(ADP-ribose) polymerase 1 (PARP1)	NM_001618	CCAAGCCAGTTCAGGACCTCATGG ATCTGCCTTTTGCTCAGCTTC
Tumor necrosis factor (TNFα)	NM_000594	CTCTTCTGCCTGCTGCACTTTGATG GGCTACAGGCTTGTCACTC
Human receptor (TNFRSF)-interacting serine-threonine kinase 1 (RIPK1)	NM_003804	TATCCCAGTGCCTGAGACCAACGT AGGCTCCAATCTGAATGCCAG
β-Actin (ACTB)	NM_001101	CACCATTGGCAATGAGCGGTTCAG GTCTTTGCGGATGTCCACGT
Glyceraldehyde-3-phosphadehydrogenase (GAPDH)	NM_002046	ACCACCCTGTTGCTGTAGCCAAGT CTCCTCTGACTTCAACAGCG

Cells were treated using all IC_{50} values extrapolated from the previous cell viability assay (Table 6), and comparable doses were tested for empty HA-g-PLA/HCDs. No significant differences in gene expression were measured in HA-g-PLA/HCDs treated cells, with insignificant effects on the activation of a death response, comparable to the gene expression profile relative to unexposed MDA-MB-231. Overlapping profiles also occurred in NIR-treated cells and NIR-treated MDA-MB-231 after HA-g-PLA/HCDs incubation which remained like controls (Figure 74). This corroborates cell viability data highlighting the high cytocompatibility profile of the HA-g-PLA/HCDs after 24 h of incubation. As expected, MDA-MB-231 exposure to Doxo provided a different gene expression pattern than untreated cells. Among the gene set analyzed, some genes associated with apoptotic cell death exhibited significant differential expression (Figure 74a). In particular, the expression of proapoptotic genes such as TNFα, BAX, and CASP7 was increased, accompanied by a reduction of the gene expression levels of pro-survival factors as BCL2 (Figure 74b). These results confirm the activation of the apoptotic cell death pathway in response to Doxo at the IC_{50} values [332,333]. A concurrent upregulation of BECN1 and BCL-XL also emerges. It is well-known that BECN1 plays a pivotal role in autophagosome formation [334,335]. Therefore the cross-talk between apoptosis and autophagy [336], which may transform the commitment toward a specific pathway, could also be active in this experimental setting. Considering the magnitude of the measured changes, according to cell viability data, Similar mRNA expression profiles were also obtained after NIR exposure to Doxo-treated cells (Figure 74). This suggests that the laser treatment, as carried out, does not employ additional effects on Doxo on MDA-MB-231 viability. The laser treatment of MDA-MB-231 cells incubated with HA-g-PLA/HCDs@Doxo resulted in a transcriptional pattern similar to those above measured. However, it should be noted that the combination of NIR photothermal treatment and Doxo-related DNA damages reinforce the upregulation of the pro-apoptotic genes BAX and CASP7 and a huge downregulation of the anti-apoptotic gene BCL2, resulting in the activation of apoptosis programmed cell death. The transcriptional response of MCF-7 upon HA-g-PLA/HCDs exposure was quite different, showing that the mRNA levels of some genes appeared slightly increased (Figure 74a). Similar profiles also occurred in irradiated cells. However, these alterations do not result in the engagement toward a specific cell death pathway at the used dosage. However, this transcriptional pattern in response to HA-g-PLA/HCDs may be related to the major susceptibility of MCF-7. The expression profiles of NIR irradiated MCF-7 cells treated with HA-g-PLA/HCDs revealed the upregulation of proapoptotic members, including CASP7, CASP9, BAX. At the same time, the pro-survival genes were downregulated (BCL2) or unchanged (BCL-XL) (Figure 74). Interestingly, also genes involved in autophagy (BECN1) and necroptosis (TNFα) were upregulated, thus suggesting an overall response to laser treatment, MCF-7-specific, via different cell death pathways [224]. As expected, the transcriptional response of MCF-7 upon Doxo exposure with or without irradiation provided a different gene expression pattern. The upregulation of proapoptotic genes (CASP7 and BAX), and the reduction of BCL2 mRNA level (Figure 74) [332,333] As discussed above for MDA-MB-231, the simultaneous upregulation of BECN1 and BCL-XL suggests different death pathways [337]. This is particularly remarkable in MCF-7 cell lines showing alteration of apoptotic level because of P53 and CASP3 status on MCF-7 [338–340]. Interestingly, this gene expression signature was powered upon MCF-7 exposure to HA-g-PLA/HCDs@Doxo with and without NIR-laser exposure. In addition to BCL2 downregulation and increased mRNA levels of CASP7 and BAX, upregulation of TNFα and RIPK1 was also reported (Figure 74). TNFα and

RIPK1 are implicated in the activation of the necroptotic pathway. The possible concurrent activation of necroptosis mechanisms has been particularly interesting as a promising alternative route of cell death for overcoming apoptosis resistance. Therefore, it is reasonable to hypothesize that the concurrent activation of different death mechanisms reinforces the antitumor effect [316,341–344].

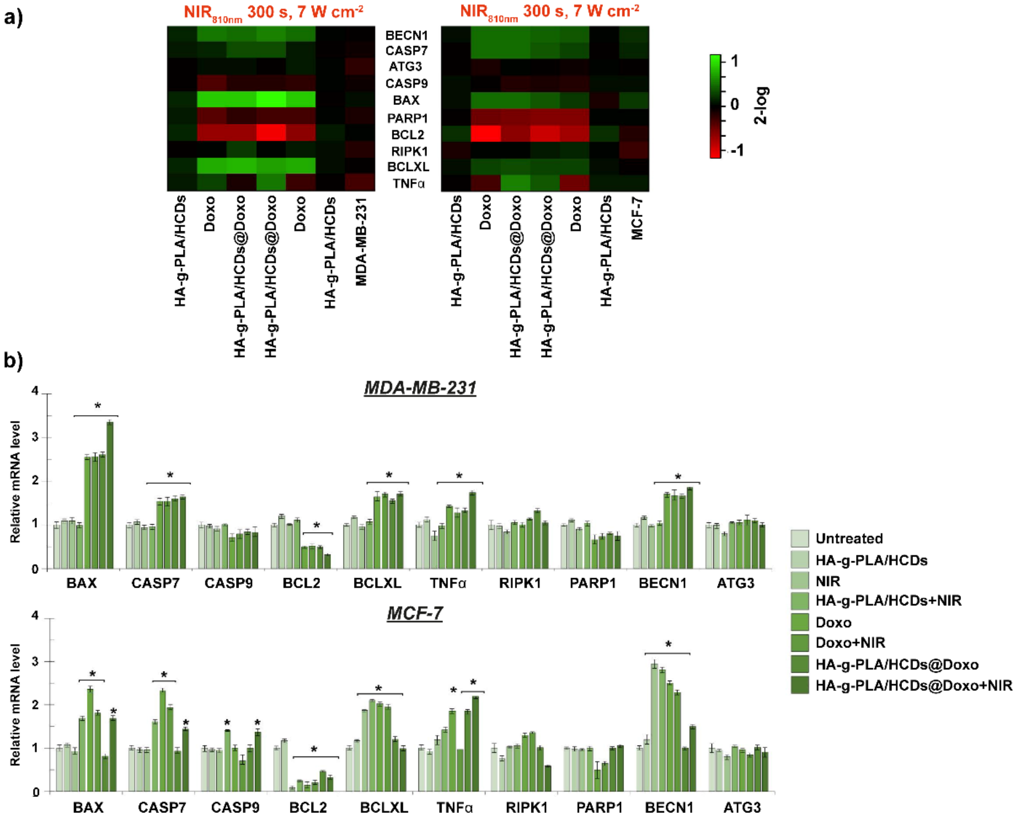

Figure 74. *Cell death pathway-focused gene expression analyses in MCF-7 and MDA-MB-231. Heat map representation of the mean-cantered data of RT-qPCR results showing the mRNA levels of analyzed genes in presence of HA-g-PLA/HCDs or HA-g-PLA/HCDs@Doxo or Doxo with respect with or without laser irradiation (a). Gene expression values are colored from red (low) to green (high). Bar graph of the pathway focused on gene expression profiling in response to treatments. Bars represent mean value ± SD; values were considered statistically significant at* $p \leq 0.05$ *(b).*

4.5.13. Cell internalization study of HA-g-PLA-HCDs in vitro

To evaluate the targeting ability of HA-g-PLA-HCDs mediated by HA shell to recognize CD44 receptors overexpressed in cancer cells efficiently and to be internalized by receptor-mediated endocytosis was investigated on both MDA-MB-231 and MFC-7 cell lines. Fluorescence microscopy ($\lambda_{Ex} = 559$) was employed to track the nanosystem in living breast cancer cells (MDA-MB-231 and MCF-7), exploiting their capability to act as a contrast agent in fluorescence imaging (FLI). In detail, the cell uptake was evaluated after 4 h and 24 h of incubation with HA-g-PLA-HCDs at a concentration of 0.1 mg mL^{-1} (Figure 75a-b). The HA-g-PLA/HCDs appear well internalized in both cancer cell lines after 4 h, showing an excellent contrast in FLI (Figure 75a-b). Taking in mind that nuclear pores have a diameter of about 10 nm, smaller than that of HA-g-PLA/HCDs of about 300 nm, the nuclear contrast displayed could be ascribed to HCDs released and efficiently diffused inside nuclei and through cells. Therefore, it is possible to hypothesize that the intracellular microenvironment induces HA-g-PLA/HCDs disassembling, releasing ultrasmall HCDs ($d \approx 4.5$ nm), which may cross nuclear pores. Besides, the intracellular disassembling of the superstructures explains the remarkable anticancer effect observed. A similar trend was observed after 24 h of incubation (Figure 75a-b). Besides, relative fluorescence intensities calculated by fluorescing micrographs suggest a higher uptake for the MDA-MB-231 cell line (Figure 76c). To understand the role of the HA shell and CD44 receptors in cell internalization, the same experiment was performed under the same conditions on bronchial epithelial cells (16-HBE) negative to CD44 membrane receptors [345]. As expected, the microscope images (Figure 75c) do not show cell uptake in the red channel up to 24 h from the incubation. This experiment suggests that the uptake of these superstructures can preferentially employ the CD44 receptor.

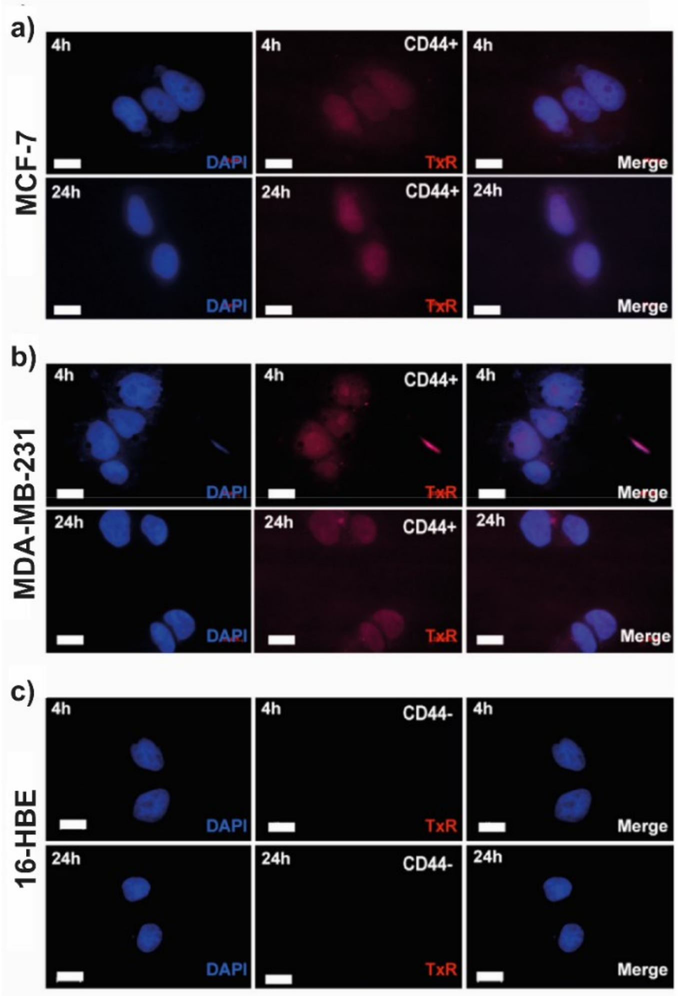

Figure 75. *Uptake study by fluorescence microscopy of HA-g-PLA/HCDs after 4 h and 24 h of incubation on CD44$^+$-cell lines (a-b) (MCF-7 and MDA-MB-231) and CD44$^-$-cell line (c) (16-HBE).*

To validate this hypothesis, cell internalization was evaluated by saturating CD44 receptors with free HA, displacing HA pendants of the HA-g-PLA/HCDs. Thus, both cell lines were pre-incubated with a solution of free HA for 30 minutes and then treated with the nanosystem at the same concentration above explored. After that, the uptake was evaluated by fluorescence microscopy. As seen in Figure 76a-b, the CD44 receptor displacement with free HA completely abolished the red fluorescence intensity also after 24 h of incubation (about 1 % if compared with untreated cells, Figure 76c), confirming that HA-g-PLA/HCDs internalization occurs through a mechanism of CD44 receptor-mediated endocytosis.

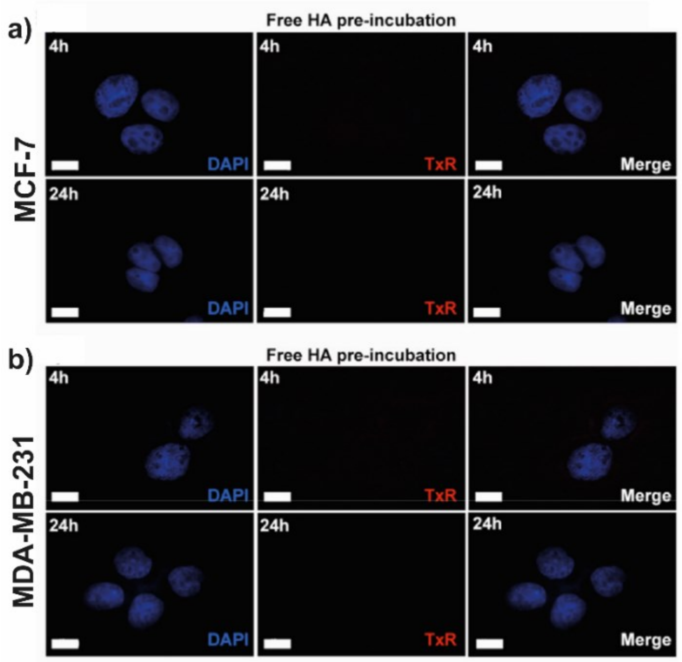

c)

Cells	FL^{4h}_{red} (a.u.)	FL^{24h}_{red} (a.u.)	FL^{24h}_{red} * (a.u.)
MCF-7	585±54	898±41	11±0.1
MDA-MB-231	942±60	1420±97	17±0.3
16-HBE	10±0.4	14±0.8	n.a.

* Cells pre-incubated with free HA (25 μg mL^{-1}) for 24h

Figure 76. *Uptake study by fluorescence microscopy of HA-g-PLA/HCDs after 24 h of incubation on MCF-7 (a) and MDA-MB-231 (b) pre-incubated with free HA.*

4.5.14. Conclusion

In this work, NIR-responsive hybrid nanocomposites (HA-g-PLA/HCDs) were designed as self-assembled nanostructured for targeted drug delivery and image-guided photothermal therapy. The core-shell nanostructures were composed of amphiphilic PLA-grafted hyaluronic acid (HA-g-PLA) encapsulating hydrophobic carbon nanodots (HCDs) into the hydrophobic core. The coating of hyaluronic acid confers targeting ability to the micelle-like nanostructures versus the CD44 receptors overexpressed in cancer cells, favoring the selective accumulation of doxorubicin. Moreover, the biodegradable and biocompatible amphiphilic shell permits the stabilization HCDs in a physiological medium. On the other hand, HCDs allow to impinge fluorescent properties (fluorescent imaging) and photothermal conversion capacity (selective cell death by hyperthermia) to the HA-g-PLA/HCDs nanostructures, but also to maximize the drug loading (DL% > 9) of doxorubicin due to the increased hydrophobic surface and provide a NIR-triggered drug release. The strategic combination of the HCDs and the PLA-grafted hyaluronic acid coating allows for obtaining in a single theranostic nanoplatform a multimodal tool for targeted cancer therapy and monitoring. The HCDs were synthesized by the surface passivation of red-emitting CDs with octylamine and then encapsulated into the hydrophobic core of HA-g-PLA core-shell structures. DLS analyses revealed that the incorporation of HCDs represents an effective strategy to induce the formation of collapsed nanostructures two times smaller (300 nm) than that obtained without HCDs. The biological characterization in vitro proved the biocompatibility and the cell internalization through CD44-mediated endocytosis of HA-g-PLA/HCDs, and demonstrated the capacity of HA-g-PLA/HCDs@Doxo to efficiently combine hyperthermia and NIR-triggered drug release using an 810 nm laser (300 s, 7 W cm^{-2}). The effectiveness of the chemo-photothermal approaches using HA-g-PLA/HCDs@Doxo under NIR-light exposure was also proved by gene expression analysis of regulated cell death (RCD) pathways that demonstrated the activation of necroptosis and apoptosis. Therefore, the strategic design of HA-g-PLA/HCDs@Doxo makes them promising candidates as non-invasive theranostic agents for precise chemo-photothermal eradication of solid tumors, overcoming cancer apoptosis resistances.

4.6. β-Cyclodextrin decorated multicolor N,S-doped carbon nanodots as theranostic nanoplatform for the delivery of sildenafil in breast cancer

The focus of the present work is the design of β-cyclodextrins decorated multicolor carbon nanodots as theranostic nanoplatforms for the delivery of sildenafil in breast cancer therapy. The rational idea is to exploit CD as a fluorescent contrast agent and cyclodextrins for their well-known capability to form host-guest complexes, in order to maximize the drug loading. To fulfill this goal, in a first step highly homogeneous crystalline N,S-doped CDs were synthesized by an innovative solvothermal synthetic route giving rise to high-resolution fluorescence imaging nanotools. Successively, CDs, surface passivated with a short alkyne end-capped PEG_4 by amide coupling, were orthogonally functionalized with modified 6-azido-6-deoxy-β-cyclodextrins by azide-alkyne Huisgen cycloaddition, obtaining a nanoplatform with a well-ordered architecture (CDs-PEG_4-β-Cdx). Afterward, this latter was loaded with sildenafil (CDs-PEG_4- β-Cdx@SD, DL=20.57 % w/w), chosen as an off-label drug for its emerging potential in cancer therapy as an inhibitor of phosphodiesterase 5 (PDE-5). Both CDs-PEG_4- β-Cdx and CDs-PEG_4- β-Cdx@SD were widely characterized in terms of physico-chemical and biological properties. CDs-PEG_4- β-Cdx@SD proved to be a potential nanoplatform in cancer theranostics due to the surprisingly selective anticancer effect on 16-HBE and MCF-7 corresponding to pharmacologically inactive concentrations of sildenafil (Figure 77). This evidence is particularly interesting from the perspective of sildenafil repositioning; however, it needs further investigation in order to understand the pathways involved in the recorded cytotoxic effect.

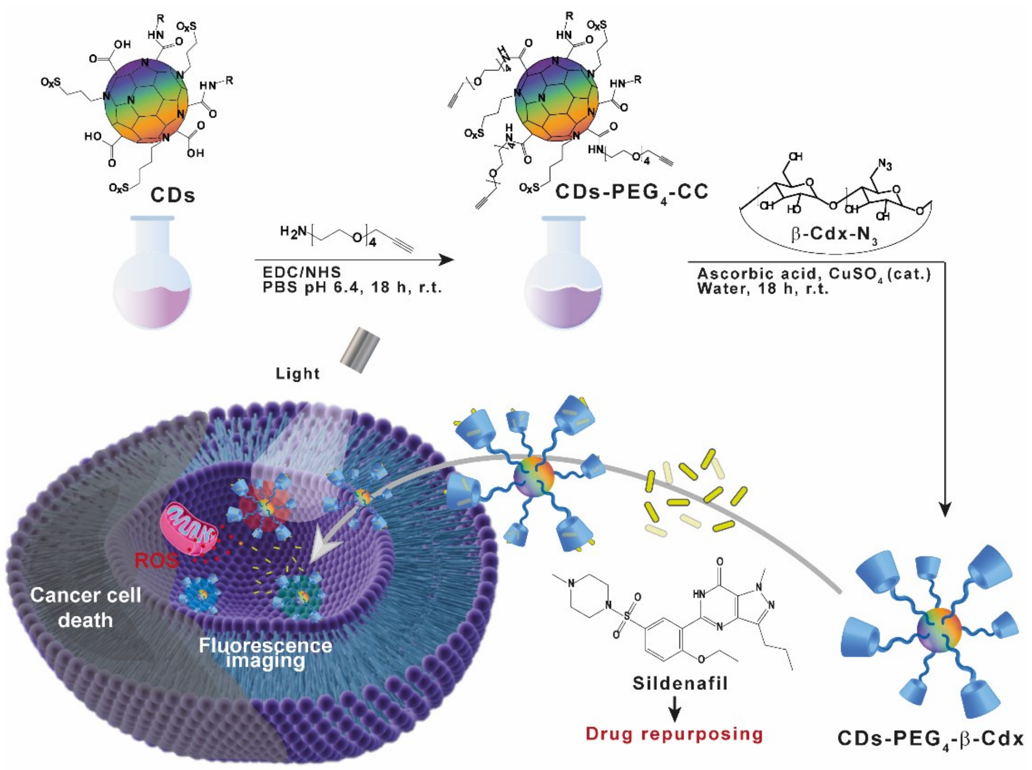

***Figure** 77. Graphical abstract.*

4.6.1. Synthesis and characterization of alkyne-derivate CDs

Carbon Nanodots (CDs) were produced by a modified solvothermal method from urea, citric acid, and indocyanine green (ICG) in DMF, as reported in Section 4.2. [159]. The strategic synthetic scheme was designed to obtain homogeneous crystalline CDs (d = 5.3 ± 0.4 nm) core- and surface-doped with nitrogen and sulfur atoms with improved red fluorescence (QY=4 %) and photothermal conversion capacity (≈ 32 %). Briefly, an equimolar amount of citric acid and urea (core nitrogen doping agent) was exploited as a donor of hydroxyl, carboxyl, and amide surface groups, while a non-stoichiometric amount of ICG (core sulfur doping agent) was used to introduce sulfonate/sulfoxide, surface groups. The subpopulations of CDs were isolated and purified by size exclusion chromatography (SEC) [158], which conducts two different fractions of CDs characterized by a blue/green selective emission and a multicolor emission from the blue to the red region, respectively. For the applicative purposes of this work, it was selected the second fraction for the successive steps of functionalization. The selected N, S co-doped carbon nanodots, named N,S-CDs, were characterized by a versatile and functional surface, particularly rich in carboxyl groups, amenable to further functionalization through the chemistry of carbodiimides. In light of this evidence, the alkyne derivate of CDs, named CDs-CC, was synthesized by amide coupling with a heterodifunctional polyethylene glycol (PEG_{400}) bearing amine and alkyne end-groups. As reported in Figure 78, the PEG-linker was orthogonally conjugated to the N,S-CDs surface exploiting the amine terminals and the surface carboxyl functions, respectively, in presence of N-(3-dimethylaminopropyl)-N′-ethylcarbodiimide (EDC) and N-hydroxysuccinimide (NHS) as coupling agents.

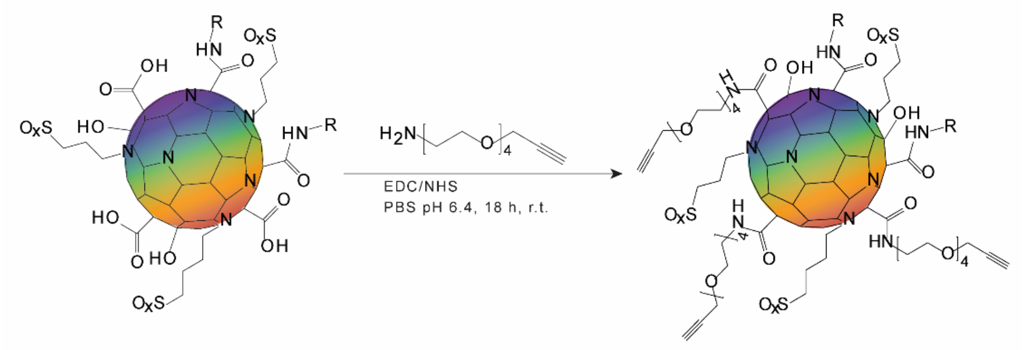

Figure 78. *Synthesis scheme by amide coupling of CDs-PEG_4-CC.*

The effective surface functionalization was evaluated by FT-IR analysis of CDs- PEG_4-CC in comparison to nude N,S-CDs. In Figure 79, N,S-CDs spectra show diverse diagnostic peaks relative to the carboxyl (OH stretching 3420 cm^{-1} and CO stretching 1715 cm^{-1}) and sulfonate/sulfoxide (stretching 1391 and 1283 cm^{-1}) groups. The derivate CDs- PEG_4-CC spectra displayed marked peaks attributable to amide stretching (1641 cm^{-1}) and a reduction of OH stretching (3420 cm^{-1}) relative to carboxyl groups, accompanied by the C-O-C vibrations (1088 cm^{-1}) attributable to the chains of PEG and aliphatic C-H vibrations (2960-2922 cm^{-1}), confirming that the surface PEGylation by amide coupling successfully occurred.

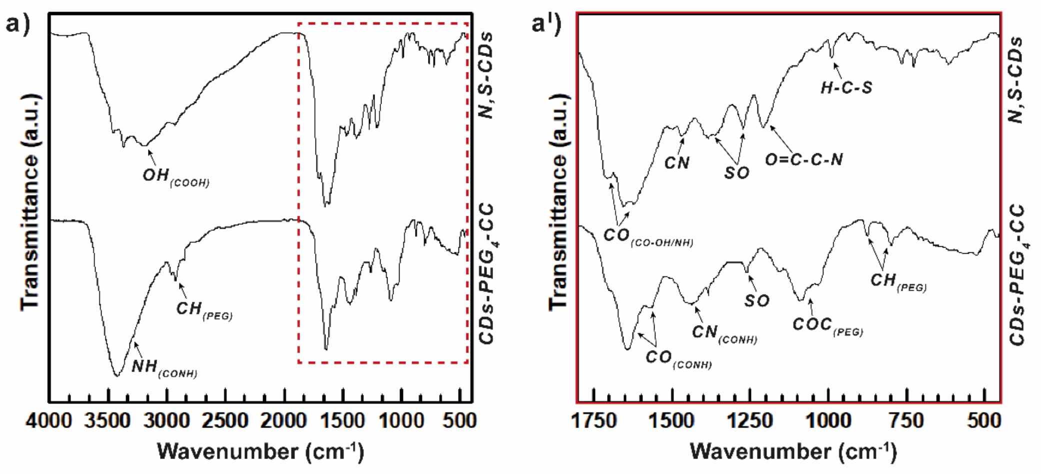

Figure 79. *FT-IR spectra of .N,S-CDs, and CDs-PEG$_4$-CC (a). The focus of FT-IR spectra in the range 450-1800 cm^{-2} (a’).*

4.6.2. Synthesis of 6-deoxy-6-azide-β-cyclodextrin (β-Cdx-N$_3$)

The 6-Monoazide-β-cyclodextrin was synthesized by primary hydroxyl mono-substitution with an azide group through two steps of synthesis. The first step provides the activation of 6-OH by mono-tosylation following a protocol reported in the literature [346]. The 6-O-Monotosyl-β-cyclodextrin (β-Cdx-OTs) was obtained by one-step and reproducible reaction between β-Cdx and p-toluensulfonyl-chloride in aqueous NaOH at pH 11 (Figure 80). The strongly basic reaction medium allowed to solubilize the β-cyclodextrin, avoiding the common use of organic solvents. In alternative to purification by crystallization or precipitation in an organic solvent, which conducts to a low yield and degree of purity, it was exploited the lower aqueous solubility of β-Cdx-OTs than that of β-Cdx and p-toluenesulfonic acid by the use of cationic exchange resin. In detail, the addiction of resin in the H$^+$ form induces the rapid acidification of the reaction solution by exchanging the H$^+$ with sodium cations of NaOH solution inducing the efficient precipitation of β-Cdx-OTs. Successively, the exchange resin was removed by filtration, while the non-reacted reagent and subproduct of activation were eliminated by washing the precipitate with water. Subsequently, β-Cdx-N$_3$ was synthesized by treating the β-Cdx-OTs with an excess of sodium azide in order to promote nucleophilic substitution of the p-toluensulfonic group with the azide group, according to reference protocol [347].

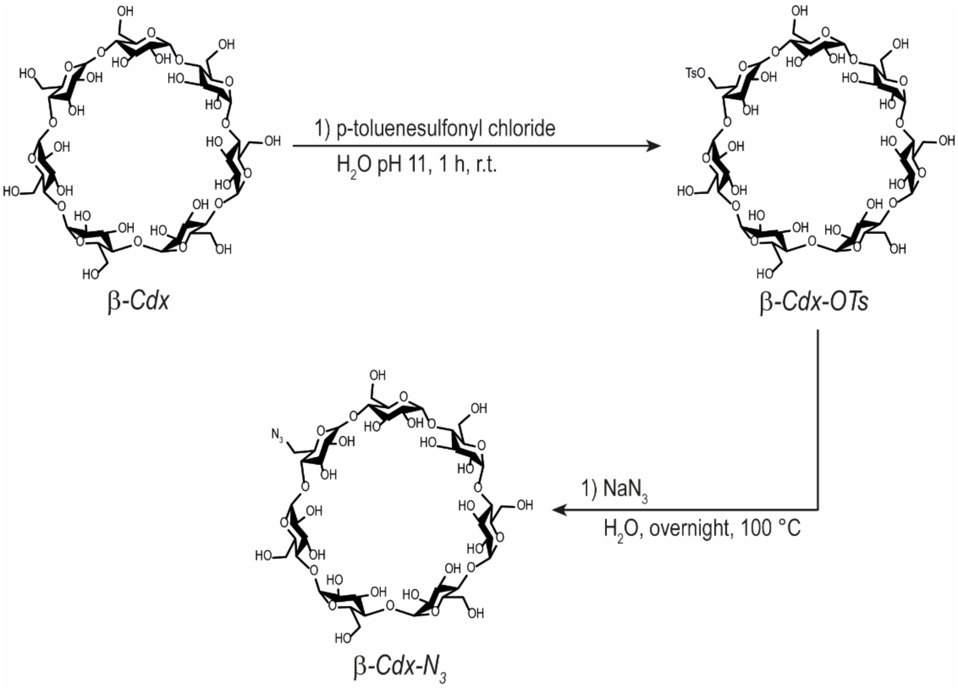

Figure 80. *Synthesis scheme of β-Cyclodextrin-tosyl (β-Cdx-Ots) and β-Cyclodextrin-azide (β-Cdx-N_3).*

4.6.3. Chemical characterization of β-Cdx-N_3 and intermediate

The effective mono-tosylation of β-Cdx-N_3 was confirmed by ^{1}H-NMR analysis (Figure 81). The β-Cys-OTs spectra showed peculiar droplet peaks of aromatic protons at 7.74-7.72 and 7.43-7.40 ppm, and a singlet peak of methyl at 2.41 ppm attributable to the p-toluenesulfonic group, which confirms the functionalization efficiently occurred. The mono-substitution was verified by comparing the integral of the peak at 2.41 ppm with that of the anomeric proton at 4.83-4.76 ppm. The integral ratio corresponds to 7:1 confirming the tosylation of a single D-glucopyranose residue. Furthermore, taking into account that the tosyl group has a deshielding effect on neighboring hydrogens, it was evaluated the shift to lower fields of the proton peaks of the derivatized $C6^I$ and the adjacent $C5^I$ to confirm the substitution of the seven primary hydroxyl group. Effectively, it was observed the downfield peak shift at 4.33-4.29 ppm for the two protons of $C6^I$ and at 4.18 ppm for the proton of $C5^I$ [347].

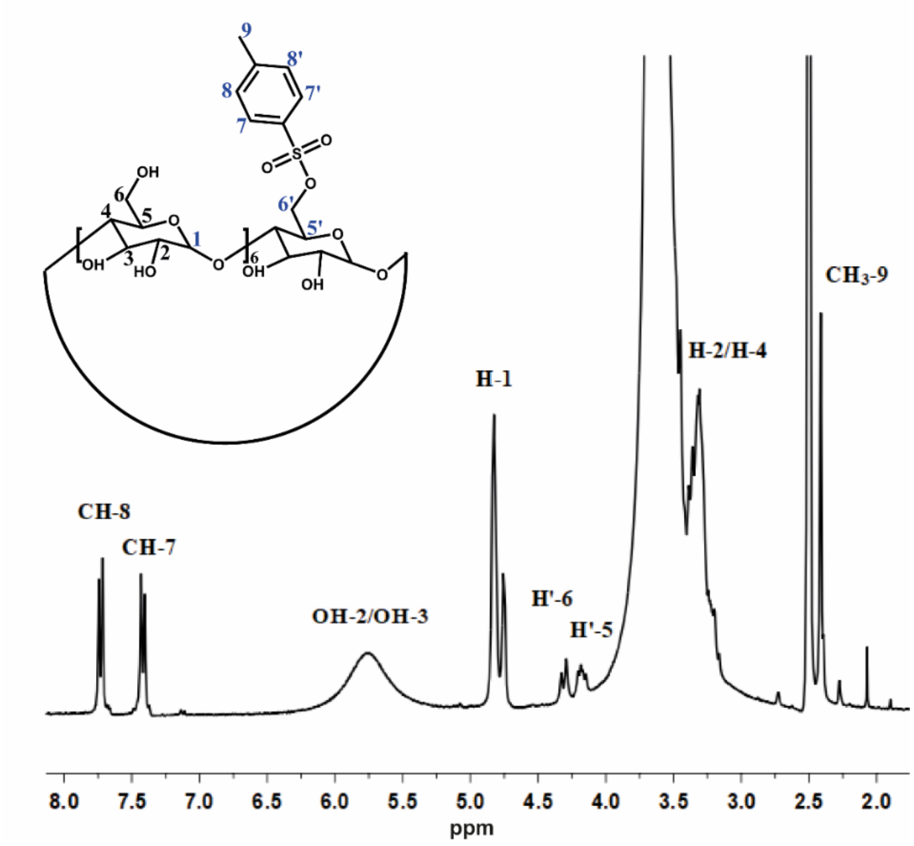

Figure 81. *^{1}H-NMR of β-Cyclodextrin-tosyl (β-Cdx-Ots) (300 MHz, DMSO-d$_6$).*

The nucleophilic substitution was also confirmed by ^{1}H-NMR analysis (Figure 82). The ^{1}H-NMR spectrum of the product does not have the characteristic peaks of the p-toluenesulfonic group shown in Figure 81. In order to verify the actual monosubstitution of the p-toluenesulfonic group with the azide group, a comparison was made between the peak at 4.82 ppm associated with the anomeric hydrogen (H1) and the peak at 4.57 ppm attributed to the hydrogen of the hydroxyl in position six. It was calculated that the ratio of the integrals related to the hydrogen and hydroxyl peaks is 7:6, therefore, out of 7 monomers of the cyclodextrin only six have the hydroxyl in position six.

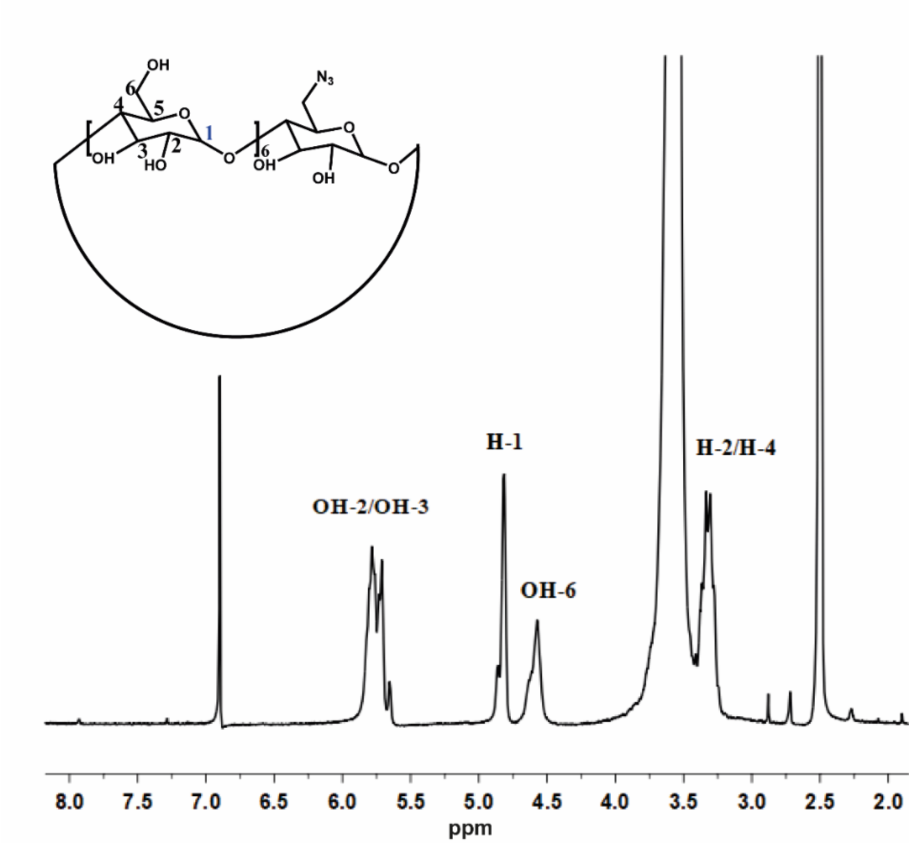

Figure 82. *^{1}H-NMR of β-Cyclodextrin-azide (β-Cdx-N_3) (300 MHz, DMSO-d_6).*

4.6.4. Synthesis of hybrid nanosystems CDs-PEG$_4$-β-Cdx

The conjugate between CDs and Cyd was obtained by Huisgen 1,3-dipolar Cu(I)-catalyzed cycloaddition between the alkyne functions of CDs and the azide groups of the modified cyclodextrins. The cycloaddition reaction leads to the formation of 1, 2, 3 triazole rings by click chemistry characterized by mild reaction conditions and high yield (>98 %) (Figure 83). Specifically, the copper-catalyzed cycloaddition variant was chosen because it is found to be regioselective and very rapid. In addition, the selective formation of the triazole ring between the azide at the C6 position of the Cyd and the alkyne-terminal extremities of the PEG-alkyne chains of the carbon nanodots was ensured by the presence of only one azide group available for binding to the alkyne functions.

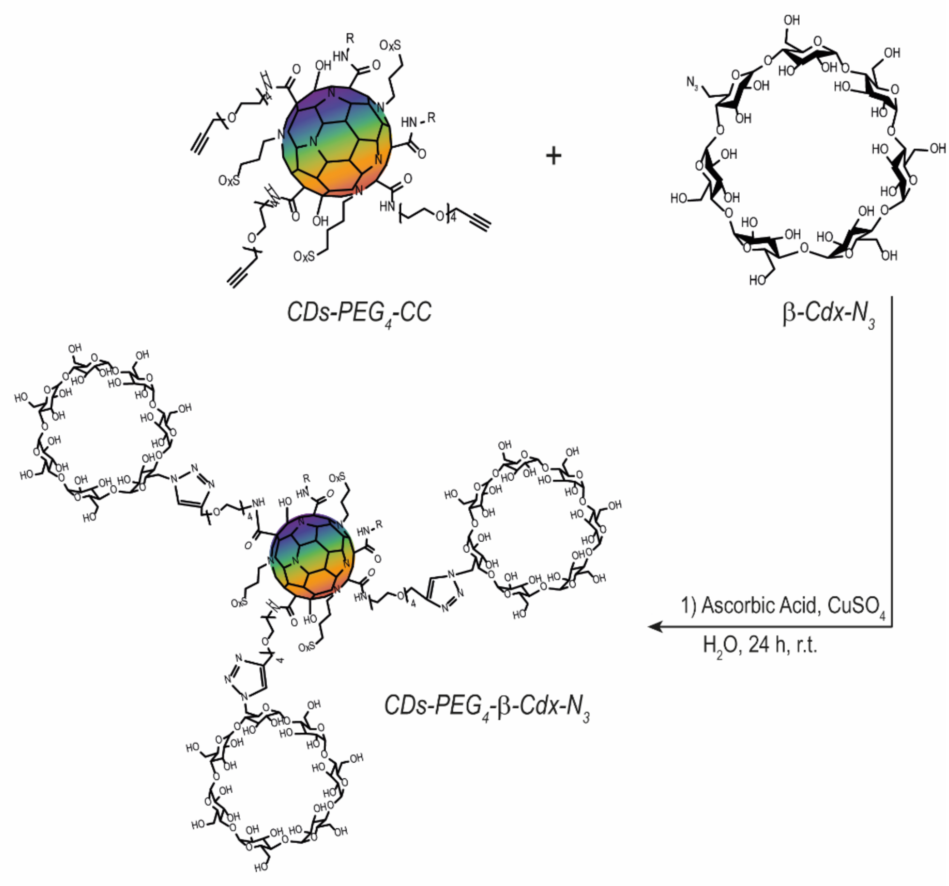

Figure 83. *The synthesis scheme of CDs-PEG$_4$-β-Cdx conjugate.*

This synthesis scheme resulted in an ordered structure in which each carbon-based core is diametrically functionalized on the surface with modified cyclodextrins. The rational introduction of cyclodextrins to the surface plays a dual role, stabilizing carbon nanodots on the surface in an aqueous environment and maximizing the amount of active ingredient that can be incorporated and delivered to the target site.

4.6.5. Physico-chemical characterization of CDs-PEG$_4$-β-Cdx

In order to verify conjugate formation and evaluate its composition, differential scanning calorimetry coupled with thermogravimetric analysis (DSC/TGA) of both conjugate and precursors was performed (Figure 84). As shown in Figure 83a, the conjugate undergoing to different transformations than both precursors, indicating that the conjugation resulted in the formation of a new chemical entity through the establishment of new covalent bonds. In detail, cyclodextrins undergo thermal decomposition only from 230 °C, corresponding to the loss of 60 % of total mass (Figure 84b). This phenomenon is attributable to the loss of surface functional groups. On the other hand, Pegylated CDs show a typical melting decomposition at 130 °C, considering that an endothermic peak without corresponding weight loss is observed, soon after accompanied by a sudden weight loss from 180 °C to 550 °C. However, the thermal curve of the conjugate shows a trend comparable to that of the CDs-PEG$_4$-CC, but with some small differences. By comparing the DSC and TGA data, it is possible to determine the percentage by weight of the conjugate cyclodextrins by evaluating the weight loss recorded in the conjugate corresponding to the cyclodextrin endothermic degradation. This analysis shows that cyclodextrins constitute 55% w/w of the CDs-PEG$_4$-Cdx sample.

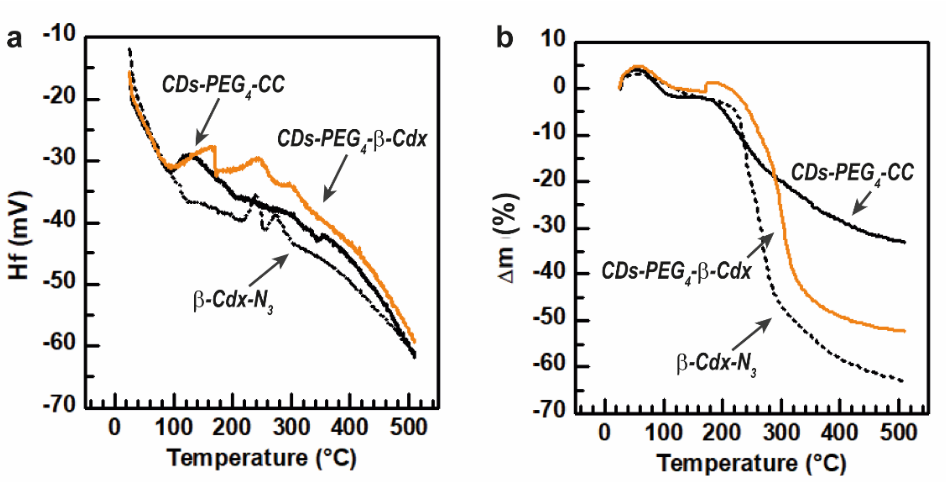

Figure 84. *DSC coupled TGA analysis of CDs-PEG$_4$-CC, β-Cdx-N$_3$, and CDs-PEG$_4$-β-Cdx.*

The conjugate CDs-PEG$_4$-Cdx was characterized from a dimensional point of view by atomic force spectroscopy (AFM) (Figure 85a-a'). The AFM images show that the conjugates have an average diameter of 8.15 nm. Taking into account that the carbon core has an average diameter of 5 nm and that the cyclodextrins have an average external diameter of 1.5 nm, the diameter increase of about 3 nm is compatible with the presence of cyclodextrins distributed on the surface of the carbon core (Figure 85b). Indeed, the increased average size over 5 nm is particularly desired for drug delivery systems to avoid premature and rapid filtration by the glomerular basement membrane (cut-off 5 nm) and renal excretion. Slow renal excretion of the nanocarrier allows a major half-life and an increased possibility to reach high concentrations in tumor tissues to prevent MDR phenomena.

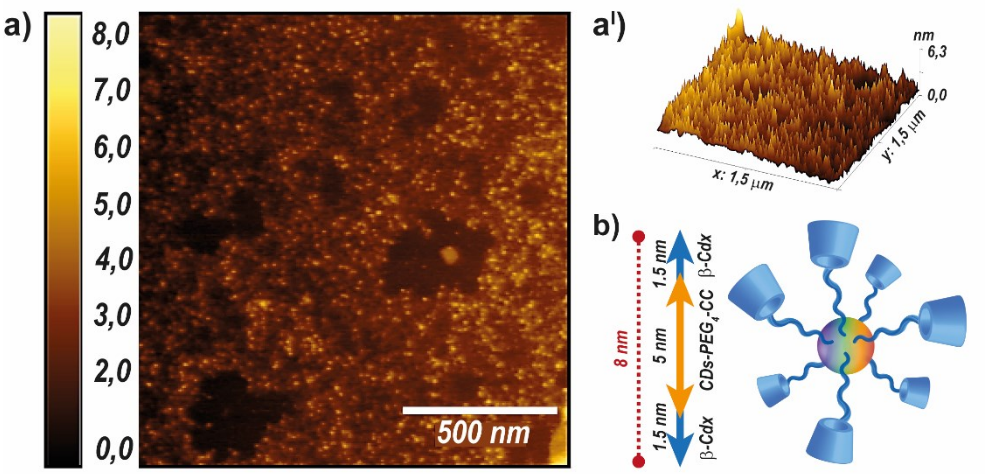

Figure 85. *AFM micrographs of CDs-PEG$_4$-β-Cdx (a-a'). Schematic representation of CDs-PEG$_4$-β-Cdx architecture (b).*

4.6.6. Optical characterization of CDs-PEG$_4$-β-Cdx and intermediates

The CDs sample displays a complex optical absorption spectrum in the entire UV/vis range with several peculiar bands at 350 nm, 463 nm, and 543 nm with a shoulder at 645 nm (Figure 86). After PEGylation (CDs-PEG$_4$-CC) and conjugation with β-Cdx-N3 (CDs-PEG$_4$-β-Cdx) the absorption spectra preserve the typical profile of native CDs, but with some differences. In particular, it is possible to observe a minor ratio I_{350nm}/I_{463nm} and I_{350nm}/I_{543nm}, due to the reduced intensity of the peak in the blue region at 350 nm (Figure 86a). Following the absorption spectra, as reported in Figure 86b, the fluorescence spectra of CDs-PEG$_4$-β-Cdx and intermediates were recorded upon excitation at 360 nm and 540 nm. Effectively, the PEGylation leads to a moderate reduction of the blue emission at about 450 nm which is observed in both CDs-PEG$_4$-CC and CDs-PEG$_4$-β-Cdx. Indeed, it is interesting to highlight a red shift of the emission band under excitation at 540 nm of about 30 nm and a more pronounced shoulder at 639 nm in the CDs-PEG$_4$-β-Cdx sample. Therefore, the changed profile of the absorption spectra effectively reflects the emission profile of the samples. As evidenced in the literature [2,158,182], the emission phenomena involve the surface state of CDs, explaining well the different absorption and emission behaviors after PEGylation and successive conjugation with β-Cdx. The preservation of the multicolor emission profile and the improved fluorescence in the red region of the final conjugate is particularly interesting in light of the applicative purpose of the present work.

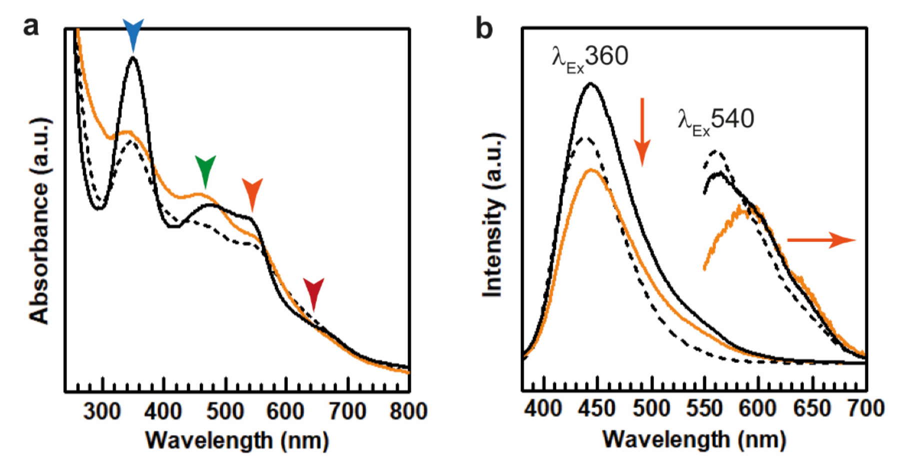

Figure 86. *UV spectra (a) and emission spectra under excitation at 360 and 540 nm (b) of nude CDs (dotted black lines), CDs-PEG$_4$-CC (compact black lines), and CDs-PEG$_4$-β-Cdx (compact orange lines).*

4.6.7. Preparation of Sildenafil-loaded CDs-PEG$_4$-β-Cdx (CDs-PEG$_4$-β-Cdx@SD)

β-Cyclodextrin (β-Cdx), a cyclic oligosaccharide consisting of seven glucose units linked by 1-4 glycoside bonds, is well-known for its capacity to form inclusion complexes with a plethora of hydrophobic drugs by including them in the hydrophobic cavity [348,349]. The driving forces for the formation of the complex β-Cdx/drugs include the enthalpic contribution of the water molecules released from the cavity of the β-Cdx, electrostatic, Van der Waals, and hydrophobic interactions, and hydrogen bonds [350]. Therefore, the rational conjugation of modified β-Cdx on the surface of CDs-PEG$_4$-CC was performed in order to improve the aqueous solubility and dissolution rate of poorly soluble drugs, improving the delivery of a functional amount of drug to the targeted site.

Here, sildenafil citrate was proposed as an off-label drug, due to the increasing interest in the repurposing of phosphodiesterase-5 (PDE-5) inhibitors in cancer therapy [351,352]. The mechanism of action of sildenafil consists in the inhibition of PDE5 that mediates the hydrolysis of cyclic guanosine monophosphate (cGMP) to guanosine monophosphate (GMP), resulting in the increased cellular concentration of cGMP and consequent activation of GMP-dependent protein kinase (PKG) [353–355].

Nowadays, selective PDE-5 inhibitors like sildenafil was approved by the EMA and FDA in the treatment of erectile dysfunction and pulmonary arterial hypertension [352].

However, there are increasing studies that demonstrate the potential use of sildenafil in cancer therapy firstly as chemo-adjuvants in combination with diverse conventional anticancer approaches (e.g. radiotherapy, chemotherapy), but also alone as an emerging anticancer drug [356–359]. Some works proposed the employment of sildenafil as an adjuvant of doxorubicin in the treatment of diverse cancer diseases (e.g. breast cancer, prostate cancer, colorectal cancer), demonstrating a useful strategy to improve the cytotoxic effect of doxorubicin [360–363]. Another study proposed the use of sildenafil in monotherapy for the treatment of B-cell lymphoma demonstrating that sildenafil can induce cell death through caspase dependent-apoptosis [364]. In ref. [358] high concentrations of sildenafil were tested in vivo for the treatment of colon cancer, reporting a moderate cytotoxic effect and a reduction of tumor size after treatment with a high dosage. Therefore, in this work the designed hybrid nanoparticle of CDs-PEG$_4$-β-Cdx was employed for the delivery of sildenafil in cancer treatment. Sildenafil was loaded into β-Cdx cavities of the CDs-PEG$_4$-β-Cdx by kneading method exploiting a mixture of ethanol/water which evaporates during the mixture to favor the encapsulation of the drug. The drug loading approach and the introduction of cyclodextrins as a complexing element allow obtaining a high drug loading of about 20.57 % corresponding to an encapsulation efficiency of 87.50 % among the percentage of cyclodextrin in the final conjugate (CDs-PEG$_4$-β-Cdx@SD).

4.6.8. Study of drug release in physiological conditions

The drug release kinetic from CDs-PEG$_4$-β-Cdx@SD was evaluated in PBS pH 7.4 containing 1 % Tween 80 in order to improve the solubility of sildenafil citrate. The kinetic of drug release was obtained by plotting the amount of sildenafil citrate released in the function of time (Figure 87). The obtained cumulative drug release kinetic showed slow and controlled release over time of CDs-PEG$_4$-β-Cdx@SD, reaching the plateau after 24 h up to 48 h corresponding to the drug release of about 48 %. On the contrary, after 24 h of incubation, 90 % of free sildenafil diffused through the dialysis membrane. It is also important to note a burst effect in the case of free sildenafil as evidenced by the 65 % of diffusion after only 4 h of incubation corresponding to 25 % more than the drug release from CDs-PEG$_4$-β-Cdx@SD. Therefore, the CDs-PEG$_4$-β-Cdx@SD allows for maximization of the sildenafil drug loading, but also to obtain a controlled and prolonged release over time of sildenafil.

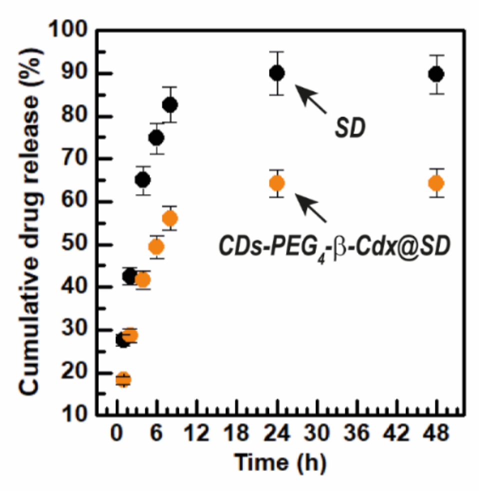

Figure 87. *The cumulative drug release profile of CDs-PEG$_4$-β-Cdx@SD and diffusion profile of free sildenafil (SD) in PBS pH 7.4 with 1 % of Tween 80.*

4.6.9. Uptake study on 2-D cell model in vitro

The capacity of internalization and the consequent intracellular localization of CDs-PEG$_4$-β-Cdx was evaluated on MCF-7, 16-HBE, and NHDF after 24 h of incubation, by fluorescence microscopy in a multichannel fashion. As reported in Figure 88, a marked contrast in fluorescence was observed in all channels demonstrating a good internalization of CDs-PEG$_4$-β-Cdx in all cell lines. However, some differences in terms of intracellular localization were observed comparing the three different cell lines. In particular, a nuclear localization was evidenced only in the MCF-7 cell line (Figure 88a-a^{V}) accompanied by a vesicular localization as particularly evidenced in the channel of dapi (Figure 88a). In contrast, in NHDF and 16-HBE it was highlighted a cytoplasmatic localization (Figure 88b-c^{V}). However, it is possible to observe a cytoplasmic diffuse fluorescent signal in NHDF (Figure 88c-c^{V}), which is not observed in 16-HBE (Figure 88b-b^{V}). Therefore, it is possible to hypothesize that, similarly to MCF-7, the system in 16-HBE is mainly associated with vesicles, while in NHDF it is widely distributed in the cytosol. This hypothesis is also supported by the micrographs in brightfield evidencing numerous vesicles formation (Figure 88a^{IV}, b^{IV}).

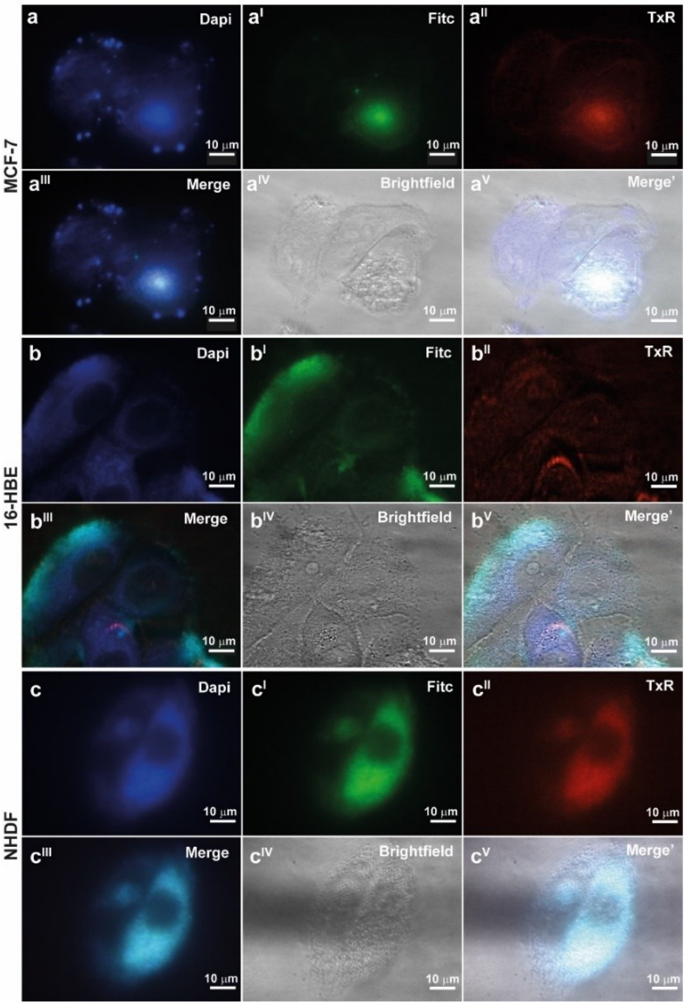

Figure 88. *Uptake study of CDs-PEG$_4$-β-Cdx after 24 h of incubation.*

4.6.10. Cytocompatibility assay and cytotoxicity study of CDs-PEG$_4$-β-Cdx@SD in vitro

The cytocompatibility of CDs-PEG$_4$-β-Cdx and the cytotoxicity profile of CDs-PEG$_4$-β-Cdx@SD were evaluated on MCF-7, 16-HBE, and NHDF after 24 h and 48 h of incubation. As illustrated in Figure 89, some differences in terms of CDs-PEG$_4$-β-Cdx cytocompatibility were revealed between the diverse cell lines tested. After 24 h of incubation on 16-HBE, the system showed good cytocompatibility in the whole range of concentrations tested. Conversely, a moderate reduction in cytocompatibility was evident at the two highest concentrations tested on MCF-7 and NHDF. This trend was also shown after 48 h of incubation on MCF-7 and NHDF, while on 16-HBE it is possible to observe a change in the cytocompatibility profile with moderate cytotoxicity even at lower concentrations (Figure 89a').

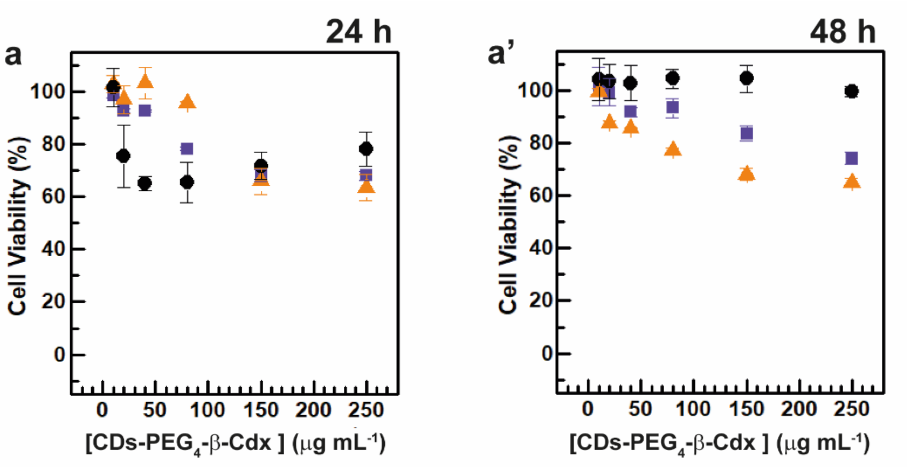

Figure 89. *Cytocompatibility assay of CDs-PEG$_4$-β-Cdx on MCF-7 (black circle), 16-HBE (violet square), and NHDF (orange triangle) after 24 h and 48 h of incubation.*

According to the literature, the use of sildenafil alone in this concentration range did not show any cytotoxic effect in any cell line tested. Surprisingly, after 24 h and 48 h of incubation (Figure 90), the cells treated with the CDs-PEG$_4$-β-Cdx@SD show an important cytotoxic effect, especially in the MCF-7 and 16-HBE cell lines. In particular, there is a significant difference in terms of cytotoxic effect between the cells treated with free sildenafil and those with CDs-PEG$_4$-β-Cdx@SD at the two highest drug concentrations tested.

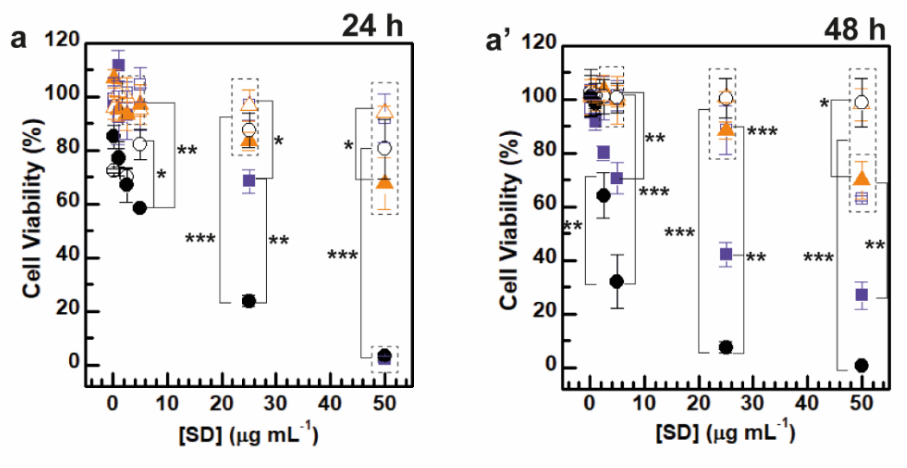

Figure 90. *Cytotoxicity study of CDs-PEG$_4$-β-Cdx@SD (close symbols) and free SD (open symbols) on MCF-7 (black circle), 16-HBE (violet square), and NHDF (orange triangle) after 24 h and 48 h of incubation.*

This is particularly evident comparing the IC_{50} values extrapolated from the cytotoxicity profiles (Table 8). In detail, similarly to all cell lines treated with free sildenafil, the NHDFs treated with the CDs-PEG$_4$-β-Cdx@SD never reach the IC_{50} value within the range of tested concentrations. On the contrary, in MCF-7 and 16-HBE was highlighted a potential antitumor effect corresponding to an IC_{50} value at 24 h equal to 6 and 35 µm mL^{-1}, respectively, and approximately halved to 3 and 19 µm mL^{-1} after 48 h.

Table 8. *IC_{50} values of CDs-PEG$_4$-β-Cdx, CDs-PEG$_4$-β-Cdx@SD, and free sildenafil on NHDF, 16-HBE, and MCF-7 after 24 and 48 h of incubation.*

Cell lines	Samples	IC_{50}^{24h}	IC_{50}^{48h}
NHDF	CDs-PEG$_4$-β-Cdx	> 250 µg mL^{-1}	> 250 µg mL^{-1}
	CDs-PEG$_4$-β-Cdx@SD	> 50 µg mL^{-1}	> 50 µg mL^{-1}
	Sildenafil (SD)	> 50 µg mL^{-1}	> 50 µg mL^{-1}
16-HBE	CDs-PEG$_4$-β-Cdx	> 250 µg mL^{-1}	> 250 µg mL^{-1}
	CDs-PEG$_4$-β-Cdx@SD	6 µg mL^{-1}	3 µg mL^{-1}
	Sildenafil (SD)	> 50 µg mL^{-1}	> 50 µg mL^{-1}
MCF-7	CDs-PEG$_4$-β-Cdx	> 250 µg mL^{-1}	> 250 µg mL^{-1}
	CDs-PEG$_4$-β-Cdx@SD	35 µg mL^{-1}	19 µg mL^{-1}
	Sildenafil (SD)	> 50 µg mL^{-1}	> 50 µg mL^{-1}

In order to understand this selective cytotoxic effect observed on MCF-7 and 16-HBE, firstly it is important to underline the cellular profile of 16-HBE. 16-HBE, also known as 16-HBE14o, is an SV40-immortalized human bronchial epithelial cell showing different cell growth, epithelial morphology, and functions than that of human normal bronchial epithelial cells (HNBEC). As reported in diverse studies in the literature, 16-HBE cannot be compared to normal cells, but rather it is proposed as an ideal model for understanding airway pathology and disease like cystic fibrosis [365,366]. Therefore, the cytotoxic effect recorded on MCF-7 and 16-HBE treated with CDs-PEG$_4$-β-Cdx@SD can be traduced to an anticancer effect (Figure 90). As previously anticipated, sildenafil as an inhibitor of phosphodiesterase 5 (PDE-5) promotes cGMP/NO accumulation and the successive activation of cGMP-dependent protein kinase (PKG) [352,353,359]. Different PDE isoenzymes have been proposed as cancer therapeutic targets, but in particular high levels of PDE-5 have been found in different types of cancer such as breast cancer, colorectal cancer, leukemia, and prostate cancer [355,367]. Moreover, diverse evidence indicates that the cGMP signaling pathway is aberrantly regulated in diverse cancers, including breast cancer, suggesting that the axes PDE-5/cGMP/PKG could be a potential target with anticancer outcomes. In particular, PKG activation has been recognized as an apoptotic effector through its interaction with β-catenin whose over-activation diminished cell growth and induced apoptosis of cancer cells [353,359]. However, the use of sildenafil alone at this concentration is not correlated to a cytotoxic effect (Figure 89) [356–358,368] In light of these considerations, it is possible to hypothesize that the selective cytotoxic effect on abnormal cell lines like MCF-7 and 16-HBE could be ascribed to a combinatorial effect of sildenafil and nanocarrier. More in detail, in previous work it was demonstrated that the N,S-doped CDs employed in the preparation of CDs-PEG$_4$-β-Cdx show an intrinsic anticancer effect due to its capacity to interact with mitochondrial membranes inducing an increased ROS generation and consequent cancer cell death (Section 4.2.) [159]. It is possible to assume that this activity will be preserved also after functionalization in CDs-PEG$_4$-β-Cdx@SD. Therefore, similarly to the mechanism of action proposed to explain the increased anticancer effect of doxorubicin (able to induce ROS production) in combination with sildenafil, the selective anticancer effect of CDs-PEG$_4$-β-Cdx@SD could be ascribed to crosstalk between the induced-high level of ROS and NO [359,369]. In conclusion, the anticancer effect of CDs-PEG$_4$-β-Cdx@SD on MCF-7 and 16-HBE could be ascribed to the high levels of NO and ROS induced by sildenafil and CDs-PEG$_4$-β-Cdx, respectively, that can conduct to the generation of cytotoxic molecule of peroxy-nitrate [370,371]. The CDs-PEG$_4$-β-Cdx nanosystem would therefore play a triple role, as a drug delivery system, contrast agent in fluorescence, and cytotoxic agent, paving the way for a new idea of combined therapy with sildenafil. However, this study requires further investigation in order to confirm the effective crosstalk between NO and ROS or to better understand the origins of selective cytotoxicity induced by CDs-PEG$_4$-β-Cdx@SD.

4.6.11. Conclusion

In this work, hybrid nanosystems were developed by the surface functionalization in two steps of N,S-doped CDs with modified β-cyclodextrin (CDs-PEG$_4$-β-Cdx). The nanostructures were synthesized adopting a convergent scheme of synthesis which allows obtaining an ordered architecture composed of β-cyclodextrin diametrically distributed on the CDs surface. The rational design of CDs-PEG$_4$-β-Cdx efficiently combines the multicolor fluorescence properties of CDs with the well-known capability of β-Cdx to form host-guest complexes with hydrophobic drugs, as demonstrated by the elevated drug loading (up to 20 %). Here, sildenafil was chosen as a repurposing drug in the treatment of breast cancer. Surprisingly, the study of cytotoxicity in vitro on three different cell lines (MCF-7, 16-HBE, and NHDF) highlighted an effective anticancer effect on MCF-7 and 16-HBE at a low dosage which was not evidenced on normal cells such as NHDF. Moreover, the anticancer profile revealed for sildenafil-loaded CDs-PEG$_4$-β-Cdx (CDs-PEG$_4$-β-Cdx@SD) was not observed in no cell lines treated with free sildenafil. These promising data suggest a selective anticancer effect of sildenafil delivered by CDs-PEG$_4$-β-Cdx. Although the present work needs further investigations, it is possible to hypothesize that the cytotoxic effect recorded is due to the combination of the ability of sildenafil to induce an increment of NO and the increased production of ROS caused by N,S-doped CDs in cancer cells. The cross-talk between NO and ROS could explain the recorded selective cytotoxic effect of CDs-PEG$_4$-β-Cdx@SD, but it needs deeply further investigation. This hypothesis could pave the way for the development of innovative combined therapies with sildenafil that do not involve the use of a conventional chemotherapy drug.

5. Research contributions

The design of several synthetic pathways from different combinations of reagents has allowed exploring the potential of nitrogen-doped and nitrogen-sulfur-codoped carbon nanodots with a characteristic structural, optical, and biological profile. In particular, the key role of operating pressure on the profiling of CDs was studied, demonstrating for the first time the possibility of promoting the formation of highly homogeneous, red-fluorescent CDs with peculiar photothermal conversion properties by performing the synthesis at high-pressure values ($P>18.5$ bar). The second pre-posed goal was to overcome one of the biggest application limitations of CDs such as extremely low yields, typically < 3 % w/w. To this end, a new and efficient purification scheme was developed that resulted in the highest yield reported in the literature of 44.78 % w/w, offering the possibility of synthesizing CDs on a large scale. In a successive work, it was developed a novel surface functionalization strategy by transesterification, takes advantage of the melting-extrusion process for the first time. The extrusion-induced transesterification was demonstrated to be an efficient, scalable, and industrialize method useful as a strategy to modulate the surface and optical profile of CDs and prepare nanosystems and nanocomposites. Finally, through the design of hybrid nanostructures (e.g., polymeric nanoparticles, polymeric core-shell structures, modified cyclodextrin conjugates) for the delivery of different classes of drugs (e.g. irinotecan, doxorubicin, sildenafil), the applicative potential of CDs has been successfully expanded, demonstrating the potential of proposed nanoplatforms to combine fluorescence imaging and combined therapeutic approach (e.g., N,S-CDs-induced ROS production, photothermal therapy and/or chemotherapy) in the treatment of breast cancer

6. Experimental Part

6.1. Pressure-dependent synthesis of N-doped carbon nanodots as a tool to modulate their physico-chemical and optical profile

6.1.1. Materials

Citric acid (99.5 %), urea (99 %), N, N-dimethylformamide (DMF), Sephadex® G-25 and G-15, ethyl acetate (Chromasolv), dialysis tubing (MWCO 2 kDa) was purchased from Sigma Aldrich (Milan, Italy). MDA-MB-231 cell lines were purchased from Sigma Aldrich (Milan, Italy) and cultured in supplemented Dulbecco's Minimum Essential Medium (DMEM) (EuroClone, Milan, Italy) supplemented with 10 % fetal bovine serum (FBS, EuroClone, Milan, Italy) 1 % of penicillin/streptomycin (10,000 U mL^{-1} and 10 mg mL^{-1} respectively, Euroclone, Milan, Italy) and 1 % of L-glutamine (EuroClone, Milan, Italy), at 37 °C in 5 % CO_2 humidified atmosphere. Cell Titer 96 Aqueous One Solution Cell Proliferation assay (MTS solution) was purchased from Promega (Madison, WI, USA).

6.1.2. Synthesis of N-doped Carbon Nanodots (CDs)

Carbon Nanodots were prepared from urea (20 g, 99.83 mmol) and citric acid (10 g, 15.62 mmol) in 100 mL of DMF in solvothermal conditions at 160 °C for 4 h. The synthesis was replicated at three different pressure conditions, 8 bar, 13 bar, and 18.5 bar, due to the use of an autoclave (Büchi AG, Miniclave steel type 3, Gschwaderstrasse, Switzerland) which allows for modulating the reaction pressure. At the different pressure conditions, three types of CDs were obtained, named $CDs_{18.5bar}$, $CDs_{13bar,}$ and CDs_{8bar}. The products were treated in the same way. The reaction was cooled down to room temperature and the product was precipitated drop by drop in 300 mL of ethyl acetate under stirring. The precipitate was retrieved by centrifuging at 10.000 rpm and 25 °C for 15 min. The powder was dispersed in water by cycles of sonication (15 min × 3) and filtered on a 0.2 μm membrane filter by Buckner funnel. Successively, in the first step, the $CDs_{18.5bar}$, CDs_{13bar} were purified by gel permeation chromatography (GPC) with a column packed in turn with Sephadex G-25. Then, the fractions of $CDs_{18.5bar}$, $CDs_{13bar,}$ and CDs_{8bar}, showing a red fluorescence were selected and unified, respectively. In a second step, crude CDs_{8bar} and the selected fractions of $CDs_{18.5bar}$ and CDs_{13bar} were purified by size exclusion chromatography (SEC) using a glass column (100 cm length, 1.5 cm diameter) packed in turn with Sephadex G-25 and G-15. Fractions collected for each sample were combined according to the optical properties and subsequently freeze-dried.

6.1.3. Physico-chemical characterization of N-doped CDs

Atomic force microscopy (AFM) was employed to evaluate the size distributions of the $CDs_{18.5bar}$, CDs_{13bar}, and CDs_{8bar}. Samples were deposited on a mica substrate and then dried in a vacuum. The measurements were performed in air with a Bruker FAST-SCAN microscope working in soft tapping mode using a FAST SCAN A probe (Billerica, MA, USA) having a triangular shape, nominal tip radius of 5 nm and nominal spring constant of 17 N/m. The tip velocity on the surface and the PID gains were optimized to give a higher scan rate compatible with a reliable scan of the surface. The optimal tip velocity was found to be 20 $\mu m\ s^{-1}$. The scan size was fixed at a value of 5 μm × 5 μm. To obtain a reliable estimation of the size distribution of the nanoparticles, a large number of them were obtained from the images and singly analyzed. The analysis consisted of the estimation of the height of the particle concerning the background plane and consequently, considering only well-isolated nanoparticles. In particular, the height was estimated by assessing the section of the AFM surface along a line throwing the highest point of the nanoparticle. The surface functional groups of CDs were studied by Fourier transform infrared (FTIR) using a PerkinElmer Spectrum Two™ IR spectrometer (Waltham, MA, USA). Samples were prepared as pellets of KBr and then dried in a vacuum for analysis.

6.1.4. Optical characterization

The absorption properties of each fraction of $CDs_{18.5bar}$, CDs_{13bar}, and CDs_{8bar} were assessed using a double beam spectrophotometer (JASCO V-560, Tokyo, Japan), recording the spectra in the range of 200–700 nm. The fluorescence emission properties were identified by an intensified CCD camera (FLIR T1K/T1020, Wilsonville, OR, USA) under 600 nm laser excitation. The optical analysis was performed on diluted aqueous dispersions of CDs in a 1 cm cuvette. Based on the absorption and emission spectra, the fraction of each synthesis with the best red emission under excitation at 600 nm was selected.

The photothermal capacity of the selected fractions of CDs was evaluated by exciting an aqueous dispersion of CDs (0.2 mL, 0.1 mg mL^{-1}) with an 810 nm diode laser (GBox 15A/B by GIGA Laser, Wuhan, China) with power density of 5 W cm^{-2}. The temperature was monitored at fixed intervals of time of laser exposure by an optic fiber detector (CEM®, Charlotte, NC, USA). Pure water (0.2 mL) was used as a control.

6.1.5. ζ-Potential study by Dynamic-Light Scattering (DLS) analysis

Dynamic light scattering (DLS) measurements were performed on the dispersion of $CDs_{18.5bar}$, CDs_{13bar}, and CDs_{8bar} (0.5 mg mL^{-1}) in both ultrapure water and supplemented DMEM at 37 °C using a Malvern Zetasizer NanoZS instrument (Malvern Panalytical ltd, Almelo, Netherlands) equipped with a 532 nm laser with a fixed scattering angle of 173°. ζ-Potential analyses were achieved at the same conditions used for the DLS measurements and applying the principle of laser Doppler velocity and phase analysis light scattering (M3-PALS technique) and analyzing the electrophoretic mobility of the particles for 2 min at 37 °C under constant electric field. The average ζ-Potential was calculated from the electrophoretic mobility using the Smoluchowski relationship and assuming that $K \times a >> 1$ (where K and a are the Debye-Hückel parameter and particle radius, respectively) [372]. Each sample was analyzed in triplicate.

6.1.6. Biological characterization in vitro

The cytocompatibility of the previously selected fractions of CDs was evaluated by MTS assay (Promega) on human breast cancer cell lines (MDA-MB-231 by Sigma Aldrich, Milan, Italy). Cells were seeded with a density of 1.5×10^4 cells/well (0.2 mL) on a 96-multiwell plate and grown in supplemented Dulbecco's Minimum Essential Medium (DMEM) at 37 °C and 5 % of CO_2. After 24 h, the medium was replaced with 0.2 mL of CDs dispersion in fresh culture medium at a concentration ranging from 1 to 0.05 mg mL^{-1}. After 48 h of incubation, MTS assay was performed replacing the dispersion of CDs in DMEM with MTS solution in DMEM composed of 0.1 mL of fresh medium and 20 μL of MTS solution. After 2 h of incubation, the absorbance at 492 nm was measured using a microplate reader (Eppendorf PlateReader AF2200, Hamburg, Germany).

Untreated cells were used as negative control. The NIR-triggered photothermal ablation of MDA-MB-231 induced by $CDs_{18.5bar}$, CDs_{13bar}, and CDs_{8bar} was evaluated in another experimental set. Cells were seeded with a density of 1.5×10^4 cells/well (0.2 mL) in a 96-multiwell, as described above. Cells were incubated with the dispersions of CDs in DMEM (1–0.05 mg mL^{-1}). After 48 h, each well was irradiated with an 810 nm laser for 300 s with power fitted at 5 W cm^{-2}. The hyperthermic effect was reported as a percentage reduction of cell viability against the control cells. All culture experiments were performed in triplicate.

6.1.7. Study of cell uptake on 2-D MDA-MB-231 cell culture model

The capacity of $CDs_{18.5bar}$, CDs_{13bar}, and CDs_{8bar} to enter into MDA-MB-231 was evaluated by fluorescence microscopy in a multichannel fashion after 6 h of incubation. Cells were seeded in an 8-well plate at a density of 1×10^4 cells/well (0.2 mL) and growth in DMEM at 37 °C and 5 % of CO_2. After 24 h, the medium was replaced with an equal volume of CDs dispersion in fresh medium (0.25 mg mL^{-1}). After 6 h, nuclei were stained with 40, 6-diamidino-2-phenylindole (DAPI). Each well was washed twice with DPBS pH 7.4 (0.2 mL x 2) and DAPI solution (0.2 mL) was added. After 10 min of incubation, cells were washed with DPBS (0.2 mL × 2). Micrographs were recorded using an Axio Cam MRm fluorescence microscope (Zeiss, Oberkochen, Germany).

6.2. Innovative decagram-scale synthesis of multicolor N,S-doped carbon nanodots as photothermal nanotools with selective anticancer properties

6.2.1. Materials

Citric acid (99 %), urea (99.5 %), indocyanine green (ICG, 99.5 %), anhydrous N, N-dimethylformamide (DMF), Sephadex® G15-G25 and DPBS pH 7.4 were purchased from Sigma Aldrich and used as received. ROS/Superoxide Detection Assay Kit (Cell-based) was purchased from Abcam and used following the instructions provided. Dulbecco's Modified Eagle Medium (DMEM), fetal bovine serum (FBS), l-glutamine, penicillin, streptomycin, and amphotericin B were purchased from ®Euroclone (Milan, Italy). 4′,6-diamidino2-phenylindole (DAPI) were purchased from Life Technologies. CellTiter 96® AQueous One Solution Cell Proliferation Assay (MTS) was purchased from Promega (Milan, Italy). Human breast cancer cell lines (MCF-7, MDA-MB-231, and SKBr-3) were obtained from “Istituto Zooprofilattico Sperimentale della Lombardia e dell’ Emilia Romagna”, Italy. Human dermal fibroblasts (NHDF), pre-neoplastic human mammary cells (MCF-10A), and human bronchial epithelial cells (16-HBE) were purchased from Life Technologies. Cell lines were cultured in DMEM, containing 10 % (v/v) FBS, 100 units per ml penicillin G, 100 μg mL^{-1} streptomycin, and 2 mM L-glutamine at 37 °C in a humidified atmosphere of 5 % CO_2.

6.2.2. Synthesis of N,S-doped Carbon Nanodots

N,S-CDs were synthesized from urea (11.56 g, 57.7 mmol), citric acid (36.95 g, 57.7 mmol), and indocyanine green (0.1 g, 0.129 mmol) in 100 mL of anhydrous DMF. The reaction was kept in solvothermal condition at 170 °C for 6 h (P_{max} = 25 bar, P_{min} = 16 bar) by using a still autoclave (Büchi AG, Miniclave steel type 3, Gschwaderstrasse, Switzerland). Successively, the organic solvent was removed by a rotary evaporator (25 mbar, 80 °C) and the brownish solid residue was redispersed in 150 mL of ultrapure water by sonication (15 min x 5). The aqueous dispersion of N,S-CDs was filtered through a paper filter and 0.45 µm membrane filter, and then purified by size exclusion chromatography (SEC) using a column packed in turn with Sephadex G15-G25. Successively, based on their UV/FL absorption spectra collected fractions were preliminarily characterized and unified to give rise to two main samples, named F1 and

F2, used for further characterizations. Only the F2 that was shown to be the most fluorescence and purified fraction was selected for the deep physico-chemical and biological characterizations. Yields: F1, 11.693 g (24.05 %); F2, 10.076 g (20.73 %).

6.2.3. Structural characterization of N,S-doped CDs

Atomic force microscopy (AFM) was exploited to assess the diameter distribution of CDs using a Bruker FAST-SCAN microscope equipped with a closed-loop scanner (X, Y, Z maximum scan region: 35 μm, 35 μm, 3 μm, respectively). The diameter of N,S-CDs were extrapolated from AFM micrographs based on their heights. Scans were recorded in soft tapping mode using a FAST-SCAN-A probe with an apical radius of about 5 nm. The sample was prepared by depositing 15 μl of N,S-CDs aqueous solution (0.1 mg mL^{-1}) on a mica substrate and dried in a vacuum before the analysis.

HR-TEM measurements were performed to characterize the structure of CDs by an aberration-corrected FEI Titan3 80-300 microscope at 300 keV electron energy. The sample was prepared at room temperature by the deposition of a drop of the aqueous solution of CDs on a commercial 400 μm mesh Cu-grid (Plano 01824) covered by a holey amorphous carbon film (nominal thickness of 3 nm).

6.2.4. Physico-chemical characterization

Surface functional groups of N,S-CDs were evaluated by FT-IR using a PerkinElmer Spectrum Two™ IR spectrometer (Waltham, MA, USA) and recording the spectrum in the range of 4000-400 cm^{-1}. Samples were prepared as KBr pellets and dried in vacuum before the analysis.

XPS analyses were performed for the surface elemental analysis of N,S-CDs by a PHI 5000 Versa Probe II (ULVAC-PHI, Inc.); source: Kα, 1486.6 eV; beam: 200 mm, 50 W; time per step: 10 ms; energy step: 0.10 eV; pass energy: 23.50 eV; analyzer mode: FAT. The sample was prepared by depositing an aqueous dispersion (500 μL, 0.5 mg mL^{-1}) on a thin aluminum plate and drying it under vacuum (0.1 mbar) for 24 h before the analysis. The carbon (C 1s) line at 284.8 eV was used as reference energy.

DSC-coupled TGA analyses were performed using a DSC/TGA 131 EVO (by SETARAM Instruments). Measurements of N,S-CDs were carried out under nitrogen atmosphere (flow rate 1 mL min^{-1}). The analysis was performed using about 5 mg of sample in a closed alumina crucible. The heating rate applied was: 10 °C min^{-1} in the range of 30–600 °C. Thermogram data were normalized to the unit weight.

6.2.5. Optical characterization of N,S-CDs

The optical absorption measurements have been performed on a N,S-CDs aqueous dispersion in a quartz 1 cm cuvette by using a Star Line ULS2048CLEVO single-beam optical fiber spectrophotometer (Avantes, Apeldoorn, The Netherlands) equipped with a dual halogen-deuterium light source (spectral range of 200-1200 nm). Steady-state emission spectra were recorded on an intensified CCD camera, integrating the signal during temporal windows of 100 μs starting from the excitation laser pulse. Samples were photoexcited by using a tunable laser (OPO – optical parametric oscillator) that provides 5 ns pulses at 10 Hz. Time-resolved measurements were recorded in the same setup integrating the signal during temporal windows of 0.5 ns and varying the delay from the laser peak. The accuracy of the time constant of the decay is about 0.2 ns.

6.2.6. Determination of the photothermal conversion capacity of N,S-CDs

Photothermal kinetics were evaluated on the dispersion of N,S-CDs in ultrapure water at different concentrations (0.1, 0.25, and 0.5 mg mL^{-1}) and testing diverse power densities (1.25, 2.5, and 5 W cm^{-2}). The study was performed by irradiating a dispersion of N,S-CDs ultrapure water (0.2 mL) using an 810 nm diode laser (GBox 15A/B by GIGA Laser, Wuhan, China) for 200 seconds. The kinetics of hyperthermia was obtained by reporting the temperature as a function of scheduled time intervals of irradiation. The increment of temperature was registered using an optical fiber detector (CEM®, Cologno al Serio, Italy). Ultrapure water (0.2 mL) treated with the same laser power was used as control. The photothermal conversion capacity of N,S-CDs aqueous dispersion under laser irradiation with power fitted ad 2.5 W cm^{-2} was evaluated also by using a Flir T250 thermal imaging camera recording one photo every 30 seconds. Each experiment was repeated three times and values are reported as an average.

For the evaluation of the photothermal conversion efficiency, an aqueous solution of N,S-CDs contained in a quartz cuvette was irradiated with an 800 nm pulsed Ti: Sapphire laser (SOLSTICE, Spectra-Physics, 2.5 W cm^{-2} maximum intensity, 5 kHz maximum repetition rate), following the increment of temperature using a Flir T250 Infra-Red infrared camera (resolution of 240 × 180 pixels, sensitivity of 80 mK NETD/0.08 °C and measurable temperature range of −20 / 350 °C). Experiments were repeated at different concentrations, and for different incoming beam intensities obtained by changing the repetition rate of the pulsed laser. Pure water sample treated at the same experimental conditions was used as control.

6.2.7. Cytocompatibility study of N,S-CDs with and without NIR-laser exposure

The cytocompatibility of N,S-CDs was studied in vitro on 2D models of breast cancer cell lines (MDA-MB-231, MCF-7, and SKBr-3), a pre-neoplastic breast cell line (MCF-10-A) and normal cell lines (NHDF and 16-HBE) by MTS assay (Promega). Cells were seeded at a density of 1.5×10^4 cells/well in a 96-wells plate and grown in supplemented Dulbecco's Minimum Essential Medium (DMEM) at 37 °C and 5 % CO_2. After 24 h, the medium was replaced with N,S-CDs dispersion in DMEM at different concentrations (200 µL, 1-0.05 mg mL^{-1}). After 48 h of incubation, the medium was removed and each well was washed two times with DPBS pH 7.4 (200 µL x 2). Successively, MTS solution in DMEM, composed of 100 µL of fresh medium and 20 µL of MTS, was incubated for an additional 2 h. Untreated cells were used as positive control (100 % cell viability). Then, absorbance at 492 nm was measured by using a microplate reader (Multiskan, Thermo, U.K.) and cell viability was normalized with that of the control. In a parallel experimental set was evaluated the NIR-triggered photothermal effects induced by N,S-CDs using the same procedure above described. Briefly, cells incubated with N,S-CDs for 48 h were irradiated for 200 sec with an 810 nm diode laser (GBox 15A/B di GIGA Laser) with power fitted at 2.5 W cm^{-2}. The cell viability was evaluated by MTS assay, as described above. All biological experiments were performed in triplicate and values are reported as an average.

6.2.8. Evaluation of Cell Reactive Oxygen Species (ROS)

For the evaluation of the total reactive oxygen species (H_2O_2, OH^- and ROO^-), cells were cultured as previously reported and incubated with 5-(-6)-carboxy-2,7-dichlorodihydrofluorescein diacetate (DCFH-DA) probe for 50 min. After this time, the medium was removed and cells were incubated with a dispersion of N,S-CDs in DMED at different concentrations ranging from 0.1, 0.25, 0.5 to 1 mg mL^{-1} at 37 °C for 24 h. The relative amount of ROS was obtained by measuring fluorescence at 527 nm (λ_{ex} = 485 nm) using a microplate reader (AF2200 Eppendorf) and comparing results with untreated controls. Solutions of tert-butyl hydroperoxide (50 µM) and dextran (0.1 mg mL^{-1}) were used as positive and negative controls, respectively. The same experiment was repeated to establish the effect of NIR-laser treatment, exposing cells incubated with N,S-CDs to an 810 nm laser (2.5 W cm^{-2}) for 200 s before measuring fluorescence at 527 nm. All assays were performed in at least three individual experiments, each comprising no less than six replicates.

6.2.9. Cell uptake study on cell culture model in vitro

Cell uptake study was performed on the different cell lines above described by fluorescence microscopy in a multichannel fashion. Cells were seeded at a density of 5×10^3 cells/well in an 8-wells plate and cultured in DMEM at 37 °C and 5 % CO_2. After 24 h, the medium was replaced with a dispersion of N,S-CDs in fresh culture medium (200 µL, 0.25 mg mL^{-1}). After 2, 6, and 24 h of incubation, the medium was removed, each well was washed twice with DPBS pH 7.4 (200 µL x 2) and cells were fixed with 4 % buffered formalin. Nuclei were stained with 4′,6-diamidino-2-phenylindole (DAPI). Micrographs were recorded by a fluorescence microscope using an Axio Cam MRm (Zeiss).

6.3. Advanced surface functionalization strategy of N,S-doped carbon nanodots via heterophase melt-extrusion transesterification with Poly (D, L-lactide)

6.3.1. Materials

Urea (99 %), citric acid (99.5 %), Indocyanine green (ICG, 99.5 %), anhydrous N, N-dimethylformamide (DMF), Sephadex® G15-G25, dialysis tubing MWCO 2 kDa, poly(D,L-lactide) acid terminated (Mw 14 kDa), chloroform, dichloromethane (DCM), phosphate buffer saline (PBS) were purchased from Sigma Aldrich (Milan, Italy). Size exclusion chromatography (SEC) traces were obtained using an Agilent 1260 Infinity equipped with Yarra™ 3 µm columns connected in series to a right angle (RA) and low angle (LA) light scattering (LS) detectors, and a refractive index (RI) detector. The mobile phase was 0.01 M LiBr in DMF (flow 0.8 mL min^{-1}). Dulbecco's Modified Eagle Medium (DMEM), fetal bovine serum (FBS), L-glutamine, penicillin, streptomycin, and amphotericin B were purchased from EuroClone (Milan, Italy). CellTiter 96® AQueous One Solution Cell Proliferation Assay (MTS) was purchased from Promega (Milan, Italy).

6.3.2. Surface functionalization of N,S-CDs with PLA (PLA-coated CDs) by reactive-extrusion transesterification

Multicolor carbon nanodots were synthesized as reported in Section 5.4.2. N,S-CDs (100 mg, 2.98 mg mL^{-1}) were dispersed in acetone/water (95:5) by sonicating. Then, the colloidal dispersion was added dropwise to a homogeneous solution of 20 % w/v PLA in chloroform (100 mL), obtaining a CDs/PLA dispersion. Then, the dark orange blend was kept under stirring overnight at room temperature. Successively, about 30 mL of organic solvent was removed by a rotary evaporator, and the obtained slurry was distributed on a glass crystallizer to favor the slowly remove of solvents at room temperature overnight. The obtained brown CDs/PLA film was cut into small chops. Successively, CDs/PLA chops (20 g) were introduced into the extruder at the barrel section (Noztek Pro Filament Extruder – UK), and extruded at 185 °C to give rise to filaments composed by PLA-coated CDs (CDs-PLA) in a matrix of PLA.

6.3.3. Chemical characterization of CDs-PLA and intermediate

FTIR and ATR analysis of PLA, CDs, CDs/PLA, and CDs-PLA were performed to explore interactions established between PLA chains and the CDs surface before and after the extrusion process. FTIR and ATR measurements were carried out using a Bruker Alpha II spectrometer, recording the spectra in the range between 400 and 4000 cm^{-1}. CDs were analyzed as a dry powder, while PLA, CDs/PLA, and CDs-PLA samples were prepared as films by solvent casting method from dispersion in chloroform.

To attain the chemical composition and structural features of the CDs-PLA for successive analysis, the latter was purified by gel permeation chromatography (GPC) using a column packed with Sephadex® LH-20 resin and DCM as eluent. The sample was prepared by solubilizing CDs-PLA (500 mg) in DCM (10 mL), and purifying the solution by GPC (flow 0.2 mL min^{-1}) to isolate only PLA-coated CDs present in the blend. Colorless fractions of pure PLA and brownish fractions of PLA-coated CDs were collected and analyzed by ^1H NMR (Bruker 300 MHz) in $CDCl_3$.

^1H NMR of CDs-PLA conjugates sample (300 MHz, [D1] $CHCl_3$, 25 °C): $\delta = 1.56–1.59$ (d, 3H PLA, –O–CO–$CH(CH_3)$–O–, PLA), 5.12–5.19 ppm (q, 1H PLA –O–CO–CH(CH3)–, PLA).

6.3.4. Differential Scanning Calorimetry (DSC) and ThermoGravimetric Analysis (TGA) analysis of CDs-PLA

The thermal stability of the CDs-PLA and the nature of interactions taking place between CDs and PLA after extrusion were evaluated by differential scanning calorimetry (DSC) coupled with thermogravimetric analysis (TGA). Pure CDs and PLA were analyzed as controls. The analyses were performed using a DSC/TGA 131 EVO (by SETARAM Instr.) under nitrogen flow (1 mL min^{-1}). The heating rate was: 30–600 °C, 10 °C min^{-1}.

6.3.5. Optical characterization of CDs-PLA

The optical absorption measurements were performed in a 1 cm quartz cuvette by a Star Line ULS2048CLEVO single-beam optical fiber spectrophotometer (Avantes) equipped with a dual halogen-deuterium light source in a spectral range of 200–900 nm. Steady-state emission spectra were recorded on an intensified CCD camera integrating the signal during temporal windows of 1 ms from the excitation laser pulse. A tunable laser (OPO

– optical parametric oscillator) providing 5 ns pulses at 10 Hz has been employed to excite the samples. Time-resolved measurements were recorded in the same setup integrating the signal in a shorter temporal window that lasts 0.5 ns and varying the delay from the laser pulse. The accuracy of the time constant of the decay is about 0.2 ns.

Quantum yield (QY) values were estimated by measuring the emission and absorption of the sample in an integrating sphere. The samples have been excited by laser diodes peaking at 405 nm and 532 nm.

6.4. Production of PLGA nanoparticles incorporating N-doped carbon nanodots for image-guided chemo-photothermal therapy of breast cancer

6.4.1. Materials

Urea (99 %), citric acid (99.5 %), N, N-dimethylformamide (DMF), ethanol absolute, Sephadex G15 and G25, dialysis tubing (MWCO 2 kDa), poly (D, L lactide-co-glycolide) (PLGA) (lactide/glycolide ratio 50:50 Mw 7000–14,000), irinotecan hydrochloride, dimethyl sulfoxide (DMSO), phosphate buffer saline (PBS) were purchased from Sigma Aldrich (Milan, Italy). Supplemented Dulbecco's Minimum Essential Medium (DMEM) supplemented with 10 % fetal bovine serum (FBS, Euroclone, Milan, Italy), 1 % of penicillin/streptomycin (10,000 U mL^{-1} and 10 mg mL^{-1}, respectively), 1 % of L-glutamine were purchased from Euroclone, Milan, Italy). Cell Titer 96 Aqueous One Solution Cell Proliferation assay (MTS solution) was purchased from Promega (Milan, Italy). Human breast cancer cell lines (MDA-MB-231) were obtained from "Istituto Zooprofilattico Sperimentale della Lombardia e dell' Emilia Romagna", Italy. Cell lines were cultured in DMEM, containing 10 % (v/v) FBS, 100 units per ml penicillin G, 100 μg mL^{-1} streptomycin, and 2 mM L-glutamine at 37 °C in a humidified atmosphere of 5 % CO_2.

6.4.2. Synthesis and characterization of N-doped Carbon Nanodots

CDs were synthesized as mentioned in our previous work [3,158,224]. Briefly, carbon nanodots were prepared by dissolving citric acid (3 g) and urea (6 g) in anhydrous DMF (30 mL). The reaction was conducted in solvothermal conditions at 160 °C for 4 h in a mini autoclave. The crude product was precipitated dropwise in ethanol and the precipitate was collected by centrifuging at 10.000 rpm for 10 min. Then, the pellets were dispersed in ultrapure water by sonicating. The water dispersion of CDs with different sizes was purified by size exclusion chromatography (SEC) using a column packed in turn with three types of Sephadex in series (G25, G15, G10). Subsequently, only the fractions with good fluorescence emission in the red region and NIR-sensitive photothermal properties were selected and deeply characterized. Atomic force microscopy (AFM, Bruker FAST-SCAN) (Milan, Italy) was performed to evaluate the size distribution of CDs. The analyses were achieved in soft tapping mode. The sample was prepared by depositing a CDs aqueous dispersion (0.1 mg L^{-1}, 10 μL) on a mica substrate and dried in a vacuum (10 mbar). The surface functional groups of CDs were evaluated by FT-IR spectroscopy (Bruker Alpha II spectrometer) (Milan, Italy). The sample was prepared as pellets of KBr.

6.4.3. Preparation of PLGA-CDs nanoparticles by nanoprecipitation technique

To prepare PLGA-CDs1% nanoparticles, PLGA (99 mg) and CDs (1 mg) were dispersed in 10 mL of DMSO. The organic mixture was put in a burette and added drop by drop to 100 mL of distilled water under continuous stirring and it was left under stirring for 1 h. Then, the aqueous dispersion was filtered on a paper filter and dialyzed against water overnight (Visking Dialysis Tubing 18/32", 2000 molecular weight cut-offs). Subsequently, the content of dialysis was aliquoted to test the influence of different types and amounts of cryoprotectant agents (e.g. sucrose 1 %, sucrose 2 %, sucrose 5 %, trehalose 2 %, PVP 10 %, lactose 1 %, lactose 2 %, lactose 5 %) on nanoparticles aggregation pre- and post-freeze-drying. In the same way, PLGA-CDs20% nanoparticles were prepared by dissolving 80 mg of PLGA and 20 mg of CDs in DMSO. Drug-loaded nanoparticles (PLGA-CDs1%@IT and PLGA-CDs20%@IT) were also prepared, adding 25 mg of irinotecan hydrochloride to the solutions described above.

6.4.4. Dynamic Light Scattering Measurements (DLS)

Size distribution and stability after freezing were evaluated by DLS measurements performed on 1 mL of fresh sample, prepared as described above, and also on lyophilized samples at 25 °C using a Malvern Zetasizer NanoZS instrument (Rome, Italy) equipped with a 532 nm laser with a fixed scattering angle of 173°, and the Dispersion Technology Software 7.02 software (Malvern Panalytical ltd, Almelo, The Netherlands). Zeta-potential measurements were performed by aqueous electrophoresis measurements, recorded at 25 °C using the same apparatus for the DLS measurement. The Zeta-potential values (mV) were calculated from electrophoretic mobility using the Smoluchowski relationship. All analyses were performed in triplicate.

6.4.5. Atomic Force Microscopy analysis of PLGA-CDs nanoparticles

Atomic Force Microscopy (AFM, Bruker FAST-SCAN) (Milan, Italy) was employed to evaluate the size distribution and morphology of the dried PLGA-CDs nanoparticles. The measurements were performed in a soft tapping mode and using a triangular tip with an apical radius of about 5 nm. Each micrograph was obtained with a resolution comparable to the tip radius. The sample was prepared by depositing a dilute aqueous dispersion of the samples on a mica substrate and dried under vacuum (10 mBar) before the observation.

6.4.6. Optical characterization

The optical absorption properties of CDs and the hybrid PLGA-CDs nanoparticles were carried out by a double beam spectrophotometer (Shimadzu UV-2401PC) (Milan, Italy) in a 1 cm quartz cuvette, recording the spectra in the range of 200-700nm. The emission spectra were recorded under excitation at 540 nm by using a spectrofluorometer (Shimadzu RF-5301PC) (Milan, Italy). The optical measurements were performed on diluted aqueous dispersions.

The photothermic effect was evaluated by irradiating an aqueous dispersion of either PLGA-CDs1% or PLGA-CDs20% (0.2 mL, 0.1 mg mL^{-1}) with an 810 nm diode laser (GBox 15A/B by GIGA Laser, Wuhan, China) with a power density of 7 and 2.5 W cm^{-2}, respectively, for 300 s. At fixed intervals, the increment of the temperature of the dispersion at set intervals of exposure time was recorded using an optical fiber detector (CEM®, Cologno al Serio, Italy). An equal volume of water (0.2 mL) was used as control.

6.4.7. Drug-loading of PLGA-CDs nanoparticles (PLGA-CDs1%@IT and PLGA-CDs20%@IT)

The drug payload was evaluated by dissolving a known amount of PLGA-CDs@IT nanoparticles (~5 mg) in acetonitrile (400 µL) under magnetic stirring for 2 h. Then, the sample was filtered through a syringe filter of 0.45 nm and HPLC mobile phase was obtained by adding methanol (400 µL) and PBS pH 3.5 (1.2 mL). The amount of irinotecan loaded inside the PLGA-CDs@IT nanoparticles was determined by HPLC analysis. Analyses were performed with a mobile phase constituted by a mixture of 0.03 N PBS pH 3.5/CH_3CN/MeOH 60:20:20 and a flow rate of 1 mL min^{-1}. The column used was C_6 phenyl by Phenomenex® (Castel Maggiore, Italy) with the temperature settled at 25 °C, and the detection wavelength at 366 nm. The obtained peak area of the chromatogram was compared with a calibration curve obtained by plotting areas versus standard solution concentrations of IT in the range of 0.001 – 0.0001 mg/mL (y = 106872x, R2 = 0.9999). The drug loading obtained was 3.15 and 4.73 % (w/w) for PLGA-CDs1%@ITandPLGA-CDs20%@IT nanoparticles, respectively. The encapsulation efficiency was 16 and 24 %, respectively.

6.4.8. Cumulative drug-release of PLGA-CDs1%@IT and PLGA-CDs20%@IT nanoparticles

For drug release kinetic studies, an amount of PLGA-CDs1%@IT nanoparticles and PLGA-CDs20%@IT nanoparticles equivalent to a drug concentration of 0.2 mg mL^{-1} was dispersed in PBS pH 7.4 (1 mL) and placed into a dialysis tubing (MWCO 2 kDa) against 9 mL of PBS at 37 °C under orbital stirring (100 rpm). At defined set times, 200 µL of the external medium was withdrawn and replaced with an equal volume of fresh medium up to 48 h. The photothermal triggered drug release was evaluated by irradiating (before the dialysis process) the dispersion of either PLGA-CDs1%@IT nanoparticles or PLGA-CDs20%@IT NPs in PBS pH 7.4 (0.2 mg mL^{-1}) by 810 nm diode laser (GBox 15A/B by GIGA Laser, Wuhan, China) for 200 s with power fitted at 7 Wcm^{-2} and 100 s with power fitted at 2.5 W cm^{-2}, respectively. The amount of IT released was calculated by HPLC analysis as described for drug loading determination.

6.4.9. In Vitro Anticancer Activity of PLGA-CDs20%@IT nanoparticles

The anticancer activity of the IT-loaded PLGA-CDs20% nanoparticles (PLGA-CDs20%@IT) was evaluated in vitro on the MDA-MB-231 breast cancer cell line. Cells were seeded at a density of 2×10^4 cells/well in a 96-wells plate and grown in DMEM. After 24 h, the medium was replaced with 0.2 mL of PLGA-CDs20%@IT dispersion in fresh culture medium at different concentrations corresponding to equivalent concentrations of irinotecan ranging from 5 to 150 µg mL^{-1}. After 24 and 48 h of incubation, cell viability was assessed by the MTS assay. In detail, samples were removed and each well was washed twice with DPBS pH 7.4 (0.2 mL x 2), and 120 µL of MTS solution in DMEM (DMEM/MTS 6:1) was added to each well. Then, cells were incubated for an additional 2 h at 37 °C before reading the absorbance at 492 nm by using a microplate reader (Multiskan, Thermo, U.K.). A solution of irinotecan hydrochloride at the same concentration was used as positive control, while the used cryoprotectant (PVP) at the corresponding concentrations was used as negative control.

In another experimental set, the NIR-triggered photothermal ablation of cells was evaluated by irradiating the cells treated with PLGA-CDs20%@IT using an 810 nm laser diode for 100 s with a power density of 2.5 W cm^{-2}. Cells were seeded in a 96-well plate at a density of 2×10^4 cells/well (200 µL) and grown in DMEM. After 24 h, cells were incubated with PLGA-CDs20%@IT (5–150 µg mL^{-1}) for 24 or 48 h and then irradiated with the laser before performing MTS assay as above described. The increase in temperature inside each well owing to the photothermal effect was previously evaluated at the same experimental conditions tested in vitro by irradiating the dispersions of the nanosystem in DMEM. The temperature inside the wells was monitored by using a fiber optic and reported as function of exposure time.

6.4.10. Study of cell internalization on 2-D cell culture in vitro

Cell uptake of PLGA-CDs1% and PLGA-CDs20% nanoparticles (0.5 mg mL^{-1}) was evaluated by fluorescence microscopy on MDA-MB-231. Cells were seeded at a density of 1×10^4 cells/well (200 µL) in an 8-well plate and growth in DMEM. After 24 h, the medium was replaced with an equal volume of sample dispersion in fresh medium (0.5 mg mL^{-1}). After different incubation times (4, 6, and 24 h), nuclei were stained with 4,6-diamidino-2-phenylindole (DAPI) after washing twice cells with DPBS pH 7.4 (200 µL x 2), adding the DAPI solution (100 µL) and incubating cells for 10 min. Cells were then washed up with fresh DPBS (200 µL x 3) and images were recorded by a fluorescence microscope using a Zeiss Axio Cam MRm MRm (Zeiss AG, Oberkochen, Germany). Micrographs were recorded in a multichannel fashion.

6.5. Hydrophobic N-doped carbon nanodots coated with hyaluronic acid as NIR-responsive hybrid nanosystems useful in cancer theranostics

6.5.1. Materials

Urea (99 %), citric acid (99.5 %), N, N-dimethylformamide (DMF), ethanol absolute, dialysis tubing (MWCO 14 kDa), Sephadex G15 and G25, poly(D, L-lactide) acid terminated (PLA; Mw 13.000), doxorubicin hydrochloride, diethylamine (DEA, 99.5 %), trimethylamine (TEA; 99.5 %) dimethyl sulfoxide (DMSO), N, N'-dicyclohexylcarbodiimide (DCC; 99 %), N-hydroxysuccinimide (NHS; 99.5%) phosphate buffer saline (PBS), triethylamine and octylamine, were purchased from Sigma Aldrich (Milan, Italy). Hyaluronic acid (HA) having a low weight-average molecular weight was prepared by acidic degradation of biotechnological HA sodium salt (MW 1500 kDa) which has been a generous gift from Novagenit s.r.l. (Italy). The Molecular weight distribution of the HA and its derivative were determined by size exclusion chromatography (SEC) apparatus equipped with a pump system, a Universal column (particle size 5 μm), and a 410-differential refractometer (DRI) as a concentration detector, all from Waters (USA). The molecular weight (221 kDa, Mw/Mn=1.85) was evaluated by using HA standards (range 100– 800 kDa) from Hyalose (USA), 200 mM phosphate buffer pH 6.5/MeOH 90:10 (v/v) as a mobile phase, 36±0.1 °C, and flow rate 0.6 mL min^{-1}. 1H-NMR spectra were recorded using a Bruker Avance II 300 spectrometer operating at 300.12 MHz. Dulbecco's Modified Eagle Medium (DMEM), fetal bovine serum (FBS), l-glutamine, penicillin, streptomycin, and amphotericin B were purchased from ®Euroclone (Milan, Italy). 4′,6-diamidino2-phenylindole (DAPI) were purchased from Life Technologies. CellTiter 96® AQueous One Solution Cell Proliferation Assay (MTS) was purchased from Promega (Milan, Italy). Human breast cancer cell lines (MCF-7 and MDA-MB-231) were obtained from “Istituto Zooprofilattico Sperimentale della Lombardia e dell’ Emilia Romagna”, Italy. Human bronchial epithelial cells (16-HBE) were purchased from Life Technologies. Cell lines were cultured in DMEM, containing 10 % (v/v) FBS, 100 units per ml penicillin G, 100 μg mL^{-1} streptomycin, and 2 mM L-glutamine at 37 °C in a humidified atmosphere of 5 % CO_2.

6.5.2. Synthesis of hyaluronic acid grafted poly(D,L-lactide) copolymer (HA-g-PLA)

The N-hydroxysuccinimide (NHS) derivative of PLA, namely PLA-NHS, was obtained as previously reported [373]. Separately, a tetrabutylammonium (TBA, 1 eq.) salified HA ($\overline{M}$n = 112 kDa, PD = 1.64), named HA-TBA (600 mg), was solubilized in DMSO (48 mL) and DEA (576 µL) used as a catalyst. Then, PLA-NHS (50 mg) was dissolved in anhydrous DMSO (6 mL) and added to the HA-TBA solution drop by drop for about 1 h under magnetic stirring. The reaction was kept under argon atmosphere at 40 °C for 48 h, and, subsequently, the TBA was removed by ion exchange with sodium cations by transient the organic solution in a cationic exchange resin (Dowex 50W×8-200). Then, the solution was precipitated in acetone and washed up in the same solvent five times. Finally, HA-g-PLA was dispersed in water and dialyzed against a sodium chloride aqueous solution (5 % w/v) for 3 days and water for 2 days by using dialysis tubing (MWCO 14.000 Da). The product was recovered as a white powder after freeze-drying. Yield: 71 % w/w.

^{1}H-NMR (300 MHz, D_2O/THF, 25 °C): δ 1.57 and δ 1.68 (2d, 3H PLA, –O–CO–CH(CH_3)–O– of PLA), δ 2.12 (s, 3H HA, –NH–CO–CH_3), δ 5.40 ppm (m, 1H PLA –O–CO–CH(CH_3)– of PLA).

SEC: $\overline{M}$n = 168 kDa : $\overline{M}$ w = 225 kDa; PD = 1.34

6.5.3. Evaluation of the critical aggregation concentration (CAC) of graft copolymer HA-g-PLA

The critical aggregation concentration was estimated spectrofluorimetrically by pyrene assay based on the use of pyrene as a hydrophobic fluorescent probe. Briefly, 5 µl of pyrene solution in acetone (6×10^{-5} M) was deposited in a tube test and left up to complete evaporation of acetone. Then, 500 µl of water dispersion of HA-g-PLA copolymers with a concentration within 9×10^{-4} - 0.25 mg mL^{-1} was added and left overnight before the analysis. Then, the emission spectra were recorded under excitation at 333 nm. The I_1/I_3 ratio of the intensities of the first and third peaks of the fluorescence spectrum of pyrene was used to detect the formation of polymeric micelles.

6.5.4. Synthesis and chemical characterization of hydrophobic carbon nanodots (HCDs)

Carbon nanodots (CDs) were prepared as reported in Section 5.4.2. Only fractions of CDs with homogeneous dimensions, good red fluorescence, and NIR-sensitive photothermal property were selected for the synthesis of hydrophobic CDs (HCDs). HCDs were synthesized by solubilizing CDs (20 mg) in DMF (5 mL) and adding octylamine (C_8) (26 µl, 0.157 mmol), N, N'-dicyclohexylcarbodiimide (DCC) (32.38 mg, 0.157 mmol) and N-Hydroxysuccinimide (NHS) (18.07 mg, 0.157 mmol) at once under vigorous stirring. The reaction was kept under stirring (40 rpm) at room temperature for 24 h. Then, the product was filtered on a paper filter and purified by dialysis (1 kDa) against water pH 5 for 3 days. Finally, the product was retrieved by centrifuging at 13.000 rpm for 15 min. The pellet was freeze-dried to get a dark powder of HCDs.

FT-IR spectroscopy (Bruker Alpha II spectrometer) was employed to investigate the surface functional groups of both starting CDs and HCDs used as KBr pellets. Spectra were recorded within the range 400- 4000 cm^{-1} (scan times: 24; resolution: 4 cm^{-1}).

Additionally, the degree of surface functionalization with C_8 moieties of HCDs was studied by ^1H-NMR using an exact amount of acetone (5 µL) used as internal standard. Samples were prepared in DMF-d_6.

6.5.5. Contact angle measurements

Surface wettability was evaluated by contact angle measurements performed using a DSA25 by Kruss Germany. In order to assess the equilibrium time, the contact angle was measured after 5 min from the deposition of the water drop.

6.5.6. Optical characterization of HCDs

The optical absorption properties of CDs and HCDs were carried out using a double-beam spectrophotometer (Shimadzu UV-2401PC). The measurements were performed on CDs and HCDs dispersion in DMF recording the spectra in the range of 200-800 nm. The fluorescence properties were evaluated using a spectrofluorometer (Shimadzu RF-5301PC) under excitation at 540 nm and a resolution of 2 nm.

The photothermal conversion properties of CDs ($\approx 4.289 \times 10^{14}$ nanoparticles) and HCDs ($\approx 3.002 \times 10^{14}$ nanoparticles) were investigated by irradiating aqueous dispersions (0.1 mg mL^{-1}, 0.2 mL) with an 810 nm diode laser (GBox 15A/B by GIGA Laser) with power fitted at 5 W cm^{-2} for 300 s. The hyperthermia kinetics were recorded by monitoring the temperature at scheduled exposure time intervals by using a fiber optic detector (CEM®, Cologno al Serio, Italy).

6.5.7. Preparation of hyaluronic acid-coated HCDs (HA-g-PLA/HCDs) by self-assembling

To prepare the hyaluronic acid-coated hydrophobic carbon nanodots, HCDs were dispersed in DMSO (2 mg mL^{-1}, 2 mL), and added dropwise to an aqueous dispersion of HA-g-PLA (2 mg mL^{-1}, 10 mL). The mixture was left under stirring at 4 °C overnight, then purified by exhaustive dialysis (MWCO 12-14 kDa) and retrieved as brownish sponge powder after freeze-drying.

6.5.8. Dynamic light scattering (DLS) measurements of zeta-average and zeta-potential

DLS measurements were performed to evaluate the size distribution of HA-g-PLA/HCDs nanoparticles by using a Malvern Zetasizer NanoZS instrument equipped with a 632 nm laser with a fixed scattering angle of 173 °. The analyses were carried out on 1 mL of HA-g-PLA/HCDs dispersion in PBS pH 7.4 (0.2 mg mL^{-1}). Z-average and PDI were extrapolated from the analysis of the correlogram. Zeta-potential analyses were performed by aqueous electrophoresis measurements at 25 °C on HA-g-PLA/HCDs dispersion in 0.01 mM KCl (0.2 mg mL^{-1}), using the same apparatus for the DLS measurements. The Zeta-potential values (mV) were calculated from electrophoretic mobility using the Smoluchowski relationship.

6.5.9. Stability determination of HA-g-PLA/HCDs in aqueous dispersion

The HA-g-PLA/HCDs stability was evaluated under physiological (PBS pH 7.4) and tumor microenvironment conditions (acetate buffer pH 5.5) at 37 °C up to 72 h of incubation. The size distribution of samples was measured at established time intervals by DLS as above described and reported as a function of the incubation time.

6.5.10. Preparation of Doxo-loaded hyaluronic acid-coated HCDs (HA-g-PLA/HCDs@Doxo) by self-assembling

The HA-g-PLA/HCDs@Doxo were prepared as above described, but adding Doxo (6.25 mg) and TEA (7.5 µl) to the dispersion of HCDs in DMSO before self-assembling. The mixture was left under stirring at 4 °C overnight, then purified by exhaustive dialysis (MWCO 12-14 kDa) and retrieved as red sponge powder after freeze-drying. Furthermore, the powder was redispersed in ultrapure water (1.5 mL) and the free drug eventually present was removed by gel permeation chromatography (GPC) using a column packed in turn with Sephadex G-25 as the stationary phase and ultrapure water as eluent. A reddish sponge was obtained after freeze-drying. Yield: 67 %.

6.5.11. Drug-loading and drug-release determination of HA-g-PLA/HCDs@Doxo

The drug loading of HA-g-PLA/HCDs@Doxo was calculated spectrophotometrically measuring the absorbance at 481 nm and comparing data with those of a calibration curve obtained with free Doxo standards (R2 =0.998; 0.1-0.025 mg mL^{-1}). Samples were prepared by dispersing a known amount of HA-g-PLA/HCDs@Doxo in DMSO/H_2O/0.1 N HCl (1:0.9:0.1) by sonication before the analysis. The same amount of empty micelles was used to subtract the absorbance owing to scattering phenomena and CDs absorption. For the drug release kinetic experiments, either an amount of HA-g-PLA/HCDs@Doxo corresponding to a drug concentration of 0.115 mg mL^{-1} or free Doxo was dispersed either in PBS pH 7.4 (2.5 mL) or acetate buffer pH 5.5 (2.5 mL) and placed into a dialysis tubing (MWCO 2 kDa) against 20 mL of the same medium. At scheduled time intervals, 0.5 mL of the external medium was withdrawn and replaced with an equal volume of fresh medium. The cumulative drug release was obtained by calculating the amount of Doxo released spectrophotometrically as function of time using the same procedure above reported. The photothermal-triggered drug release kinetics were evaluated by irradiating the dispersion of HA-g-PLA/HCDs@Doxo at pH 7.4 or 5.5 (eq. Doxo = 0.115 mg mL^{-1}) before the dialysis process, using a NIR diode laser with a power density of 5 W cm^{-2} for 300 s. The heating kinetic was previously evaluated at the same condition used in the drug release study.

6.5.12. Cytocompatibility study of the HA-g-PLA/HCDs nanoparticles

The cytocompatibility of the HA-g-PLA/HCDs was evaluated in vitro on two different human breast cancer cell lines (MDA-MB-231 and MCF-7) by MTS assay. Cells were seeded at a density of 1.5×10^4 cells/well (200 μl) in a 96-wells plate and grown in supplemented Dulbecco's Minimum Essential Medium (DMEM). After 24 h, the medium was replaced with a dispersion of HA-g-PLA/HCDs in fresh culture medium (200 μl) at a concentration ranging from 0.271 - 0.00054 mg mL^{-1}. After 24 and 48 h, samples were removed and each well was washed twice with DPBS pH 7.4 (100 μl x 2) and then 100 μl of fresh DMEM and 20 μl of MTS assay solution were added. Then, cells were incubated for an additional 2 h at 37 °C and 5 % CO_2 before reading the absorbance at 492 nm using a Microplate Reader (Multiskan Ex, Thermo Labsystems, Finland). Cell viability was expressed as a percentage of living cells compared to the untreated cells used as control (taken as 100 %).

6.5.13. Anticancer activity determination of the HA-g-PLA/HCDs@Doxo with and without NIR-laser treatment

The anticancer activity of the HA-g-PLA/HCDs@Doxo was assessed as above described by MTS assay, testing different concentrations of micelles corresponding to an equivalent concentration of free Doxo ranging from 50 to 0.1 μM. The anticancer effect was reported as cell viability reduction of two breast cancer cell lines (MDA-MB-231 and MCF-7), against untreated control cells, after 24 and 48 h of treatment. In another experimental set, the combined effect of NIR-triggered hyperthermia and Doxo local release was studied by irradiating both cancer cell lines incubated with an increasing amount of HA-g-PLA/HCDs@Doxo to an 810 nm diode laser with power fitted at 7 W cm^{-2} for 300 s. In particular, cells were seeded at a density of 1.5×10^4 cells/well (200 μl) in a 96-wells plate and grown in DMEM. After 24 h, the medium was replaced with a dispersion of either HA-g-PLA/HCDs@Doxo (50 to 0.1 μM) or an equivalent amount of the bare HA-g-PLA/HCDs (0.271 - 0.00054 mg mL^{-1}) in fresh DMEM and incubated for 24 or 48 h. After this time, each well was irradiated and washed twice with DPBS pH 7.4 (200 μl x 2) before performing the MTS assay as described above. The temperature increment as a function of the laser exposure time was previously evaluated at the intermediate concentration tested in vitro (30 μg mL^{-1}). The anticancer activity of the compound was compared with those of free Doxo at the same concentrations considered, treated, and untreated with NIR laser. All experimental biological set was performed in triplicate.

6.5.14. Procedure RNA extraction and first-strand cDNA synthesis

For the evaluation of gene expression, cells were seeded in a 96-wells plate at a density of 10^4 cells/well (200 µl) and after 24 h, the medium was replaced with a dispersion of either HA-g-PLA/HCDs, HA-g-PLA/HCDs@Doxo or free Doxo in DMEM (200 µl), at a concentration suitable to reduce cell viability of 50 % (IC_{50}). After 24 h of incubation, each well was irradiated with a diode laser with power fitted at 7 W cm^{-2} for 300 s. In parallel, the same experiment was performed without laser irradiation. Total RNA was purified from control and treated cells using Trizol Reagent (Invitrogen Corporation, Carlsbad, USA) and following the manufacturer's instructions. RNA concentrations and purity (Abs260, Abs260/280, and Abs260/230) were spectrophotometrically tested using Eppendorf 6131 BioPhotometer (Eppendorf AG, Hamburg, Germany). RNA integrity was checked on 1.5 % agarose denaturing gel and RNAs were stored at -80 °C for future use. Purified RNA was treated with Deoxyribonuclease I, Amplification Grade (Sigma-Aldrich) to remove any residual genomic DNA contamination, and DNAseI was inactivated by adding 50 mM EDTA. First-strand cDNA was synthesized from DNAseI-treated RNA samples (about 100 ng) using the High-Capacity cDNA Reverse Transcription Kit (Thermo Fischer Scientific) following the manufacturer's instructions. All the cDNAs were tested by PCR using GAPDH, and ACTB primers and were diluted 1:10 before use in Real-Time qPCR experiments.

6.5.15. Evaluation of gene expression by real-time quantitative polymerase chain reaction (qPCR)

The qPCRs were carried out using the BIO-RAD CFX96 system with BrightGreen 5X qPCR MasterMix (Applied Biological Materials Inc, Richmond, Canada) as detection chemistry. The ACTB and GAPDH were selected as control genes due to their expression stability in all the tested conditions. A normalization factor was calculated based on geometric averaging of the expression level of these reference genes and used to quantify the expression levels of the target genes [224]. Quantitative real-time PCRs were performed according to the manufacturer's recommended procedures, and each reaction was performed in triplicate. The amplification conditions were the following: initial denaturation at 95 °C for 10 min and 40 cycles of 95 °C for 30 s and 60 °C for 50 s, followed by a melting curve from 60 to 95 °C. In order to confirm the amplification of the specific gene, amplicons were detected by agarose gel analysis after each PCR. Experiments were performed in triplicate. Gene expression results presented as heat maps were obtained via Heatmapper (available at http://heatmapper.ca/expression/). The mRNA levels are represented as mean centered. Gene expression results are reported in bar charts and expressed as a mean value ± SD. Significant differences between values of different treated groups and the reference control groups were determined by t-test using Statistica 6.0 (StatSoft, Tulsa, OK, USA). The p-values less than 0.05 were considered statistically significant.

6.5.16. Cell uptake study of HA-g-PLA/HCDs on cell culture model in vitro

The cell uptake of HA-g-PLA/HCDs o was evaluated on MDA-MB-231, MCF-7, and 16-HBE using an Axio Cam MRm (Zeiss) fluorescence microscope in a multichannel fashion. Cells were seeded at a density of 1×10^4 cells/well (200 µl) in an 8-wells plate and grown in DMEM. After 24 h, the medium was replaced with a dispersion of the sample in fresh DMEM (25 g mL^{-1}) and incubated for 4 h and 24 h. Successively, the dispersion was removed, cells were washed twice with DPBS pH 7.4 (200 µl x 2) and nuclei were stained with 4′,6- diamidino-2-phenylindole (DAPI) by adding 100 µl of DAPI solution and incubating for 5 minutes. For the MCF-7 and MDA-MB-231 cell lines, uptake studies were repeated by pre-incubating with a HA solution (150 L, 10 g mL^{-1}) for 30 minutes before adding HA-g-PLA/CDs (125 µl, 50 µg mL^{-1}). After 4 h and 24 h, the medium was removed, cells were washed with fresh PBS pH 7.4 (200 µL x 2) and nuclei were stained by adding 100 µL of DAPI solution for 5 minutes. Before acquiring the uptake images, each well was washed with DPBS pH 7.4 (200 µL x 3). Cells self-fluorescence was removed by setting up the microscope using untreated cells.

6.6. β-Cyclodextrin decorated multicolor N,S-doped carbon nanodots as theranostic nanoplatform for the delivery of sildenafil in breast cancer

6.6.1. Materials

Urea (99 %), citric acid (99.5 %), amino-PEG$_4$-alkyne, p-toluenesulfonyl chloride, 1-Ethyl-3-(3-dimethyl aminopropyl) carbodiimide (EDC), N-Hydroxysuccinimide (NHS, 99.5 %), L-ascorbic acid (99 %), copper (II) sulfate, 1,1,2,2-tetrachloroethane, sildenafil citrate (pharmaceutical secondary standard), SpectraPor® Float-A-Lyzer®G2 (MWCO 100-500 Da), SpectraPor® Pre-wetted RC Tubing (MWCO 1kDa), Cation exchange resin Dowex® (50 W x 8 100-200 mesh), Phosphate Buffered Saline (PBS) and Dulbecco's phosphate-buffered saline (DPBS) were purchased from Sigma Aldrich (Milan, Italy). β-cyclodextrin (99 %) and sodium azide (NaN_3 99.5 %) were purchased from Fisher Scientific (Milan, Italy). Dulbecco's Minimum Essential Medium (DMEM), fetal bovine serum (FBS), L-glutamine, penicillin, streptomycin, and amphotericin B were purchased from EuroClone (Milan, Italy). CellTiter 96® AQueous One Solution Cell Proliferation Assay (MTS) was purchased from Promega (Milan, Italy).

6.6.2. Synthesis and physico-chemical characterization of Alkyne-Carbon Dots (CDs-PEG$_4$-CC)

Carbon dots (20 mg, 2.86 mg mL^{-1}) were dispersed in phosphate saline buffer (PBS) pH 6.4, and amino-PEG$_4$-alkyne (25 mg) were added. The pH was adjusted to 6.4 and 1-Ethyl-3-(3-dimethyl aminopropyl) carbodiimide (EDC) (24.92 mg, 0.13 mmol) and N-Hydroxysuccinimide (NHS) (14.96 mg, 0.13 mmol) were added under stirring. The reaction was performed at pH 6.4 for 24 h and purified by SpectraPor® Float-A-Lyzer®G2 (MWCO 100-500 Da) for 36 h. The product was freeze-dried to get the CDs-PEG$_4$-CC (yield: 77.3 %).

The surface functional groups of crude CDs and CDs-PEG$_4$-CC were investigated by Fourier-transform infrared spectroscopy (FT-IR) in the range of 4000-400 cm^{-1}. Samples were prepared as KBr pellets and dried in vacuum. Measurements were performed using a PerkinElmer Spectrum Two™ IR spectrometer (Waltham, MA, USA).

6.6.3. Synthesis and characterization of 6-O-Monotosyl-β-cyclodextrin (β-Cdx-OTs)

β-Cyclodextrin (β-Cdx) (10 g, 8.8 mmol) was dispersed in 90 mL of water and 35.2 mL (88 mmol) of 2.5 N NaOH was slowly added under magnetic stirring. After complete dispersion of β-Cdx, p-toluenesulfonyl chloride (2.52 mg, 13.22 mmol) was added in five portions and the suspension was stirred for 1 h at room temperature. The product was filtered through a folded paper filter and washed with 10 mL of ultrapure water. The filtered solution was added to 91 mL of pre-swollen cation exchange resin (Dowex®, 50 W x 8 100-200 mesh) and kept under stirring for 20 minutes. Then, the exchange resin was removed by vacuum filtration through a Büchner funnel with glass wool and washed with water. The white precipitate was filtered through a paper filter on a Büchner funnel and washed with acetone. The white powder (β-Cdx-OTs) was dried under vacuum (yield: 31 %).

^{1}H-NMR was used to evaluate the degree of functionalization (% w/w). Sample of β-Cdx-OTs was prepared in DMSO d_6.

^{1}H NMR (300 MHz): δ 7.74-7.72 (2H, H_8 **Ph**), δ 7.43-7.40 (2H, H_7 **Ph**), δ5.75 (14H, OH-2/OH-3), δ 4.83-4.76 (7H, $\mathbf{H_1}$ Cdx), δ 4.33-4.29 (2H, $\mathbf{H'_6}$ Cdx, overlap with water), δ 4.18 (1H, $\mathbf{H'_5}$ Cdx, overlap with water), δ 3.31 (14H, $\mathbf{H_2/H_4}$ Cdx, overlap with water), δ 2.14 (3H, Ph-C$\mathbf{H_3}$) ppm.

6.6.4. Synthesis and characterization of 6-Monoazide-β-cyclodextrin (β-Cdx-N_3)

β-Cdx-OTs (2.5 mg, 1.95 mmol) was dispersed in water (250 mL) and sodium azide (2.5 mg, 38.45 mmol) was added under magnetic stirring into a round-bottomed flask equipped with a condenser. After turning on the water for the condenser, the reaction was heated at 100 °C with an oil bath and kept refluxing overnight under stirring (500 rpm). The reaction was cooled down to room temperature and the mixture was filtered through a paper filter. The filtrate was concentrated to about 15 mL under reduced pressure and 1,1,2,2-tetrachloroethane (3 mL) was added dropwise to the concentrated filtrate. The resulting emulsion was kept stirring for 30 minutes and the aqueous phase was removed by centrifugation (3000 rpm, 5 min.). The organic solvent was distilled under reduced

pressure, leaving a solid residue. The residue was recrystallized using hot water and the precipitate obtained at a low temperature was retrieved by centrifuging (3000 rpm, 5 min.). This step was executed twice. The white solid (β-Cdx-N_3) was dried under vacuum overnight. Samples of β-Cdx-N_3 for ^{1}H NMR analysis were prepared in DMSO d_6.
^{1}H NMR (300 MHz): δ 6.90 ($C_2H_2Cl_4$ trace), δ 5.78-5.65 (14H, OH-2/OH-3 Cdx), δ 4.82 (7H, **H_1** Cdx), δ 4.57 (6H, OH-6 Cdx), δ 3.33-3.30 (14H, **H_2/H_4** Cdx, overlap with water).

6.6.5. Cycloaddition of alkyne-CDs and azide-β-Cdx (CDs-PEG_4-β-Cys)

CDs-PEG_4-β-Cys were obtained by dispersion of CDs-PEG_4-CC (10 mg) and N_3- β-Cdx (20 mg) in 6 mL of water. Copper (II) sulfate (4 mg- 10 % cat.) and ascorbic acid (15 mg- 10 % cat.) were dispersed in 0.5 mL of water and added to the reaction mixture as catalyst. The reaction was kept under nitrogen atmosphere and magnetic stirring overnight. Cation exchange resin (Dowex®, 50 W x 8 100-200 mesh) was added to the mixture and after 10 minutes of stirring, the resin was eliminated by filtration through a Büchner funnel with glass wool. The filtrate product was purified by gel permeation chromatography using a Sephadex G15. The fractions obtained were freeze-dried obtaining a violet powder (CDs-PEG_4-β-Cdx).

6.6.6. Physico-chemical characterization of CDs-PEG_4-β-Cdx and precursors

The size distribution of CDs-PEG_4-β-Cdx was evaluated based on their height from the atomic force microscopy (AFM) images. The sample was prepared by depositing 10 µL of aqueous dispersion of CDs-PEG_4-β-Cdx (0.1 mg mL^{-1}) on a mica substrate and then dried in vacuum. AFM measurements were carried out in air using a Bruker FAST-SCAN microscope equipped with a closed-loop scanner (X, Y, Z maximum scan region: 35 µm, 35 µm, 3 µm, respectively). Scans were obtained in soft tapping mode using a FAST-SCAN-A probe with an apical radius of about 5 nm and each image was obtained with a resolution comparable to the tip radius.
The conjugation ratio between CDs-PEG_4-CC and β-Cdx-N_3 was assessed by DSC and TGA analysis, using a DSC/TGA 131 EVO (by SETARAM Instr.). The analyses were performed using about 4 mg of dried powder of either CDs-PEG_4-CC, β-Cdx-N_3, or CDs-

PEG$_4$-β-Cdx and were placed into an aluminum crucible under nitrogen flow (1 mL min^{-1}).

6.6.7. Optical characterization of CDs-PEG$_4$-β-Cdx and precursors

The optical absorption and emission properties of CDs, CDs-PEG$_4$-CC, and CDs-PEG$_4$-β-Cdx were evaluated on aqueous dispersions of CDs and CDs-PEG$_4$-CC (0.25 mg mL^{-1}). The absorption spectra were carried out by using a double-beam spectrophotometer (Shimadzu UV-2401PC) recording the spectra in the range of 200-800 nm. The emission spectra under excitation at 360 and 540 nm were recorded by a spectrofluorometer (Jasco FP-8500). The photothermal conversion capacity of CDs, CDs-PEG$_4$-CC, and CDs-PEG$_4$-β-Cdx was assessed by irradiating a dispersion of each sample (0.1 mg mL^{-1}) with an 810 nm diode laser (GBox 15A/B di GIGA Laser) at 5 W cm^{-2} for 300 s. At the scheduled intervals of time (Δt=50 s) the temperature was measured by an optical fiber (CEM®). Water was used as control.

6.6.8. Preparation of Sildenafil-loaded CDs-PEG$_4$-β-Cdx nanosystems (CDs-PEG$_4$-β-Cdx@SD)

CDs-PEG$_4$-β-Cdx@SD were prepared via the kneading method. In particular, dried powders of CDs-PEG$_4$-β-Cdx (20 mg) and sildenafil citrate (SD, 5 mg) were pounded in a mortar until a homogeneous mixture was obtained. The powders were then kneaded adding several aliquots of a mixture of ethanol/water (ratio 2:1, V_{tot} 3 mL) which has been let evaporate during the process, obtaining a thin film that was thereafter suspended in ultrapure water (4 mL). The suspension was stirred for 1 h and subsequently dialyzed for 1h against water, using a SpectraPor® Float-A-Lyzer®G2 (MWCO 100-500 Da). The product was retrieved as brown powder via freeze-drying.

6.6.9. Drug-loading and drug-release determination of CDs-PEG$_4$-β-Cdx@SD

The SC content of loaded CDs-PEG$_4$-β-Cdx was determined via HPLC analysis as reported in the literature [374], with some modifications. CDs-PEG$_4$-β-Cdx@SC were dissolved in a mixture of acetonitrile/water (pH=4) 35:65, which represents the eluent solution for HPLC analysis, and stirred via sonication (2 h). The analysis of the sample

was performed using an Agilent 1260 infinity HPLC System and a C_6-Phenyl column (Phenomenex®) in isocratic conditions, with the mobile phase previously described (flow rate 0,8 mL min^{-1}, temperature 25 °C). The UV absorption of SD was detected at 291 nm. The retention time was 4,8 min. The sample's peak area was compared with a calibration curve obtained plotting peak areas versus concentration of SD standard solutions ranging from 0,1 to 0,005 mg mL^{-1} ($y=28705x$, $R^2=0,999$).
For the evaluation of drug release kinetic, either free SC or CDs-PEG_4-β-Cdx@SD, in such quantity as to obtain an equivalent drug concentration (0,19 mg mL^{-1}), were dissolved in a PBS solution (pH=7.4) containing 1 % Tween 80 and placed into a dialysis tubing of 1 kDa MWCO against 10 mL of the same medium. At scheduled time intervals (1, 2, 4, 6, 8, 24, and 48 h), 0,5 mL of the extern medium was withdrawn and replaced with fresh medium. The amount of SD in each sampling was determined by HPLC, using the method previously described for the drug loading determination. The samples' peak areas were compared with a calibration curve obtained plotting peak areas versus concentration of SC standards solutions in Phosphate Buffered Saline (PBS) (pH=7.4) containing 1 % Tween 80, at concentration ranging from 0,019 to 0,001 mg mL^{-1} ($y=89220x$, $R^2=1$). The obtained data were used to calculate the drug's cumulative release over time.

6.6.10. Cytocompatibility study of CDs-PEG_4-β-Cdx and CDs-PEG_4-β-Cdx@SD

The cytocompatibility of conjugate CDs-PEG_4-β-Cdx was evaluated in vitro on normal cell line (human bronchial epithelial cell, 16-HBE, and normal human dermal fibroblast, NHDF) and cancer cell line (breast cancer cell, MCF-7). Each cell line was seeded on a 96 wells-plate with a cell density of 1.5×10^4 for well and cultured in Dulbecco's Minimum Essential Medium (DMEM) at 37 °C and 5 % CO_2. After 24 h of incubation, the culture medium was replaced with a dispersion of CDs-PEG_4-β-Cdx in fresh medium (200 µL) at different concentrations (0.6-0.01 mg mL^{-1}). After 24 h the dispersion was removed and each well was washed three times with Dulbecco's phosphate-buffered saline (DPBS) at pH 7.4. Then, cell viability was evaluated by MTS assay, treating each well with 100 µL of fresh DMEM and 20 µL of MTS solution. After 2 h of incubation, the absorbance at 492 nm was measured by using a microplate reader (Multiskan, Thermo, U.K.).

Untreated cells were used as control. The data of absorbance were reported in terms of cell viability against control (viability 100 %) in the function of compound concentration. Cytotoxicity of both free SC and CDs-PEG$_4$-β-Cdx@SD was evaluated by MTS assay as above described, using different concentrations corresponding to equivalent concentrations of free drug ranging from 5×10^{-2} to 5×10^{-5} mg mL^{-1}.

All biological experiments were performed in triplicate.

6.6.11. Cell uptake of CDs-PEG$_4$-β-Cdx on 2-D cell culture model in vitro

The capacity of cell internalization of CDs-PEG$_4$-β-Cdx was performed in vitro on 16-HBE, NHDF, and MCF-7 cell models. In detail, cells were seeded on an 8 wells-plate at a cell density of 5×10^3 per well and cultured in DMEM for 24 h. Successively, the medium was replaced with 200 µL of CDs-PEG$_4$-β-Cdx dispersion in DMEM (0.15 mg mL^{-1}). After 24 h of incubation, the medium was removed and each well was washed three times with DPBS and fixed with a 4 % solution of buffered formaldehyde. Cell uptake images were recorded with a fluorescence microscope Axio Cam MRm (Zeiss).

7. References

1. Mauro, N.; Utzeri, M.A.; Varvarà, P.; Cavallaro, G. Functionalization of Metal and Carbon Nanoparticles with Potential in Cancer Theranostics. *Molecules* **2021**, doi:10.3390/molecules26113085.
2. Sciortino, A.; Cannizzo, A.; Messina, F. Carbon Nanodots: A Review—From the Current Understanding of the Fundamental Photophysics to the Full Control of the Optical Response. *C 2018, Vol. 4, Page 67* **2018**, *4*, 67, doi:10.3390/C4040067.
3. Mauro, N.; Utzeri, M.A.; Buscarino, G.; Sciortino, A.; Messina, F.; Cavallaro, G.; Giammona, G. Pressure-Dependent Tuning of Photoluminescence and Size Distribution of Carbon Nanodots for Theranostic Anticancer Applications. *Materials (Basel).* **2020**, *13*, 4899, doi:10.3390/ma13214899.
4. Mauro, N.; Utzeri, M.A.; Drago, S.E.; Nicosia, A.; Costa, S.; Cavallaro, G.; Giammona, G. Hyaluronic Acid Dressing of Hydrophobic Carbon Nanodots: A Self-Assembling Strategy of Hybrid Nanocomposites with Theranostic Potential. *Carbohydr. Polym.* **2021**, doi:10.1016/j.carbpol.2021.118213.
5. Łukasiewicz, S.; Czeczelewski, M.; Forma, A.; Baj, J.; Sitarz, R.; Stanisławek, A. Breast Cancer—Epidemiology, Risk Factors, Classification, Prognostic Markers, and Current Treatment Strategies—An Updated Review. *Cancers (Basel).* **2021**, *13*, 1–30, doi:10.3390/cancers13174287.
6. Moolgavkar, S.H.; Luebeck, E.G. Multistage Carcinogenesis and the Incidence of Human Cancer. *Genes Chromosom. Cancer* **2003**, *38*, 302–306, doi:10.1002/gcc.10264.
7. Hanahan, D.; Weinberg, R.A. The Hallmarks of Cancer. *Cell* **2022**, *100*, 57–70, doi:10.1107/S2059798322003928.
8. Sung, H.; Ferlay, J.; Siegel, R.L.; Laversanne, M.; Soerjomataram, I.; Jemal, A.; Bray, F. Global Cancer Statistics 2020: GLOBOCAN Estimates of Incidence and Mortality Worldwide for 36 Cancers in 185 Countries. *CA. Cancer J. Clin.* **2021**, *71*, 209–249, doi:10.3322/caac.21660.
9. Ferlay, J.; Laversanne, M.; Ervik, M.; Lam, F.; Colombet, M.; Mery, L.; Piñeros, M.; Znaor, A.; Soerjomataram, I.; Bray, F. Global Cancer Observatory: Cancer Tomorrow. International Agency for Research on Cancer.
10. Tavassoli, F.A. *Pathology and Genetics of Tumours of the Breast and Female Genital Organs; World Health Organization Classification of Tumours*; 2003;
11. Dai, X.; Li, T.; Bai, Z.; Yang, Y.; Liu, X.; Zhan, J.; Shi, B. Breast Cancer Intrinsic Subtype Classification, Clinical Use and Future Trends. *Am J Cancer Res* **2015**, *5*, 2929–2943.
12. Bardou, V.J.; Arpino, G.; Elledge, R.M.; Osborne, C.K.; Clark, G.M. Progesterone Receptor Status Significantly Improves Outcome Prediction over Estrogen Receptor Status Alone for Adjuvant Endocrine Therapy in Two Large

Breast Cancer Databases. *J. Clin. Oncol.* **2003**, *21*, 1973–1979, doi:10.1200/JCO.2003.09.099.

13. Visvader, J.E. Cells of Origin in Cancer. *Nature* **2011**, *469*, 314–322, doi:10.1038/nature09781.

14. Veronesi, U.; Boyle, P.; Goldhirsch, A.; Orecchia, R.; Viale, G. Breast Cancer. *Lancet* **2005**, *365*, 1727–1741, doi:10.1016/S0140-6736(05)66546-4.

15. Torre, L.A.; Bray, F.; Siegel, R.L.; Ferlay, J.; Lortet-Tieulent, J.; Jemal, A. Global Cancer Statistics, 2012. *CA. Cancer J. Clin.* **2015**, *65*, 87–108, doi:10.3322/CAAC.21262.

16. Koboldt, D.C.; Fulton, R.S.; McLellan, M.D.; Schmidt, H.; Kalicki-Veizer, J.; McMichael, J.F.; Fulton, L.L.; Dooling, D.J.; Ding, L.; Mardis, E.R.; et al. Comprehensive Molecular Portraits of Human Breast Tumours. *Nat. 2012 4907418* **2012**, *490*, 61–70, doi:10.1038/nature11412.

17. Prat, A.; Parker, J.S.; Karginova, O.; Fan, C.; Livasy, C.; Herschkowitz, J.I.; He, X.; Perou, C.M. Phenotypic and Molecular Characterization of the Claudin-Low Intrinsic Subtype of Breast Cancer. *Breast Cancer Res.* **2010**, *12*, 1–18, doi:10.1186/BCR2635.

18. Dean-Colomb, W.; Esteva, F.J. Her2-Positive Breast Cancer: Herceptin and Beyond. *Eur. J. Cancer* **2008**, *44*, 2806–2812, doi:10.1016/J.EJCA.2008.09.013.

19. Dunnwald, L.K.; Rossing, M.A.; Li, C.I. Hormone Receptor Status, Tumor Characteristics, and Prognosis: A Prospective Cohort of Breast Cancer Patients. *Breast Cancer Res.* **2007**, *9*, doi:10.1186/BCR1639.

20. Feng, Y.; Spezia, M.; Huang, S.; Yuan, C.; Zeng, Z.; Zhang, L.; Ji, X.; Liu, W.; Huang, B.; Luo, W.; et al. Breast Cancer Development and Progression: Risk Factors, Cancer Stem Cells, Signaling Pathways, Genomics, and Molecular Pathogenesis. *Genes Dis.* **2018**, *5*, 77–106, doi:10.1016/j.gendis.2018.05.001.

21. Cheang, M.C.U.; Voduc, D.; Bajdik, C.; Leung, S.; McKinney, S.; Chia, S.K.; Perou, C.M.; Nielsen, T.O. Basal-like Breast Cancer Defined by Five Biomarkers Has Superior Prognostic Value than Triple-Negative Phenotype. *Clin. Cancer Res.* **2008**, *14*, 1368–1376, doi:10.1158/1078-0432.CCR-07-1658.

22. Hudis, C.A.; Gianni, L. Triple-Negative Breast Cancer: An Unmet Medical Need. *Oncologist* **2011**, *16*, 1–11, doi:10.1634/THEONCOLOGIST.2011-S1-01.

23. Gonçalves, H.; Guerra, M.R.; Duarte Cintra, J.R.; Fayer, V.A.; Brum, I.V.; Bustamante Teixeira, M.T. Survival Study of Triple-Negative and Non–Triple-Negative Breast Cancer in a Brazilian Cohort. *Clin. Med. Insights Oncol.* **2018**, *12*, doi:10.1177/1179554918790563.

24. Januškevičienė, I.; Petrikaitė, V. Heterogeneity of Breast Cancer: The Importance of Interaction between Different Tumor Cell Populations. *Life Sci.* **2019**, *239*, 117009, doi:10.1016/j.lfs.2019.117009.

25. Andrechek, E.R.; Nevins, J.R.; Andrechek, E.R.; Nevins, J.R. Mouse Models of Cancers: Opportunities to Address Heterogeneity of Human Cancer and Evaluate

Therapeutic Strategies. *J Mol Med* **2010**, *88*, 1095–1100, doi:10.1007/s00109-010-0644-z.

26. Tlsty, T.D.; Coussens, L.M. Tumor Stroma and Regulation of Cancer Development. *Annu. Rev. Pathol.* **2006**, *1*, 119–150, doi:10.1146/annurev.pathol.1.110304.100224.
27. Cassidy, J.W.; Caldas, C.; Bruna, A. Maintaining Tumor Heterogeneity in Patient-Derived Tumor Xenografts. *Cancer Res.* **2015**, *75*, 2963–2968, doi:10.1158/0008-5472.CAN-15-0727.
28. Whiteside, T.L. The Tumor Microenvironment and Its Role in Promoting Tumor Growth. *Oncogene* **2008**, *27*, 5904–5912, doi:10.1038/onc.2008.271.
29. Mcmillin, D.W.; Negri, J.M.; Mitsiades, C.S. The Role of Tumour-Stromal Interactions in Modifying Drug Response: Challenges and Opportunities. *Nat. Rev. Drug Discov.* **2013**, *12*, 217–228, doi:10.1038/nrd3870.
30. Li, J.J.; Tsang, J.Y.; Tse, G.M. Tumor Microenvironment in Breast Cancer—Updates on Therapeutic Implications and Pathologic Assessment. *Cancers (Basel).* **2021**, *13*, doi:10.3390/cancers13164233.
31. Bahcecioglu, G.; Basara, G.; Ellis, B.W.; Ren, X.; Zorlutuna, P. Breast Cancer Models: Engineering the Tumor Microenvironment. *Acta Biomater.* **2020**, *106*, 1–21, doi:10.1016/j.actbio.2020.02.006.
32. Soysal, S.D.; Tzankov, A.; Muenst, S.E. Role of the Tumor Microenvironment in Breast Cancer. *Pathobiology* **2015**, *82*, 142–152, doi:10.1159/000430499.
33. Atiya, H.; Frisbie, L.; Pressimone, C.; Coffman, L. *Mesenchymal Stem Cells in the Tumor Microenvironment*; 2020; Vol. 1234; ISBN 9783030371838.
34. Anderson, N.M.; Simon, M.C. The Tumor Microenvironment. *Curr. Biol.* **2020**, *30*, R921–R925, doi:10.1016/j.cub.2020.06.081.
35. Junttila, M.R.; De Sauvage, F.J. Influence of Tumour Micro-Environment Heterogeneity on Therapeutic Response. *Nat. 2013 5017467* **2013**, *501*, 346–354, doi:10.1038/nature12626.
36. Hanahan, D.; Weinberg, R.A. Hallmarks of Cancer: The next Generation. *Cell* **2011**, *144*, 646–674, doi:10.1016/J.CELL.2011.02.013.
37. Martinez-Outschoorn, U.E.; Lisanti, M.P.; Sotgia, F. Catabolic Cancer-Associated Fibroblasts Transfer Energy and Biomass to Anabolic Cancer Cells, Fueling Tumor Growth. *Semin. Cancer Biol.* **2014**, *25*, 47–60, doi:10.1016/J.SEMCANCER.2014.01.005.
38. Sugimoto, H.; Mundel, T.M.; Kieran, M.W.; Kalluri, R. Identification of Fibroblast Heterogeneity in the Tumor Microenvironment. *Cancer Biol. Ther.* **2006**, *5*, 1640–1646, doi:10.4161/CBT.5.12.3354.
39. Bonnans, C.; Chou, J.; Werb, Z. Remodelling the Extracellular Matrix in Development and Disease. *Nat. Rev. Mol. Cell Biol.* **2014**, *15*, 786–801, doi:10.1038/NRM3904.

40. Roy, D.M.; Walsh, L.A. Candidate Prognostic Markers in Breast Cancer: Focus on Extracellular Proteases and Their Inhibitors. *Breast Cancer Targets Ther.* **2014**, *6*, 81–91, doi:10.2147/BCTT.S46020.

41. Lu, P.; Weaver, V.M.; Werb, Z. The Extracellular Matrix: A Dynamic Niche in Cancer Progression. *J. Cell Biol.* **2012**, *196*, 395–406, doi:10.1083/JCB.201102147.

42. Waks, A.G.; Winer, E.P. Breast Cancer Treatment: A Review. *JAMA - J. Am. Med. Assoc.* **2019**, *321*, 288–300, doi:10.1001/jama.2018.19323.

43. Feng, Y.; Spezia, M.; Huang, S.; Yuan, C.; Zeng, Z.; Zhang, L.; Ji, X.; Liu, W.; Huang, B.; Luo, W.; et al. Breast Cancer Development and Progression: Risk Factors, Cancer Stem Cells, Signaling Pathways, Genomics, and Molecular Pathogenesis. *Genes Dis.* **2018**, *5*, 77–106, doi:10.1016/J.GENDIS.2018.05.001.

44. Anampa, J.; Makower, D.; Sparano, J.A. Progress in Adjuvant Chemotherapy for Breast Cancer: An Overview. *BMC Med.* **2015**, *13*, 1–13, doi:10.1186/s12916-015-0439-8.

45. Beral, V.; Bull, D.; Doll, R.; Peto, R.; Reeves, G.; Skegg, D.; Colditz, G.; Hulka, B.; La Vecchia, C.; Magnusson, C.; et al. Familial Breast Cancer: Collaborative Reanalysis of Individual Data from 52 Epidemiological Studies Including 58 209 Women with Breast Cancer and 101 986 Women without the Disease. *Lancet* **2001**, *358*, 1389–1399, doi:10.1016/S0140-6736(01)06524-2.

46. Moorthi, C.; Manavalan, R.; Kathiresan, K. Nanotherapeutics to Overcome Conventional Cancer Chemotherapy Limitations. *J. Pharm. Pharm. Sci.* **2011**, *14*, 67–77, doi:10.18433/J30C7D.

47. Holohan, C.; Van Schaeybroeck, S.; Longley, D.B.; Johnston, P.G. Cancer Drug Resistance: An Evolving Paradigm. *Nat. Rev. Cancer* **2013**, *13*, 714–726, doi:10.1038/NRC3599.

48. Corrie, P.G. Cytotoxic Chemotherapy: Clinical Aspects. *Medicine (Baltimore).* **2008**, *36*, 24–28, doi:10.1016/j.mpmed.2007.10.012.

49. Holohan, C.; Van Schaeybroeck, S.; Longley, D.B.; Johnston, P.G. Cancer Drug Resistance: An Evolving Paradigm. *Nat. Rev. Cancer* **2013**, *13*, 714–726, doi:10.1038/nrc3599.

50. Dittmer, J.; Leyh, B. The Impact of Tumor Stroma on Drug Response in Breast Cancer. *Semin. Cancer Biol.* **2015**, *31*, 3–15, doi:10.1016/j.semcancer.2014.05.006.

51. Longley, D.B.; Johnston, P.G. Molecular Mechanisms of Drug Resistance. *J. Pathol.* **2005**, *205*, 275–292, doi:10.1002/PATH.1706.

52. Sun, Y. Tumor Microenvironment and Cancer Therapy Resistance. *Cancer Lett.* **2016**, *380*, 205–215, doi:10.1016/j.canlet.2015.07.044.

53. Swanton, C. Intratumor Heterogeneity: Evolution through Space and Time. *Cancer Res.* **2012**, *72*, 4875–4882, doi:10.1158/0008-5472.

54. Gottesman, M.M.; Fojo, T.; Bates, S.E. Multidrug Resistance in Cancer: Role of ATP–Dependent Transporters. *Nat. Rev. Cancer 2002 21* **2002**, *2*, 48–58, doi:10.1038/nrc706.

55. Robey, R.W.; Pluchino, K.M.; Hall, M.D.; Fojo, A.T.; Bates, S.E.; Gottesman, M.M. Revisiting the Role of ABC Transporters in Multidrug-Resistant Cancer. *Nat. Rev. Cancer* **2018**, *18*, 452–464, doi:10.1038/s41568-018-0005-8.

56. Triller, N.; Korošec, P.; Kern, I.; Košnik, M.; Debeljak, A. Multidrug Resistance in Small Cell Lung Cancer: Expression of P-Glycoprotein, Multidrug Resistance Protein 1 and Lung Resistance Protein in Chemo-Naive Patients and in Relapsed Disease. *Lung Cancer* **2006**, *54*, 235–240, doi:10.1016/j.lungcan.2006.06.019.

57. Zalcberg, J.; Hu, X.F.; Slater, A.; Parisot, J.; El-Osta, S.; Kantharidis, P.; Chou, S.T.; Parkin, J.D. MRP1 Not MDR1 Gene Expression Is the Predominant Mechanism of Acquired Multidrug Resistance in Two Prostate Carcinoma Cell Lines. *Prostate Cancer Prostatic Dis. 2000 32* **2000**, *3*, 66–75, doi:10.1038/sj.pcan.4500394.

58. Doyle, L.A.; Yang, W.; Abruzzo, L. V; Krogmann, T.; Gao, Y.; Rishi, A.K.; Ross, D.D. A Multidrug Resistance Transporter from Human MCF-7 Breast Cancer Cells (Mitoxantroneanthracyclinestransporter Proteins). **1998**, *95*, 15665–15670.

59. Ganoth, A.; Merimi, K.C.; Peer, D. Overcoming Multidrug Resistance with Nanomedicines. *Expert Opin. Drug Deliv.* **2015**, *12*, 223–238, doi:10.1517/17425247.2015.960920.

60. Peer, D.; Karp, J.M.; Hong, S.; Farokhzad, O.C.; Margalit, R.; Langer, R. Nanocarriers as an Emerging Platform for Cancer Therapy. *Nat. Nanotechnol.* **2007**, *2*, 751–760, doi:10.1038/NNANO.2007.387.

61. Wicki, A.; Witzigmann, D.; Balasubramanian, V.; Huwyler, J. Nanomedicine in Cancer Therapy: Challenges, Opportunities, and Clinical Applications. *J. Control. Release* **2015**, *200*, 138–157, doi:10.1016/j.jconrel.2014.12.030.

62. Tran, S.; DeGiovanni, P.-J.; Piel, B.; Rai, P. Cancer Nanomedicine: A Review of Recent Success in Drug Delivery. *Clin. Transl. Med.* **2017**, *6*, e44, doi:10.1186/S40169-017-0175-0.

63. von Roemeling, C.; Jiang, W.; Chan, C.K.; Weissman, I.L.; Kim, B.Y.S. Breaking Down the Barriers to Precision Cancer Nanomedicine. *Trends Biotechnol.* **2017**, *35*, 159–171, doi:10.1016/J.TIBTECH.2016.07.006.

64. Shi, J.; Kantoff, P.W.; Wooster, R.; Farokhzad, O.C. Cancer Nanomedicine: Progress, Challenges and Opportunities. *Nat. Rev. Cancer 2016 171* **2016**, *17*, 20–37, doi:10.1038/nrc.2016.108.

65. Kajani, A.A.; Javanmard, S.H.; Asadnia, M.; Razmjou, A. Recent Advances in Nanomaterials Development for Nanomedicine and Cancer. **2021**, doi:10.1021/acsabm.1c00591.

66. Yetisgin, A.A.; Cetinel, S.; Zuvin, M.; Kosar, A.; Kutlu, O. Therapeutic

Nanoparticles and Their Targeted Delivery Applications. *Molecules* **2020**, *25*, doi:10.3390/MOLECULES25092193.

67. García, K.P.; Zarschler, K.; Barbaro, L.; Barreto, J.A.; O'Malley, W.; Spiccia, L.; Stephan, H.; Graham, B. Zwitterionic-Coated "Stealth" Nanoparticles for Biomedical Applications: Recent Advances in Countering Biomolecular Corona Formation and Uptake by the Mononuclear Phagocyte System. *Small* **2014**, *10*, 2516–2529, doi:10.1002/SMLL.201303540.

68. Chow, A.; Brown, B.D.; Merad, M. Studying the Mononuclear Phagocyte System in the Molecular Age. *Nat. Rev. Immunol.* **2011**, *11*, 788–798, doi:10.1038/nri3087.

69. Desai, N. Nanotechnology in Drug Development. **2012**, doi:10.1208/s12248-012-9339-4.

70. Miele, E.; Spinelli, G.P.; Miele, E.; Tomao, F.; Tomao, S. Albumin-Bound Formulation of Paclitaxel (Abraxane ® ABI-007) in the Treatment of Breast Cancer. *Int. J. Nanomedicine* **2009**, 4–99.

71. Chen, B.; Dai, W.; He, B.; Zhang, H.; Wang, X.; Wang, Y.; Zhang, Q. Current Multistage Drug Delivery Systems Based on the Tumor Microenvironment. *Theranostics* **2017**, *7*, 538–558, doi:10.7150/THNO.16684.

72. Liu, J.; Yu, M.; Zhou, C.; Zheng, J. Renal Clearable Inorganic Nanoparticles: A New Frontier of Bionanotechnology. *Mater. Today* **2013**, *16*, 477–486, doi:10.1016/j.mattod.2013.11.003.

73. Stylianopoulos, T.; Wong, C.; Bawendi, M.G.; Jain, R.K.; Fukumura, D. Multistage Nanoparticles for Improved Delivery into Tumor Tissue. *Methods Enzymol.* **2012**, *508*, 109–130, doi:10.1016/B978-0-12-391860-4.00006-9.

74. Trédan, O.; Galmarini, C.M.; Patel, K.; Tannock, I.F. Drug Resistance and the Solid Tumor Microenvironment. *JNCI J. Natl. Cancer Inst.* **2007**, *99*, 1441–1454, doi:10.1093/JNCI/DJM135.

75. Liu, M.; Du, H.; Zhang, W.; Zhai, G. Internal Stimuli-Responsive Nanocarriers for Drug Delivery: Design Strategies and Applications. *Mater. Sci. Eng. C* **2017**, *71*, 1267–1280, doi:10.1016/j.msec.2016.11.030.

76. Wicki, A.; Witzigmann, D.; Balasubramanian, V.; Huwyler, J. Nanomedicine in Cancer Therapy: Challenges, Opportunities, and Clinical Applications. *J. Control. Release* **2015**, *200*, 138–157, doi:10.1016/J.JCONREL.2014.12.030.

77. Blanco, E.; Shen, H.; Ferrari, M. Principles of Nanoparticle Design for Overcoming Biological Barriers to Drug Delivery. *Nat. Biotechnol.* **2015**, *33*, 941–951, doi:10.1038/NBT.3330.

78. Kalluri, R. Basement Membranes: Structure, Assembly and Role in Tumour Angiogenesis. *Nat. Rev. Cancer* **2003**, *3*, 422–433, doi:10.1038/NRC1094.

79. Rosenblum, D.; Joshi, N.; Tao, W.; Karp, J.M.; Peer, D. Progress and Challenges towards Targeted Delivery of Cancer Therapeutics. *Nat. Commun.* **2018**, *9*, doi:10.1038/s41467-018-03705-y.

80. Chauhan, V.P.; Stylianopoulos, T.; Martin, J.D.; Popovic´5, Z.; Popovic´5, P.; Chen, O.; Kamoun, W.S.; Bawendi, M.G.; Fukumura, D.; Jain, R.K. Normalization of Tumour Blood Vessels Improves the Delivery of Nanomedicines in a Size-Dependent Manner. **2012**, doi:10.1038/NNANO.2012.45.

81. Hobbs, S.K.; Monsky, W.L.; Yuan, F.; Roberts, W.G.; Griffith, L.; Torchilin, V.P.; Jain, R.K. Regulation of Transport Pathways in Tumor Vessels: Role of Tumor Type and Microenvironment. *Proc. Natl. Acad. Sci. U. S. A.* **1998**, *95*, 4607, doi:10.1073/PNAS.95.8.4607.

82. Tang, L.; Fan, T.M.; Borst, L.B.; Cheng, J. Synthesis and Biological Response of Size-Specific, Monodisperse Drug–Silica Nanoconjugates. **2012**, doi:10.1021/NN300149C.

83. Wong, C.; Stylianopoulos, T.; Cui, J.; Martin, J.; Chauhan, V.P.; Jiang, W.; Popovíc, Z.; Jain, R.K.; Bawendi, M.G.; Fukumura, D. Multistage Nanoparticle Delivery System for Deep Penetration into Tumor Tissue. *Proc. Natl. Acad. Sci. U. S. A.* **2011**, *108*, 2426–2431, doi:10.1073/PNAS.1018382108.

84. Jain, R.K.; Stylianopoulos, T. Delivering Nanomedicine to Solid Tumors. *Nat. Rev. Clin. Oncol. 2010 711* **2010**, *7*, 653–664, doi:10.1038/nrclinonc.2010.139.

85. Stacker, S.A.; Williams, S.P.; Karnezis, T.; Shayan, R.; Fox, S.B.; Achen, M.G. Lymphangiogenesis and Lymphatic Vessel Remodelling in Cancer. *Nat. Rev. Cancer* **2014**, *14*, 159–172, doi:10.1038/NRC3677.

86. Shi, Y.; van der Meel, R.; Chen, X.; Lammers, T. The EPR Effect and beyond: Strategies to Improve Tumor Targeting and Cancer Nanomedicine Treatment Efficacy. *Issue 17 Theranostics* **2020**, *10*, 7921–7924, doi:10.7150/thno.49577.

87. Pearce, A.K.; O'Reilly, R.K. Insights into Active Targeting of Nanoparticles in Drug Delivery: Advances in Clinical Studies and Design Considerations for Cancer Nanomedicine. *Bioconjug. Chem.* **2019**, *30*, 2300–2311, doi:10.1021/acs.bioconjchem.9b00456.

88. Allen, T.M. Ligand-Targeted Therapeutics in Anticancer Therapy. *Nat. Rev. Cancer* **2002**, *2*, 750–763, doi:10.1038/NRC903.

89. Bareford, L.M.; Swaan, P.W. Endocytic Mechanisms for Targeted Drug Delivery. *Adv. Drug Deliv. Rev.* **2007**, *59*, 748–758, doi:10.1016/J.ADDR.2007.06.008.

90. Marcucci, F.; Lefoulon, F. Active Targeting with Particulate Drug Carriers in Tumor Therapy: Fundamentals and Recent Progress. *Drug Discov. Today* **2004**, *9*, 219–228, doi:10.1016/S1359-6446(03)02988-X.

91. Byrne, J.D.; Betancourt, T.; Brannon-Peppas, L. Active Targeting Schemes for Nanoparticle Systems in Cancer Therapeutics. *Adv. Drug Deliv. Rev.* **2008**, *60*, 1615–1626, doi:10.1016/J.ADDR.2008.08.005.

92. Allen, T.M. Ligand-Targeted Therapeutics in Anticancer Therapy. *Nat. Rev. Cancer 2002 210* **2002**, *2*, 750–763, doi:10.1038/nrc903.

93. Chauhan, V.P.; Jain, R.K. Strategies for Advancing Cancer Nanomedicine. *Nat. Mater.* **2013**, *12*, 958–962, doi:10.1038/NMAT3792.

94. de la Rica, R.; Aili, D.; Stevens, M.M. Enzyme-Responsive Nanoparticles for Drug Release and Diagnostics. *Adv. Drug Deliv. Rev.* **2012**, *64*, 967–978, doi:10.1016/j.addr.2012.01.002.

95. Go, Y.M.; Jones, D.P. Redox Compartmentalization in Eukaryotic Cells. *Biochim. Biophys. Acta - Gen. Subj.* **2008**, *1780*, 1273–1290, doi:10.1016/j.bbagen.2008.01.011.

96. Zhang, F.; Braun, G.B.; Pallaoro, A.; Zhang, Y.; Shi, Y.; Cui, D.; Moskovits, M.; Zhao, D.; Stucky, G.D. Mesoporous Multifunctional Upconversion Luminescent and Magnetic "Nanorattle" Materials for Targeted Chemotherapy. *Nano Lett.* **2012**, *12*, 61–67, doi:10.1021/nl202949y.

97. Schroeder, A.; Honen, R.; Turjeman, K.; Gabizon, A.; Kost, J.; Barenholz, Y. Ultrasound Triggered Release of Cisplatin from Liposomes in Murine Tumors. *J. Control. Release* **2009**, *137*, 63–68, doi:10.1016/j.jconrel.2009.03.007.

98. Chen, K.J.; Liang, H.F.; Chen, H.L.; Wang, Y.; Cheng, P.Y.; Liu, H.L.; Xia, Y.; Sung, H.W. A Thermoresponsive Bubble-Generating Liposomal System for Triggering Localized Extracellular Drug Delivery. *ACS Nano* **2013**, *7*, 438–446, doi:10.1021/nn304474j.

99. Lu, J.; Choi, E.; Tamanoi, F.; Zink, J.I. Light-Activated Nanoimpeller-Controlled Drug Release in Cancer Cells. *Small* **2008**, *4*, 421–426, doi:10.1002/smll.200700903.

100. Plassat, V.; Wilhelm, C.; Marsaud, V.; Ménager, C.; Gazeau, F.; Renoir, J.M.; Lesieur, S. Anti-Estrogen-Loaded Superparamagnetic Liposomes for Intracellular Magnetic Targeting and Treatment of Breast Cancer Tumors. *Adv. Funct. Mater.* **2011**, *21*, 83–92, doi:10.1002/adfm.201001450.

101. Heiden, M.G.V.; Cantley, L.C.; Thompson, C.B. Understanding the Warburg Effect: The Metabolic Requirements of Cell Proliferation. *Science (80-.).* **2009**, *324*, 1029–1033, doi:10.1126/science.1160809.

102. Gatenby, R.A.; Gillies, R.J. Why Do Cancers Have High Aerobic Glycolysis? *Nat. Rev. Cancer* **2004**, *4*, 891–899, doi:10.1038/nrc1478.

103. He, X.; Li, J.; An, S.; Jiang, C. PH-Sensitive Drug-Delivery Systems for Tumor Targeting. *Ther. Deliv.* **2013**, *4*, 1499–1510, doi:10.4155/tde.13.120.

104. Egeblad, M.; Werb, Z. New Functions for the Matrix Metalloproteinases in Cancer Progression. *Nat. Rev. Cancer* **2002**, *2*, 161–174, doi:10.1038/nrc745.

105. Kessenbrock, K.; Plaks, V.; Werb, Z. Matrix Metalloproteinases: Regulators of the Tumor Microenvironment. *Cell* **2010**, *141*, 52–67, doi:10.1016/j.cell.2010.03.015.

106. He, Q.; Chen, J.; Yan, J.; Cai, S.; Xiong, H.; Liu, Y.; Peng, D.; Mo, M.; Liu, Z. Tumor Microenvironment Responsive Drug Delivery Systems. *Asian J. Pharm. Sci.* **2020**, *15*, 416–448, doi:10.1016/J.AJPS.2019.08.003.

107. Kuppusamy, P.; Li, H.; Ilangovan, G.; Cardounel, A.J.; Zweier, J.L.; Yamada, K.; Krishna, M.C.; Mitchell, J.B. Noninvasive Imaging of Tumor Redox Status and Its Modification by Tissue Glutathione Levels. *Cancer Res.* **2002**, *62*, 307–312.

108. P. Kuppusamy, H. Li, G. Ilangovan, A.J. Cardounel, J.L. Zweier, K. Yamada, et al. Noninvasive Imaging of Tumor Redox Status and Its Modification by Tissue Glutathione Levels1 | Cancer Research | American Association for Cancer Research. *Cancer Res.* **2002**, *62*, 307–312.

109. Kim, H.; Kim, S.; Park, C.; Lee, H.; Park, H.J.; Kim, C. Glutathione-Induced Intracellular Release of Guests from Mesoporous Silica Nanocontainers with Cyclodextrin Gatekeepers. *Adv. Mater.* **2010**, *22*, 4280–4283, doi:10.1002/adma.201001417.

110. Li, J.; Huo, M.; Wang, J.; Zhou, J.; Mohammad, J.M.; Zhang, Y.; Zhu, Q.; Waddad, A.Y.; Zhang, Q. Redox-Sensitive Micelles Self-Assembled from Amphiphilic Hyaluronic Acid-Deoxycholic Acid Conjugates for Targeted Intracellular Delivery of Paclitaxel. *Biomaterials* **2012**, *33*, 2310–2320, doi:10.1016/j.biomaterials.2011.11.022.

111. Sun, Y.; Yan, X.; Yuan, T.; Liang, J.; Fan, Y.; Gu, Z.; Zhang, X. Disassemblable Micelles Based on Reduction-Degradable Amphiphilic Graft Copolymers for Intracellular Delivery of Doxorubicin. *Biomaterials* **2010**, *31*, 7124–7131, doi:10.1016/j.biomaterials.2010.06.011.

112. M., S.M.; Veeranarayanan, S.; Maekawa, T.; D., S.K. External Stimulus Responsive Inorganic Nanomaterials for Cancer Theranostics. *Adv. Drug Deliv. Rev.* **2019**, *138*, 18–40, doi:10.1016/j.addr.2018.10.007.

113. Karimi, M.; Ghasemi, A.; Sahandi Zangabad, P.; Rahighi, R.; Moosavi Basri, S.M.; Mirshekari, H.; Amiri, M.; Shafaei Pishabad, Z.; Aslani, A.; Bozorgomid, M.; et al. *Smart Micro/Nanoparticles in Stimulus-Responsive Drug/Gene Delivery Systems*; Royal Society of Chemistry, 2016; Vol. 45; ISBN 1485733111.

114. Mo, S.; Coussios, C.C.; Seymour, L.; Carlisle, R. Ultrasound-Enhanced Drug Delivery for Cancer. *Expert Opin. Drug Deliv.* **2012**, *9*, 1525–1538, doi:10.1517/17425247.2012.739603.

115. Mody, V. V.; Cox, A.; Shah, S.; Singh, A.; Bevins, W.; Parihar, H. Magnetic Nanoparticle Drug Delivery Systems for Targeting Tumor. *Appl. Nanosci.* **2014**, *4*, 385–392, doi:10.1007/S13204-013-0216-Y.

116. Arruebo, M.; Fernández-Pacheco, R.; Ibarra, M.R.; Santamaría, J. Magnetic Nanoparticles for Drug Delivery. *Nano Today* **2007**, *2*, 22–32, doi:10.1016/S1748-0132(07)70084-1.

117. Kresge, A.J. Synthetic Micelle Sensitive to IR Light via a Two-Photon Process. *Chemtracts* **2005**, *18*, 546–548.

118. Linsley, C.S.; Wu, B.M. Recent Advances in Light-Responsive on-Demand Drug-Delivery Systems. *Ther. Deliv.* **2017**, *8*, 89–107, doi:10.4155/TDE-2016-

0060.

119. Ryu, J.H.; Lee, S.; Son, S.; Kim, S.H.; Leary, J.F.; Choi, K.; Kwon, I.C. Theranostic Nanoparticles for Future Personalized Medicine. *J. Control. Release* **2014**, *190*, 477–484, doi:10.1016/j.jconrel.2014.04.027.

120. Mura, S.; Couvreur, P. Nanotheranostics for Personalized Medicine. *Adv. Drug Deliv. Rev.* **2012**, *64*, 1394–1416, doi:10.1016/j.addr.2012.06.006.

121. Kumar, R.; Shin, W.S.; Sunwoo, K.; Kim, W.Y.; Koo, S.; Bhuniya, S.; Kim, J.S. Small Conjugate-Based Theranostic Agents: An Encouraging Approach for Cancer Therapy. *Chem. Soc. Rev.* **2015**, *44*, 6670–6683, doi:10.1039/C5CS00224A.

122. Xie, J.; Lee, S.; Chen, X. Nanoparticle-Based Theranostic Agents. *Adv. Drug Deliv. Rev.* **2010**, *62*, 1064–1079, doi:10.1016/j.addr.2010.07.009.

123. Pan, D. Theranostic Nanomedicine with Functional Nanoarchitecture. *Mol. Pharm.* **2013**, *10*, 781–782, doi:10.1021/mp400044j.

124. Lee, D.E.; Koo, H.; Sun, I.C.; Ryu, J.H.; Kim, K.; Kwon, I.C. Multifunctional Nanoparticles for Multimodal Imaging and Theragnosis. *Chem. Soc. Rev.* **2012**, *41*, 2656–2672, doi:10.1039/C2CS15261D.

125. Terreno, E.; Castelli, D.D.; Viale, A.; Aime, S. Challenges for Molecular Magnetic Resonance Imaging. *Chem. Rev.* **2010**, *110*, 3019–3042, doi:10.1021/cr100025t.

126. De Jong, M.; Essers, J.; Van Weerden, W.M. Imaging Preclinical Tumour Models: Improving Translational Power. *Nat. Rev. Cancer* **2014**, *14*, 481–493, doi:10.1038/nrc3751.

127. Sun, C.; Lee, J.S.H.; Zhang, M. Magnetic Nanoparticles in MR Imaging and Drug Delivery. *Adv. Drug Deliv. Rev.* **2008**, *60*, 1252–1265, doi:10.1016/J.ADDR.2008.03.018.

128. Huang, X.; Zhang, F.; Zhu, L.; Choi, K.Y.; Guo, N.; Guo, J.; Tackett, K.; Anilkumar, P.; Liu, G.; Quan, Q.; et al. Effect of Injection Routes on the Biodistribution, Clearance, and Tumor Uptake of Carbon Dots. *ACS Nano* **2013**, *7*, 5684–5693, doi:10.1021/NN401911K.

129. Lee, N.; Choi, S.H.; Hyeon, T. Nano-Sized CT Contrast Agents. *Adv. Mater.* **2013**, *25*, 2641–2660, doi:10.1002/ADMA.201300081.

130. Shilo, M.; Reuveni, T.; Motiei, M.; Popovtzer, R. Nanoparticles as Computed Tomography Contrast Agents: Current Status and Future Perspectives. *Nanomedicine* **2012**, *7*, 257–269, doi:10.2217/NNM.11.190.

131. Tepper, S.J. Computed Tomography - An Increasing Source of Radiation Exposure: CommentaryTepper, S. J. (2008). Computed Tomography - An Increasing Source of Radiation Exposure: Commentary. Headache, 48(4), 657. Https://Doi.Org/10.1111/j.1526-4610.2008.01071.X. *Headache* **2008**, *48*, 657.

132. Wang, L. V.; Hu, S. Photoacoustic Tomography: In Vivo Imaging from

Organelles to Organs. *Science (80-.).* **2012**, *335*, 1458–1462, doi:10.1126/science.1216210.

133. Nie, L.; Chen, X. Structural and Functional Photoacoustic Molecular Tomography Aided by Emerging Contrast Agents. *Chem. Soc. Rev.* **2014**, *43*, 7132–7170, doi:10.1039/c4cs00086b.
134. Rao, J.; Dragulescu-Andrasi, A.; Yao, H. Fluorescence Imaging in Vivo: Recent Advances. *Curr. Opin. Biotechnol.* **2007**, *18*, 17–25, doi:10.1016/j.copbio.2007.01.003.
135. He, X.; Wang, K.; Cheng, Z. In Vivo Near-Infrared Fluorescence Imaging of Cancer with Nanoparticle-Based Probes. *Wiley Interdiscip. Rev. Nanomedicine Nanobiotechnology* **2010**, *2*, 349–366, doi:10.1002/wnan.85.
136. Prabhu, P.; Patravale, V. The Upcoming Field of Theranostic Nanomedicine: An Overview. *J. Biomed. Nanotechnol.* **2012**, *8*, 859–882, doi:10.1166/jbn.2012.1459.
137. Sajja, H.K.; East, M.P.; Mao, H.; Wang, A.Y.; Nie, S.; Yang, L. Development of Multifunctional Nanoparticles for Targeted Drug Delivery and Non-Invasive Imaging of Therapeutic Effect. *Curr. Drug Discov. Technol.* **2009**, *6*, 43, doi:10.2174/157016309787581066.
138. Bharali, D.J.; Mousa, S.A. Emerging Nanomedicines for Early Cancer Detection and Improved Treatment: Current Perspective and Future Promise. *Pharmacol. Ther.* **2010**, *128*, 324–335, doi:10.1016/J.PHARMTHERA.2010.07.007.
139. Ho, Y.P.; Leong, K.W. Quantum Dot-Based Theranostics. *Nanoscale* **2010**, *2*, 60–68, doi:10.1039/B9NR00178F.
140. Zrazhevskiy, P.; Gao, X. Multifunctional Quantum Dots for Personalized Medicine. *Nano Today* **2009**, *4*, 414–428, doi:10.1016/J.NANTOD.2009.07.004.
141. Lee, C.; Kwon, W.; Beack, S.; Lee, D.; Park, Y.; Kim, H.; Hahn, S.K.; Rhee, S.W.; Kim, C. Biodegradable Nitrogen-Doped Carbon Nanodots for Non-Invasive Photoacoustic Imaging and Photothermal Therapy. *Theranostics* **2016**, *6*, 2196–2208, doi:10.7150/thno.16923.
142. Li, H.; Kang, Z.; Liu, Y.; Lee, S.T. Carbon Nanodots: Synthesis, Properties and Applications. *J. Mater. Chem.* **2012**, *22*, 24230–24253, doi:10.1039/c2jm34690g.
143. Soni, N.; Singh, S.; Sharma, S.; Batra, G.; Kaushik, K.; Rao, C.; Verma, N.C.; Mondal, B.; Yadav, A.; Nandi, C.K. Absorption and Emission of Light in Red Emissive Carbon Nanodots. *Chem. Sci.* **2021**, *12*, 3615–3626, doi:10.1039/d0sc05879c.
144. Roy, P.; Chen, P.C.; Periasamy, A.P.; Chen, Y.N.; Chang, H.T. Photoluminescent Carbon Nanodots: Synthesis, Physicochemical Properties and Analytical Applications. *Mater. Today* **2015**, *18*, 447–458, doi:10.1016/j.mattod.2015.04.005.
145. Cayuela, A.; Soriano, M.L.; Carrillo-Carrión, C.; Valcárcel, M. Semiconductor and Carbon-Based Fluorescent Nanodots: The Need for Consistency. *Chem.*

Commun. **2016**, *52*, 1311–1326, doi:10.1039/C5CC07754K.

146. Sciortino, A.; Mauro, N.; Buscarino, G.; Sciortino, L.; Popescu, R.; Schneider, R.; Giammona, G.; Gerthsen, D.; Cannas, M.; Messina, F. β-C3N4 Nanocrystals: Carbon Dots with Extraordinary Morphological, Structural, and Optical Homogeneity. *Chem. Mater.* **2018**, *30*, 1695–1700, doi:10.1021/acs.chemmater.7b05178.

147. Ethan LeCroy, G.; Kumar Sonkar, S.; Yang, F.; Monica Veca, L.; Wang, P.; Tackett, K.N.; Yu, J.-J.; Vasile, E.; Qian, H.; Liu, Y.; et al. Toward Structurally Defined Carbon Dots as Ultracompact Fluorescent Probes. **2014**, doi:10.1021/nn406628s.

148. Sun, Y.-P.; Zhou, B.; Lin, Y.; Wang, W.; Shiral Fernando, K.A.; Pathak, P.; Jaouad Meziani, M.; Harruff, B.A.; Wang, X.; Wang, H.; et al. Quantum-Sized Carbon Dots for Bright and Colorful Photoluminescence., doi:10.1021/ja062677d.

149. Park, Y.; Yoo, J.; Lim, B.; Kwon, W.; Rhee, S.W. Improving the Functionality of Carbon Nanodots: Doping and Surface Functionalization. *J. Mater. Chem. A* **2016**, *4*, 11582–11603, doi:10.1039/c6ta04813g.

150. Baker, S.N.; Baker, G.A.; Baker, S.N.; Baker, G.A. Luminescent Carbon Nanodots: Emergent Nanolights. *Angew. Chemie Int. Ed.* **2010**, *49*, 6726–6744, doi:10.1002/ANIE.200906623.

151. Hu, S.; Liu, J.; Yang, J.; Wang, Y.; Cao, • Shirui Laser Synthesis and Size Tailor of Carbon Quantum Dots. **2011**, doi:10.1007/s11051-011-0638-y.

152. Reyes, D.; Camacho, M.; Camacho, M.; Mayorga, M.; Weathers, D.; Salamo, G.; Wang, Z.; Neogi, A. Laser Ablated Carbon Nanodots for Light Emission. *Nanoscale Res. Lett.* **2016**, *11*, doi:10.1186/s11671-016-1638-8.

153. Li, H.; He, X.; Kang, Z.; Huang, H.; Liu, Y.; Liu, J.; Lian, S.; Him Tsang, C.A.; Yang, X.; Lee, S.-T.; et al. Quantum Dots Water-Soluble Fluorescent Carbon Quantum Dots and Photocatalyst Design, doi:10.1002/anie.200906154.

154. Arcudi, F.; Ďorďević, L.; Prato, M. Design, Synthesis, and Functionalization Strategies of Tailored Carbon Nanodots. *Acc. Chem. Res.* **2019**, *52*, 2070–2079, doi:10.1021/acs.accounts.9b00249.

155. Miao, P.; Han, K.; Tang, Y.; Wang, B.; Lin, T.; Cheng, W. Recent Advances in Carbon Nanodots: Synthesis, Properties and Biomedical Applications. *Nanoscale* **2015**, *7*, 1586–1595, doi:10.1039/c4nr05712k.

156. Zhu, H.; Wang, X.; Li, Y.; Wang, Z.; Yang, F.; Yang, X. Microwave Synthesis of Fluorescent Carbon Nanoparticles with Electrochemiluminescence Properties. *Chem. Commun.* **2009**, 5118–5120, doi:10.1039/B907612C.

157. Hu, B.; Wang, K.; Wu, L.; Yu, S.H.; Antonietti, M.; Titirici, M.M. Engineering Carbon Materials from the Hydrothermal Carbonization Process of Biomass. *Adv. Mater.* **2010**, *22*, 813–828, doi:10.1002/ADMA.200902812.

158. Scialabba, C.; Sciortino, A.; Messina, F.; Buscarino, G.; Cannas, M.; Roscigno,

G.; Condorelli, G.; Cavallaro, G.; Giammona, G.; Mauro, N. Highly Homogeneous Biotinylated Carbon Nanodots: Red-Emitting Nanoheaters as Theranostic Agents toward Precision Cancer Medicine. *ACS Appl. Mater. Interfaces* **2019**, *11*, 19854–19866, doi:10.1021/acsami.9b04925.

159. Mauro, N.; Utzeri, M.A.; Sciortino, A.; Messina, F.; Cannas, M.; Popescu, R.; Gerthsen, D.; Buscarino, G.; Cavallaro, G.; Giammona, G. Decagram-Scale Synthesis of Multicolor Carbon Nanodots: Self-Tracking Nanoheaters with Inherent and Selective Anticancer Properties. *ACS Appl. Mater. Interfaces* **2022**, acsami.1c19599, doi:10.1021/ACSAMI.1C19599.

160. Arcudi, F.; Dordevic, L.; Prato, M. Synthesis, Separation, and Characterization of Small and Highly Fluorescent Nitrogen-Doped Carbon Nanodots. *Angew. Chemie - Int. Ed.* **2016**, *55*, 2107–2112, doi:10.1002/ANIE.201510158.

161. Crista, D.M.A.; da Silva, J.C.G.E.; da Silva, L.P. Evaluation of Different Bottom-up Routes for the Fabrication of Carbon Dots. *Nanomaterials* **2020**, *10*, 1–15, doi:10.3390/nano10071316.

162. Huo, X.; Shen, H.; Xu, Y.; Shao, J.; Liu, R.; Zhang, Z. Fluorescence Properties of Carbon Dots Synthesized by Different Solvents for PH Detector. *Opt. Mater. (Amst).* **2022**, *123*, 111889, doi:10.1016/j.optmat.2021.111889.

163. Li, L.; Dong, T. Photoluminescence Tuning in Carbon Dots: Surface Passivation or/and Functionalization, Heteroatom Doping. *J. Mater. Chem. C* **2018**, *6*, 7944–7970, doi:10.1039/c7tc05878k.

164. Pan, D.; Zhang, J.; Li, Z.; Wu, M. Hydrothermal Route for Cutting Graphene Sheets into Blue-Luminescent Graphene Quantum Dots., doi:10.1002/adma.200902825.

165. Fuyuno, N.; Kozawa, D.; Miyauchi, Y.; Mouri, S.; Kitaura, R.; Shinohara, H.; Yasuda, T.; Komatsu, N.; Matsuda, K.; Fuyuno, N.; et al. Drastic Change in Photoluminescence Properties of Graphene Quantum Dots by Chromatographic Separation. **2014**, doi:10.1002/adom.201400200.

166. Shinde, D.B.; Pillai, V.K. Electrochemical Preparation of Luminescent Graphene Quantum Dots from Multiwalled Carbon Nanotubes., doi:10.1002/chem.201201043.

167. Messina, F.; Sciortino, L.; Popescu, R.; Venezia, A.M.; Sciortino, A.; Buscarino, G.; Agnello, S.; Schneider, R.; Gerthsen, D.; Cannas, M.; et al. Fluorescent Nitrogen-Rich Carbon Nanodots with an Unexpected β-C3N4 Nanocrystalline Structure. *J. Mater. Chem. C* **2016**, *4*, 2598–2605, doi:10.1039/C5TC04096E.

168. Sciortino, L.; Sciortino, A.; Popescu, R.; Schneider, R.; Gerthsen, D.; Agnello, S.; Cannas, M.; Messina, F. Tailoring the Emission Color of Carbon Dots through Nitrogen-Induced Changes of Their Crystalline Structure. **2018**, doi:10.1021/acs.jpcc.8b04514.

169. Bourlinos, A.B.; Stassinopoulos, A.; Anglos, D.; Zboril, R.; Karakassides, M.; Giannelis, E.P. Surface Functionalized Carbogenic Quantum Dots. *Small* **2008**, *4*, 455–458, doi:10.1002/smll.200700578.

170. Tong, G.; Wang, J.; Wang, R.; Guo, X.; He, L.; Qiu, F.; Wang, G.; Zhu, B.; Zhu, X.; Liu, T. Amorphous Carbon Dots with High Two-Photon Fluorescence for Cellular Imaging Passivated by Hyperbranched Poly(Amino Amine). *J. Mater. Chem. B* **2015**, *3*, 700–706, doi:10.1039/C4TB01643B.

171. Margraf, J.T.; Strauss, V.; Guldi, D.M.; Clark, T. The Electronic Structure of Amorphous Carbon Nanodots. **2015**, doi:10.1021/jp510620j.

172. Peng, H.; Travas-Sejdic, J.; Polymer, † Simple Aqueous Solution Route to Luminescent Carbogenic Dots from Carbohydrates. *Chem. Mater* **2009**, *21*, 5563, doi:10.1021/cm901593y.

173. Sun, Y.P.; Zhou, B.; Lin, Y.; Wang, W.; Fernando, K.A.S.; Pathak, P.; Meziani, M.J.; Harruff, B.A.; Wang, X.; Wang, H.; et al. Quantum-Sized Carbon Dots for Bright and Colorful Photoluminescence. *J. Am. Chem. Soc.* **2006**, *128*, 7756–7757, doi:10.1021/ja062677d.

174. Schipper, M.L.; Iyer, G.; Koh, A.L.; Cheng, Z.; Ebenstein, Y.; Aharoni, A.; Keren, S.; Bentolila, L.A.; Li, J.; Rao, J.; et al. Particle Size, Surface Coating, and PEGylation Influence the Biodistribution of Quantum Dots in Living Mice. *Small* **2009**, *5*, 126–134, doi:10.1002/smll.200800003.

175. Li, Y.; Bai, G.; Zeng, S.; Hao, J. Theranostic Carbon Dots with Innovative NIR-II Emission for in Vivo Renal-Excreted Optical Imaging and Photothermal Therapy. *ACS Appl. Mater. Interfaces* **2019**, *11*, 4737–4744, doi:10.1021/acsami.8b14877.

176. Xu, Z.Q.; Yang, Q.Q.; Lan, J.Y.; Zhang, J.Q.; Peng, W.; Jin, J.C.; Jiang, F.L.; Liu, Y. Interactions between Carbon Nanodots with Human Serum Albumin and γ-Globulins: The Effects on the Transportation Function. *J. Hazard. Mater.* **2016**, *301*, 242–249, doi:10.1016/J.JHAZMAT.2015.08.062.

177. Bao, X.; Yuan, Y.; Chen, J.; Zhang, B.; Li, D.; Zhou, D.; Jing, P.; Xu, G.; Wang, Y.; Holá, K.; et al. In Vivo Theranostics with Near-Infrared-Emitting Carbon Dots—Highly Efficient Photothermal Therapy Based on Passive Targeting after Intravenous Administration. *Light Sci. Appl.* **2018**, *7*, 1–11, doi:10.1038/s41377-018-0090-1.

178. Zhu, S.; Wang, L.; Li, B.; Song, Y.; Zhao, X.; Zhang, G.; Zhang, S.; Lu, S.; Zhang, J.; Wang, H.; et al. Investigation of Photoluminescence Mechanism of Graphene Quantum Dots and Evaluation of Their Assembly into Polymer Dots. *Carbon N. Y.* **2014**, *77*, 462–472, doi:10.1016/J.CARBON.2014.05.051.

179. Peng, J.; Gao, W.; Kumar Gupta, B.; Liu, Z.; Romero-Aburto, R.; Ge, L.; Song, L.; Alemany, L.B.; Zhan, X.; Gao, G.; et al. Graphene Quantum Dots Derived from Carbon Fibers. **2012**, doi:10.1021/nl2038979.

180. Eda, G.; Lin, Y.Y.; Mattevi, C.; Yamaguchi, H.; Chen, H.A.; Chen, I.S.; Chen, C.W.; Chhowalla, M. Blue Photoluminescence from Chemically Derived Graphene Oxide. *Adv. Mater.* **2010**, *22*, 505–509, doi:10.1002/ADMA.200901996.

181. Li, H.; He, X.; Kang, Z.; Huang, H.; Liu, Y.; Liu, J.; Lian, S.; Him Tsang, C.A.;

Yang, X.; Lee, S.-T.; et al. Quantum Dots Water-Soluble Fluorescent Carbon Quantum Dots and Photocatalyst Design**., doi:10.1002/anie.200906154.

182. Sciortino, A.; Ferrante, F.; Mauro, N.; Buscarino, G.; Sciortino, L.; Giammona, G.; Cannas, M.; Duca, D.; Messina, F. Disclosing the Emissive Surface Traps in Green-Emitting Carbon Nanodots. *Carbon N. Y.* **2021**, *173*, 454–461, doi:10.1016/J.CARBON.2020.11.030.

183. Zhu, S.; Song, Y.; Zhao, X.; Shao, J.; Zhang, J.; Yang, B. The Photoluminescence Mechanism in Carbon Dots (Graphene Quantum Dots, Carbon Nanodots, and Polymer Dots): Current State and Future Perspective. *Nano Res. 2014 82* **2015**, *8*, 355–381, doi:10.1007/S12274-014-0644-3.

184. Zhang, Y.; Hu, Y.; Lin, J.; Fan, Y.; Li, Y.; Lv, Y.; Liu, X. Excitation Wavelength Independence: Toward Low-Threshold Amplified Spontaneous Emission from Carbon Nanodots. *ACS Appl. Mater. Interfaces* **2016**, *8*, 25454–25460, doi:10.1021/acsami.6b08315.

185. Sciortino, A.; Marino, E.; Van Dam, B.; Schall, P.; Cannas, M.; Messina, F. Solvatochromism Unravels the Emission Mechanism of Carbon Nanodots. *J. Phys. Chem. Lett* **2016**, *7*, 3419–3423, doi:10.1021/acs.jpclett.6b01590.

186. Ghosh, S.; Chizhik, A.M.; Karedla, N.; Dekaliuk, M.O.; Gregor, I.; Schuhmann, H.; Seibt, M.; Bodensiek, K.; Schaap, I.A.T.; Schulz, O.; et al. Photoluminescence of Carbon Nanodots: Dipole Emission Centers and Electron-Phonon Coupling. *Nano Lett.* **2014**, *14*, 5656–5661, doi:10.1021/nl502372x.

187. Demchenko, A.P.; Dekaliuk, M.O. The Origin of Emissive States of Carbon Nanoparticles Derived from Ensemble-Averaged and Single-Molecular Studies. *Nanoscale* **2016**, *8*, 14057–14069, doi:10.1039/c6nr02669a.

188. van Dam, B.; Nie, H.; Ju, B.; Marino, E.; J Paulusse, J.M.; Schall, P.; Li, M.; Dohnalová van Dam, K.B.; Marino, E.; Schall, P.; et al. Communication Excitation-Dependent Photoluminescence from Single-Carbon Dots. *Small* **2017**, *13*, 48, doi:10.1002/smll.201702098.

189. Zheng, M.; Li, Y.; Liu, S.; Wang, W.; Xie, Z.; Jing, X. One-Pot To Synthesize Multifunctional Carbon Dots for Near Infrared Fluorescence Imaging and Photothermal Cancer Therapy. *ACS Appl. Mater. Interfaces* **2016**, *8*, doi:10.1021/acsami.6b07453.

190. Li, D.; Han, D.; Qu, S.N.; Liu, L.; Jing, P.T.; Zhou, D.; Ji, W.Y.; Wang, X.Y.; Zhang, T.F.; Shen, D.Z. Supra-(Carbon Nanodots) with a Strong Visible to near-Infrared Absorption Band and Efficient Photothermal Conversion. *Light Sci. Appl.* **2016**, *5*, 1–8, doi:10.1038/lsa.2016.120.

191. Geng, B.; Yang, D.; Pan, D.; Wang, L.; Zheng, F.; Shen, W.; Zhang, C.; Li, X. NIR-Responsive Carbon Dots for Efficient Photothermal Cancer Therapy at Low Power Densities. *Carbon N. Y.* **2018**, *134*, 153–162, doi:10.1016/j.carbon.2018.03.084.

192. Wu, Y.; Liu, X.; Wu, Q.; Yi, J.; Zhang, G. Differentiation and Determination of Metal Ions Using Fluorescent Sensor Array Based on Carbon Nanodots. *Sensors*

Actuators, B Chem. **2017**, *246*, 680–685, doi:10.1016/j.snb.2017.02.132.

193. Zhou, L.; Lin, Y.; Huang, Z.; Ren, J.; Qu, X. Carbon Nanodots as Fluorescence Probes for Rapid, Sensitive, and Label-Free Detection of Hg2+ and Biothiols in Complex Matrices. *Chem. Commun.* **2012**, *48*, 1147–1149, doi:10.1039/C2CC16791C.

194. Shi, B.; Su, Y.; Zhang, L.; Huang, M.; Liu, R.; Zhao, S. Nitrogen and Phosphorus Co-Doped Carbon Nanodots as a Novel Fluorescent Probe for Highly Sensitive Detection of Fe 3+ in Human Serum and Living Cells. **2016**, doi:10.1021/acsami.6b01325.

195. Mei, S.; Wei, X.; Hu, Z.; Wei, C.; Su, D.; Yang, D.; Zhang, G.; Zhang, W.; Guo, R. Amphipathic Carbon Dots with Solvent-Dependent Optical Properties and Sensing Application. *Opt. Mater. (Amst).* **2019**, *89*, 224–230, doi:10.1016/J.OPTMAT.2019.01.021.

196. Zhang, T.; Dong, S.; Zhao, F.; Deng, M.; Fu, Y.; Lü, C. Tricolor Emissive Carbon Dots for Ultra-Wide Range PH Test Papers and Bioimaging. *Sensors Actuators, B Chem.* **2019**, *298*, doi:10.1016/J.SNB.2019.126869.

197. Li, Y.; Premathilaka, S.; Liu, C.; Zhang, F.; Hu, J.; Gao, W.; Zhang, M. Article 605028 (2021) A Mini Review on PH-Sensitive Photoluminescence in Carbon Nanodots. *Front. Chem* **2021**, *8*, 605028, doi:10.3389/fchem.2020.605028.

198. Zhao, J.-L.; Luo, Q.-Y.; Ruan, Q.; Chen, K.; Liu, C.; Redshaw, C.; Jin, Z. Red/Green Tunable-Emission Carbon Nanodots for Smart Visual Precision PH Sensing. *Cite This Chem. Mater* **2021**, *33*, 6091–6098, doi:10.1021/acs.chemmater.1c01620.

199. Qian, Z.; Ma, J.; Shan, X.; Feng, H.; Shao, L.; Chen, J. Highly Luminescent N-Doped Carbon Quantum Dots as an Effective Multifunctional Fluorescence Sensing Platform., doi:10.1002/chem.201304374.

200. Wang, C.; Jiang, K.; Wu, Q.; Wu, J.; Zhang, C. "Turn-on" Nanothermometer in Living Cells., doi:10.1002/chem.201602795.

201. Chandra, S.; Pathan, S.H.; Mitra, S.; Modha, B.H.; Goswami, A.; Pramanik, P. Tuning of Photoluminescence on Different Surface Functionalized Carbon Quantum Dots{. **2012**, doi:10.1039/c2ra00030j.

202. Onyancha, R.B.; Ukhurebor, K.E.; Aigbe, U.O.; Mogire, N.B.; Chanzu, I.; Kitoto, V.A.; Kusuma, H.S.; Darmokoesoemo, H. A Review of the Capabilities of Carbon Dots for the Treatment and Diagnosis of Cancer-Related Diseases. *J. Drug Deliv. Sci. Technol.* **2022**, 103946, doi:10.1016/J.JDDST.2022.103946.

203. Baker, S.N.; Baker, G.A. Luminescent Carbon Nanodots: Emergent Nanolights. *Angew. Chemie Int. Ed.* **2010**, *49*, 6726–6744, doi:10.1002/ANIE.200906623.

204. Wang, H.; Mukherjee, S.; Yi, J.; Banerjee, P.; Chen, Q.; Zhou, S. Biocompatible Chitosan-Carbon Dot Hybrid Nanogels for NIR-Imaging-Guided Synergistic Photothermal-Chemo Therapy. *ACS Appl. Mater. Interfaces* **2017**, *9*, 18639–18649, doi:10.1021/acsami.7b06062.

205. Mauro, N.; Utzeri, M.A.; Drago, S.E.; Buscarino, G.; Cavallaro, G.; Giammona, G. Carbon Nanodots as Functional Excipient to Develop Highly Stable and Smart PLGA Nanoparticles Useful in Cancer Theranostics. *Pharm. 2020, Vol. 12, Page 1012* **2020**, *12*, 1012, doi:10.3390/PHARMACEUTICS12111012.

206. Zou, L.; Wang, H.; He, B.; Zeng, L.; Tan, T.; Cao, H.; He, X.; Zhang, Z.; Guo, S.; Li, Y. Current Approaches of Photothermal Therapy in Treating Cancer Metastasis with Nanotherapeutics. *Theranostics* **2016**, *6*, 762–772, doi:10.7150/THNO.14988.

207. Bogart, L.K.; Pourroy, G.; Murphy, C.J.; Puntes, V.; Pellegrino, T.; Rosenblum, D.; Peer, D.; Lévy, R. Nanoparticles for Imaging, Sensing, and Therapeutic Intervention. *ACS Nano* **2014**, *8*, 3107–3122, doi:10.1021/nn500962q.

208. Beik, J.; Abed, Z.; Ghoreishi, F.S.; Hosseini-Nami, S.; Mehrzadi, S.; Shakeri-Zadeh, A.; Kamrava, S.K. Nanotechnology in Hyperthermia Cancer Therapy: From Fundamental Principles to Advanced Applications. *J. Control. Release* **2016**, *235*, 205–221, doi:10.1016/J.JCONREL.2016.05.062.

209. Chu, K.F.; Dupuy, D.E. Thermal Ablation of Tumours: Biological Mechanisms and Advances in Therapy. *Nat. Rev. Cancer* **2014**, *14*, 199–208, doi:10.1038/nrc3672.

210. Chen, Q.; Wen, J.; Li, H.; Xu, Y.; Liu, F.; Sun, S. Recent Advances in Different Modal Imaging-Guided Photothermal Therapy. *Biomaterials* **2016**, *106*, 144–166, doi:10.1016/j.biomaterials.2016.08.022.

211. Chen, Q.; Liang, C.; Wang, X.; He, J.; Li, Y.; Liu, Z. An Albumin-Based Theranostic Nano-Agent for Dual-Modal Imaging Guided Photothermal Therapy to Inhibit Lymphatic Metastasis of Cancer Post Surgery. *Biomaterials* **2014**, *35*, 9355–9362, doi:10.1016/j.biomaterials.2014.07.062.

212. Mauro, N.; Scialabba, C.; Cavallaro, G.; Licciardi, M.; Giammona, G. Biotin-Containing Reduced Graphene Oxide-Based Nanosystem as a Multieffect Anticancer Agent: Combining Hyperthermia with Targeted Chemotherapy. *Biomacromolecules* **2015**, *16*, 2766–2775, doi:10.1021/acs.biomac.5b00705.

213. Sarkar, S.; Levi-Polyachenko, N. Conjugated Polymer Nano-Systems for Hyperthermia, Imaging and Drug Delivery. *Adv. Drug Deliv. Rev.* **2020**, doi:10.1016/j.addr.2020.01.002.

214. Lavrik, I.; Golks, A.; Krammer, P.H. Death Receptor Signaling. *J. Cell Sci.* **2005**, *118*, 265–267, doi:10.1242/jcs.01610.

215. Wang, S.; El-Deiry, W.S. TRAIL and Apoptosis Induction by TNF-Family Death Receptors. *Oncogene* **2003**, *22*, 8628–8633, doi:10.1038/sj.onc.1207232.

216. Gross, A.; McDonnell, J.M.; Korsmeyer, S.J. BCL-2 Family Members and the Mitochondria in Apoptosis. *Genes Dev.* **1999**, *13*, 1899–1911, doi:10.1101/gad.13.15.1899.

217. Adams, J.M.; Cory, S. The Bcl-2 Protein Family: Arbiters of Cell Survival. *Science (80-.).* **1998**, *281*, 1322–1326, doi:10.1126/SCIENCE.281.5381.1322.

218. Su, Z.; Yang, Z.; Xie, L.; Dewitt, J.P.; Chen, Y. Cancer Therapy in the Necroptosis Era. *Cell Death Differ.* **2016**, *23*, 748–756, doi:10.1038/cdd.2016.8.

219. Sharifi, M.; Hosseinali, S.H.; Saboury, A.A.; Szegezdi, E.; Falahati, M. Involvement of Planned Cell Death of Necroptosis in Cancer Treatment by Nanomaterials: Recent Advances and Future Perspectives. *J. Control. Release* **2019**, *299*, 121–137, doi:10.1016/j.jconrel.2019.02.007.

220. Gong, Y.; Fan, Z.; Luo, G.; Yang, C.; Huang, Q.; Fan, K.; Cheng, H.; Jin, K.; Ni, Q.; Yu, X.; et al. The Role of Necroptosis in Cancer Biology and Therapy. *Mol. Cancer* **2019**, *18*, doi:10.1186/S12943-019-1029-8.

221. Chen, Q.; Kang, J.; Fu, C. The Independence of and Associations among Apoptosis, Autophagy, and Necrosis. *Signal Transduct. Target. Ther.* **2018**, doi:10.1038/s41392-018-0018-5.

222. Su, Z.; Yang, Z.; Xie, L.; Dewitt, J.P.; Chen, Y. Cancer Therapy in the Necroptosis Era. *Cell Death Differ.* **2016**, *23*, 748–756, doi:10.1038/CDD.2016.8.

223. Zang, X.; Song, J.; Li, Y.; Han, Y. Targeting Necroptosis as an Alternative Strategy in Tumor Treatment: From Drugs to Nanoparticles. *J. Control. Release* **2022**, *349*, 213–226, doi:10.1016/j.jconrel.2022.06.060.

224. Nicosia, A.; Cavallaro, G.; Costa, S.; Utzeri, M.A.; Cuttitta, A.; Giammona, G.; Mauro, N. Carbon Nanodots for On Demand Chemophotothermal Therapy Combination to Elicit Necroptosis: Overcoming Apoptosis Resistance in Breast Cancer Cell Lines. *Cancers 2020, Vol. 12, Page 3114* **2020**, *12*, 3114, doi:10.3390/CANCERS12113114.

225. Zhou, B.; Guo, Z.; Lin, Z.; Zhang, L.; Jiang, B.P.; Shen, X.C. Recent Insights into Near-Infrared Light-Responsive Carbon Dots for Bioimaging and Cancer Phototherapy. *Inorg. Chem. Front.* **2019**, *6*, 1116–1128, doi:10.1039/c9qi00201d.

226. Choi, Y.; Kim, S.; Choi, M.H.; Ryoo, S.R.; Park, J.; Min, D.H.; Kim, B.S. Highly Biocompatible Carbon Nanodots for Simultaneous Bioimaging and Targeted Photodynamic Therapy in Vitro and in Vivo. *Adv. Funct. Mater.* **2014**, *24*, 5781–5789, doi:10.1002/ADFM.201400961.

227. Perillo, B.; Di Donato, M.; Pezone, A.; Di Zazzo, E.; Giovannelli, P.; Galasso, G.; Castoria, G.; Migliaccio, A. ROS in Cancer Therapy: The Bright Side of the Moon. *Exp. Mol. Med.* **2020**, *52*, 192–203, doi:10.1038/s12276-020-0384-2.

228. Huang, P.; Lin, J.; Wang, X.; Wang, Z.; Zhang, C.; He, M.; Wang, K.; Chen, F.; Li, Z.; Shen, G.; et al. Light-Triggered Theranostics Based on Photosensitizer-Conjugated Carbon Dots for Simultaneous Enhanced-Fluorescence Imaging and Photodynamic Therapy. *Adv. Mater.* **2012**, *24*, 5104–5110, doi:10.1002/adma.201200650.

229. Lovell, J.F.; Liu, T.W.B.; Chen, J.; Zheng, G. Activatable Photosensitizers for Imaging and Therapy. *Chem. Rev.* **2010**, *110*, 2839–2857, doi:10.1021/cr900236h.

230. Zhang, L.; Lin, Z.; Yu, Y.X.; Jiang, B.P.; Shen, X.C. Multifunctional Hyaluronic Acid-Derived Carbon Dots for Self-Targeted Imaging-Guided Photodynamic Therapy. *J. Mater. Chem. B* **2018**, *6*, 6534–6543, doi:10.1039/c8tb01957f.

231. Guo, X.L.; Ding, Z.Y.; Deng, S.M.; Wen, C.C.; Shen, X.C.; Jiang, B.P.; Liang, H. A Novel Strategy of Transition-Metal Doping to Engineer Absorption of Carbon Dots for near-Infrared Photothermal/Photodynamic Therapies. *Carbon N. Y.* **2018**, *134*, 519–530, doi:10.1016/j.carbon.2018.04.001.

232. Huang, P.; Lin, J.; Wang, X.; Wang, Z.; Zhang, C.; He, M.; Wang, K.; Chen, F.; Li, Z.; Shen, G.; et al. Light-Triggered Theranostics Based on Photosensitizer-Conjugated Carbon Dots for Simultaneous Enhanced-Fluorescence Imaging and Photodynamic Therapy. **2012**, doi:10.1002/adma.201200650.

233. Zhang, T.; Qu, J.; Yao, Y.; Zhang, Y.; Ma, Y.; Wu, D.; Cao, Y.; Yang, M.; Zhang, Y.; Tang, M.; et al. N-Doped Carbon Dots Triggered the Induction of ROS-Mediated Cytoprotective Autophagy in Hepa1-6 Cells. *Chemosphere* **2020**, *251*, doi:10.1016/J.CHEMOSPHERE.2020.126440.

234. Zheng, W.; Wei, M.; Li, S.; Le, W. Nanomaterial-Modulated Autophagy: Underlying Mechanisms and Functional Consequences. *Nanomedicine* **2016**, *11*, 1417–1430, doi:10.2217/NNM-2016-0040.

235. Ryter, S.W.; Cloonan, S.M.; Choi, A.M.K. Autophagy: A Critical Regulator of Cellular Metabolism and Homeostasis. *Mol. Cells* **2013**, *36*, 7–16, doi:10.1007/S10059-013-0140-8.

236. Li, Y.; Wu, S.; Zhang, J.; Zhou, R.; Cai, X. Sulphur Doped Carbon Dots Enhance Photodynamic Therapy via PI3K/Akt Signalling Pathway. *Cell Prolif.* **2020**, *53*, doi:10.1111/CPR.12821.

237. Fang, C.; Gu, L.; Smerin, D.; Mao, S.; Xiong, X. The Interrelation between Reactive Oxygen Species and Autophagy in Neurological Disorders. *Oxid. Med. Cell. Longev.* **2017**, *2017*, doi:10.1155/2017/8495160.

238. Havrdova, M.; Hola, K.; Skopalik, J.; Tomankova, K.; Petr, M.; Cepe, K.; Polakova, K.; Tucek, J.; Bourlinos, A.B.; Zboril, R. Toxicity of Carbon Dots-Effect of Surface Functionalization on the Cell Viability, Reactive Oxygen Species Generation and Cell Cycle. *Carbon N. Y.* **2016**, *99*, 238–248, doi:10.1016/J.CARBON.2015.12.027.

239. Zuowei Ji, Durga M. Arvapalli, Wendi Zhang, Ziyu Yin, and J.W. Nitrogen and Sulfur Co-Doped Carbon Nanodots in Living EA.Hy926 and A549 Cells: Oxidative Stress Effect and Mitochondria Targeting. *J. Mater. Sci.* **2020**, *14*, 58–60, doi:10.1557/s0883769400063247.

240. Abbasi Kajani, A.; Haghjooy Javanmard, S.; Asadnia, M.; Razmjou, A. Recent Advances in Nanomaterials Development for Nanomedicine and Cancer. *ACS Appl. Bio Mater.* **2021**, *4*, 5908–5925, doi:10.1021/ACSABM.1C00591.

241. Kumari, P.; Ghosh, B.; Biswas, S. Nanocarriers for Cancer-Targeted Drug Delivery. *https://doi.org/10.3109/1061186X.2015.1051049* **2015**, *24*, 179–191, doi:10.3109/1061186X.2015.1051049.

242. Sharifi, M.; Hosseinali, S.H.; Saboury, A.A.; Szegezdi, E.; Falahati, M. Involvement of Planned Cell Death of Necroptosis in Cancer Treatment by Nanomaterials: Recent Advances and Future Perspectives. *J. Control. Release* **2019**, *299*, 121–137, doi:10.1016/j.jconrel.2019.02.007.

243. Choi, Y.; Kim, S.; Choi, M.H.; Ryoo, S.R.; Park, J.; Min, D.H.; Kim, B.S. Highly Biocompatible Carbon Nanodots for Simultaneous Bioimaging and Targeted Photodynamic Therapy In Vitro and In Vivo. *Adv. Funct. Mater.* **2014**, *24*, 5781–5789, doi:10.1002/ADFM.201400961.

244. Tian, Z.; Zhang, X.; Li, D.; Zhou, D.; Jing, P.; Shen, D.; Qu, S.; Zboril, R.; Rogach, A.L.; Tian, Z.; et al. Full-Color Inorganic Carbon Dot Phosphors for White-Light-Emitting Diodes. *Adv. Opt. Mater.* **2017**, *5*, 1700416, doi:10.1002/ADOM.201700416.

245. Zhang, Q.; Yue, S.; Quilty, C.D.; Jin, Y.-S.; Wang, P.; Teng, S.-H.; Demazeau, G. Solvothermal Processes: New Trends in Materials Chemistry. *J. Phys. Conf. Ser.* **2008**, *121*, 082003, doi:10.1088/1742-6596/121/8/082003.

246. Feng, S.H.; Li, G.H. Hydrothermal and Solvothermal Syntheses. *Mod. Inorg. Synth. Chem. Second Ed.* **2017**, 73–104, doi:10.1016/B978-0-444-63591-4.00004-5.

247. Huo, F.; Liang, W.; Tang, Y.; Zhang, W.; Liu, X.; Pei, D.; Wang, H.; Jia, W.; Jia, P.; Yang, F. Full-Color Carbon Dots with Multiple Red-Emission Tuning: On/off Sensors, in Vitro and in Vivo Multicolor Bioimaging. *J. Mater. Sci.* **2019**, *54*, 6815–6825, doi:10.1007/S10853-019-03370-6.

248. Aggarwal, P.; Hall, J.B.; McLeland, C.B.; Dobrovolskaia, M.A.; McNeil, S.E. Nanoparticle Interaction with Plasma Proteins as It Relates to Particle Biodistribution, Biocompatibility and Therapeutic Efficacy. *Adv. Drug Deliv. Rev.* **2009**, *61*, 428–437, doi:10.1016/J.ADDR.2009.03.009.

249. Petros, R.A.; Desimone, J.M. Strategies in the Design of Nanoparticles for Therapeutic Applications. *Nat. Rev. Drug Discov. 2010 98* **2010**, *9*, 615–627, doi:10.1038/nrd2591.

250. Dawson, A.; Allan, D.R.; Belmonte, S.A.; Clark, S.J.; David, W.I.F.; McGregor, P.A.; Parsons, S.; Pulham, C.R.; Sawyer, L. Effect of High Pressure on the Crystal Structures of Polymorphs of Glycine. *Cryst. Growth Des.* **2005**, *5*, 1415–1427, doi:10.1021/CG049716M.

251. Bao, L.; Liu, C.; Zhang, Z.L.; Pang, D.W. Photoluminescence-Tunable Carbon Nanodots: Surface-State Energy-Gap Tuning. *Adv. Mater.* **2015**, *27*, 1663–1667, doi:10.1002/adma.201405070.

252. Zhou, F.; Da, X.; Ou, Z.; Wu, B.; Resasco, D.E.; Chen, W.R. Cancer Photothermal Therapy in the Near-Infrared Region by Using Single-Walled Carbon Nanotubes. **2009**, *14*, 021009, doi:10.1117/1.3078803.

253. Ghosh, S.; Dutta, S.; Gomes, E.; Carroll, D.; D'Agostino, R.; Olson, J.; Guthold, M.; Gmeiner, W.H. Increased Heating Efficiency and Selective Thermal Ablation of Malignant Tissue with DNA-Encased Multiwalled Carbon Nanotubes. *ACS*

Nano **2009**, *3*, 2667–2673, doi:10.1021/NN900368B.

254. Mauro, N.; Scialabba, C.; Agnello, S.; Cavallaro, G.; Giammona, G. Folic Acid-Functionalized Graphene Oxide Nanosheets via Plasma Etching as a Platform to Combine NIR Anticancer Phototherapy and Targeted Drug Delivery. *Mater. Sci. Eng. C* **2020**, *107*, 110201, doi:10.1016/J.MSEC.2019.110201.

255. Mauro, N.; Scialabba, C.; Pitarresi, G.; Giammona, G. Enhanced Adhesion and in Situ Photothermal Ablation of Cancer Cells in Surface-Functionalized Electrospun Microfiber Scaffold with Graphene Oxide. *Int. J. Pharm.* **2017**, *526*, 167–177, doi:10.1016/J.IJPHARM.2017.04.045.

256. Sroka, R.; Schaffer, M.; Fuchs, C.; Pongratz, T.; Schrader-Reichard, U.; Busch, M.; Schaffer, P.M.; Dü, E.; Baumgartner, R. Effects on the Mitosis of Normal and Tumor Cells Induced by Light Treatment of Different Wavelengths. *Lasers Surg. Med.* **1999**, *25*, 263–271, doi:10.1002/(SICI)1096-9101(1999)25:3.

257. Zhang, P.; Hu, C.; Ran, W.; Meng, J.; Yin, Q.; Li, Y. Recent Progress in Light-Triggered Nanotheranostics for Cancer Treatment. *Theranostics* **2016**, *6*, 948, doi:10.7150/THNO.15217.

258. Chen, Q.; Wen, J.; Li, H.; Xu, Y.; Liu, F.; Sun, S. Recent Advances in Different Modal Imaging-Guided Photothermal Therapy. *Biomaterials* **2016**, *106*, 144–166, doi:10.1016/J.BIOMATERIALS.2016.08.022.

259. Zheng, M.; Zhao, P.; Luo, Z.; Gong, P.; Zheng, C.; Zhang, P.; Yue, C.; Gao, D.; Ma, Y.; Cai, L. Robust ICG Theranostic Nanoparticles for Folate Targeted Cancer Imaging and Highly Effective Photothermal Therapy. *ACS Appl. Mater. Interfaces* **2014**, *6*, 6709–6716, doi:10.1021/AM5004393.

260. Nam, J.; Son, S.; Ochyl, L.J.; Kuai, R.; Schwendeman, A.; Moon, J.J. Chemo-Photothermal Therapy Combination Elicits Anti-Tumor Immunity against Advanced Metastatic Cancer. *Nat. Commun. 2018 91* **2018**, *9*, 1–13, doi:10.1038/s41467-018-03473-9.

261. Fernald, K.; Kurokawa, M. Evading Apoptosis in Cancer. *Trends Cell Biol.* **2013**, *23*, 620–633, doi:10.1016/J.TCB.2013.07.006.

262. Chen, D.; Ganesh, S.; Wang, W.; Amiji, M. The Role of Surface Chemistry in Serum Protein Corona-Mediated Cellular Delivery and Gene Silencing with Lipid Nanoparticles. *Nanoscale* **2019**, *11*, 8760–8775, doi:10.1039/C8NR09855G.

263. Li, Y.; Lee, J.S. Insights into Characterization Methods and Biomedical Applications of Nanoparticle–Protein Corona. *Mater. 2020, Vol. 13, Page 3093* **2020**, *13*, 3093, doi:10.3390/MA13143093.

264. Tiwari, A.; Bhatia, P.; Randhawa, J.K. Systematic Spectroscopic Investigation of Structural Changes and Corona Formation of Bovine Serum Albumin over Magneto-Fluorescent Nanoparticles. *Dalt. Trans.* **2020**, *49*, 12380–12389, doi:10.1039/D0DT02414G.

265. Maity, A.; Pal, U.; Chakraborty, B.; Sengupta, C.; Sau, A.; Chakraborty, S.;

Basu, S. Preferential Photochemical Interaction of Ru (III) Doped Carbon Nano Dots with Bovine Serum Albumin over Human Serum Albumin. *Int. J. Biol. Macromol.* **2019**, *137*, 483–494, doi:10.1016/J.IJBIOMAC.2019.06.126.

266. Song, Y.; Wang, H.; Zhang, L.; Lai, B.; Liu, K.; Tan, M. Protein Corona Formation of Human Serum Albumin with Carbon Quantum Dots from Roast Salmon. *Food Funct.* **2020**, *11*, 2358–2367, doi:10.1039/C9FO02967B.

267. Czarnecka, J.; Wisniewski, M.; Forbot, N.; Bolibok, P.; Terzyk, A.P.; Roszek, K. Cytotoxic or Not? Disclosing the Toxic Nature of Carbonaceous Nanomaterials through Nano-Bio Interactions. *Materials (Basel).* **2020**, *13*, 1–13, doi:10.3390/MA13092060.

268. Khanal, D.; Lei, Q.; Pinget, G.; Cheong, D.A.; Gautam, A.; Yusoff, R.; Su, B.; Yamaguchi, S.; Kondyurin, A.; Knowles, J.C.; et al. The Protein Corona Determines the Cytotoxicity of Nanodiamonds: Implications of Corona Formation and Its Remodelling on Nanodiamond Applications in Biomedical Imaging and Drug Delivery. *Nanoscale Adv.* **2020**, *2*, 4798–4812, doi:10.1039/D0NA00231C.

269. Şimşek, S.; Şüküroğlu, A.A.; Yetkin, D.; Özbek, B.; Battal, D.; Genç, R. DNA-Damage and Cell Cycle Arrest Initiated Anti-Cancer Potency of Super Tiny Carbon Dots on MCF7 Cell Line. *Sci. Reports 2020 101* **2020**, *10*, 1–14, doi:10.1038/s41598-020-70796-3.

270. Ji, Z.; Arvapalli, D.M.; Zhang, W.; Yin, Z.; Wei, J. Nitrogen and Sulfur Co-Doped Carbon Nanodots in Living EA.Hy926 and A549 Cells: Oxidative Stress Effect and Mitochondria Targeting. *J. Mater. Sci.* **2020**, *55*, 6093–6104, doi:10.1007/S10853-020-04419-7.

271. Miao, W.; Shim, G.; Kim, G.; Lee, S.; Lee, H.J.; Kim, Y.B.; Byun, Y.; Oh, Y.K. Image-Guided Synergistic Photothermal Therapy Using Photoresponsive Imaging Agent-Loaded Graphene-Based Nanosheets. *J. Control. Release* **2015**, *211*, 28–36, doi:10.1016/J.JCONREL.2015.05.280.

272. Calixto, G.M.F.; Bernegossi, J.; De Freitas, L.M.; Fontana, C.R.; Chorilli, M.; Grumezescu, A.M. Nanotechnology-Based Drug Delivery Systems for Photodynamic Therapy of Cancer: A Review. *Mol. 2016, Vol. 21, Page 342* **2016**, *21*, 342, doi:10.3390/MOLECULES21030342.

273. Estebanez, N.; González-Béjar, M.; Pérez-Prieto, J. Polysulfonate Cappings on Upconversion Nanoparticles Prevent Their Disintegration in Water and Provide Superior Stability in a Highly Acidic Medium. *ACS Omega* **2019**, *4*, 3012–3019, doi:10.1021/ACSOMEGA.8B03015.

274. Sui, L.; Jin, W.; Li, S.; Liu, D.; Jiang, Y.; Chen, A.; Liu, H.; Shi, Y.; Ding, D.; Jin, M. Ultrafast Carrier Dynamics of Carbon Nanodots in Different PH Environments. *Phys. Chem. Chem. Phys.* **2016**, *18*, 3838–3845, doi:10.1039/C5CP07558K.

275. Yang, H.; Liu, Y.; Guo, Z.; Lei, B.; Zhuang, J.; Zhang, X.; Liu, Z.; Hu, C. Hydrophobic Carbon Dots with Blue Dispersed Emission and Red Aggregation-

Induced Emission. *Nat. Commun.* **2019**, doi:10.1038/s41467-019-09830-6.

276. Qian, M.; Du, Y.; Wang, S.; Li, C.; Jiang, H.; Shi, W.; Chen, J.; Wang, Y.; Wagner, E.; Huang, R. Highly Crystalline Multicolor Carbon Nanodots for Dual-Modal Imaging-Guided Photothermal Therapy of Glioma. *ACS Appl. Mater. Interfaces* **2018**, doi:10.1021/acsami.7b19716.

277. Hua, X.W.; Bao, Y.W.; Zeng, J.; Wu, F.G. Ultrasmall All-In-One Nanodots Formed via Carbon Dot-Mediated and Albumin-Based Synthesis: Multimodal Imaging-Guided and Mild Laser-Enhanced Cancer Therapy. *ACS Appl. Mater. Interfaces* **2018**, *10*, 42077–42087, doi:10.1021/acsami.8b16065.

278. Breitenborn, H.; Dong, J.; Piccoli, R.; Bruhacs, A.; Besteiro, L. V.; Skripka, A.; Wang, Z.M.; Govorov, A.O.; Razzari, L.; Vetrone, F.; et al. Quantifying the Photothermal Conversion Efficiency of Plasmonic Nanoparticles by Means of Terahertz Radiation. *APL Photonics* **2019**, *4*, doi:10.1063/1.5128524.

279. Chen, W.R.; Adams, R.L.; Carubelli, R.; Nordquist, R.E. Laser-Photosensitizer Assisted Immunotherapy: A Novel Modality for Cancer Treatment. *Cancer Lett.* **1997**, *115*, 25–30, doi:10.1016/S0304-3835(97)04707-1.

280. Savchuk, O.A.; Carvajal, J.J.; Massons, J.; Aguiló, M.; Díaz, F. Determination of Photothermal Conversion Efficiency of Graphene and Graphene Oxide through an Integrating Sphere Method. *Carbon N. Y.* **2016**, *103*, 134–141, doi:10.1016/j.carbon.2016.02.075.

281. Choi, Y.; Kim, S.; Choi, M.-H.; Ryoo, S.-R.; Park, J.; Min, D.-H.; Kim, B.-S. Photodynamic Therapy: Highly Biocompatible Carbon Nanodots for Simultaneous Bioimaging and Targeted Photodynamic Therapy In Vitro and In Vivo (Adv. Funct. Mater. 37/2014). *Adv. Funct. Mater.* **2014**, *24*, 5774–5774, doi:10.1002/ADFM.201470245.

282. Chien, Y.H.; Chan, K.K.; Anderson, T.; Kong, K.V.; Ng, B.K.; Yong, K.T. Advanced Near-Infrared Light-Responsive Nanomaterials as Therapeutic Platforms for Cancer Therapy. *Adv. Ther.* **2019**, *2*, doi:10.1002/ADTP.201800090.

283. Labavić, D.; Ladjimi, M.T.; Courtade, E.; Pfeuty, B.; Thommen, Q. Mammalian Cell Sensitivity to Hyperthermia in Various Cell Lines: A New Universal and Predictive Description. **2020**, *37*, 506–516, doi:10.1080/02656736.2020.1762005.

284. Savchuk, O.A.; Carvajal, J.J.; Massons, J.; Aguiló, M.; Díaz, F. Determination of Photothermal Conversion Efficiency of Graphene and Graphene Oxide through an Integrating Sphere Method. *Carbon N. Y.* **2016**, *103*, 134–141, doi:10.1016/J.CARBON.2016.02.075.

285. Kim, T.H.; Sirdaarta, J.P.; Zhang, Q.; Eftekhari, E.; St. John, J.; Kennedy, D.; Cock, I.E.; Li, Q. Selective Toxicity of Hydroxyl-Rich Carbon Nanodots for Cancer Research. *Nano Res.* **2018**, *11*, 2204–2216, doi:10.1007/S12274-017-1838-2.

286. Wang, C.; Jiang, K.; Wu, Q.; Wu, J.; Zhang, C. Green Synthesis of Red-Emitting

Carbon Nanodots as a Novel "Turn-on" Nanothermometer in Living Cells. *Chem. - A Eur. J.* **2016**, *22*, 14475–14479, doi:10.1002/CHEM.201602795.

287. del Rosal, B.; Jia, B.; Jaque, D. Beyond Phototherapy: Recent Advances in Multifunctional Fluorescent Nanoparticles for Light-Triggered Tumor Theranostics. *Adv. Funct. Mater.* **2018**, *28*, 1–25, doi:10.1002/adfm.201803733.

288. Wang, J.; Qiu, J. A Review of Carbon Dots in Biological Applications. *J. Mater. Sci.* **2016**, *51*, 4728–4738, doi:10.1007/S10853-016-9797-7.

289. Namdari, P.; Negahdari, B.; Eatemadi, A. Synthesis, Properties and Biomedical Applications of Carbon-Based Quantum Dots: An Updated Review. *Biomed. Pharmacother.* **2017**, *87*, 209–222, doi:10.1016/j.biopha.2016.12.108.

290. Yan, F.; Jiang, Y.; Sun, & X.; Bai, Z.; Zhang, Y.; Zhou, X. Surface Modification and Chemical Functionalization of Carbon Dots: A Review., doi:10.1007/s00604-018-2953-9.

291. Zhang, M.; Moore, R.B.; Long, T.E. Melt Transesterification and Characterization of Segmented Block Copolyesters Containing 2,2,4,4-Tetramethyl-1,3-Cyclobutanediol. *J. Polym. Sci. Part A Polym. Chem.* **2012**, *50*, 3710–3718, doi:10.1002/POLA.26176.

292. Vaidya, A.A.; Hussain, I.; Gaugler, M.; Smith, D.A. Synthesis of Graft Copolymers of Chitosan-Poly(Caprolactone) by Lipase Catalysed Reactive Extrusion. *Carbohydr. Polym.* **2019**, *217*, 98–109, doi:10.1016/J.CARBPOL.2019.03.081.

293. Ren, J.; Stagi, L.; Innocenzi, P. Fluorescent Carbon Dots in Solid-State: From Nanostructures to Functional Devices. *Prog. Solid State Chem.* **2021**, *62*, doi:10.1016/J.PROGSOLIDSTCHEM.2020.100295.

294. Bastioli, C.; Cella, G.; Deltredici, G.; Milizia, T. Biodegradable Polyesters Obtained by Reactive Extrusion 2004.

295. Siqi Xue, Zhenguo Liu, Ting Liu, E.S. TRANSESTERIFICATION OF POLYESTERS 2006, 1–11.

296. Kim, H.J.; Hillmyer, M.A.; Ellison, C.J. Enhanced Polyester Degradation through Transesterification with Salicylates. *J. Am. Chem. Soc* **2021**, *143*, 8, doi:10.1021/jacs.1c07229.

297. Dave, K.; Gomes, V.G. Bioresorbable Poly(Lactic Acid) and Organic Quantum Dot-Based Nanocomposites: Luminescent Scaffolds for Enhanced Osteogenesis and Real-Time Monitoring. *J. Nanostructure Chem.* **2022**, *12*, 951–962, doi:10.1007/s40097-021-00456-z.

298. Ruiz, A.J.; Garg, S.; Streeter, S.S.; Giallorenzi, M.K.; LaRochelle, E.P.M.; Samkoe, K.S.; Pogue, B.W. 3D Printing Fluorescent Material with Tunable Optical Properties. *Sci. Reports 2021 111* **2021**, *11*, 1–10, doi:10.1038/s41598-021-96496-0.

299. Hedayati, F.; Moshiri-Gomchi, N.; Assaran-Ghomi, M.; Sabahi, S.; Bahri-Laleh, N.; Mehdipour-Ataei, S.; Mokhtari-Aliabad, J.; Mirmohammadi, S.A.

Preparation and Properties of Enhanced Nanocomposites Based on PLA/PC Blends Reinforced with Silica Nanoparticles. *Polym. Adv. Technol.* **2020**, *31*, 566–573, doi:10.1002/PAT.4797.

300. Qian, M.; Du, Y.; Wang, S.; Li, C.; Jiang, H.; Shi, W.; Chen, J.; Wang, Y.; Wagner, E.; Huang, R. Highly Crystalline Multicolor Carbon Nanodots for Dual-Modal Imaging-Guided Photothermal Therapy of Glioma. **2018**, doi:10.1021/acsami.7b19716.

301. Bolhassani, A.; Javanzad, S.; Saleh, T.; Hashemi, M.; Aghasadeghi, M.R.; Sadat, S.M. Polymeric Nanoparticles. **2013**, *10*, 321–332, doi:10.4161/HV.26796.

302. Su, C.; Liu, Y.; Li, R.; Wu, W.; Fawcett, J.P.; Gu, J. Absorption, Distribution, Metabolism and Excretion of the Biomaterials Used in Nanocarrier Drug Delivery Systems. *Adv. Drug Deliv. Rev.* **2019**, *143*, 97–114, doi:10.1016/J.ADDR.2019.06.008.

303. Kumari, A.; Yadav, S.K.; Yadav, S.C. Biodegradable Polymeric Nanoparticles Based Drug Delivery Systems. *Colloids Surfaces B Biointerfaces* **2010**, *75*, 1–18, doi:10.1016/J.COLSURFB.2009.09.001.

304. Mauro; Cavallaro; Giammona Near-Infrared, Light-Triggered, On-Demand Anti-Inflammatories and Antibiotics Release by Graphene Oxide/Elecrospun PCL Patch for Wound Healing. *C — J. Carbon Res.* **2019**, *5*, 63, doi:10.3390/C5040063.

305. Pitarresi, G.; Martorana, A.; Palumbo, F.S.; Fiorica, C.; Giammona, G. New Gellan Gum-Graft-Poly(D,L-Lactide-Co-Glycolide) Copolymers as Promising Bioinks: Synthesis and Characterization. *Int. J. Biol. Macromol.* **2020**, *162*, 1653–1667, doi:10.1016/J.IJBIOMAC.2020.07.254.

306. Craparo, E.F.; Drago, S.E.; Giammona, G.; Cavallaro, G. Production of Polymeric Micro- and Nanostructures with Tunable Properties as Pharmaceutical Delivery Systems. *Polymer (Guildf).* **2020**, *200*, 122596, doi:10.1016/J.POLYMER.2020.122596.

307. Kumari, A.; Yadav, S.K.; Yadav, S.C. Biodegradable Polymeric Nanoparticles Based Drug Delivery Systems. *Colloids Surfaces B Biointerfaces* **2010**, *75*, 1–18, doi:10.1016/J.COLSURFB.2009.09.001.

308. Danhier, F.; Ansorena, E.; Silva, J.M.; Coco, R.; Le Breton, A.; Préat, V. PLGA-Based Nanoparticles: An Overview of Biomedical Applications. *J. Control. Release* **2012**, *161*, 505–522, doi:10.1016/J.JCONREL.2012.01.043.

309. Pandita, D.; Kumar, S.; Lather, V. Hybrid Poly(Lactic-Co-Glycolic Acid) Nanoparticles: Design and Delivery Prospectives. *Drug Discov. Today* **2015**, *20*, 95–104, doi:10.1016/J.DRUDIS.2014.09.018.

310. Ghitman, J.; Biru, E.I.; Stan, R.; Iovu, H. Review of Hybrid PLGA Nanoparticles: Future of Smart Drug Delivery and Theranostics Medicine. *Mater. Des.* **2020**, *193*, 108805, doi:10.1016/J.MATDES.2020.108805.

311. Fonte, P.; Soares, S.; Sousa, F.; Costa, A.; Seabra, V.; Reis, S.; Sarmento, B.

Stability Study Perspective of the Effect of Freeze-Drying Using Cryoprotectants on the Structure of Insulin Loaded into PLGA Nanoparticles. *Biomacromolecules* **2014**, *15*, 3753–3765, doi:10.1021/BM5010383.

312. Hernández-Giottonini, K.Y.; Rodríguez-Córdova, R.J.; Gutiérrez-Valenzuela, C.A.; Peñuñuri-Miranda, O.; Zavala-Rivera, P.; Guerrero-Germán, P.; Lucero-Acuña, A. PLGA Nanoparticle Preparations by Emulsification and Nanoprecipitation Techniques: Effects of Formulation Parameters. *RSC Adv.* **2020**, *10*, 4218–4231, doi:10.1039/C9RA10857B.

313. Jeong, Y.I.; Shim, Y.H.; Kim, C.; Lim, G.T.; Choi, K.C.; Yoon, C. Effect of Cryoprotectants on the Reconstitution of Surfactant-Free Nanoparticles of Poly(DL-Lactide-Co-Glycolide). **2008**, *22*, 593–601, doi:10.1080/02652040500162659.

314. Jaque, D.; Martínez Maestro, L.; Del Rosal, B.; Haro-Gonzalez, P.; Benayas, A.; Plaza, J.L.; Martín Rodríguez, E.; García Solé, J. Nanoparticles for Photothermal Therapies. *Nanoscale* **2014**, *6*, 9494–9530, doi:10.1039/C4NR00708E.

315. Taghizadehghalehjoughi, A.; Hacimuftuoglu, A.; Cetin, M.; Ugur, A.B.; Galateanu, B.; Mezhuev, Y.; Okkay, U.; Taspinar, N.; Taspinar, M.; Uyanik, A.; et al. Effect of Metformin/Irinotecan-Loaded Poly-Lactic-Co-Glycolic Acid Nanoparticles on Glioblastoma: In Vitro and in Vivo Studies. **2018**, *13*, 1595–1606, doi:10.2217/NNM-2017-0386.

316. Wang, H.; Mukherjee, S.; Yi, J.; Banerjee, P.; Chen, Q.; Zhou, S. Biocompatible Chitosan-Carbon Dot Hybrid Nanogels for NIR-Imaging-Guided Synergistic Photothermal-Chemo Therapy. *ACS Appl. Mater. Interfaces* **2017**, *9*, 18639–18649, doi:10.1021/ACSAMI.7B06062.

317. Choi, K.Y.; Han, H.S.; Lee, E.S.; Shin, J.M.; Almquist, B.D.; Lee, D.S.; Park, J.H. Hyaluronic Acid–Based Activatable Nanomaterials for Stimuli-Responsive Imaging and Therapeutics: Beyond CD44-Mediated Drug Delivery. *Adv. Mater.* **2019**, *31*, doi:10.1002/ADMA.201803549.

318. Huang, Y.-Q.; Sun, L.-J.; Zhang, R.; Hu, J.; Liu, X.-F.; Jiang, R.-C.; Fan, Q.-L.; Wang, L.-H.; Huang, W. Hyaluronic Acid Nanoparticles Based on a Conjugated Oligomer Photosensitizer: Target-Specific Two-Photon Imaging, Redox-Sensitive Drug Delivery, and Synergistic Chemo-Photodynamic Therapy. **2019**, doi:10.1021/acsabm.9b00130.

319. Hill, T.K.; Abdulahad, A.; Kelkar, S.S.; Marini, F.C.; Long, T.E.; Provenzale, J.M.; Mohs, A.M. Indocyanine Green-Loaded Nanoparticles for Image-Guided Tumor Surgery. **2015**, doi:10.1021/bc5005679.

320. Amorim, S.; Soares da Costa, D.; Mereiter, S.; Pashkuleva, I.; Reis, C.A.; Reis, R.L.; Pires, R.A. Multilayer Platform to Model the Bioactivity of Hyaluronic Acid in Gastric Cancer. *Mater. Sci. Eng. C* **2021**, *119*, 111616, doi:10.1016/J.MSEC.2020.111616.

321. Chen, X.; Liu, Z.; Parker, S.G.; Zhang, X.; Gooding, # J Justin; Ru, Y.; Liu, Y.; Zhou, Y. Light-Induced Hydrogel Based on Tumor-Targeting Mesoporous Silica

Nanoparticles as a Theranostic Platform for Sustained Cancer Treatment. **2016**, doi:10.1021/acsami.6b02562.

322. Mauro, N.; Drago, S.E.; Cavallaro, G.; Giammona, G. Near-Infrared, Light-Triggered, On-Demand Anti-Inflammatories and Antibiotics Release by Graphene Oxide/Elecrospun PCL Patch for Wound Healing. *C 2019, Vol. 5, Page 63* **2019**, *5*, 63, doi:10.3390/C5040063.

323. Pravata, L.; Braud, C.; Boustta, M.; Ghzaoui, A. El; Tømmeraas, K.; Guillaumie, F.; Schwach-Abdellaoui, K.; Vert, M. New Amphiphilic Lactic Acid Oligomer-Hyaluronan Conjugates: Synthesis and Physicochemical Characterization., doi:10.1021/bm700843m.

324. Fiorica, C.; Mauro, N.; Pitarresi, G.; Scialabba, C.; Palumbo, F.S.; Giammona, G. Double-Network-Structured Graphene Oxide-Containing Nanogels as Photothermal Agents for the Treatment of Colorectal Cancer. **2017**, doi:10.1021/acs.biomac.6b01897.

325. Some, S.; Gwon, A.R.; Hwang, E.; Bahn, G.H.; Yoon, Y.; Kim, Y.; Kim, S.H.; Bak, S.; Yang, J.; Jo, D.G.; et al. Cancer Therapy Using Ultrahigh Hydrophobic Drug-Loaded Graphene Derivatives. *Sci. Reports 2014 41* **2014**, *4*, 1–9, doi:10.1038/srep06314.

326. Sciortino, A.; Gazzetto, M.; Buscarino, G.; Popescu, R.; Schneider, R.; Giammona, G.; Gerthsen, D.; Rohwer, E.J.; Mauro, N.; Feurer, T.; et al. Disentangling Size Effects and Spectral Inhomogeneity in Carbon Nanodots by Ultrafast Dynamical Hole-Burning. *Nanoscale* **2018**, *10*, 15317–15323, doi:10.1039/C8NR02953A.

327. Yang, H.; Liu, Y.; Guo, Z.; Lei, B.; Zhuang, J.; Zhang, X.; Liu, Z.; Hu, C. Hydrophobic Carbon Dots with Blue Dispersed Emission and Red Aggregation-Induced Emission. *Nat. Commun. 2019 101* **2019**, *10*, 1–11, doi:10.1038/s41467-019-09830-6.

328. Smith, A.M.; Mancini, M.C.; Nie, S. Bioimaging: Second Window for in Vivo Imaging. *Nat. Nanotechnol.* **2009**, *4*, 710–711, doi:10.1038/NNANO.2009.326.

329. Huang, Y.-Q.; Sun, L.-J.; Zhang, R.; Hu, J.; Liu, X.-F.; Jiang, R.-C.; Fan, Q.-L.; Wang, L.-H.; Huang, W. Hyaluronic Acid Nanoparticles Based on a Conjugated Oligomer Photosensitizer: Target-Specific Two-Photon Imaging, Redox-Sensitive Drug Delivery, and Synergistic Chemo-Photodynamic Therapy. **2019**, doi:10.1021/acsabm.9b00130.

330. Pitarresi, G.; Palumbo, F.S.; Albanese, A.; Fiorica, C.; Picone, P.; Giammona, G. Self-Assembled Amphiphilic Hyaluronic Acid Graft Copolymers for Targeted Release of Antitumoral Drug. **2010**, *18*, 264–276, doi:10.3109/10611860903434027.

331. Nam, J.; Son, S.; Ochyl, L.J.; Kuai, R.; Schwendeman, A.; Moon, J.J. Chemo-Photothermal Therapy Combination Elicits Anti-Tumor Immunity against Advanced Metastatic Cancer. *Nat. Commun. 2018 91* **2018**, *9*, 1–13, doi:10.1038/s41467-018-03473-9.

332. Minotti, G.; Menna, P.; Salvatorelli, E.; Cairo, G.; Gianni, L. Anthracyclines: Molecular Advances and Pharmacologic Developments in Antitumor Activity and Cardiotoxicity. *Pharmacol. Rev.* **2004**, *56*, 185–229, doi:10.1124/PR.56.2.6.

333. Pilco-Ferreto, N.; Calaf, G.M. Influence of Doxorubicin on Apoptosis and Oxidative Stress in Breast Cancer Cell Lines. *Int. J. Oncol.* **2016**, *49*, 753–762, doi:10.3892/IJO.2016.3558.

334. Luo, S.; Rubinsztein, D.C. Apoptosis Blocks Beclin 1-Dependent Autophagosome Synthesis: An Effect Rescued by Bcl-XL. *Cell Death Differ.* **2010**, *17*, 268–277, doi:10.1038/CDD.2009.121.

335. Kim, H.; Kwak, G.; Kim, K.; Yoon, H.Y.; Kwon, I.C. Theranostic Designs of Biomaterials for Precision Medicine in Cancer Therapy. *Biomaterials* **2019**, *213*, doi:10.1016/J.BIOMATERIALS.2019.05.018.

336. Chen, Q.; Kang, J.; Fu, C. The Independence of and Associations among Apoptosis, Autophagy, and Necrosis. *Signal Transduct. Target. Ther.* **2018**, *3*, doi:10.1038/S41392-018-0018-5.

337. Goodall, M.L.; Fitzwalter, B.E.; Zahedi, S.; Wu, M.; Rodriguez, D.; Mulcahy-Levy, J.M.; Green, D.R.; Morgan, M.; Cramer, S.D.; Thorburn, A. The Autophagy Machinery Controls Cell Death Switching between Apoptosis and Necroptosis. *Dev. Cell* **2016**, *37*, 337–349, doi:10.1016/j.devcel.2016.04.018.

338. Shi, G.; Jia, P.; Chen, H.; Bao, L.; Feng, F.; Tang, H. Necroptosis Occurs in Osteoblasts during Tumor Necrosis Factor-α Stimulation and Caspase-8 Inhibition. *Brazilian J. Med. Biol. Res.* **2018**, *52*, doi:10.1590/1414-431X20187844.

339. Jänicke, R.U. MCF-7 Breast Carcinoma Cells Do Not Express Caspase-3. *Breast Cancer Res. Treat. 2008 1171* **2008**, *117*, 219–221, doi:10.1007/S10549-008-0217-9.

340. Singh, T.R.; Shankar, S.; Srivastava, R.K. HDAC Inhibitors Enhance the Apoptosis-Inducing Potential of TRAIL in Breast Carcinoma. *Oncogene* **2005**, *24*, 4609–4623, doi:10.1038/SJ.ONC.1208585.

341. Gong, Y.; Fan, Z.; Luo, G.; Yang, C.; Huang, Q.; Fan, K.; Cheng, H.; Jin, K.; Ni, Q.; Yu, X.; et al. The Role of Necroptosis in Cancer Biology and Therapy. *Mol. Cancer 2019 181* **2019**, *18*, 1–17, doi:10.1186/S12943-019-1029-8.

342. Jouan-Lanhouet, S.; Arshad, M.I.; Piquet-Pellorce, C.; Martin-Chouly, C.; Le Moigne-Muller, G.; Van Herreweghe, F.; Takahashi, N.; Sergent, O.; Lagadic-Gossmann, D.; Vandenabeele, P.; et al. TRAIL Induces Necroptosis Involving RIPK1/RIPK3-Dependent PARP-1 Activation. *Cell Death Differ.* **2012**, *19*, 2003–2014, doi:10.1038/CDD.2012.90.

343. Y. Lin; A. Devin; Y. Rodriguez; Z. G. Liu. Cleavage of the Death Domain Kinase RIP by Caspase-8 Prompts TNF-Induced Apoptosis. **1999**, doi:10.1101/gad.13.19.2514.

344. Molnár, T.; Mázló, A.; Tslaf, V.; Szöllősi, A.G.; Emri, G.; Koncz, G. Current

Translational Potential and Underlying Molecular Mechanisms of Necroptosis. *Cell Death Dis. 2019 1011* **2019**, *10*, 1–21, doi:10.1038/s41419-019-2094-z.

345. Pandolfi, L.; Frangipane, V.; Bocca, C.; Marengo, A.; Genta, E.T.; Bozzini, S.; Morosini, M.; D'Amato, M.; Vitulo, S.; Monti, M.; et al. Hyaluronic Acid–Decorated Liposomes as Innovative Targeted Delivery System for Lung Fibrotic Cells. *Mol. 2019, Vol. 24, Page 3291* **2019**, *24*, 3291, doi:10.3390/MOLECULES24183291.

346. Tripodo, G.; Wischke, C.; Neffe, A.T.; Lendlein, A. Efficient Synthesis of Pure Monotosylated Beta-Cyclodextrin and Its Dimers. *Carbohydr. Res.* **2013**, *381*, 59–63, doi:10.1016/J.CARRES.2013.08.018.

347. Tang, W.; Ng, S.C. Facile Synthesis of Mono-6-Amino-6-Deoxy-α-, β-, γ-Cyclodextrin Hydrochlorides for Molecular Recognition, Chiral Separation and Drug Delivery. *Nat. Protoc.* **2008**, *3*, 691–697, doi:10.1038/NPROT.2008.37.

348. Challa, R.; Ahuja, A.; Ali, J.; Khar, R.K. Cyclodextrins in Drug Delivery: An Updated Review. *AAPS PharmSciTech* **2005**, *6*, 329–357, doi:10.1208/pt060243.

349. Yang, T.; Huang, J.L.; Wang, Y.T.; Zheng, A.Q.; Shu, Y.; Wang, J.H. β-Cyclodextrin-Decorated Carbon Dots Serve as Nanocarriers for Targeted Drug Delivery and Controlled Release. *ChemNanoMat* **2019**, *5*, 479–487, doi:10.1002/cnma.201800528.

350. Uekama, K. Cyclodextrins in Drug Delivery System. *Adv. Drug Deliv. Rev.* **2005**, *36*, 1–2, doi:10.1016/S0169-409X(98)00051-9.

351. Cruz-Burgos, M.; Losada-Garcia, A.; Cruz-Hernández, C.D.; Cortés-Ramírez, S.A.; Camacho-Arroyo, I.; Gonzalez-Covarrubias, V.; Morales-Pacheco, M.; Trujillo-Bornios, S.I.; Rodríguez-Dorantes, M. New Approaches in Oncology for Repositioning Drugs: The Case of PDE5 Inhibitor Sildenafil. *Front. Oncol.* **2021**, *11*, 1–13, doi:10.3389/fonc.2021.627229.

352. Pantziarka, P.; Sukhatme, V.; Crispino, S.; Bouche, G.; Meheus, L.; Sukhatme, P. Repurposing Drugs in Oncology (ReDO)—Selective PDE5 Inhibitors as Anti-Cancer Agents. *Ecancermedicalscience* **2018**, *12*, 1–22, doi:10.3332/ecancer.2018.824.

353. Camacho-arroyo, I.; Gonzalez-covarrubias, V.; Morales-pacheco, M.; Trujillo-bornios, S.I. New Approaches in Oncology for Repositioning Drugs : The Case of PDE5 Inhibitor Sildena Fi L. **2021**, *11*, 1–13, doi:10.3389/fonc.2021.627229.

354. Pantziarka, P.; Sukhatme, V.; Crispino, S.; Bouche, G.; Meheus, L.; Sukhatme, V.P. Repurposing Drugs in Oncology (ReDO)— Selective PDE5 Inhibitors as Anti-Cancer Agents. **1853**, 1–22, doi:10.3332/ecancer.2018.824.

355. Piazza, G.A.; Ward, A.; Chen, X.; Maxuitenko, Y.; Coley, A.; Aboelella, N.S.; Buchsbaum, D.J.; Boyd, M.R.; Keeton, A.B. PDE5 and PDE10 Inhibition Activates CGMP / PKG Signaling to Block Wnt / b -Catenin Transcription , Cancer Cell Growth , and Tumor Immunity. *Drug Discov. Today* **2020**, *25*, 1521–1527, doi:10.1016/j.drudis.2020.06.008.

356. Marques, J.G.; Gaspar, V.M.; Markl, D.; Costa, E.C.; Gallardo, E.; Correia, I.J. Co-Delivery of Sildenafil (Viagra ®) and Crizotinib for Synergistic and Improved Anti-Tumoral Therapy. **2014**, 2516–2528, doi:10.1007/s11095-014-1347-x.

357. Ghorbani, M.; Zarei, M.; Mahmoodzadeh, F.; Roshangar, L.; Nikzad, B. Improvement of Delivery and Anticancer Activity of Doxorubicin by Sildenafil Citrate Encapsulated with a New Redox and PH-Responsive Nanogel. *Int. J. Polym. Mater. Polym. Biomater.* **2020**, *0*, 1–10, doi:10.1080/00914037.2020.1765362.

358. Xiao-Long Mei, Yang Yang, Y.-J.Z.; Li, Y.; Zhao, J.-M.; Qiu, J.-G.; Zhang, W.-J.; Qi-Wei; Jiang; Xue, Y.-Q.; Zheng, D.-W.; Chen, Y.; et al. Sildenafil Inhibits the Growth of Human Colorectal Cancer in Vitro and in Vivo. *Am J Cancer Res* **2015**, *11*, 3311–3324, doi:10.3892/or.2015.3857.

359. Keats, T.; Rosengren, R.J.; Ashton, J.C. The Rationale for Repurposing Sildenafil for Lung Cancer Treatment. **2018**, 367–374, doi:10.2174/1871520617666171103100959.

360. Das, A.; Durrant, D.; Mitchell, C.; Mayton, E.; Hoke, N.N.; Salloum, F.N.; Park, M.A.; Qureshi, I.; Lee, R.; Dent, P.; et al. Sildenafil Increases Chemotherapeutic Efficacy of Doxorubicin in Prostate Cancer and Ameliorates Cardiac Dysfunction. *Proc. Natl. Acad. Sci. U. S. A.* **2010**, *107*, 18202–18207, doi:10.1073/PNAS.1006965107.

361. Das, A.; Durrant, D.; Mitchell, C.; Dent, P.; Batra, S.K.; Kukreja, R.C. Sildenafil (Viagra) Sensitizes Prostate Cancer Cells to Doxorubicin-Mediated Apoptosis through CD95. **2016**, *7(4):4399-413, doi:10.18632/oncotarget.6749*.

362. Di, X.; Gennings, C.; Bear, H.D.; Graham, L.J.; Sheth, C.M.; White, K.L.; Gewirtz, D.A. Influence of the Phosphodiesterase-5 Inhibitor, Sildenafil, on Sensitivity to Chemotherapy in Breast Tumor Cells. *Breast Cancer Res. Treat.* **2010**, doi:10.1007/s10549-010-0765-7.

363. Lin, F.; Hoogendijk, L.; Buil, L.; Beijnen, J.H.; Van Tellingen, O. Sildenafil Is Not a Useful Modulator of ABCB1 and ABCG2 Mediated Drug Resistance in Vivo. *Eur. J. Cancer* **2013**, *49*, 2059–2064, doi:10.1016/J.EJCA.2012.12.028.

364. Sarfati, M.; Mateo, V.; Baudet, S.; Rubio, M.; Fernandez, C.; Davi, F.; Binet, J.L.; Delic, J.; Merle-Béral, H. Sildenafil and Vardenafil, Types 5 and 6 Phosphodiesterase Inhibitors, Induce Caspase-Dependent Apoptosis of B-Chronic Lymphocytic Leukemia Cells. *Blood* **2003**, *101*, 265–269, doi:10.1182/BLOOD-2002-01-0075.

365. Feng, W.; Guo, J.; Huang, H.; Xia, B.; Liu, H.; Li, J.; Lin, S.; Li, T.; Liu, J.; Li, H. Human Normal Bronchial Epithelial Cells: A Novel in Vitro Cell Model for Toxicity Evaluation. *PLoS One* **2015**, *10*, 1–14, doi:10.1371/journal.pone.0123520.

366. Cozens, A.L.; Yezzi, M.J.; Kunzelmann, K.; Ohrui, T.; Chin, L.; Eng, K.; Finkbeiner, W.E.; Widdicombe, J.H.; Gruenert, D.C. CFTR Expression and

Chloride Secretion in Polarized Immortal Human Bronchial Epithelial Cells. *Am. J. Respir. Cell Mol. Biol.* **1994**, *10*, 38–47, doi:10.1165/ajrcmb.10.1.7507342.

367. Lin, C.; Lin, G.; Xin, Z.; Lue, T.F. Expression , Distribution and Regulation of Phosphodiesterase 5. **2006**, 3439–3457.

368. Greish, K.; Fateel, M.; Abdelghany, S.; Rachel, N.; Bakhiet, M.; Alsaie, A. Sildenafil Citrate Improves the Delivery and Anticancer Activity of Doxorubicin Formulations in a Mouse Model of Breast Cancer. *J. Drug Target.* **2017**, *0*, 000, doi:10.1080/1061186X.2017.1405427.

369. Booth, L.; Roberts, J.L.; Cruickshanks, N.; Conley, A.; Durrant, D.E.; Das, A.; Fisher, P.B.; Kukreja, R.C.; Grant, S.; Poklepovic, A.; et al. Phosphodiesterase 5 Inhibitors Enhance Chemotherapy Killing in Gastrointestinal/Genitourinary Cancer Cells. *Mol. Pharmacol.* **2014**, *85*, 408–419, doi:10.1124/MOL.113.090043.

370. Yarlagadda, K.; Hassani, J.; Foote, I.P.; Markowitz, J. The Role of Nitric Oxide in Melanoma. *Biochim. Biophys. Acta - Rev. Cancer* **2017**, *1868*, 500–509, doi:10.1016/j.bbcan.2017.09.005.

371. Mishra, D.; Patel, V.; Banerjee, D. Nitric Oxide and S-Nitrosylation in Cancers: Emphasis on Breast Cancer. *Breast Cancer Basic Clin. Res.* **2020**, *14*, doi:10.1177/1178223419882688.

372. Mauro, N.; Schillaci, D.; Varvarà, P.; Cusimano, M.G.; Geraci, D.M.; Giuffrè, M.; Cavallaro, G.; Maida, C.M.; Giammona, G. Branched High Molecular Weight Glycopolypeptide with Broad-Spectrum Antimicrobial Activity for the Treatment of Biofilm Related Infections. *ACS Appl. Mater. Interfaces* **2018**, *10*, 318–331, doi:10.1021/ACSAMI.7B16573.

373. Palumbo, F.S.; Pitarresi, G.; Mandracchia, D.; Tripodo, G.; Giammona, G. New Graft Copolymers of Hyaluronic Acid and Polylactic Acid: Synthesis and Characterization. *Carbohydr. Polym.* **2006**, *66*, 379–385, doi:10.1016/J.CARBPOL.2006.03.023.

374. Ghasemian, E.; Vatanara, A.; Rouholamini Najafabadi, A.; Rouini, M.R.; Gilani, K.; Darabi, M. Preparation, Characterization and Optimization of Sildenafil Citrate Loaded PLGA Nanoparticles by Statistical Factorial Design. *DARU J. Pharm. Sci.* **2013**, *21*, 68, doi:10.1186/2008-2231-21-68.

Acknowledgments

Thanks to AteN Center for the technique and strumental support to perform the Atomic Force Spectroscopy Analysis (AFM) (Laboratorio di Meccanica dei Materiali e dei Biomateriali), thermal camera measurements, contact angle measurements and Size Exclusion Chromatography (SEC) analysis (Laboratorio di Preparazione e Analisi dei Biomateriali).